Exact Quantum Monte Carlo Methods for Correlated Electron Systems

Dissertation

zur Erlangung des akademischen Grades

Doktor der Naturwissenschaften

am Fachbereich

Physik, Mathematik und Informatik

der Johannes Gutenberg-Universität Mainz

Daniel C. Rost

geboren in Wiesbaden

Mainz, 04. Mai 2015

Eingereicht am: 04.05.2015

im Fachbereich Physik, Mathematik und Informatik

1. Gutachter der Dissertation:

2. Gutachter der Dissertation:

Contents

1. Introduction

The central goal in the field of condensed matter theory is the fundamental understanding of physical phenomena observed in various materials, as well as reliable predictions of their properties in all parameter regimes, resolutions, and on all length scales. In particular, within the huge range of different types of materials, the class of strongly correlated systems turned out to be candidates for exotic effects, like non-classical electronic properties and magnetic ordering phenomena. These phenomena are not only interesting due to the underlying fundamental physical effects, but also due to their important role for technical applications. Famous examples are Mott metal-insulator transitions [Mot68] and high-temperature superconductivity [LW06].

For a full (non-relativistic) description of condensed matter, the problem can be described by the following general Hamiltonian (cf., e.g., [Czy08]):

$$\hat{\mathbf{H}} = \underbrace{\sum_{k=1}^{N_K} \frac{\hat{\mathbf{P}}_k^2}{2M_k}}_{E_{\text{kin}}\ \text{core}} + \underbrace{\sum_{i=1}^{N_e} \frac{\hat{\mathbf{p}}_i^2}{2m_e}}_{E_{\text{kin}}e^-} + \underbrace{\sum_{i<j} \frac{e^2}{|\mathbf{r}_i - \mathbf{r}_j|}}_{e^-e^-\text{int.}} + \underbrace{\sum_{l<m} \frac{e^2 Z_l Z_m}{|\mathbf{R}_l - \mathbf{R}_m|}}_{\text{core core int.}} - \underbrace{\sum_{r,s} \frac{e^2 Z_r}{|\mathbf{R}_r - \mathbf{r}_s|}}_{e^-\ \text{core int.}} . \quad (1.1)$$

This formulation was already stated in the 1920s, early after the discovery of the Schrödinger equation in 1926 [Sch26]. The atomic theory of solid-state physics and chemistry was fundamentally defined. Even though Eq. (1.1) was found more than 90 years ago, a fully satisfying solution is still not found today. The complexity of the theory was realized by Paul Dirac already in 1929 [Dir29]:

> *"The underlying physical laws necessary for the mathematical theory of a large part of physics and the whole of chemistry are thus completely known, and the difficulty is only that the exact application of these laws leads to equations much too complicated to be soluble. It therefore becomes desirable that approximate practical methods of applying quantum mechanics should be developed, which can lead to an explanation of the main features of complex atomic systems without too much computation."*

Still, Paul Dirac's awareness describes the special character of the research in the field of solid-state theory perfectly. We are not able to solve Eq. (1.1) for the $\mathcal{O}(\sim 10^{80})$ atoms in the universe (*"Theory of almost everything"* [LP00]), not even for a small piece of matter $\mathcal{O}(\sim 10^{23})$. The two major methodological approaches in solid-state theory are the development of models that are able to capture specific physical properties and the development of numerical tools, to solve these still highly

complicated quantum mechanical problems. However, the usage of abstract models, combined with the understanding of their controlled approximation, provides a powerful tool for a deep understanding of the connection between underlying physics and observed phenomena.

In this thesis, I will focus on numerical methods for the solution of two models for strongly correlated electron systems: The fermionic *Hubbard model* [Hub59] and the *Kondo lattice model* [Kon64, Don77]. Both models emerge from a *tight-binding approach* and describe localized electrons. The Hubbard model gained not only relevance beyond the electronic context in the theory of strongly correlated systems, but also received even more attention recently, due to rapid progress in the field of ultra-cold quantum gases [GME$^+$02, Blo05], in which it is possible to realize the Hubbard model in experiments on optical lattices. Coulomb interactions are treated purely locally in the Hubbard model; this picture corresponds to the physical mechanisms in transition-metal compounds (e.g., vanadium(III) oxide) [IFT98] where the interacting electrons are confined in narrow d- and f-shells. One of the great achievements of the Hubbard model was the correct prediction of the Mott metal-insulator transition [KV04, Blü02]. After more than 50 years since the original proposal of the model, there are still remaining questions, e.g., to which extent the physics of high-temperature superconductors is captured by the model.

The Kondo lattice model is a candidate for the description of *heavy fermion materials* (e.g., $CeAl_3$ [EBF$^+$85]), which show a strong effective mass renormalization in the Fermi liquid state and several other phases like superconductivity [SAB$^+$79] and various magnetic orderings [NRLC97]. In the simplest case, the Kondo lattice model describes free electrons that are coupled to local moments via a spin-spin interaction. The characteristic physics emerges from a competition between the *Kondo screening* [Kon64] of the local moments (singlet formation) and Ruderman-Kittel-Kasuya-Yosida (RKKY) interaction [RK54] (magnetic ordering). The latter is an indirect interaction, caused by the polarization of the conduction electrons. Both models will be discussed in Chap. 2 in more detail.

Different numerical approaches are used and combined in this project. Starting from small systems, the models are solved for finite lattices using direct quantum Monte Carlo (QMC) simulations [FMNR01], where the original d-dimensional quantum problem is mapped on a $(d+1)$-dimensional classical problem, which can be solved with classical Monte Carlo methods. The most severe limitation of these methods is the restriction to small clusters ($N \leq 400$). Properties in the thermodynamic limit have to be estimated by finite-size extrapolations, based on various simulations of the problem using different system sizes.

Approaching the problem from the limit of infinite dimensions, the *dynamical mean-field theory* (DMFT) [MH89a, MH89b, MV89] provides insight from an effective mean-field point of view. The original lattice problem is mapped on a single interacting impurity, embedded in an non-interacting bath. The method neglects all local fluctuations and is exact in the limit of infinite dimensions, respectively coordination number. This approach can be improved using quantum cluster extensions [MJPH05]. Here a small cluster of interacting sites, instead of a single impurity, is considered. This cluster is, again, coupled to a non-interacting bath. These cluster DMFT methods can treat local correlation up to the extent of the

cluster. However, (cluster) DMFT still defines a non-trivial quantum problem, which has to be solved. The efficient solution of these impurity problems will be a main topic in this thesis.

Structure of this Thesis

In Chap. 2, the models studied in this project are considered. We introduce the Hubbard model and the Kondo lattice model (KLM) and discuss their basic properties. The theoretical background that is needed for the algorithm development is reviewed in Chap. 3. We start with the derivation of the Blankenbecler-Scalapino-Sugar quantum Monte Carlo (BSS-QMC) algorithm, which solves the Hubbard model and the KLM on finite clusters (Sec. 3.1). The BSS-QMC simulations result in Green functions in imaginary time, so we attach an excursus on analytical continuation, which is needed for obtaining real-frequency quantities.

The formalism of DMFT and its cluster extensions, as well as the calculation scheme for two-particle quantities is described in Sec. 3.2.

In Chap. 4, the development of a multigrid BSS-QMC scheme, which is free of systematic errors and valid in the thermodynamic limit, is presented. This algorithm is applied to the Mott transition in the two-dimensional Hubbard model at half-filling in Chap. 5. The integration of this unbiased BSS-QMC into the (cluster) DMFT framework is described in Chap. 6. Beside the solution of BSS-QMC related issues regarding the integration of the multigrid method into the DMFT self-consistency, we contribute algorithmic approaches for an efficient representation of the mean-field bath, needed for Hamiltonian based impurity solver. This problem was often discussed in the context of exact diagonalization. The impurity solver, developed in this project, is applied to the Mott transition in infinite dimension in Chap. 7. Here we study the impact of systematic biases in the impurity solver on the phase transition. In Chap. 8, we combine direct lattice calculations and the cluster DMFT framework for investigations of the momentum dependence of the self-energy. The impact on different models of the (cluster) DMFT approximation, the truncation of the self-energy, is contrasted: the (anisotropic) Hubbard model in two-dimensions at half-filling, the doped Hubbard model, and the KLM. We finish with a conclusion and an outlook in Chap. 9.

Inclusion of Related Publications

To some extent, several parts of the presented thesis are published in peer reviewed papers. Technical details of the multigrid Trotter extrapolation procedure and the elimination of finite-size errors in BSS-QMC data, discussed in Chap. 4, were published in [RGAB12], the appendix of [SGR$^+$15], and [RB15]. The full picture of the Mott transition in the two-dimensional Hubbard model, presented in Chap. 5, with additional data from the dynamical vertex approximation data by Schäfer et al. is published in [SGR$^+$15]. The algorithmic development of the unbiased BSS-QMC impurity solver for the single-site DMFT (Sec. 6.2) and the application on the Mott transition in infinite dimensions (Chap. 7) are published in [RAB13].

2. Models: Hubbard Model & Kondo Lattice Model

The numerical algorithms, developed in this project, are applied to the Hubbard and the Kondo lattice model. In this chapter, the fundamental properties of these models are discussed and all important notations will be fixed. The Hubbard model is described in Sec. 2.1 and we focus our attention on the Kondo lattice model in Sec. 2.2.

2.1. Hubbard Model

The Hubbard model is based on the concepts of the tight-binding approximation [Wan37, KS54], in which the electrons are assumed to be strongly localized at the ions of the underlying lattice structure. It is assumed that electrons in low-lying atomic shells close to the nuclei (*core electrons*) will not be excited, but form an effective particle with the nuclei. This weakens the original potential of the crystal. Further, the long-range Coulomb potential of the outer *valence electrons* is screened to an effectively more short-range potential, which justifies the following approximations. In the limit of strong localization and effective short-range interactions, this physical picture leads to the Hubbard model, which describes electrons that live on a given lattice, can *hop* between the lattice sites (kinetic term), and only interact with each other, if two electrons are located on the same site (on-site interaction). This is illustrated in Fig. 2.1 (a).

In second quantization [Sch08], the kinetic part can be written as

$$\hat{\mathbf{H}}_{\text{kin}} = \sum_{i,j,\sigma} t_{ij}\ \hat{\mathbf{c}}^{\dagger}_{i\sigma}\hat{\mathbf{c}}_{j\sigma} \equiv -t \sum_{\langle ij\rangle,\sigma} \left(\hat{\mathbf{c}}^{\dagger}_{i\sigma}\hat{\mathbf{c}}_{j\sigma} + h.c.\right). \tag{2.1}$$

The matrix t_{ij} determines the hopping amplitude and encodes the underlying lattice and band structure. One often simplifies to uniform nearest neighbor hopping t and a single band, represented by the notation $\langle i,j\rangle$ (right hand side). The spin degree of freedom is denoted by $\sigma \in \{\uparrow,\downarrow\}$.

To describe the interaction term, one starts with the most general form for a two-particle operator

$$\hat{\mathbf{U}} = \frac{1}{2}\sum_{i,j,k,l} A_{ijkl}\ \hat{\mathbf{c}}^{\dagger}_{i\sigma_i}\hat{\mathbf{c}}^{\dagger}_{j\sigma_j}\hat{\mathbf{c}}_{k\sigma_k}\hat{\mathbf{c}}_{l\sigma_l}. \tag{2.2}$$

In the case of Coulomb interaction

$$A_{ijkl} = \left\langle i,j \left| \frac{e^2}{|\mathbf{r}_i - \mathbf{r}_j|} \right| k,l \right\rangle.$$

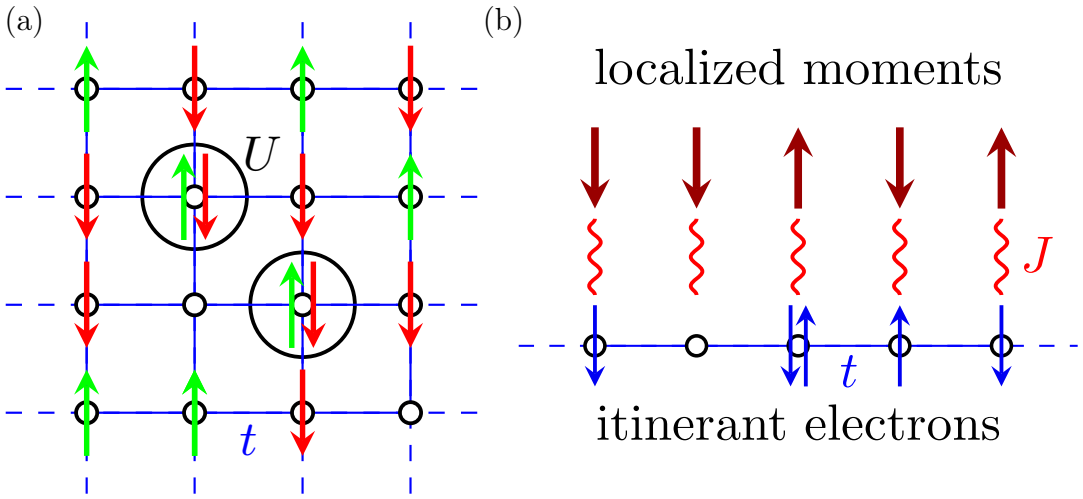

Figure 2.1. – (a) Illustration of the Hubbard model. Electrons can hop, gaining kinetic energy t, and interact only with each other, when sitting on the same site, with Hubbard interaction U. (b) Illustration of the Kondo lattice model. Itinerant band of non-interacting conduction electrons, which couple via a spin dependent interaction J with localized magnetic moments.

This long-range interaction is still too complicated to be treated with currently available methods, so we have to approximate the problem further. One way is to assume the interaction as purely on-site.

Under these assumptions, the Hubbard Hamiltonian with Coulomb interaction U and chemical potential μ, reads:

$$\hat{\mathbf{H}} = \sum_{i,j,\sigma} t_{ij} \left(\hat{\mathbf{c}}^{\dagger}_{i\sigma} \hat{\mathbf{c}}_{j\sigma} + \text{h.c.} \right) + \sum_{i} U_i \, \hat{\mathbf{n}}_{i\uparrow} \hat{\mathbf{n}}_{i\downarrow} - \mu \sum_{i} \left(\hat{\mathbf{n}}_{i\uparrow} + \hat{\mathbf{n}}_{i\downarrow} \right) \, . \tag{2.3}$$

We will use the convention that $\mu = 0$ corresponds to the half-filled case, i.e., a density of $\langle n \rangle$=1. This relates to shifting the chemical potential by $U/2$. The energy and temperature units are gauged in the way that $k_B \equiv 1$ and $t \equiv 1$.

The kinetic and interaction terms do not commute, which forestalls the possibility of a simultaneous diagonalization. So the solution of Eq. (2.3) remains non-trivial, at least aside from special limits, e.g., the Fermi gas ($U = 0$) or Heisenberg ($U \to \infty$) limits.

In one spatial dimension, the semi-analytic Bethe ansatz and the density matrix renormalization group (DMRG) [Whi92, WH93, Sch05] yield reliable high-precision results. In the opposite limit of infinite dimensions, the dynamical mean-field theory (DMFT) [MV89, GKKR96] provides deep insight. However, in the interesting case of two (and three) dimensions, less is understood. E.g., a complete picture of the full pseudogap physics [LW06, AFG10, RGAB12] and the connection to high-T_c superconductivity is still not satisfyingly found. In this work, we tackle the problem of two spatial dimensions with finite-size lattice quantum Monte Carlo, combined with sophisticated extrapolations to the thermodynamic limit, as well as cluster extensions to DMFT.

In the last two decades, even more special attention was attributed to the Hubbard model, since novel developments in the field of ultra-cold quantum gases on optical lattices granted a direct, experimental access to the Hubbard physics [MGW+03, WES+11]. In these experiments, atoms are trapped with interfering lasers that produce a potential pattern forming one-, two- or three-dimensional lattices. Due to the confinement of atoms in this artificial lattice and tunneling processes between the minima, the system is described by the Hubbard Hamiltonian Eq. (2.3) with an additional confining potential of the trap. These kinds of experiments offer the possibility for direct comparison with theoretical model calculations. Complementary to experiments with solid-state materials, calculations of the Hubbard model can be proven in a different parameter regime: while cold atoms on optical lattices realize finite-size Hubbard systems with few bands, correlated solid-state systems show long-range interaction potentials with a large number of interacting bands and electrons behave relativistically.

2.2. Kondo Lattice Model

Similar to the Hubbard model, the Kondo lattice model (KLM) describes correlated electrons from a tight-binding point of view. But instead of an on-site Coulomb interaction between the electrons, it includes a spin-spin interaction between itinerant electrons in the conduction band and localized magnetic impurities, as depicted in Fig. 2.1 (b). The KLM is closely related to the *Kondo effect* [Kon64], which occurs in various materials (first discovered in gold, copper and lead [WJdHvdB34]). The Kondo effect leads to a logarithmic divergence of the electrical resistivity at low-temperatures and can be explained as scattering process of itinerant conduction band electrons due to interaction with local moments. This functional behavior replaces the quadratic temperature dependence in a Fermi liquid description. The KLM turned out to be important for the description of *heavy fermion* materials, where, within the Fermi liquid phase, the effective mass is strongly enhanced ($m^* \sim 1000\ m_e$). These materials are characterized by physically rich phase diagrams, containing, e.g., various types of magnetic ordering, quantum criticality, and superconducting phases. Consequently, the model is studied in many research projects [LW07, Pfl09]. Examples for real materials are rare earth or actinide compounds [KKB+07], where partially filled f-orbitals serve as magnetic impurities. Also low-dimensional systems like *GaAs* quantum dots or carbon nanotubes are part of ongoing research [LAN+12].

In the theoretical treatment, the KLM describes these materials as a periodic formation of local spin degrees of freedom ($f^\dagger$) that interact with conduction electrons ($c^\dagger$) via a local interaction J. In terms of Pauli matrices σ one can write the Hamiltonian:

$$H_{\mathrm{KLM}} = \sum_{ij,\sigma} t_{ij}\, c^\dagger_{i\sigma} c_{j\sigma} + J \sum_i \mathbf{S_i}^f \cdot \mathbf{S_i}^c, \tag{2.4}$$

$$\mathbf{S_i}^\alpha = \frac{1}{2} \sum_{\sigma\sigma'} \alpha^\dagger_{i\sigma} \sigma_{\sigma\sigma'} \alpha_{i\sigma'} \quad \text{with} \quad \alpha = f, c\ .$$

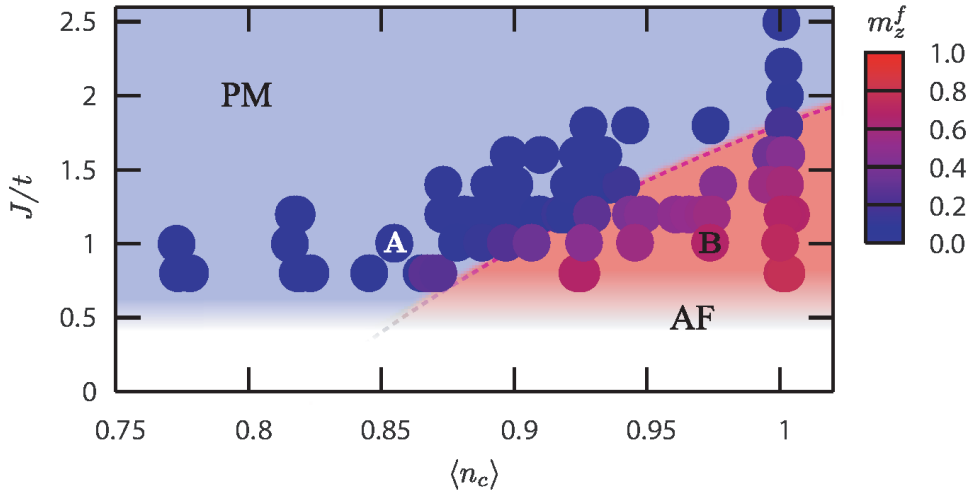

Figure 2.2. – Recent DCA study from Martin et al. [MA08]: Phase diagram of the KLM, obtained with DCA. The considered parameter regime is limited, due to poor scaling with the inverse temperature of the numerical method.

In the KLM two effects compete: an indirect Ruderman-Kittel-Kasuya-Yosida (RKKY) type interaction [RK54] between the localized moments via a polarization cloud of conduction electrons and a singlet formation between conduction electrons and the magnetic impurities [Wil75, KmWW80] (Kondo screening of the local moments). The RKKY interaction prefers a magnetic ordered state, while the singlet formation leads to a disordered state.

One major challenge regarding the numerical treatment of the KLM is the need for reaching ultra-low temperatures. It has been shown that the important coherence temperature scale, determined by the interaction strength J, is directly connected to the Kondo scale of a single impurity [BGG00, Ass04]:

$$T_K = e^{-t/J} \ . \tag{2.5}$$

Many state-of-the-art methods suffer from poor temperature scaling and are not able to reach the exponentially small temperature regime. Therefore it is no surprise that questions related to the topology of the Fermi surface and the role of superconductivity in the KLM are still open issues. E.g., a recent study [MA08], using the dynamical cluster approximation, could not resolve the full ground-state phase diagram (Fig. 2.2) of the KLM, due to restrictions by scaling issues towards small temperatures. In this project the problem is approached by the dynamical cluster approximation, a cluster extension to the dynamical mean-field theory combined with a numerically exact quantum Monte Carlo solver, which is more effective at ultra-low temperatures than comparable currently available algorithms.

3. Methods: QMC & Dynamical Cluster Approximation

In Chap. 2, the model Hamiltonians, which are considered in this project, and their properties were reviewed. Both, the Hubbard model and the Kondo lattice model (KLM) are not analytically solvable, apart from special cases, e.g., one spatial dimension. In this section, we will discuss the numerical approaches that form the basis for our investigations, namely the Blankenbecler-Scalapino-Sugar quantum Monte Carlo (BSS-QMC) algorithm and the dynamical mean-field theory (DMFT), including its cluster extensions. Further, we will describe the new algorithmic achievements, developed in the scope of this project, in detail. The presented work addresses mainly the simulation of two-dimensional systems. Here, both models are candidates for the description of real materials, in which physical properties of particular interest emerge from quasi two-dimensional structures. Examples are the high-T_c superconductors (e.g., cuprates) [Sca06,SWGK11], corresponding to the two-dimensional doped Hubbard model, or quasi two-dimensional heavy fermion compounds like $CeCoIn_5$ [SU91, IYM$^+$03, BZV$^+$13], connected to the KLM, which show unconventional superconductivity.

Already in the 1980s, QMC methods were used for studying Hubbard type models [Cep80, BSS81, HF86]. However, QMC suffers from the famous fermionic sign problem [LGS$^+$90] and is mostly restricted to small lattices and high temperatures. Sufficiently large systems and low enough temperatures can only be reached for special cases, where the sign problem is absent, e.g., at particle hole symmetry [ARH$^+$03,HH04]. A complementary approach, which was very successful in the last two decades, is the dynamical mean-field theory (DMFT) [MH89a, MH89b, MV89]. Starting from the limit of infinite dimensions and with a momentum-independent self-energy, many physical properties of strongly correlated systems could be described, down to the relatively small dimension $d = 3$, e.g., the essence of the Mott metal insulator transition could be captured [GKKR96, Blü02]. In contrast, DMFT fails in the case of two and lower dimensions, where long-range order is forbidden by the Mermin Wagner theorem at finite temperatures [MW66, Hoh67] and local spatial fluctuations become more important [GRP$^+$12, RGAB12, SGR$^+$15]. To describe these systems correctly, non-local contributions to the self-energy beyond DMFT have to be taken into account. These can be included by diagrammatic extensions, e.g., the dynamical vertex approximation [TKH07], or cluster extensions [MJPH05] like cellular DMFT and dynamical cluster approximation. We will concentrate on the latter approach in this work. In Sec. 3.1 the most important steps of the deviations of the BSS-QMC are recalled. We also show the origin of the systematic bias in the method, which has to be eliminated later. In Sec. 3.2 the formalism of

(cluster) DMFT is reviewed and the key elements for the application of BSS-QMC as impurity solver is described.

3.1. Blankenbecler-Scalapino-Sugar Quantum Monte Carlo

The Blankenbecler-Scalapino-Sugar quantum Monte Carlo (BSS-QMC) was proposed in 1981 and developed to solve Hubbard type Hamiltonians on a finite-size lattice [BSS81]. We will briefly review the steps that are important for understanding the possibilities and challenges of the BSS-QMC. For a more detailed view we refer to the existing literature, e.g., [ATB12].

3.1.1. Derivation

The two major parts forming the derivation of the BSS-QMC algorithm are a Trotter-Suzuki decomposition of the partition function and a Hubbard-Stratonovich transformation of the Hamiltonian. Let us first specify the notation. Analogue to Eq. (2.1), $\hat{\mathbf{c}}^\dagger_{i\sigma}$ ($\hat{\mathbf{c}}_{i\sigma}$) denote the electron creation (annihilation) operator on site i with spin $\sigma = \{\uparrow, \downarrow\}$ and h denotes a hermitian matrix. For a quadratic Hamiltonian

$$\hat{\mathbf{H}} = \hat{\mathbf{c}}^\dagger_{i\sigma} h_{ij} \hat{\mathbf{c}}_{j\sigma} \ , \tag{3.1}$$

the expectation value $\langle \hat{\mathbf{O}} \rangle$ of an observable $\hat{\mathbf{O}}$ and the partition function Z can generally be written as traces [FW71]

$$\langle \hat{\mathbf{O}} \rangle = Z^{-1} \ \mathrm{tr} \left[\hat{\mathbf{O}} \ e^{-\beta \hat{\mathbf{H}}} \right] \tag{3.2}$$

$$Z = \mathrm{tr} \left[-\beta \hat{\mathbf{H}} \right] , \tag{3.3}$$

where the inverse temperature is denoted by $\beta = 1/T$. All units are chosen in in the way that $k_B \equiv 1$. Using the formula for the n-dimensional Gauß integration [BSM08]

$$\int_{-\infty}^{+\infty} \int_{-\infty}^{+\infty} \dots \int_{-\infty}^{+\infty} dx_1 dx_2 \dots dx_n \ e^{-\mathbf{x} A \mathbf{x}^T} = \frac{\pi^{n/2}}{\sqrt{\det(A)}} \tag{3.4}$$

$$\text{with } \mathbf{x} \in \mathbb{R}, A \in \mathbb{R} \times \mathbb{R}$$

and under consideration of the fermionic anti-commutation relations, one can integrate out the fermionic degrees of freedom, so the trace transforms into a determinant of a matrix [Hir85]:

$$Z = \det\left[\mathbb{1} - e^{-\beta h}\right]. \tag{3.5}$$

In the specific case of Hubbard type Hamiltonians, Eq. (3.5) is not applicable directly, because it is valid for quadratic Hamiltonians only. So the Hubbard Hamiltonian Eq. (2.3), which contains fermionic operators of quartic order in the interaction term, has to be transformed. To find a purely quadratic representation, one first splits the kinetic and interaction part using a Trotter decomposition [Suz76]:

$$\begin{aligned} e^{-\beta\left(\hat{\mathbf{H}}_{\text{kin}}+\hat{\mathbf{H}}_{\text{U}}\right)} &= \left[e^{-\frac{\beta}{\Lambda}\left(\hat{\mathbf{H}}_{\text{kin}}+\hat{\mathbf{H}}_{\text{U}}\right)}\right]^{\Lambda} \quad \overset{\Delta\tau:=-\beta/\Lambda}{=} \quad \left[e^{\Delta\tau\left(\hat{\mathbf{H}}_{\text{kin}}+\hat{\mathbf{H}}_{\text{U}}\right)}\right]^{\Lambda} \\ &= \left[e^{\Delta\tau\hat{\mathbf{H}}_{\text{kin}}}e^{\Delta\tau\hat{\mathbf{H}}_{\text{U}}}\right]^{\Lambda} + \mathcal{O}\left(\Delta\tau^2\right) \\ &\approx \left[e^{\Delta\tau\hat{\mathbf{H}}_{\text{kin}}}e^{\Delta\tau\hat{\mathbf{H}}_{\text{U}}}\right]^{\Lambda}. \end{aligned} \tag{3.6}$$

The Eq. (3.6) gets exact in the limit

$$\Lambda \to \infty \qquad \Leftrightarrow \qquad \Delta\tau = \frac{\beta}{\Lambda} \to 0\ . \tag{3.7}$$

At this point a systematic error is introduced, which scales with $(\Delta\tau)^2$ and implies a bias in all numerical results unless eliminated afterwards.

After rewriting the interaction term

$$\begin{aligned} \hat{\mathbf{H}}_U &= U\sum_i \hat{\mathbf{c}}^\dagger_{i\uparrow}\hat{\mathbf{c}}_{i\uparrow}\hat{\mathbf{c}}^\dagger_{i\downarrow}\hat{\mathbf{c}}_{i\downarrow} \\ &= U\sum_i \hat{\mathbf{n}}_{i\uparrow}\hat{\mathbf{n}}_{i\downarrow} \\ &= -\frac{U}{2}\sum_i \left[\left(\hat{\mathbf{n}}_{i\uparrow}-\hat{\mathbf{n}}_{i\downarrow}\right)^2 - \left(\hat{\mathbf{n}}_{i\uparrow}+\hat{\mathbf{n}}_{i\downarrow}\right)\right], \end{aligned}$$

the Hamiltonian can be expressed with quadratic order of fermionic operators and an auxiliary spin-1 Ising field σ [SSST87]. Formally, this is achieved via a discrete Hubbard-Stratonovich transformation [a similar approach as in Eq. (3.4)] [Hub59]

$$e^{-\Delta\tau U\hat{\mathbf{n}}_{i\uparrow}\hat{\mathbf{n}}_{i\downarrow}} = \frac{1}{2}\sum_{\sigma_i(l)=\pm1} e^{2\lambda_\pm\sigma_i(l)\left[\left(\hat{\mathbf{n}}_{i\uparrow}-\frac{1}{2}\right)\mp\left(\hat{\mathbf{n}}_{i\downarrow}-\frac{1}{2}\right)\right]-\frac{U\Delta\tau}{2}\left(\hat{\mathbf{n}}_{i\uparrow}+\hat{\mathbf{n}}_{i\downarrow}\right)}. \tag{3.8}$$

Here $\left[\tanh(\lambda_\pm)\right]^2 = \pm\tanh(\Delta\tau U/4)$ is introduced.

The application of the Trotter decomposition and Hubbard-Stratonovich transformation leads to the final representation of the partition function in the grand-canonical ensemble containing the transformed Hamiltonian:

$$\begin{aligned} Z &= \mathrm{Tr}\left[e^{-\beta\left(\hat{\mathbf{H}}_{kin}+\hat{\mathbf{H}}_U-\mu\hat{\mathbf{N}}\right)}\right] \\ &\approx \sum_{\sigma_i(l)=\pm1}\mathrm{Tr}\prod_{l=1}^{\Lambda} e^{-\Delta\tau\hat{\mathbf{H}}_{kin}}e^{\lambda_\pm\sum_{i,\nu=\uparrow,\downarrow}\mathcal{V}_{i\nu}(l)\hat{\mathbf{c}}^\dagger_{i\nu}\hat{\mathbf{c}}_{i\nu}} \end{aligned} \tag{3.9}$$

with:

$$\begin{aligned} \mathcal{V}_{i\uparrow} &= +\sigma_i(l) - \Delta\tau\left(\mu-\frac{U}{2}\right) \\ \mathcal{V}_{i\downarrow} &= -\sigma_i(l) - \Delta\tau\left(\mu-\frac{U}{2}\right). \end{aligned} \tag{3.10}$$

With the hopping matrix t_{ij} we use the following notation:

$$B^\nu(l) = e^{-\Delta\tau t_{ij}}e^{V^\nu_{ij}(l)}\ . \tag{3.11}$$

Now V carries the remaining factors in Eq. (3.9):

$$V^\nu_{ij}(l) = \delta_{ij}\lambda_\pm\mathcal{V}_{i\nu}(l) \tag{3.12}$$

and one can rewrite the partition function

$$Z = \sum_{\sigma_i(l)=\pm 1} \mathrm{Tr} \prod_{l=1}^{\Lambda} \underbrace{\left(e^{-\Delta\tau \hat{\mathbf{c}}_j^\dagger K_{jk} \hat{\mathbf{c}}_k} e^{\hat{\mathbf{c}}_r^\dagger V_{rs}^\uparrow(l) \hat{\mathbf{c}}_s}\right)}_{\text{spin up}} \underbrace{\left(e^{-\Delta\tau \hat{\mathbf{c}}_j^\dagger K_{jk} \hat{\mathbf{c}}_k} e^{\hat{\mathbf{c}}_r^\dagger V_{rs}^\downarrow(l) \hat{\mathbf{c}}_s}\right)}_{\text{spin down}} \tag{3.13}$$

$$Z = \sum_{\sigma_i(l)} \det\left[\mathbb{1} + B^\uparrow(\Lambda) \dots B^\uparrow(1)\right] \det\left[\mathbb{1} + B^\downarrow(\Lambda) \dots B^\downarrow(1)\right] \ . \tag{3.14}$$

The matrix K contains the hopping matrix and chemical potential:

$$K_{ij} = -\Delta\tau \left(t_{ij} + \delta_{ij}\ \mu\right). \tag{3.15}$$

The evaluation of the partition function and calculation of observables is done by standard Monte Carlo techniques, sampling over the auxiliary field using, e.g., the Metropolis Monte Carlo algorithm [MRR+53].

The most important quantity for the calculation of observables and for the integration in the framework of the dynamical mean-field theory is the one-particle Green function:

$$G_{\sigma,ij}(\tau) = -\left\langle \hat{\mathbf{c}}_{i,\sigma}(\tau) \hat{\mathbf{c}}_{j,\sigma}^\dagger(0) \right\rangle. \tag{3.16}$$

Within the BSS-QMC algorithm, the value of the Green function at time slice l for a fixed auxiliary field configuration can be calculated via

$$G_{ij}^\nu(l) = \left[\mathbb{1} + B^\nu(l) B^\nu(l-1) \dots B^\nu(1) B^\nu(\Lambda) \dots B^\nu(l+1)\right]_{ij}^{-1} \ . \tag{3.17}$$

Flipping a spin of the auxiliary field $\sigma_i(l)$ at site i and imaginary time l during a Monte Carlo sweep affects only the Green function at (i, l). One can show that the recalculation of the Green function at imaginary time $l+1$ can be simplified to a matrix vector multiplication, depending on the values at imaginary time l only $(0 \leq l\Delta\tau \leq (l+1)\Delta\tau \leq \beta)$

$$G(l+1) = B(l) G(l) B^{-1}(l). \tag{3.18}$$

This update procedure scales significantly better with the number of time slices Λ than the calculation of the full Green function Eq. (3.17). However, because of possible numerical instabilities, arising from the amplification of errors from the finite machine precision in the matrix multiplications in Eq. (3.18), a calculation of the full Green function has to be performed after a certain number of updates, using Eq. (3.17). This procedure is called *wrapping*. In total, the algorithm scales with $\mathcal{O}(N^3\Lambda)$, where N is the number of sites. The linear scaling in Λ translates into a linear scaling in the inverse temperature β at fixed Trotter discretization $\Delta\tau$. This superior scaling was the main reason for choosing the BSS-QMC as impurity solver for the dynamical mean-field theory in this research project.

The BSS-QMC can also be specified for the Kondo lattice model (KLM). The mapping was first proposed by F. F. Assaad in 1999 [Ass99]. He showed that the following auxiliary Hamiltonian, which is treatable by decoupling via a Hubbard-Stratonovich transformation similar to Eq. (3.9) and efficiently solvable with QMC [FS91, AIS97],

$$\begin{aligned}\hat{\mathbf{H}} =& -\sum_{\langle ij\rangle,\sigma} t_{ij}\ \hat{\mathbf{c}}^{\dagger}_{i,\sigma}\hat{\mathbf{c}}_{j,\sigma} - \frac{J}{4}\sum_{i}\left[\sum_{\sigma}\hat{\mathbf{c}}^{\dagger}_{i,\sigma}\hat{\mathbf{f}}_{i,\sigma} + \hat{\mathbf{f}}^{\dagger}_{i,\sigma}\hat{\mathbf{c}}_{i,\sigma}\right]^2 \\ &+ U\sum_{i}\left(\hat{\mathbf{n}}^{f}_{i,\uparrow} - \frac{1}{2}\right)\left(\hat{\mathbf{n}}^{f}_{i,\downarrow} - \frac{1}{2}\right) \\ =& -\sum_{\langle ij\rangle,\sigma} t_{ij}\ \hat{\mathbf{c}}^{\dagger}_{i,\sigma}\hat{\mathbf{c}}_{j,\sigma} + J\sum_{i}\hat{\mathbf{S}}^{c}_{i}\hat{\mathbf{S}}^{f}_{i} - J\sum_{i}\left(\hat{\mathbf{c}}^{\dagger}_{i,\sigma}\hat{\mathbf{c}}^{\dagger}_{i,-\sigma}\hat{\mathbf{f}}_{i,-\sigma}\hat{\mathbf{f}}_{i,\sigma} + h.c.\right) \\ &+ J\sum_{i}\left(\hat{\mathbf{n}}^{c}_{i}\hat{\mathbf{n}}^{f}_{i} - \hat{\mathbf{n}}^{c}_{i} - \hat{\mathbf{n}}^{f}_{i}\right) + U\sum_{i}\left(\hat{\mathbf{n}}^{f}_{i,\uparrow} - \frac{1}{2}\right)\left(\hat{\mathbf{n}}^{f}_{i,\downarrow} - \frac{1}{2}\right)\end{aligned} \tag{3.19}$$

is projected on the KLM for sufficiently large U. The first observation was that Eq. (3.19) conserves the number of double occupied states on the f orbitals. So in the case of restriction to the subspace where no f orbital is double occupied, Eq. (3.19) is equivalent to the KLM Hamiltonian [Eq. (2.4)]. In a numerical simulation this restriction is assured by setting the Coulomb interaction U on the f orbitals large enough, in order to suppress double occupancy.

3.1.2. Quantities on the Real Axis

The main result of BSS-QMC calculations are Green functions $G(\tau)$ in imaginary time, respectively in terms of Matsubara frequencies

$$G(i\omega_n) = \int_0^{\beta} d\tau e^{i\omega_n} G(\tau) \qquad \text{with} \qquad \omega_n = \frac{(2n+1)\pi}{\beta}. \tag{3.20}$$

However, for various applications one needs the quantities also on the real frequency

axis, e.g., for comparison with experiments[1]. The connection between real frequencies and Matsubara frequencies is given via the spectral representation of the Green function:

$$G(i\omega_n) = -\int_{-\infty}^{\infty} \frac{d\omega'}{\pi} \frac{\mathrm{Im}[G(\omega')]}{i\omega_n - \omega'} = \int_{-\infty}^{\infty} d\omega' \frac{A(\omega')}{i\omega_n - \omega'} \ , \tag{3.21}$$

or in terms of imaginary time:

$$G(\tau) = -\int_{-\infty}^{\infty} d\omega A(\omega) \underbrace{\frac{e^{-\tau\omega}}{1+e^{-\beta\omega}}}_{=:K(\tau,\omega)} . \tag{3.22}$$

The spectral function is associated with the imaginary part of the Green function:

$$A(\omega) = -\frac{1}{\pi}\mathrm{Im}[G(\omega)]. \tag{3.23}$$

Consequently, one has to invert Eq. (3.22) to obtain the Green function on the real-axis. Due to the fact that the Green function $G(\tau)$ is measured on a discrete grid and with a statistical error ΔG, the inversion of Eq. (3.22) is ill-posed and there exist an infinite number of solutions for $A(\omega)$. Additionally, high frequency properties of the spectral function are suppressed exponentially by the integral kernel K.

Thus, the problem has to be regularized. This is typically done by the *Maximum Entropy Method* (MEM) [Bry90, Ros12]. Main idea is to find the spectral function that reproduces the Green function most likely, i.e., finding the maximum of the probability distribution:

$$P[A|G] = \frac{P[G|A]P[A]}{P[G]}. \tag{3.24}$$

The probability for appearance of the Green function $P[G]$ drops out, because the function is given in advance. A measure for the correctness of the spectral function $A(\omega)$ is the agreement with the data:

$$P[G|A] \propto e^{-\chi^2} \ . \tag{3.25}$$

with

$$\chi^2 = \sum_i \left(\frac{G_i - \overline{G}_i}{\Delta G_i} \right)^2 \ , \tag{3.26}$$

[1] E.g., with angle-resolved photo-emission spectroscopy (ARPES).

where $\overline{G}_i$ is the Green function generated by the spectral function and G_i denotes the discrete data obtained from BSS-QMC. Here we assume uncorrelated errors for simplicity[2]. The second assumption is that the spectral function should not consist of any unphysical features and can be expressed by the Shannon entropy [Sha48]

$$S = \int d\omega \left[A(\omega) - m(\omega) - \ln\left(\frac{A(\omega)}{m(\omega)}\right) A(\omega) \right] , \tag{3.27}$$

which is a penalty term for deviations from the *model spectrum* m. The model spectrum can be used to insert additional information on the system, e.g., by using a already known spectral function from a similar problem [DHJP13]. However, in this project we will use a constant model spectrum in any case, i.e., we require smoothness only. The entropy term regularizes the problem and is inserted with a Tikhonov regularization parameter α [Bel78]:

$$P[A|G] = e^{\alpha S - \chi^2} . \tag{3.28}$$

The inversion of Eq. (3.22) is reduced to a minimization of Eq. (3.28), which can be performed with various methods. For details of the derivation, determination of the Tikhonov parameter and information on the implementation we refer to the author's diploma thesis [Ros12].

3.2. Dynamical Mean-Field Theory and Cluster Extension

Beside direct solutions of the models presented in Chap. 2, which are often restricted to small systems, an approach from the mean-field point of view turned out to be a successful tool. Mean-field ansatzes have been powerful approaches at many points in the history of statistical physics [Kad09], e.g., the Weiss mean-field theory for spin systems [Wei07]. The central idea is that the original many-particle problem is mapped on a single particle that interacts with an effective medium, which represents the former interaction with the other particles. These theories were very successful in the description of phase transitions, e.g., for the Ising model, which is, in a mean-field approach, mapped on a single spin in an effective time-independent magnetic field. The mean-field approaches are exact in the limit of infinite dimensions or coordination number respectively[3].

$$d \to \infty \qquad \Longleftrightarrow \qquad z \to \infty . \tag{3.29}$$

[2] In general one has to diagonalize the error correlation matrix σ_{ij} and work in the corresponding diagonal space.

[3] The reason for the success of $d \to \infty$ theories in three dimension is that the coordination number is significant larger than the dimension, e.g., for a cubic face-centered lattice the coordination number is already $Z = 12$.

However, a simple time-independent mean-field approach for models with enhanced quantum correlations, as the Hubbard model, fails. This can be explained with the fact that quantum fluctuations on a single-site do not vanish in the limit of infinite dimensionality. To take these fluctuations into account, the *dynamical mean-field theory* (DMFT) was developed by Metzner and Vollhardt in 1989 [MH89a, MH89b, MV89].

In this section, we will recall the main ideas of the DMFT, its limitation and corresponding extensions. For the complete picture and historical derivations we refer to the review by Georges et al. [GKKR96] for the DMFT and the review by Maier et al. [MJPH05] for quantum cluster theories.

3.2.1. Single-Site DMFT

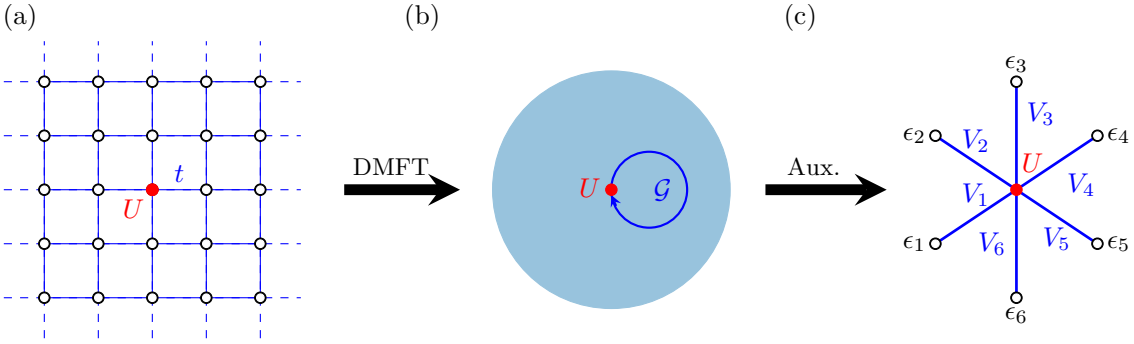

Figure 3.1. – Mapping of the original lattice problem (a), with local interaction U and hopping t, on a single impurity, embedded in an effective bath $\mathcal{G}$ (b). A discretization of the bath leads to an auxiliary Hamiltonian (treatable with ED or BSS-QMC), here with star topology (c).

As stated above, the main idea in DMFT is the mapping of the original lattice problem [Fig. 3.1 (a)] on an interacting impurity in a non-interacting bath [Fig. 3.1 (b)], represented by the *bath Green function* $\mathcal{G}$ with an action $\mathcal{A}$:

$$\begin{aligned}\mathcal{A}\left[\psi,\psi^*,\mathcal{G}\right] = &\int_0^\beta \int_0^\beta d\tau\, d\tau' \sum_\sigma \psi^*_\sigma(\tau)\, \mathcal{G}^{-1}_\sigma\, \psi_\sigma(\tau') \\ &- U \int_0^\beta d\tau\, \psi^*_\uparrow(\tau)\, \psi_\uparrow(\tau)\, \psi^*_\downarrow(\tau)\, \psi_\downarrow(\tau)\ ,\end{aligned} \tag{3.30}$$

here in imaginary time $\tau \in [0, \beta]$ and in terms of Grassmann fields ψ, ψ^*. The resulting problem, defined by the action Eq. (3.30), is still a highly non-trivial quantum problem that has to be solved with sophisticated methods. The solution will be topic in Sec. 3.2.4.

The bath Green function is the equivalent to the mean-field in classical Weiss mean-field theories, e.g., the effective magnetic field in the solution of the Ising model. In contrast to non-dynamical electronic theories, the impurity site can exchange electrons with the bath, i.e., in the case of the single band Hubbard model, the impurity can change between the states

$$|\cdot\rangle \in \{|0\rangle, |\uparrow\rangle, |\downarrow\rangle, |\uparrow\downarrow\rangle\}. \tag{3.31}$$

The bath Green function is determined by a self-consistent procedure as depicted in Fig. 3.2. The different steps are connected via Dyson equations. We recall the expression for the Green function of a non-interacting system, with dispersion $\epsilon_{\mathbf{k}}$, in momentum space and in terms of fermionic Matsubara frequencies $\omega_n = (2n+1)\pi/\beta$

$$\mathcal{G}_{\sigma,\mathbf{k}}(i\omega_n) = \frac{1}{i\omega_n + \mu - \epsilon_{\mathbf{k}}}. \tag{3.32}$$

The full Green function of the interacting system can be written as:

$$G_{\sigma,\mathbf{k}}(i\omega_n) = \frac{1}{i\omega_n + \mu - \epsilon_{\mathbf{k}} - \Sigma_{\sigma,\mathbf{k}}(i\omega_n)}\ . \tag{3.33}$$

At this point, the self-energy Σ is introduced, which represents the influence of the interaction. Eq. (3.33) can be interpreted as the defining equation for the self-energy.

The central approximation within the DMFT framework is that the self-energy is estimated as a purely local quantity. The Dyson equation reduces to

$$G^{-1}_{\sigma,\mathbf{k}}(i\omega_n) = [\mathcal{G}_{\sigma,\mathbf{k}}(i\omega_n)]^{-1} - \Sigma_{\sigma,\mathbf{k}}(i\omega_n) \overset{d\to\infty}{=} [\mathcal{G}_{\sigma,\mathbf{k}}(i\omega_n)]^{-1} - \Sigma_{\sigma}(i\omega_n)\ . \tag{3.34}$$

Finally, the local Green function is obtained by momentum space integration:

$$G_{\sigma}(i\omega_n) = \int \frac{d^d k}{(2\pi)^d} \frac{1}{i\omega_n + \mu - \epsilon_{\mathbf{k}} - \Sigma_{\sigma}(i\omega_n)}\ . \tag{3.35}$$

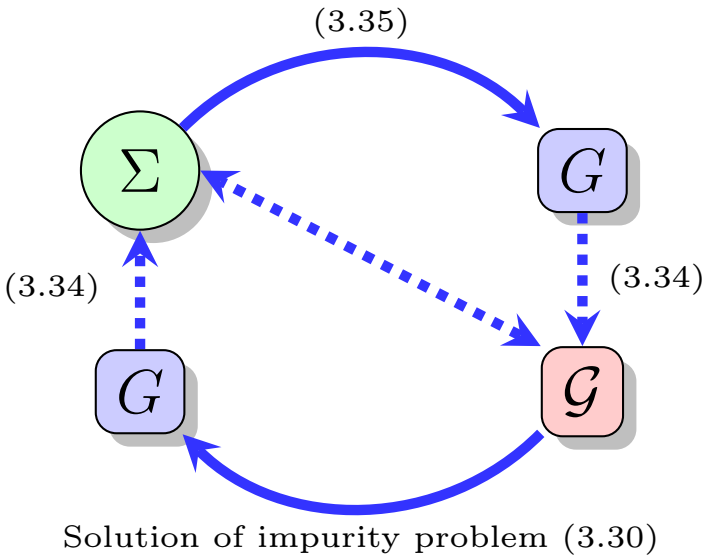

Figure 3.2. – Schematic representation of the DMFT self-consistency equations.

Self-consistency is reached, when the local Green function Eq. (3.35) and the impurity Green function G^c, obtained from the solution of the impurity problem, become identically:

$$G_\sigma(i\omega_n) \stackrel{!}{=} G^c_\sigma(i\omega_n) \ . \tag{3.36}$$

The complete self-consistency procedure is depicted in Fig. 3.2. The self-consistency loop is iterated until convergence.

Hamiltonian Representation

In the above DMFT formalism, the new quantum impurity problem is defined by Eq. (3.30), where $\mathcal{G}$ represents a continuous bath. While the most existing algorithms, like Hirsch-Fye quantum Monte Carlo (HF-QMC) [Hir85, Hir88] and continuous-time Quantum Monte Carlo, [GML+11] deal directly with this action formulation, an alternative class of available impurity solver need a Hamiltonian representation of the impurity problem. For the construction of a corresponding Hamiltonian, one needs a bath representation with a, depending on the method, finite or infinite number of discrete sites. We will come back to a comparison of the properties of different impurity solvers in Sec. 3.2.4.

Let us start with an impurity Hamiltonian to find a discrete representation of the bath. An appropriate Hamiltonian that is directly connected to the DMFT

impurity problem was suggested by P.W. Anderson in 1961 [And61]:

$$\hat{\mathbf{H}}_{\mathrm{And}} = \underbrace{\sum_{i,\sigma} \epsilon_i \hat{\mathbf{a}}^\dagger_{i\sigma} \hat{\mathbf{a}}_{i\sigma}}_{\text{bath dispersion}} + \underbrace{\sum_{l,\sigma} V_l \left(\hat{\mathbf{a}}^\dagger_{l\sigma} \hat{\mathbf{c}}_\sigma + \hat{\mathbf{c}}^\dagger_\sigma \hat{\mathbf{a}}_{l\sigma} \right)}_{\text{coupling}} + \underbrace{U \; \hat{\mathbf{c}}^\dagger_\uparrow \hat{\mathbf{c}}_\uparrow \hat{\mathbf{c}}^\dagger_\downarrow \hat{\mathbf{c}}_\downarrow}_{\text{local interaction}} \quad . \tag{3.37}$$

Here $\hat{\mathbf{a}}^\dagger_{i\sigma}$ ($\hat{\mathbf{a}}_{i\sigma}$) creates (annihilates) electrons in a non-interacting bath, and $\hat{\mathbf{c}}^\dagger_{i\sigma}$ ($\hat{\mathbf{c}}_{i\sigma}$) creates (annihilates) electrons on the impurity site. For a finite number of bath sites, the Anderson model can be visualized, e.g., through the star geometry in Fig. 3.1 (c). The parameters of the bath, i.e., bath dispersion $\{\epsilon_i\}$ and hybridization between bath sites and impurity $\{V_i\}$ have to be determined within the DMFT procedure. To build up the connection to the DMFT framework, one uses the Green function corresponding to the Hamiltonian Eq. (3.37) [GKKR96], assuming a finite number of bath sites N_b,

$$\mathcal{G}^{-1}(\omega) = \omega + \mu - \underbrace{\int_{-\infty}^{+\infty} d\omega' \frac{\Delta(\omega')}{\omega - \omega'}}_{\equiv \Gamma(\omega)} \approx \omega + \mu - \sum_{l=1}^{N_b} \frac{V_l^2}{\omega - \epsilon_l} \; . \tag{3.38}$$

The bath parameters and, thereby, the hybridization function $\Gamma(\omega)$ are determined in every DMFT iteration by fitting the functional form in Eq. (3.38) to $\mathcal{G}$, obtained from the impurity Green function and self-energy via Eq. (3.34), e.g., using a χ^2 fit[4]. After determination of the bath parameters, the Hamiltonian Eq. (3.37) can be solved by lattice quantum Monte Carlo methods (e.g., BSS-QMC) or, for a small number of bath sites, by exact diagonalization.

3.2.2. Cluster Extensions

As mentioned in Chap. 1, single-site DMFT was very successful in the context of the Hubbard model in three and higher dimensions. However, the lack of momentum dependence in the self-energy and the neglect of short-range fluctuations lead to qualitatively incorrect results for one- and two-dimensional systems. One can distinguish two major approaches for extending the single-site DMFT approximation; first, diagrammatic methods, including higher order vertices (dynamical vertex approximation [TKH07] or dual fermion approach [RKL08]) and second, cluster extensions, which describe an interacting cluster, instead of a single site, in an effective medium. In this section, we will focus on the latter class.

[4] Thus, the function

$$\chi^2 \left[\{V_{\alpha k}\}, \{\epsilon_\alpha\} \right] = \sum_{n=0}^{\mathrm{cutoff}} \left[\mathcal{G}^{\mathrm{DMFT}}(i\omega_n) - \mathcal{G}^{\mathrm{fit}}(i\omega_n; \{V_{\alpha k}\}, \{\epsilon_\alpha\}) \right]^2$$

is minimized with respect to the bath parameters.

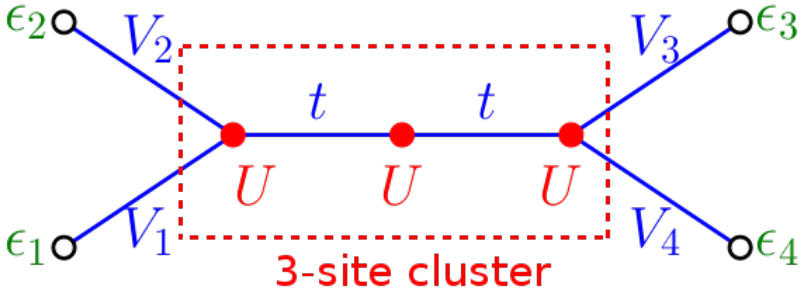

Figure 3.3. – Illustration of the Hamiltonian based representation of the cluster impurity problem in the framework of cellular DMFT.

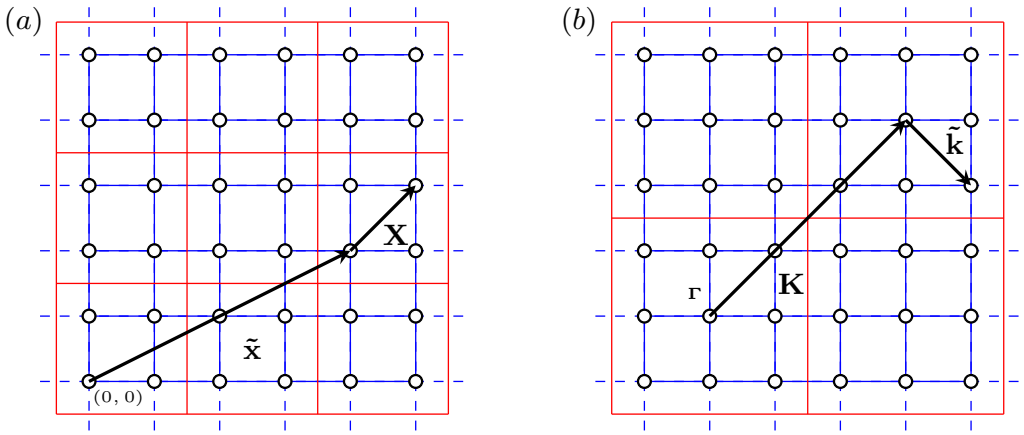

Figure 3.4. – Definition of the intra- and inter-cluster vectors within cellular DMFT and DCA. (a) real space and (b) reciprocal space.

In the framework of cluster DMFT, one can derive a real-space version, the *cellular* DMFT, using a locator expansion. Cellular DMFT does not preserve the translation symmetry of the original lattice, but retains the original matrix elements on the cluster. The non-interacting bath is coupled to the surface of the cluster. A discrete representation of this problem is shown in Fig. 3.3 for the case of the one-dimensional Hubbard model and a three-site cluster.

One can restore this symmetry and find a slightly different algorithmic approach, which is based on a truncation of the self-energy in momentum space: the dynamical cluster approximation (DCA). The DCA, in return, leads to renormalized hopping elements on the interacting cluster. The two formalisms are closely related and can be transformed into each other by certain redefinitions of phase factors and cluster Fourier transformations.

Depending on the purpose, both methods have advantages and disadvantages. During this project, a cellular DMFT and a DCA framework was implemented. On the one hand, cellular DMFT is the more generic one, because BSS-QMC, used here as impurity solver, is formulated in real space. The bath is only coupled to the surface of the cluster, so in some cases less bath sites are needed. On the other hand, DCA turned out to be more favorable for the calculation of pairing susceptibilities, due to the restoration of the translation invariance.

For the derivation of the cluster self-consistency equations, we will follow the review by Maier et al. [MJPH05] and refer to it for more detailed information. As starting point for the locator expansion is the original lattice partitioned in smaller clusters. This is sketched in Fig. 3.4 (a) for real space and Fig. 3.4 (b) for momentum space. The original vectors $\mathbf{x}$ and $\mathbf{k}$ are split in inter- and intra-cluster vectors, corresponding to Fig. 3.4

$$\mathbf{k} = \tilde{\mathbf{k}} + \mathbf{K} \qquad \mathbf{x} = \tilde{\mathbf{x}} + \mathbf{X} \; . \tag{3.39}$$

With these definitions, we will use the following definitions of Fourier transformations between functions f of inter- and intra-cluster coordinates, assuming a total number of N sites, divided in clusters with N_c sites:

$$f(\mathbf{X}, \tilde{\mathbf{x}}) = \frac{N_c}{N} \sum_{\tilde{\mathbf{k}}} e^{i\tilde{\mathbf{k}}\cdot\tilde{\mathbf{x}}} f(\mathbf{X}, \tilde{\mathbf{k}}) \tag{3.40}$$

$$f(\mathbf{X}, \tilde{\mathbf{k}}) = \sum_{\tilde{\mathbf{x}}} e^{-i\tilde{\mathbf{k}}\cdot\tilde{\mathbf{x}}} f(\mathbf{X}, \tilde{\mathbf{x}}) \tag{3.41}$$

$$f(\mathbf{X}, \tilde{\mathbf{k}}) = \frac{1}{N_c} \sum_{\mathbf{K}} e^{i(\tilde{\mathbf{k}}+\mathbf{K})\cdot\mathbf{X}} f(\mathbf{K}, \tilde{\mathbf{k}}) \tag{3.42}$$

$$f(\mathbf{K}, \tilde{\mathbf{k}}) = \sum_{\mathbf{X}} e^{-i(\tilde{\mathbf{k}}+\mathbf{K})\cdot\mathbf{X}} f(\mathbf{X}, \tilde{\mathbf{k}}). \tag{3.43}$$

The idea of the derivation of the cluster extensions to the DMFT, based on the locator expansion, is the separation of quantities in their inter- and intra-cluster contributions, and treating the influence on a single cluster, emerging from the surrounding clusters, on a mean-field level. With the convention that all quantities are $N_c \times N_c$ matrices in the intra-cluster coordinates, one writes for the hopping matrix and self-energy

$$\mathbf{t}(\tilde{\mathbf{x}}_i - \tilde{\mathbf{x}}_j) = \mathbf{t}_c \delta_{\tilde{\mathbf{x}}_i, \tilde{\mathbf{x}}_j} + \delta\mathbf{t}(\tilde{\mathbf{x}}_i - \tilde{\mathbf{x}}_j) \tag{3.44}$$

$$\mathbf{\Sigma}(\tilde{\mathbf{x}}_i - \tilde{\mathbf{x}}_j, i\omega_n) = \mathbf{\Sigma}_c(i\omega_n)\delta_{\tilde{\mathbf{x}}_i, \tilde{\mathbf{x}}_j} + \delta\mathbf{\Sigma}(\tilde{\mathbf{x}}_i - \tilde{\mathbf{x}}_j, i\omega_n). \tag{3.45}$$

With these definitions one can rewrite the Dyson equation for the Green function:

$$\mathcal{G}(\tilde{\mathbf{x}}_i - \tilde{\mathbf{x}}_j, i\omega_n) = \mathbf{G}_c(i\omega_n)\delta_{\tilde{\mathbf{x}}_i,\tilde{\mathbf{x}}_j} + \mathbf{G}_c(i\omega_n)\sum_l \left[\delta\mathbf{t}_c\delta_{\tilde{\mathbf{x}}_i,\tilde{\mathbf{x}}_l} + \delta\boldsymbol{\Sigma}(\tilde{\mathbf{x}}_i - \tilde{\mathbf{x}}_l, i\omega_n)\right]\mathcal{G}(\tilde{\mathbf{x}}_l - \tilde{\mathbf{x}}_j, i\omega_n)\ , \tag{3.46}$$

where $\mathbf{G}_c$ is the cluster Green function:

$$\mathbf{G}_c(i\omega_n) = [(i\omega_n + \mu)\mathbb{1} - \mathbf{t}_c - \boldsymbol{\Sigma}_c(i\omega_n)]^{-1}. \tag{3.47}$$

The equivalent of Eq. (3.46) in momentum space is obtained via Fourier transformation Eq. (3.41)

$$\mathcal{G}(\tilde{\mathbf{k}}, i\omega_n) = \mathbf{G}_c(i\omega_n) + \mathbf{G}_c(i\omega_n)\left[\delta\mathbf{t}_c(\tilde{\mathbf{k}}) + \delta\boldsymbol{\Sigma}(\tilde{\mathbf{k}}, i\omega_n)\right]\mathcal{G}(\tilde{\mathbf{k}}, i\omega_n). \tag{3.48}$$

Analogous to single-site DMFT, we neglect (to some extent) the momentum dependence of the self-energy, i.e., $\delta\boldsymbol{\Sigma}$ in Eq. (3.48) is dropped. The self-energy is truncated to the cluster and the equation simplifies to

$$\mathcal{G}^{-1}(\tilde{\mathbf{k}}, i\omega_n) = \mathbf{G}_c^{-1}(i\omega_n) - \delta\mathbf{t}_c(\tilde{\mathbf{k}}). \tag{3.49}$$

In the momentum space picture, the restriction implies a patching of the Brillouin zone. On these patches the self-energy is piece-wise constant. This *coarse graining* is also applied to the Green function by intra-cluster momentum integration of Eq. (3.49):

$$\mathcal{G}(i\omega_n) = \frac{N_c}{N}\sum_{\tilde{\mathbf{k}}}\mathcal{G}(\tilde{\mathbf{k}}, i\omega_n) \equiv \left[\mathbf{G}_c^{-1}(i\omega_n) - \boldsymbol{\Gamma}(i\omega_n)\right]^{-1}. \tag{3.50}$$

The resulting hybridization function $\boldsymbol{\Gamma}(i\omega_n)$ represents the effective interaction of the isolated cluster with its surrounding; the $N_c \times N_c$ matrix $\mathcal{G}(i\omega_n)$ plays a role analogous to the Weiss mean-field.

Cellular DMFT

Within the framework of the cellular DMFT, the hybridization function is determined self-consistently using equations (3.47), (3.50) and the cluster Dyson equation

$$\mathbf{\Sigma}_c(i\omega_n) = \mathcal{G}^{-1}(i\omega_n) - \mathbf{G}_c^{-1}(i\omega_n). \tag{3.51}$$

When the hybridization function is determined by Eq. (3.50) it defines the new quantum problem that has to be solved by an appropriate impurity solver, such as quantum Monte Carlo. These steps are iterated until convergence is reached.

Dynamical Cluster Approach

The approximation in cellular DMFT, directly derived from the locator expansion by neglecting the inter-cluster contribution of the self-energy, means that the phase factors $\exp(i\tilde{\mathbf{k}} \cdot \tilde{\mathbf{x}})$ in self-energy diagrams are not taken into account. The neglect of these phase factors is equivalent to a basis change of the creation and annihilation operators [Koc11]

$$\hat{\mathbf{c}}_{\mathbf{x}}(\mathbf{k}) \overset{\text{CDMFT}}{\longrightarrow} \hat{\mathbf{c}}_{\mathbf{X}}(\tilde{\mathbf{k}}) = \sum_{\tilde{\mathbf{x}}} e^{-i\tilde{\mathbf{k}}\cdot\tilde{\mathbf{x}}}\, \hat{\mathbf{c}}_{\tilde{\mathbf{x}}+\mathbf{X}}(\tilde{\mathbf{k}}) \;, \tag{3.52}$$

which results in the same hopping matrix elements on the cluster as in the original lattice, but breaks the translation symmetry. To arrive at a self-consistent formulation that restores the symmetry, one uses

$$\hat{\mathbf{c}}_{\mathbf{x}}(\mathbf{k}) \overset{\text{DCA}}{\longrightarrow} \hat{\mathbf{c}}_{\mathbf{X}}(\tilde{\mathbf{k}}) = \sum_{\tilde{\mathbf{x}}} e^{-i\tilde{\mathbf{k}}\cdot(\tilde{\mathbf{x}}+\mathbf{X})}\, \hat{\mathbf{c}}_{\tilde{\mathbf{x}}+\mathbf{X}}(\tilde{\mathbf{k}}) \tag{3.53}$$

for transforming the operators. A drawback is that the cluster hopping elements differ now from the original Hamiltonian.

Summarizing the above, in a real space picture DCA and cellular DMFT are distinguished only by different choices of the gauge [KSG08]. After restoring the translation invariance, one formulates the DCA self-consistency in terms of the cluster momenta $\mathbf{K}$ and arrives at the following scheme:

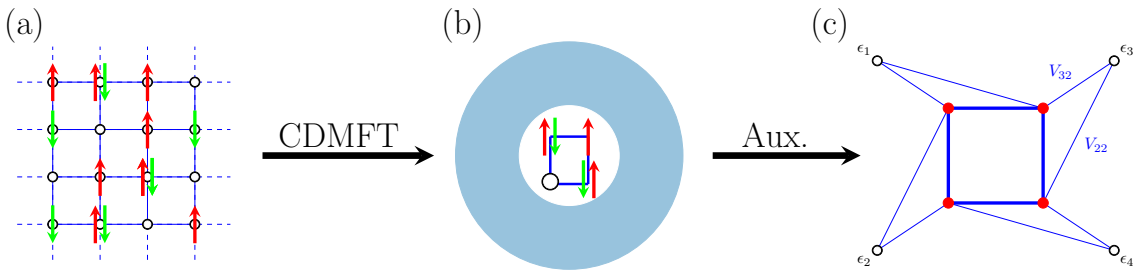

Figure 3.5. – Mapping of the original full lattice problem (a) on a cluster embedded in an effective continuous bath (b) and exemplary representation of a possible bath discretization (c), defining an auxiliary Hamiltonian that is treatable with ED or BSS-QMC.

1. Initial guess for $\mathbf{\Gamma}(i\omega_n)$ or, alternatively, for the bath Green function. At this point the original lattice geometry enters via the dispersion $\epsilon(\mathbf{k})$

$$\mathcal{G}(\mathbf{K}, i\omega_n) = [i\omega_n + \mu - \bar{\epsilon}(\mathbf{K}) - \mathbf{\Gamma}(\mathbf{K}, i\omega_n)]^{-1} \tag{3.54}$$
$$\bar{\epsilon}(\mathbf{K}) = \frac{1}{V_{\text{patch}}} \int_{\text{patch}} d\tilde{\mathbf{k}}\, \epsilon(\mathbf{K} - \tilde{\mathbf{k}}) \quad .$$

2. Solve the new quantum problem, e.g., using QMC methods, yielding the cluster Green function $\mathbf{G}_c$.

3. Calculate the new cluster self-energy

$$\mathbf{\Sigma}_c(\mathbf{K}, i\omega_n) = \mathcal{G}^{-1}(\mathbf{K}, i\omega_n) - \mathbf{G}_c^{-1}(\mathbf{K}, i\omega_n). \tag{3.55}$$

4. Obtain the coarse-grained lattice Green function via coarse graining

$$\mathbf{G}(\mathbf{K}, i\omega_n) = \frac{1}{V_{\text{patch}}} \int_{\text{patch}} d\tilde{\mathbf{k}} \left[i\omega_n + \mu - \epsilon(\mathbf{K} + \tilde{\mathbf{k}}) - \mathbf{\Sigma}_c(\mathbf{K}, i\omega_n) \right]^{-1} \quad . \tag{3.56}$$

5. Obtain the new bath Green function via the Dyson equation

$$\mathcal{G}(\mathbf{K}, i\omega_n) = \left[\mathbf{\Sigma}_c(\mathbf{K}, i\omega_n) + \mathbf{G}^{-1}(\mathbf{K}, i\omega_n) \right]^{-1} \quad . \tag{3.57}$$

6. Iterate steps 2. - 5.

The usage of the coarse-grained dispersion $\bar{\epsilon}$ reflects the fact that the cluster hopping is renormalized to an effective hopping

$$\mathbf{t}^{\text{DCA}}(\mathbf{X}_i, \mathbf{X}_j) = \frac{1}{N_c} \sum_{\mathbf{K}} e^{i(\mathbf{X}_i - \mathbf{X}_j)\cdot\mathbf{K}}\, \bar{\epsilon}(\mathbf{K}) \; . \tag{3.58}$$

The Fourier transformation is a special case of Eq. (3.42), after integrating $\tilde{\mathbf{k}}$

out. Due to the restored translation invariance, all self-consistency equations are diagonal in the cluster momenta. Thus, in contrast to cellular DMFT, no matrix inversions are needed.

Hamiltonian Representation

With the same arguments as in Sec. 3.2.1, one writes down a Hamiltonian representation for the cluster problem. In the case of cluster methods, the scalar hybridization function in Eq. (3.38) becomes a matrix in the cluster coordinates in real space and a diagonal function of the cluster momenta in momentum space:

$$\mathbf{\Gamma}(\mathbf{X}_i, \mathbf{X}_j, i\omega_n) = \sum_{\alpha}^{N_b} \frac{V_{i\alpha}^* V_{j\alpha}}{i\omega_n - \epsilon_\alpha^{\text{bath}}} \tag{3.59}$$

$$\mathbf{\Gamma}(\mathbf{K}, i\omega_n) = \sum_{\alpha}^{N_b} \frac{|V_\alpha(\mathbf{K})|^2}{i\omega_n - \epsilon_\alpha^{\text{bath}}} \ . \tag{3.60}$$

The generalization of Eq. (3.37) for the cluster problem reads (spin indices suppressed)

$$\begin{aligned}\hat{\mathbf{H}}_{\text{And}} = &\sum_{\alpha} \epsilon_\alpha^{\text{bath}} \hat{\mathbf{a}}_\alpha^\dagger \hat{\mathbf{a}}_\alpha + \sum_{i,j} t_{ij} \left(\hat{\mathbf{c}}_i^\dagger \hat{\mathbf{c}}_j + \text{h.c.} \right) + \\ &\sum_{\alpha,i} \left(V_{i\alpha}^\dagger \hat{\mathbf{a}}_\alpha^\dagger \hat{\mathbf{c}}_i + V_{i\alpha} \hat{\mathbf{a}}_\alpha \hat{\mathbf{c}}_i^\dagger \right) + U \sum_i \hat{\mathbf{n}}_{i\downarrow} \hat{\mathbf{n}}_{i\uparrow} \ .\end{aligned} \tag{3.61}$$

For the special case of $N_c = 1$, both cellular DMFT and DCA reduce to the single-site DMFT. The cluster methods become exact in the limit of infinite cluster size $N_c \to \infty$.

3.2.3. Lattice & Dispersion

In Sec. 3.2.1 and Sec. 3.2.2 the mappings of the original full lattice problem on an auxiliary problem in the (C)DMFT frameworks have been discussed. Within single-site DMFT, the original lattice structure enters only via the dispersion $\epsilon_{\mathbf{k}}$ of the non-interacting problem in Eq. (3.35) and for cluster extensions in Eq. (3.56). In cellular DMFT, the real-space hopping matrix is preserved within the cluster, so the geometry of the cluster is the same as in the original lattice. Since the cluster geometry in momentum space is arbitrary for DCA the coarse-grained dispersion Eq. (3.54) will additionally depend on the choice of the cluster pattern.

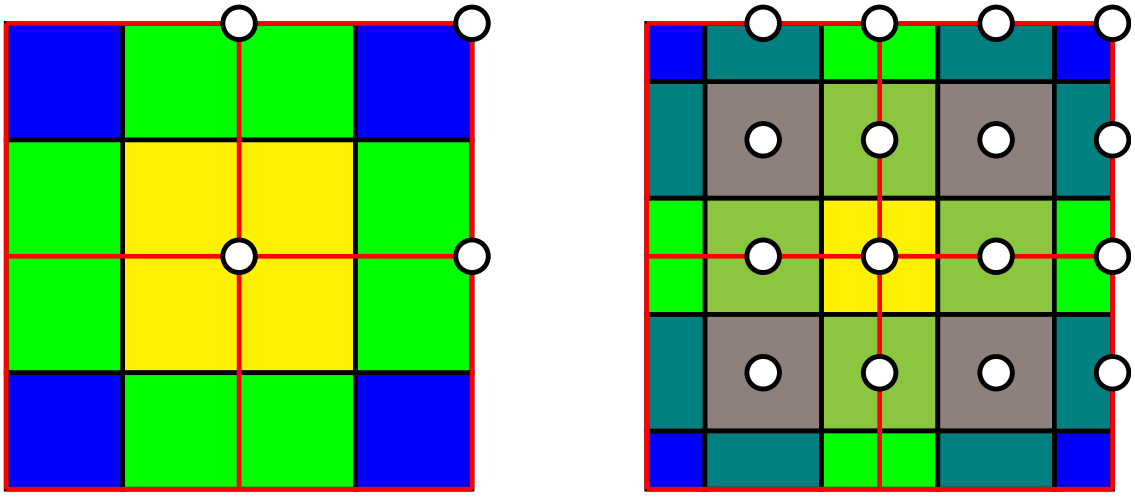

Figure 3.6. – Examples for the DCA patching of the Brillouin zone for a 2×2 cluster (left) and a 4×4 cluster (right). For a highly symmetric model, e.g., the isotropic Hubbard model on a square lattice, patches with same colors are identical and the DCA equations are only calculated for vectors within the irreducible part of the Brillouin zone.

The corresponding real space matrix elements, needed as input for the BSS-QMC impurity solver, are obtained via a Fourier transformation Eq. (3.58).

In this project, the focus is set on two-dimensional systems. Considered lattices are the square lattice with nearest neighbor-hopping t ($t_x = t_y = t, t' = 0$), the anisotropic square lattice ($t_x \neq t_y, t' = 0$) and the isotropic square lattice with additional next-nearest-neighbor hopping t' ($t_x = t_y = t, t' \neq 0$). For these systems, the dispersion is given by

$$\epsilon_{\mathbf{k}} = -\ 2\ [t_x\ \cos(k_x) + t_y\ \cos(k_y)] - 4\ t'\ \cos(k_x)\ \cos(k_y)\ , \tag{3.62}$$

which is easily obtained via a Fourier transformation of the hopping matrix.

In the DCA implementation performed as part of this thesis, the patterns for the patching of the Brillouin zone are rectangular. This is sketched in Fig. 3.6 for a 2×2 cluster (left) and a 4×4 cluster (right). In the highly symmetric case of the translationally invariant square lattice with only nearest neighbor hopping, patches with same colors are identical by symmetry. For the self-consistency equations and fitting procedure, only irreducible points of the Brillouin zone have to be taken into account.

3.2.4. Impurity Solvers

In Sec. 3.2.1 and Sec. 3.2.2, the DMFT framework and its cluster extensions were introduced. For each of the variants, the most difficult step is the solution of the new quantum problem defined by Eq. (3.38), Eq. (3.50), or Eq. (3.57), respectively.

The available tools, which can serve as impurity solver, are the main limitation for the applicability of (C)DMFT. In this section, we will discuss the main properties, strengths, and weaknesses of state-of-the-art impurity solvers and motivate why the development of an unbiased impurity solver, with a superior scaling in the inverse temperature, was a worthy goal of this thesis.

Existing impurity solvers can, in general, be partitioned in two types: direct impurity solvers, formulated in the action representation of the impurity problem, Eq. (3.30), and Hamiltonian based solvers, which map the original (cluster) DMFT problem (with a continuous bath) on an auxiliary Hamiltonian Eq. (3.61) with a finite bath.

For a long time, the Hirsch-Fye auxiliary-field quantum Monte Carlo method (HF-QMC) [HF86] has been the prevalent solver for DMFT studies at finite temperatures. The formulation of HF-QMC is very similar to the BSS-QMC, described in Sec. 3.1. In contrast to the BSS-QMC algorithm, which is tailored for finite-size lattice Hamiltonians, HF-QMC directly works on the action formulation Eq. (3.30). The algorithm requires a Trotter discretization of the path integral representation of the bath Green function in $\Lambda = \beta/\Delta\tau$ equidistant imaginary-time intervals $0 \leq \tau_i \leq \beta$ to decouple kinetic and interaction terms. Additionally, a Hubbard-Stratonovich transformation is applied on the interaction term, which replaces the electron-electron interaction with a coupling to an external binary field. This auxiliary field can be sampled with classical Monte Carlo techniques. The required matrix operations lead to a scaling with the cube of the number of time slices. Keeping the imaginary time discretization $\Delta\tau$ constant, to obtain comparable results, this translates into a cubic scaling with the inverse temperature β. The Trotter discretization introduces a systematic bias, which may be eliminated by an extrapolation of the raw results to the limit $\Delta\tau \to 0$.

More recently, such Trotter discretizations could be avoided by the development of so called continuous-time impurity solvers (CT-QMC) [GML$^+$11]. This type of impurity solvers are based on stochastic sampling of Feynman diagrams in a series expansion of the partition function. However, the available CT-QMC approaches scale also at least with the cube of β. Thus, all these direct methods scale cubically in β and can hardly approach ultra-low temperature phases, where interesting physical phenomena take place.
In the class of Hamiltonian based approaches, exact diagonalization (ED) related methods [CK94] have been the prevalent solvers so far. The original impurity problem, formulated with a continuous bath, is mapped on an effective Hamiltonian, corresponding to a discretization of this bath [Fig. 3.5 (c)], as described at the ends of Sec. 3.2.1 and Sec. 3.2.2. After diagonalization of the auxiliary Hamiltonian, the local Green function is calculated from the eigenvalues of the problem. One advantage of ED, compared to QMC methods, is the direct access to observables on the real-frequency axis. However, the discretization of the bath leads to a systematic bias, not present in direct impurity solvers. This systematic bias can be reduced by increasing the number of bath orbitals. One should also mention the ED related numerical renormalization group (NRG) [Wil75] approach to DMFT [BCP08]. Here the continuous bath is mapped on a semi-infinite chain, on which the bath pa-

Impurity solver	Scaling N	Scaling β	Systematic bias
CT-QMC	N^3/e^N	β^3	-
HF-QMC	N^3	β^3	Trotter discretization
ED/NRG	e^N	-	Bath discretization
BSS-QMC	N^3	β	Trotter discretization Bath discretization

Table 3.1. – Overview on common impurity solvers for (cluster) DMFT, judged by their scaling with bath or interacting sites N, scaling with the inverse temperature β, and systematic errors, which have to be eliminated somehow.

rameters are determined by a renormalization group approach, instead of a fitting procedure. This approach results in a chain structure, in which the contribution of more distant sites are less important. In real simulations the chain length is limited by an energy cutoff. However, ED and NRG are strongly limited, due to the exponential scaling with the number of sites of the problem (bath sites as well as impurity sites). This constraint is especially severe for multi-band models or cluster extension of DMFT.

More recently, a new Hamiltonian based impurity solver was formulated by Khatami et al. [KLB+10]. In this approach, the auxiliary problem is solved using BSS-QMC, described in Sec. 3.1. The advantage of the BSS-QMC method, compared to HF-QMC and CT-QMC, is its linear scaling in the inverse temperature. Compared to ED and NRG, BSS-QMC can easily handle large numbers of bath orbitals, due to its cubic scaling with lattice sites. However, BSS-QMC is based on a Hubbard-Stratonovich transformation and Trotter decoupling, which leads to Trotter discretization errors (analogous to HF-QMC).

A comparison of the different state-of-the-art solvers is given in Table 3.2.4. This overview gives the motivation for the major goal of this project: the development of an algorithm that is numerically exact and retains the favorable linear scaling in the inverse temperature. As was shown in the case of HF-QMC, it is possible to eliminate Trotter errors with a multigrid extrapolation method [Blü08], even on the level of Green functions and self-energies. We have already demonstrated in earlier studies that an analogous error elimination scheme can be applied to BSS-QMC and additionally, even finite-size errors can be eliminated [Ros12]. We have constructed an algorithm that is numerically exact, in the sense that the resulting Green functions do not suffer from any systematic errors. In a previous study, the proposed algorithm was applied to study pseudogaps emergent in the two-dimensional Hubbard model [RGAB12]. The numerical details of constructing an unbiased BSS-QMC algorithm and the generalization to an impurity solver for DMFT and cluster DMFT, will be discussed in Chap. 4 and Chap. 6.

3.2.5. Susceptibilities

One considered application of the efficient impurity solver with linear-in-β scaling was the investigation of the phase diagram of the two-dimensional Kondo lattice

model (KLM), described in Sec. 2.2. The idea was to extend a previous DCA study [cf. Fig. 2.2] [MA08], led by our collaborator Prof. Dr. F. F. Assaad, that was limited by the employed HF-QMC impurity solver. Because of the cubic scaling of the impurity solver with the inverse temperature it was not possible to track the exponentially small Kondo temperature down to small J [Eq. (2.5)]. Based on a recent variational Monte Carlo study [AFB14], a superconducting phase is presumed for doped systems at low temperatures. Our strategy was, to detect the onset of superconductivity via the calculation of the pairing susceptibility. The numerically expensive calculation is done after the convergence of the self-consistency cycle only. While the DCA calculations were performed within the scope of this project, the implementation of the spin susceptibility measurements into the BSS-QMC algorithm was assigned to Dr. Kuang-Shing Chen in the group of Prof. Dr. Fakher Assaad at the University of Würzburg. The algorithmic approach is similar to the calculation of spin susceptibilities in continuous-time QMC methods, which were used to identify a superconducting phase in the Hubbard model on a triangular lattice [CMY+13, Che13]. Unfortunately, Chen left science in December 2014 quite abruptly, before finishing this code and it was not possible to replace him at short notice. Thus, the investigation of the superconducting phase of the KLM is left for following studies. Instead, we concentrated on another interesting application: the momentum dependence of self-energies in the KLM and Hubbard model (Chap. 8). However, to facilitate the connection of follow-up projects, we will discuss the main ideas of the calculation of spin susceptibilities within the BSS-QMC and DCA frameworks[5].

The two-particle Green function in the particle-hole channel is defined as [ADGS75]

$$\begin{aligned}\chi_{\sigma,\sigma'}(q,k,k') = \int_0^\beta \int_0^\beta \int_0^\beta \int_0^\beta d\tau_1 d\tau_2 d\tau_3 d\tau_4 \; e^{i[(\omega_n+\nu_n)\tau_1 - \omega_n\tau_2 + \omega_{n'}\tau_3 - (\omega'_n+\nu_n)\tau_4]} \times \\ \times \langle \mathcal{T} \hat{\alpha}_{\mathbf{k}+\mathbf{q}\sigma}(\tau_1)\hat{\alpha}^\dagger_{\mathbf{k}\sigma}(\tau_2)\hat{\alpha}_{\mathbf{k}'\sigma'}(\tau_3)\hat{\alpha}^\dagger_{\mathbf{k}'+\mathbf{q}\sigma'}(\tau_4)\rangle \,, \end{aligned} \tag{3.63}$$

where $\mathcal{T}$ is the time-ordering operator, $\hat{\alpha}^\dagger$ ($\hat{\alpha}$) creation (annihilation) operators, and $\hat{\alpha} \in \{\hat{\mathbf{c}}, \hat{\mathbf{f}}\}$ corresponds to the band index [cf. Fig. 2.1 (b)]. For simplification, the combined indices $k = (\mathbf{k}, i\omega_n)$, $k' = (\mathbf{k}', i\omega'_n)$, and $q = (\mathbf{q}, i\nu_n)$ are used. The fact that only three momenta and frequencies appear, reflects the reduction of one degree of freedom in space and time due to momentum and energy conservation. Analogous to the Dyson equation, Eq. (3.34), one writes the Bethe-Salpeter equation

$$\begin{aligned}\chi_{\sigma,\sigma'}(q,k,k') = \chi^0_{\sigma,\sigma'}(q,k,k') + \\ + \chi^0_{\sigma,\sigma''}(q,k,k'')\Gamma_{\sigma'',\sigma'''}(q,k'',k''')\chi_{\sigma''',\sigma'}(q,k''',k').\end{aligned} \tag{3.64}$$

[5] At this point, I thank Dr. Kuang-Shing Chen and Prof. Dr. Fakher Assaad for the enlightening discussions and explanations.

The non-interacting susceptibility is denoted by χ^0. The irreducible vertex function Γ plays the role of the self-energy in the one-particle formalism. The corresponding DCA approximation, implies the coarse-graining of Eq. (3.64), again using capital Ks for inter-cluster vectors:

$$\begin{aligned}\chi_{\sigma,\sigma'}(q,K,K') = \chi^0_{\sigma,\sigma'}(q,K,K') + \\ +\chi^0_{\sigma,\sigma''}(q,K,K'')\Gamma_{\sigma'',\sigma'''}(q,K'',K''')\chi_{\sigma''',\sigma'}(q,K''',K').\end{aligned} \tag{3.65}$$

While the self-energy on the cluster is, within the DCA approximation, the same as the coarse-grained self-energy, this does not hold for two-particle quantities, because the self-consistency is only used on the one-particle level. Susceptibilities are calculated after fully converged DCA simulations. The coarse-grained non-interacting susceptibility[6] on the lattice is calculated from the one-particle Green function [FYC+11]:

$$\chi^0_l(q,K,K') = \delta_{\sigma,\sigma'}\delta_{\mathbf{K},\mathbf{K}'}\delta_{\omega_n,\omega'_n}\frac{N}{N_c}\sum_{\tilde{\mathbf{k}}} G_\sigma(\mathbf{K}+\tilde{\mathbf{k}},i\omega_n)G_\sigma(\mathbf{K}+\tilde{\mathbf{k}}+\mathbf{q},i\omega_n+i\nu_n). \tag{3.66}$$

The cluster susceptibilities (χ^0_c,χ_c) are calculated by the impurity solver. For corresponding vertex functions the Bethe-Salpeter-Equation is inverted. The lattice susceptibility χ_l is, finally, obtained by setting the coarse-grained lattice vertex function Γ_l equal to the cluster vertex function Γ_c:

$$\begin{aligned}\left(\chi^0_l\right)^{-1} - \left(\chi_l\right)^{-1} = \Gamma_l = \Gamma_c = \left(\chi^0_c\right)^{-1} - \left(\chi_c\right)^{-1} \\ \chi_l = \left[\left(\chi^0_l\right)^{-1} + \left(\chi_c\right)^{-1} - \left(\chi^0_c\right)^{-1}\right]^{-1} \\ = \chi^0_l[\mathbb{1} - \underbrace{\Gamma_l\chi^0_l}_{=M}]^{-1}\ .\end{aligned} \tag{3.67}$$

In the case of the pairing susceptibility $\chi_l(q,k,-k)$ and $i\omega_n \to 0$, M is the *pairing matrix*. It can be used for a classification of superconducting phases, e.g., deciding between s- and d-wave superconductivity by comparison of the the leading eigenvalues of M as function of the momentum [KMJ09].

The calculation of the cluster susceptibilities in the BSS-QMC algorithm is based on single-particle Green functions. In contrast to the calculation of single-particle

[6] The term *non-interacting susceptibility* is used to emphasize the analogies to the Dyson equation [Eq. (3.46)]. Strictly speaking, the definition is assigned to a bubble approximation involving interacting Green functions.

observables, where only equal-time Green functions are needed, the full Green function, depending on two imaginary-time variables (or Matsubara frequencies) has to be calculated. These measurements lead to a $\mathcal{O}(\beta^2)$ scaling, but have only to be done as one shot after the full convergence of the DCA self-consistency. One of the numerical challenges is the storage and processing of large Green function matrices. Rewriting the particle-hole susceptibility Eq. (3.63), with the convention that the numbers $\{1, 2, 3, 4\}$ carry all degrees of freedom[7]:

$$\chi^{\mathrm{ph}}(1,2;3,4) = \langle \mathcal{T}\hat{\alpha}_1\hat{\alpha}_2^\dagger\hat{\alpha}_3\hat{\alpha}_4^\dagger\rangle - \langle \mathcal{T}\hat{\alpha}_1\hat{\alpha}_2^\dagger\rangle \langle \mathcal{T}\hat{\alpha}_3\hat{\alpha}_4^\dagger\rangle \tag{3.68}$$

and, analogously, the particle-particle susceptibility

$$\chi^{\mathrm{pp}}(1,2;3,4) = \langle \mathcal{T}\hat{\alpha}_1\hat{\alpha}_2\hat{\alpha}_3^\dagger\hat{\alpha}_4^\dagger\rangle - \langle \mathcal{T}\hat{\alpha}_1\hat{\alpha}_2\rangle \langle \mathcal{T}\hat{\alpha}_3^\dagger\hat{\alpha}_4^\dagger\rangle = \langle \mathcal{T}\hat{\alpha}_1\hat{\alpha}_2\hat{\alpha}_3^\dagger\hat{\alpha}_4^\dagger\rangle \ . \tag{3.69}$$

In the last step, particle conservation

$$\langle \mathcal{T}\hat{\alpha}_1^\dagger\hat{\alpha}_2^\dagger\rangle = \langle \mathcal{T}\hat{\alpha}_1\hat{\alpha}_2\rangle = 0 \tag{3.70}$$

was used. Using the notation $\langle ... \rangle_{\mathrm{MC}}$ for Monte-Carlo averages and the QMC single-particle Green function G, we find for the measurement of the particle-hole susceptibility using Wick's theorem [Wic50]

$$\begin{aligned}
\langle \chi^{\mathrm{ph}}(12;34)\rangle_{\mathrm{MC}} &= \langle\langle \mathcal{T}\hat{\alpha}_1\hat{\alpha}_2^\dagger\hat{\alpha}_3\hat{\alpha}_4^\dagger\rangle\rangle_{\mathrm{MC}} - \langle\langle \mathcal{T}\hat{\alpha}_1\hat{\alpha}_2^\dagger\rangle\rangle_{\mathrm{MC}} \langle\langle \mathcal{T}\hat{\alpha}_3\hat{\alpha}_4^\dagger\rangle\rangle_{\mathrm{MC}} \\
&= \langle\langle \mathcal{T}\hat{\alpha}_1\hat{\alpha}_4^\dagger\rangle \langle \mathcal{T}\hat{\alpha}_2^\dagger\hat{\alpha}_3\rangle + \langle \mathcal{T}\hat{\alpha}_1\hat{\alpha}_2^\dagger\rangle \langle \mathcal{T}\hat{\alpha}_3\hat{\alpha}_4^\dagger\rangle\rangle_{\mathrm{MC}} - \langle G_{12}\rangle_{\mathrm{MC}} \langle G_{34}\rangle_{\mathrm{MC}} \\
&= \langle G_{12}G_{34}\rangle_{\mathrm{MC}} - \langle G_{14}G_{32}\rangle_{\mathrm{MC}} - \langle G_{12}\rangle_{\mathrm{MC}} \langle G_{34}\rangle_{\mathrm{MC}}
\end{aligned} \tag{3.71}$$

and for the particle-particle susceptibility:

$$\begin{aligned}
\langle \chi^{\mathrm{pp}}(12;34)\rangle_{\mathrm{MC}} &= \langle\langle \mathcal{T}\hat{\alpha}_1\hat{\alpha}_2\hat{\alpha}_3^\dagger\hat{\alpha}_4^\dagger\rangle\rangle_{\mathrm{MC}} \\
&= \langle\langle \mathcal{T}\hat{\alpha}_1\hat{\alpha}_4^\dagger\rangle \langle \mathcal{T}\hat{\alpha}_2\hat{\alpha}_3^\dagger\rangle\rangle_{\mathrm{MC}} \\
&= \langle G_{14}G_{23}\rangle_{\mathrm{MC}} \, .
\end{aligned} \tag{3.72}$$

In general, more terms will remain in Eq. (3.72) than written here. In the case of the KLM, they drop out due to symmetry reasons. By analyzing the Hamiltonian

[7] The formulation of the susceptibility measurements shown here were worked out in detail by Dr. Kuang-Shing Chen (unpublished).

Eq. (3.19), one finds that in the particle-particle channel only the spin configurations

$$\sigma_1 = \uparrow, \sigma_2 = \downarrow, \sigma_3 = \downarrow, \sigma_4 = \uparrow$$

and

$$\sigma_1 = \downarrow, \sigma_2 = \uparrow, \sigma_1 = \uparrow, \sigma_2 = \downarrow$$

contribute to the susceptibility[8]. Summarizing the above, for the calculations of the two-particle quantities, we need the full matrix

$$\langle G_{12} \rangle_{\mathrm{MC}} = - \left\langle \langle \mathcal{T} \hat{\mathbf{c}}_\sigma \hat{\mathbf{c}}_\sigma^\dagger \rangle \right\rangle_{\mathrm{MC}} \delta_{\sigma,\sigma'} \delta_{\alpha,\alpha'} \delta_{K,K'} \delta_{\omega,\omega'}. \tag{3.73}$$

At the time of writing, the measurements of the cluster quantities were basically included in the KLM BSS-QMC code, but not tested and combined with the DCA lattice susceptibilities. These calculations have to be shifted to a follow-up project.

[8] Not all symmetries are respected in every QMC measurement, i.e., for all auxiliary field configurations. E.g., particle conservation is respected in all configurations, but the Green functions become diagonal in the orbital index after the QMC average only:

$$\langle \mathcal{T} \hat{\mathbf{c}}_\sigma \hat{\mathbf{f}}_\sigma^\dagger \rangle \neq 0 = \left\langle \langle \mathcal{T} \hat{\mathbf{c}}_\sigma \hat{\mathbf{f}}_\sigma^\dagger \rangle \right\rangle_{\mathrm{MC}}.$$

4. Numerical Developments I: Unbiased BSS-QMC

In this chapter, the details of various numerical developments achieved in this project, are presented. These algorithms are necessary for obtaining unbiased results from BSS-QMC, for lattice studies as well as for the integration within a (cluster) DMFT framework that will be presented in Chap. 6.

4.1. Impact & Elimination of Trotter Errors

In Sec. 3.1 the derivation of the BSS-QMC algorithm was shown. One of the main steps consists of a Trotter decomposition of the Hamiltonian. This leads to systematic biases in the results of BSS-QMC simulations. Eq. (3.6) implies that the Trotter impact on observables is proportional to $\Delta\tau^2$ in leading order. To eliminate this systematic error, a set of simulations with different values of $\Delta\tau$, for fixed physical parameters, is performed. Afterwards, the final result is obtained by an extrapolation to the limit $\Delta\tau \to 0$. In Fig. 4.1, the extrapolation scheme is demonstrated for the double occupancy

$$D = \langle \hat{\mathbf{n}}_\downarrow \hat{\mathbf{n}}_\uparrow \rangle \tag{4.1}$$

for the half-filled Hubbard model on a square lattice at weak coupling $U = 2$ and moderate temperature $T = 0.10$, for different lattice sizes. Lines denote linear fits. Values at $\Delta\tau^2 = 0$ are the final extrapolated values for the double occupancy extracted from these fits. The dependence on $\Delta\tau^2$ is convincingly linear, which opens the opportunity to save computational time by using larger values of $\Delta\tau$ and performing the extrapolation[1].

In most cases, the $\Delta\tau \to 0$ extrapolation for the double occupancy and other static quantities is straight forward and absolutely reliable. However, for the calculation of dynamical quantities, like spectral functions or self-energies, one needs to perform the Trotter extrapolation on the level of the Green function. This is especially important when the BSS-QMC algorithm serves as impurity solver, as will be discussed in Chap. 6. Trotter biased Green functions, obtained from BSS-QMC calculations, do not only show a quantitative shift, but also suffer directly from the

[1] To gain the same precision for the final value without extrapolation, one has to perform a calculation using very small values of $\Delta\tau$. This calculation is computationally more expensive than the whole set of simulations used for the extrapolation.

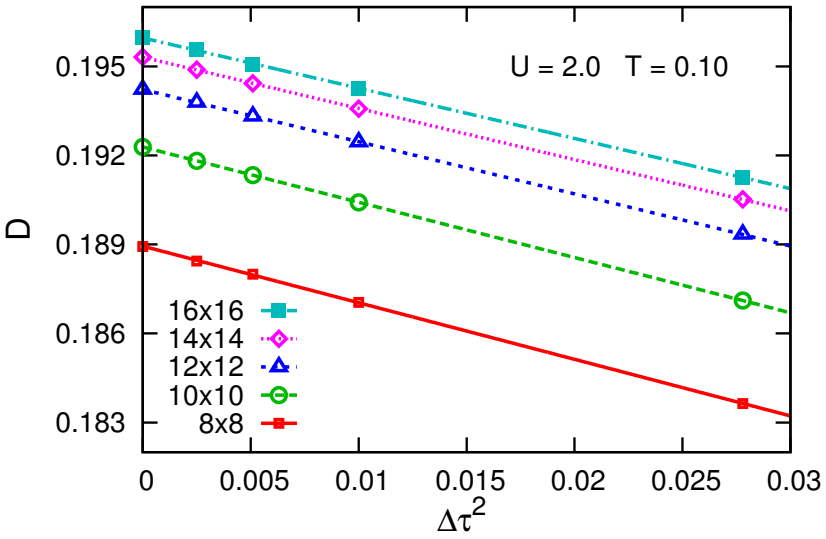

Figure 4.1. – Example for the impact and extrapolation of the systematic Trotter bias in BSS-QMC: double occupancy as function of the squared Trotter discretization $(\Delta\tau)^2$ for the half-filled Hubbard model on a square lattice at weak coupling $U = 2$ and moderate temperature $T = 0.10$ for different system sizes. Lines: linear fits for obtaining extrapolated values, marked at $(\Delta\tau)^2 = 0$.

discretization in imaginary time, i.e., the functions can only be measured on a finite grid

$$G(\tau) \approx G_i = G(\tau_i) \text{ , with } i \in [0, \ldots, \Lambda = \beta/\Delta\tau] \text{ , } \tau_i = i\Delta\tau. \tag{4.2}$$

For dynamic quantities, the Trotter extrapolation has to be carried out separately at all imaginary-time points τ. Here the problem arises that for an arbitrary choice of the $\Delta\tau$ grid, the measured raw Green functions will not share the same supporting points [symbols in the inset of Fig. 4.2 (a)]. Hence, the Green functions have to be brought on a common grid. One way to adapt the different grids is to perform a spline interpolation. However, a direct interpolation on the level of the Green function, e.g., by cubic splines, introduces a large bias, due to the non-vanishing higher derivatives of $G(\tau)$ [Blü02]. To solve this issue, an intermediate step is introduced: instead of performing a spline interpolation on the level of $G(\tau)$, we interpolate a *difference Green function* ΔG, which is defined by subtracting the BSS-QMC Green functions $\{G_{\Delta\tau_j}\}$ from a *reference Green function* G^{ref} [red solid line Fig. 4.2 (a)]:

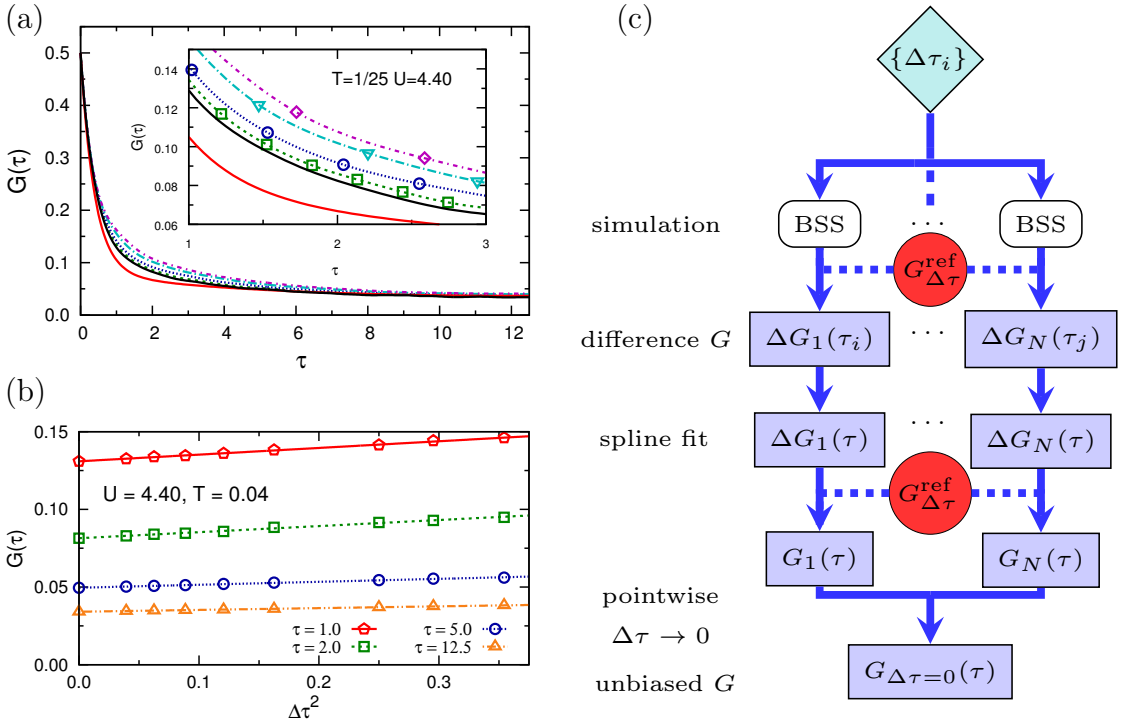

Figure 4.2. – Extrapolation scheme for Trotter biased Green functions obtained from BSS-QMC: (a) Trotter biased Green functions from BSS-QMC (symbols), reference Green function used within the extrapolation scheme (red solid line) and unbiased result (black solid line). (b) Dependence of the Green function at fixed imaginary-time points τ as function of the squared Trotter discretization error $(\Delta\tau)^2$, lines show linear fit in $(\Delta\tau)^2$. (c) Schematic representation of the multigrid extrapolation procedure.

$$\Delta G_{\Delta\tau_j}(\tau_i) = G^{\mathrm{ref}}_{\Delta\tau_j}(\tau_i) - G_{\Delta\tau_j}(\tau_i) \tag{4.3}$$

$$\text{with} \qquad G^{\mathrm{ref}}_{\Delta\tau_j}(\tau_i) = A\left(e^{-\tau/\tau_0} \pm e^{-(\beta-\tau)/\tau_0}\right) \ .$$

The $\pm$ sign indicates that, depending on the shape of the Green function, a symmetric or anti-symmetric reference Green function is used. In cases where this extrapolation scheme is applied automatically, like in the cluster DMFT self-consistency, the BSS-QMC Green functions are split in their symmetric and anti-symmetric parts in advance, and treated separately[2]. The errors, which are introduced by

[2]The reference Green function can be determined by various approaches, e.g., a high-frequency expansion of the self-energy [PWN97]. Here the general form Eq. (4.3) is used, to ensure of

a cubic spline interpolation, arise from non-vanishing higher order derivatives of $G(\tau)$. The regularization through the reference Green function is most useful, if the data and the reference Green function agree in higher order derivatives. The free parameters in Eq. (4.3) are fitted in the way that the second derivative of the data and the reference Green function agree well at $\tau \to 0$, where the contribution of higher order terms is most significant. So a minimization procedure for every BSS-QMC Green function

$$\min \left\{ \left[\frac{\delta^2}{\delta \tau_i^2} \, G^{\mathrm{ref}}_{\Delta\tau_j}(\tau_i) - \frac{\delta^2}{\delta \tau_i^2} \, G_{\Delta\tau_j}(\tau_i) \right]^2_{\tau_i \to 0} \right\} \tag{4.4}$$

is performed.

The spline interpolation yields Green functions that are still Trotter biased, but quasi continuous in imaginary time. I.e., they can be evaluated on an arbitrary fine τ grid [lines in Fig. 4.2 (a)]. Now one can perform the $\Delta\tau$ extrapolation on this grid and obtain a Green function free from significant Trotter errors and quasi continuous in imaginary time [black solid line in Fig. 4.2 (a)].

The full Trotter extrapolation scheme is sketched in Fig. 4.2 (c). For exemplary imaginary-time points, the quality of the extrapolation is demonstrated in Fig. 4.2 (b). A further advantage of the extrapolation procedure is the stability of the Fourier transformation to Matsubara frequencies,

$$G(i\omega_n) = \int_0^\beta d\tau \; G(\tau) \; e^{-i\omega_n \tau}. \tag{4.5}$$

In the case of the directly obtained BSS-QMC Green functions on the discrete time grid, the transformation Eq. (4.5) can cause unphysical features in $G(i\omega_n)$.

In a recent study, we compared the impact of finite-size effects on different quantities and parameter sets [RGAB12] in the two-dimensional Hubbard model. We found that the Green function is not equally biased at all points in momentum space. This imbalance becomes stronger in the vicinity of the crossover temperature, where antiferromagnetic fluctuations become important. Thus, for the final results, a quantitative comparison with complementary methods can only be performed after the elimination of systematic errors. The same holds for the Trotter bias. We compare the impact of the Trotter discretization on diagonal and off-diagonal Green functions in Fig. 4.3. Here for a 2×2 cluster embedded in an effective bath at the low temperature $\beta = 25$ in the Mott insulating phase ($U = 8$). While for the half-filled case the diagonal BSS-QMC Green functions are identi-

the stability of the fit in automated extrapolation procedures. These procedures are needed for large Green function matrices, with arbitrary entries, in the cluster DMFT framework; see Chap. 6.

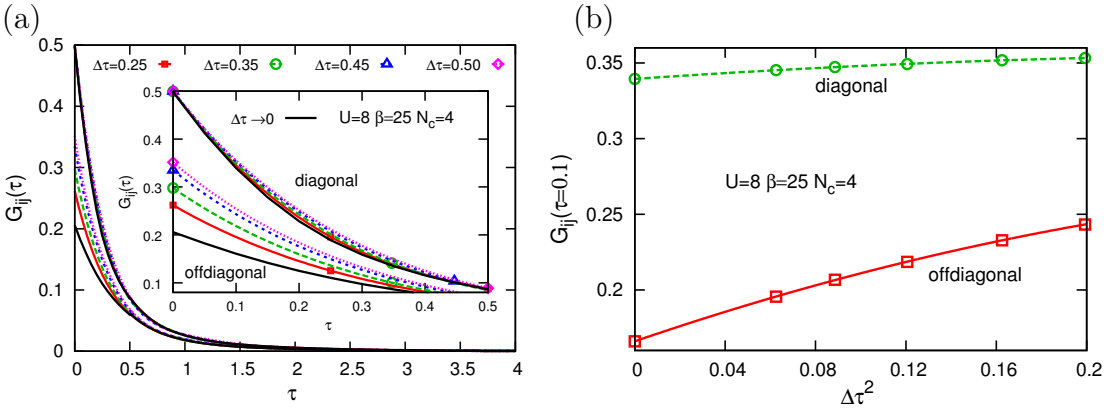

Figure 4.3. – Comparison of Trotter bias in diagonal and off-diagonal Green functions in imaginary time (a). Exemplaric $\Delta\tau \to 0$ extrapolation for $\tau = 0.1$ (b).

cally at $\tau = 0$[3], the off-diagonal Green functions [colored lines in Fig. 4.3] deviate strongly from each other and from the extrapolated result [black solid line in Fig. 4.3]. Furthermore, the maximal deviation in the off-diagonal Green functions (at $\tau = 0$) is larger than in the diagonal functions (maximum at $\tau = \beta/2$, not shown). The specific dependence on the discretization $\Delta\tau$ is shown in Fig. 4.3 (b) for $\tau = 0.1$ close to zero. Lines show quadratic fits in $(\Delta\tau)^2$, used for determination of the unbiased values. The off-diagonal elements also show more dominant quadratic $\Delta\tau^2$ contributions to the $\Delta\tau$ dependence.

We conclude that only a careful elimination of systematic errors can lead to fully consistent and meaningful results.

4.2. Unbiased Self-Energy in the Thermodynamic Limit

A quantity, which is often considered in DMFT studies for the analysis of the properties of a system, is the self-energy $\Sigma(i\omega_n)$. The self-energy can be calculated from the Green function via the Dyson equation

$$\Sigma_{\mathbf{k}}(i\omega_n) = i\omega_n + \mu - \epsilon_{\mathbf{k}} - G_{\mathbf{k}}^{-1} \quad . \tag{4.6}$$

Here, μ denotes the chemical potential and $\epsilon_{\mathbf{k}}$ the dispersion of the non-interacting problem. In direct lattice calculations, the limited cluster size is the main bias.

In this section, an algorithmic approach that yields self-energy data free from systematic errors and in the thermodynamic limit is presented. To achieve a reli-

[3]Their value is determined by the filling of the system.

able finite-size (FS) analysis, large lattices have to be considered, e.g., for the two-dimensional Hubbard model, lattice calculations up to 256 sites were performed. Due to the large amount of computer time needed for these calculations[4], we have to reduce the precision in the Monte Carlo procedure, by reducing the number of sweeps, to produced results in a reasonable time scale. After the elimination of Trotter errors of the noisy raw data, using the scheme presented in Sec. 4.1, some significant fluctuations remain inevitably in the resulting $G(\tau)$. This is illustrated in Fig. 4.4, for the Hubbard model on a 16×16 square lattice at low temperature $T = 0.04$ and weak coupling $U = 2$. Thick colored lines show data with higher precision, thin lines with lower precision (1/10th number of Monte Carlo sweeps). The extrapolated Green function is denoted by black circles. On the level of Matsubara frequencies, the lack of smoothness of the Green function in imaginary time causes non-causal features, e.g., a deviation from the $1/i\omega_n$ high-frequency behavior. This impact is more severe in the self-energy Eq. (4.6) and leads to unphysical features. This bias can be reduced by a smoothing procedure. For the self-energies, which

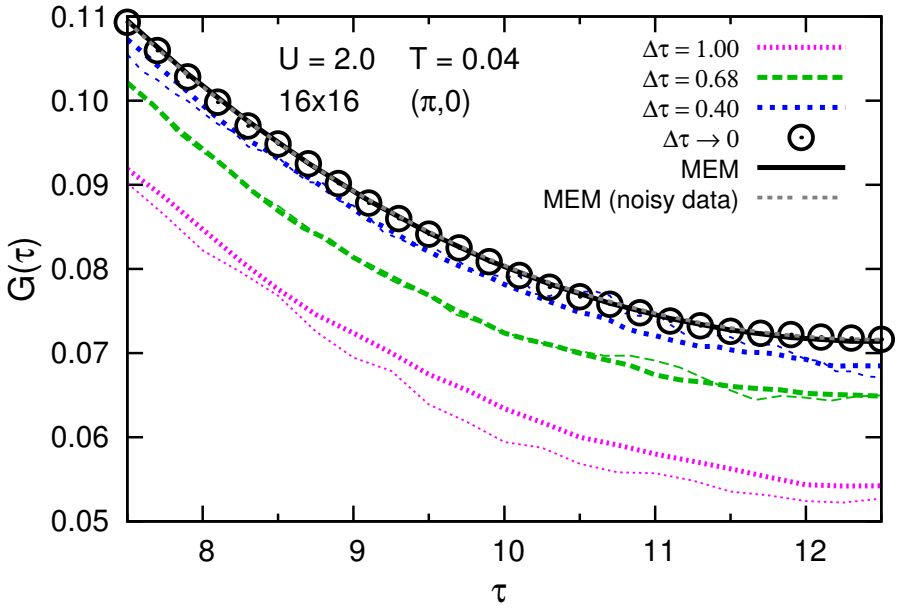

Figure 4.4. – Extrapolation of BSS-QMC Green functions to $\Delta\tau \to 0$. Analytic continuation (MEM, black line) regularizes the results of pointwise extrapolations (symbols) and yields stable results (gray line) even in the case of noisy raw data (thin colored lines).

will be shown in Chap. 5, a regularization procedure based on a maximum entropy method (MEM) [Bry90] was developed, where the corresponding spectral function $A(\omega)$ is computed via the inversion

$$G(\tau) = -\int_{-\infty}^{\infty} d\omega\, A(\omega)\, \frac{e^{-\omega\tau}}{1 + e^{-\omega\beta}} \quad . \tag{4.7}$$

[4]The BSS-QMC algorithm scales with N^3, i.e., a calculation for the 16×16 lattice takes 64 times longer than a calculation for the 8×8 lattice, if the precision is kept constant.

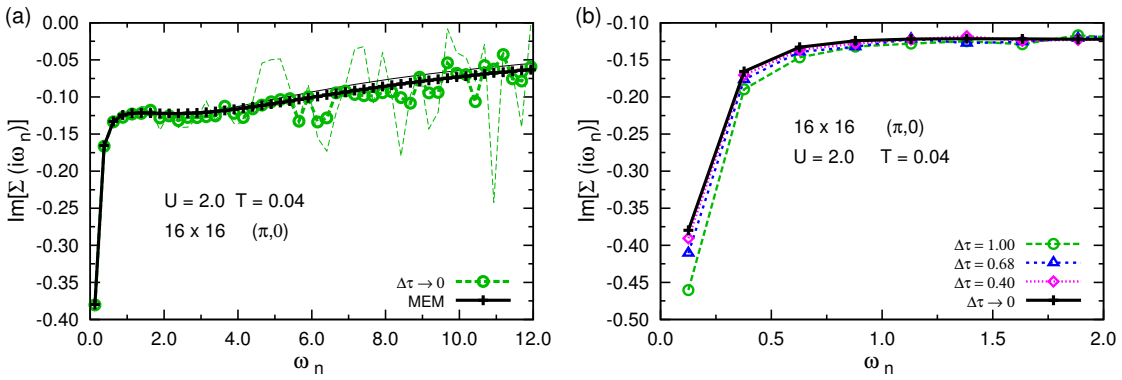

Figure 4.5. – (a) Influence of statistical noise in the raw data $G(\tau)$ on the self-energy $\Sigma(i\omega_n)$ and stabilization by MEM regularization. Thin lines: noisy data; thick lines and symbols: high precision results. (b) Impact of Trotter discretization $\Delta\tau$ on the Matsubara self-energy.

The intermediate spectral function $A(\omega)$ is used only for producing continuous and smooth Green functions $G(\tau)$ via Eq. (4.7). Even if the quality of spectral functions, calculated via MEM, can be questionable, the procedure is stable, because we are interested in $G(\tau)$ only and not in the specific form of $A(\omega)$. We can guarantee that the $G(\tau)$, calculated from Eq. (4.7), reproduces the data within the errors of the method, shown as solid line in Fig. 4.4. Notably, the results based on high- or low-precision data (thick black line vs. gray line) are hardly distinguishable and can both be used for stable computations of self-energies. So the method can yield reliable smooth unbiased Green functions, even from noisy data, which gives the great opportunity to safe up to a factor of ten in computational time, just by reducing the number of Monte Carlo sweeps. The impact of errors in the Green function on the level of the self-energy is shown in Fig. 4.5 (a). The self-energies, directly computed from the $\Delta\tau$-extrapolated data (green dashed lines), show noisy behavior at higher frequencies. This is corrected by the smoothing procedure (black solid lines). Thin lines show the results for data sets with poor statistics. The physically most important low-frequency range remains untouched. In contrast, the impact of Totter errors shown in Fig. 4.5 (b) have their major effect on the low-frequency range. Only the combination of $\Delta\tau$ extrapolation and the smoothing procedure can lead to results that are comparable to other methods, e.g., the dynamical vertex approximation (DΓA). A comparison is shown in the next section.

Extrapolation to the Thermodynamic Limit

In the previous section, we presented methods, which can produce unbiased self-energies from BSS-QMC Green function, without significant systematic errors, arising from the finite $\Delta\tau$ discretization or noisy data. However, these BSS-QMC

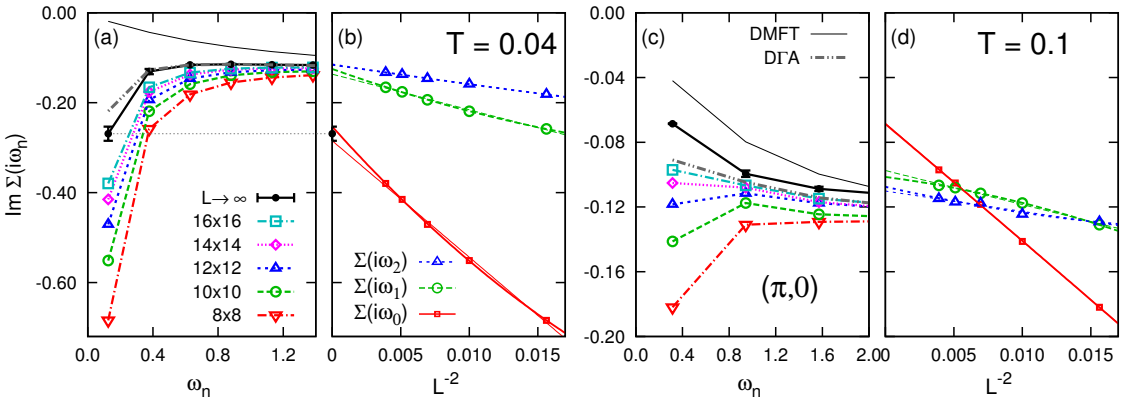

Figure 4.6. – Finite-size (FS) analysis of the self-energy on the Matsubara axis at weak coupling $U = 2$, $\mathbf{k} = (\pi, 0)$ for the two-dimensional Hubbard model on a square lattice at half-filling. FS BSS-QMC data (open symbols and broken colored lines), extrapolated BSS-QMC results in the thermodynamic limit (circles and black bold solid line), and $D\Gamma A$ data (gray line) at $T = 0.04$ (a) and $T = 0.10$ (c); also shown are momentum-independent single-site DMFT results (thin black lines). (b)+(d) FS BSS-QMC (symbols) data for the first three Matsubara frequencies versus inverse system size plus extrapolations in linear order in L^{-2} (thin lines) and quadratic order (thick lines).

self-energies still correspond to finite-size (FS) clusters. To obtain actual unbiased self-energies, one has to perform a FS extrapolation of the self-energy.

For a careful analysis of FS effects, we simulated systems from 36 up to 256 sites. The extrapolation of the self-energy to the thermodynamic limit is performed by fitting $\Sigma(i\omega_n; L)$ for every Matsubara frequency ω_n as a function of the linear system size L.

This procedure is demonstrated in Fig. 4.6 for the self-energy of the half-filled Hubbard model on $L \times L$ square lattices at the momentum point $\mathbf{k} = (\pi, 0)$. The two panels on the left hand side show results at low temperatures $T = 0.04$, the panels on the right at the elevated temperature $T = 0.10$. Fig. 4.6 (a) and Fig. 4.6 (c) show FS biased self-energies for the different lattice sizes (colored symbols and broken lines). The BSS-QMC data show large finite-size effects: the smallest systems (8×8, triangles) show insulating behavior at both temperatures, indicated by a strong enhancement of the self-energy at small ω_n. Towards larger system sizes, the insulating tendency is reduced at $T = 0.04$ and vanishes completely at $T = 0.10$. The functional dependence of the magnitude of the self-energy on the system size is shown in Fig. 4.6 (b) and Fig. 4.6 (d) for the first three Matsubara frequencies, where the strongest FS effects appear. The FS extrapolation is performed by fitting polynomials in L^{-2}: the final value is determined by the mean of a quadratic fit (thick colored lines) and a linear fit (thin colored lines) and the error is given by their difference. Only for the two smallest Matsubara frequencies a significant deviation from a linear dependence on the inverse system size is found.

The final extrapolated self-energies are free from significant Trotter bias and valid in the thermodynamic limit. They are shown as black lines and circles in

Fig. 4.6 (a) and Fig. 4.6 (c), respectively. To validate the consistency of the method, self-energies, obtained from single-site DMFT (thin black solid line) and $D\Gamma A$ (gray dashed line) are also shown. Due to the neglect of short-range interactions, the paramagnetic single-site DMFT results are expected to have a tendency towards metallic solutions, and serve here as lower boundary for the self-energy. The reasonable agreement with $D\Gamma A$ shows the high quality of the error elimination schemes. Remarkably, even the results for the 16×16 lattice deviate strongly from the correct solution. Valid results can only be obtained by careful finite-size analysis. The full picture of the comparison of the different methods, in the context of the two-dimensional Hubbard model, is discussed in Chap. 5.

5. Mott Transition in the 2d Hubbard Model

In this chapter, the methods described in Chap. 4 are used for studying the Mott metal-insulator transition of the two dimensional Hubbard model at half-filling. The study was performed within a joint project with the Graz University of Technology, where variational cluster approximation (VCA) [PAD03] calculations were performed and Vienna University of Technology, where dynamical vertex approximation (DΓA) data were produced. The full study is published in [SGR+15]. The final results are summarized in Fig. 5.1. Colored lines in the phase diagram mark phase transitions in the temperature-interaction plane, investigated in different studies using alternative numerical methods. For guidance, the mean-field

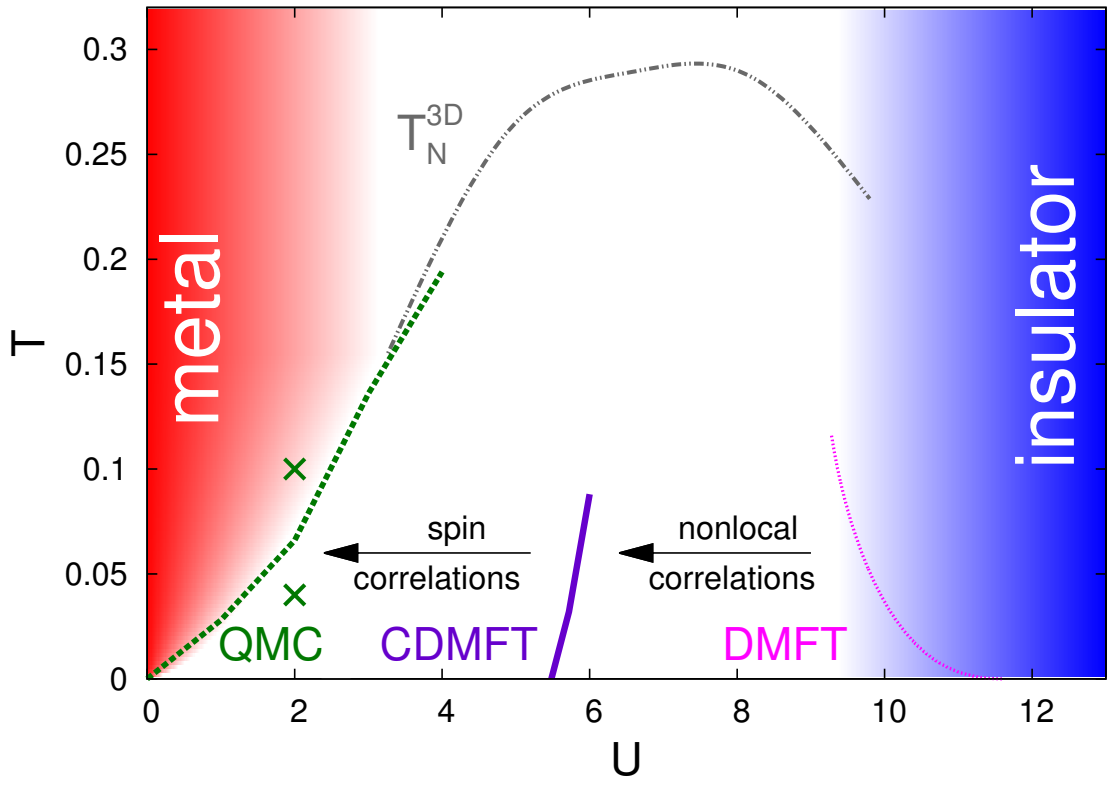

Figure 5.1. – Phase diagram of the the Hubbard model on a square lattice, obtained with complementary techniques. DMFT [Blü02,KJMP05], CDMFT [PHK08], VCA and DΓA [SGR+15] data. Unbiased BSS-QMC results for $U = 2$, $T = 0.10$ and $T = 0.04$ (green crosses).

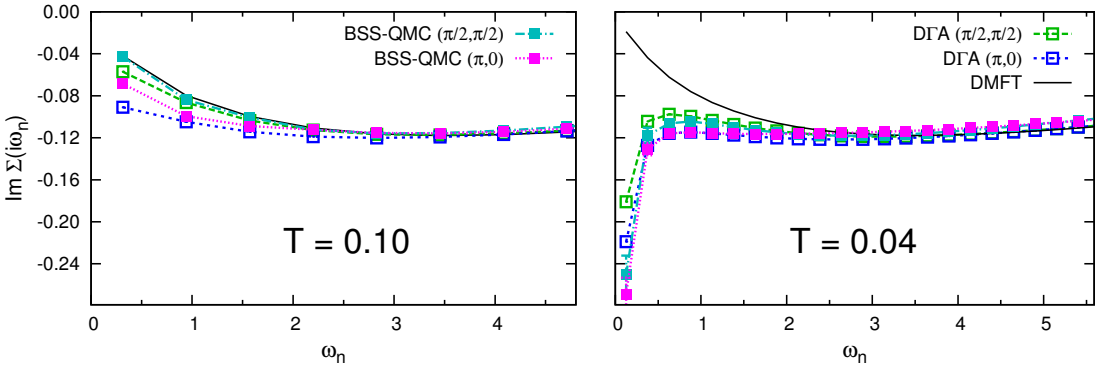

Figure 5.2. – Imaginary parts of the self-energies for $U = 2$, $T = 0.10$ (left panel) and $T = 0.04$ (right panel), corresponding to green crosses in the phase diagram Fig. 5.1. Even for this weak interaction an insulating gap opens at both showed momenta on the nodal $[\mathbf{k} = (\pi/2, \pi/2)]$ and antinodal $[\mathbf{k} = (\pi, 0)]$ points on the (non-interacting) Fermi surface. Both complementary methods, DΓA and unbiased BSS, supported the theory of the absence of the MIT at finite temperatures and interaction strengths. Not shown: vanishing real parts, due to particle hole symmetry.

Néel temperature $T_{\mathrm{N}}^{\mathrm{3D}}$ for three dimensions is shown[1](gray dashed double-dotted line). The key message of our study is that, in contrast to former studies, no Mott-Hubbard transition is found at finite temperature T and any interaction strength U. Instead, the model describes a paramagnetic insulator at low enough temperatures for any $U > 0$.

With respect to DMFT (pink dotted line), which neglects short-range correlation completely, the introduction of nonlocal correlations, e.g., by cluster extensions to DMFT (CDMFT, violet line), shifts the MIT towards lower interaction strengths. Using finite-size extrapolated unbiased BSS-QMC and DΓA, longer-range correlations are included. The green dashed line marks the transition temperature and interaction, at which a spectral gap is opened with increasing U, due to a strong enhancement of the electronic scattering rate for low frequencies [cf. Fig. 5.2]. The crossover from metallic to insulating behavior (identified by a strong enhancement of the imaginary part of the self-energy at low frequencies) at low enough temperatures is shown in Fig. 5.2 for the weak coupling $U = 2$. While at the high temperature $T = 0.10$ (left panel) both, DΓA (open squares) and unbiased BSS-QMC (filled squares) show metallic behavior, an insulating gap opens at the two most relevant points on the (non-interacting) Fermi surface, namely at the nodal $[\mathbf{k} = (\pi/2, \pi/2)]$ and at the antinodal $[\mathbf{k} = (\pi, 0)]$ point, at the lower temperature $T = 0.04$ (right panel) and corrects the metallic DMFT result (black solid line). The true solution, using BSS-QMC at these two temperatures, could only be determined by careful finite-size analysis (cf. Fig. 4.6).

[1]The shown line for $T_{\mathrm{N}}^{\mathrm{3D}}$ is rescaled to match the energy scale of the two-dimensional model ($U/\sqrt{Z} = \text{const.}$) [GRP+12].

The shift of the MIT towards $U = 0$, with the systematic inclusion of spatial correlations, shows the physical origin of the observed crossover: due to the proximity to the AF long-range ordered phase at $T = 0$, spatial AF spin correlation are enhanced. This can be shown by consideration of the static real-space spin correlation function

$$\chi_s(\mathbf{x}) = \int_0^\beta d\tau \ \langle S(\mathbf{x}, \tau) S(0, 0) \rangle \ , \tag{5.1}$$

which can be related to the correlation length ξ, using the expression for the long-distance limit [AS06]:

$$|\chi_s(x \to \infty)| \propto \sqrt{\frac{\xi}{x}} \, e^{-x/\xi}. \tag{5.2}$$

In Fig. 5.3, spin correlation functions are shown. The functions are normalized on their on-site value $\chi_s(r = 0)$ and plotted along the x direction. By fitting the functional form in Eq. (5.2) to the data, the correlation length can be estimated. Fig. 5.3 (a) shows results for BSS-QMC simulation for 16×16 lattice. While the correlation lengths at $T = 0.10$ is smaller than the cluster size and can be estimated to $\xi \approx 3.7$, the correlations decay much more slowly at the lower temperature $T = 0.04$. For the latter, one can conclude, based on the BSS-QMC results only, that the correlation length is larger than the size of the cluster. These results are confirmed by the more reliable estimation by DΓA . The estimation of $\xi \approx 4$ at $T = 0.10$ is in excellent agreement with the BSS-QMC results [Fig. 5.3 (b)]. At $T = 0.04$ [Fig. 5.3 (c)] the correlation length is in order of 10^3 and clearly exceeds the reachable cluster sizes in lattice BSS-QMC. The alternating sign reflects the short- to middle-range AF ordering. This shows unambiguously that the the extending AF fluctuations drive the 2d Hubbard model into a phase where it is a paramagnetic insulator for all interactions and low enough (but still finite) temperatures. This picture is different from a MIT at finite T, i.e., a nonzero $U_c > 0$ at $T > 0$, predicted in former (C)DMFT studies.

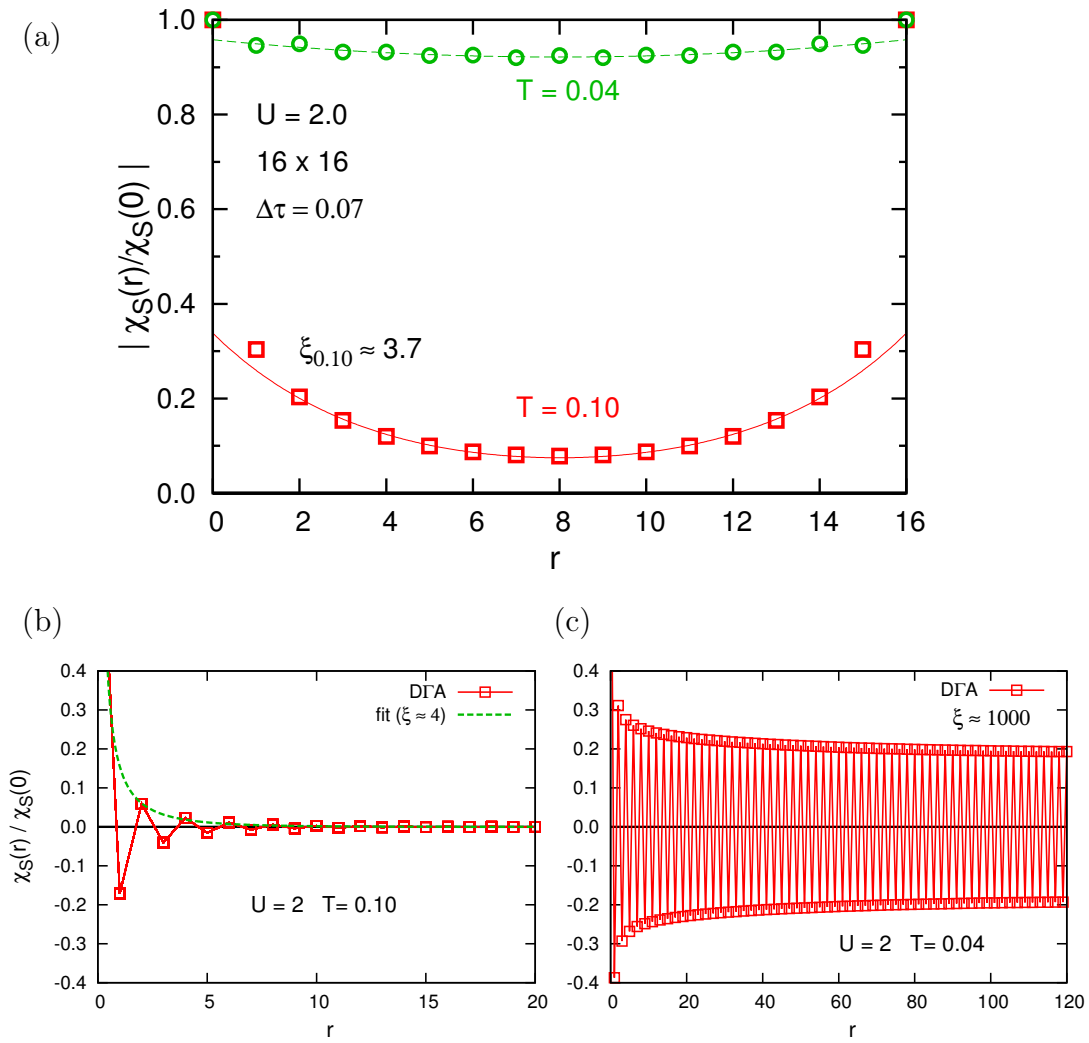

Figure 5.3. – Real-space spin correlation function. (a) The correlation length for $T = 0.10$ (red squares) from BSS-QMC calculations for a 16×16 lattice is estimated by an exponential fit (red solid line). For $T = 0.04$ (green circles) ξ is much larger than the extend of the lattice. *Lower panel:* The corresponding estimations from DΓA data [SGR+15] for $T = 0.04$ (b) and $T = 0.10$ (c) confirm the BSS-QMC results. [RB15]

6. Numerical Developments II: Unbiased BSS-QMC as Impurity Solver

In Chap. 4, a multigrid BSS-QMC scheme was discussed that yields Green functions without significant systematic errors. This multigrid BSS-QMC procedure is not only very useful for direct lattice calculations, as applied in the study of the two-dimensional Hubbard model presented in Chap. 5, but could also be useful as impurity solver for DMFT and its cluster extensions. As already highlighted in Sec. 3.2.4, combining BSS-QMC and DMFT has great potential in leading to new insights in ultra-low-temperature physics, by its superior linear scaling in the inverse temperature. In this chapter, we will discuss how the unbiased multigrid BSS-QMC is integrated in the DMFT framework in detail (Sec. 6.2) and which modifications were necessary for applications to cluster extensions of DMFT (Sec. 6.3). We will also cover algorithmic developments (Sec. 6.1), regarding the discretization of the bath, which are also important for other Hamiltonian based solvers, such as exact diagonalization (ED).

6.1. Determination of Bath Parameters

Within the DMFT framework, in every iteration step the new quantum impurity problem is defined by a bath Green function $\mathcal{G}$

$$\mathcal{G}(i\omega_n) = \left[i\omega_n + \mu - \mathbf{t} - \mathbf{\Gamma}\right]^{-1} \ , \tag{6.1}$$

which describes a continuous bath. Here μ denotes the chemical potential and $\mathbf{t}$ the Hopping matrix on the cluster. For application of Hamiltonian based solvers, one has to find a discrete representation of the bath. Starting from a given DMFT Green function, one can calculate the Hybridization function $\mathbf{\Gamma}$ via the inversion of Eq. (6.1). For the impurity Hamiltonian Eq. (3.61), the hybridization function can be written as function of the hybridization parameters $\{V_\alpha\}$ and bath dispersion $\{\epsilon_\alpha^{\text{bath}}\}$, which are undetermined at this stage

$$\mathbf{\Gamma}(i\omega_n) = \sum_{\alpha}^{N_b} \frac{V_\alpha^* V_\alpha}{i\omega_n - \epsilon_\alpha^{\text{bath}}} \ . \tag{6.2}$$

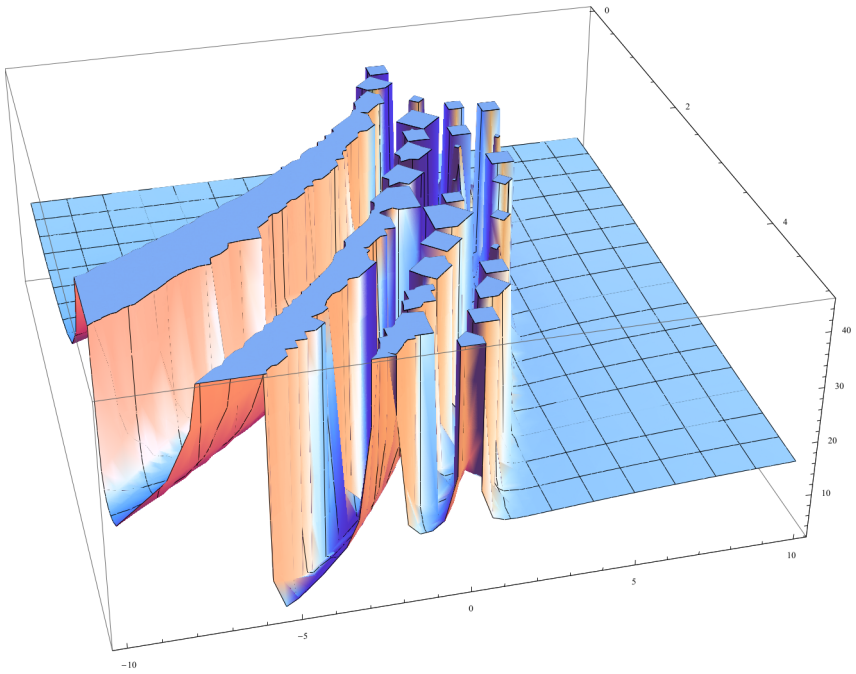

Figure 6.1. – Illustration of the complexity of the minimization procedure for the bath representation: Here for the simple case $N_b = 1$, $N_c = 2$. Scaled squared deviation χ^2 (z-axis) Eq. (6.3) as function of the bath parameters V, ϵ (x-y-plane).

The parameters are determined by a χ^2 fit, i.e., by minimizing

$$\chi^2\left[\{V_{\alpha k}\},\{\epsilon_\alpha\}\right] = \begin{cases} \sum_{ij}\sum_{n=0}^{\text{cutoff}}\left[\mathcal{G}_{ij}^{\text{DMFT}}(i\omega_n) - \mathcal{G}_{ij}^{\text{fit}}(i\omega_n;\{V_{\alpha k}\},\{\epsilon_\alpha\})\right]^2 & \begin{pmatrix}\text{cellular}\\ \text{DMFT}\end{pmatrix} \\ \sum_{\mathbf{K}}\sum_{n=0}^{\text{cutoff}}\left[\mathcal{G}_{\mathbf{K}}^{\text{DMFT}}(i\omega_n) - \mathcal{G}_{\mathbf{K}}^{\text{fit}}(i\omega_n;\{V_{\alpha k}\},\{\epsilon_\alpha\})\right]^2 & \begin{pmatrix}\text{DCA}\end{pmatrix} \end{cases} . \tag{6.3}$$

The number of chosen bath sites N_b has to be large enough to ensure that the fit fulfills the required precision. For a given number of bath sites, finding a satisfying bath representation is a crucial step for the efficiency of the solver. Goal is to gain a representation with as few sites as possible. If we recall the scaling with the number of bath orbitals of available Hamiltonian based solvers (Table 3.2.4), i.e., exponentially for ED and cubically for BSS-QMC, this will have a significant influence on the amount of computational time needed for a calculation. The fit

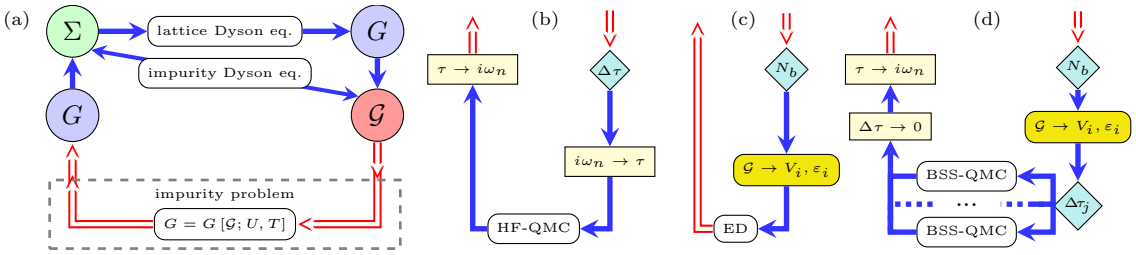

Figure 6.2. – (a) Scheme of the general DMFT self-consistency cycle, including the "impurity problem" (dashed box). Established impurity solvers include (b) the Hirsch-Fye (HF-QMC) algorithm and (c) exact diagonalization (ED). (d) The proposed algorithm approximates the bath Green function $\mathcal{G}$ in terms of the parameters V_i, ϵ_i of an auxiliary Hamiltonian Eq. (3.37) with N_b "bath" sites [like ED (c)]. Corresponding Green functions are computed using BSS-QMC for a grid $\Delta\tau_{\min} \leq \Delta\tau_j \leq \Delta\tau_{\max}$ of Trotter discretizations. The subsequent extrapolation of $\Delta\tau \to 0$ yields the Green function, free of significant Trotter errors and continuous in τ, which is easily Fourier transformed and fed back into the self-consistency cycle [RAB13].

problem in the framework of single-site DMFT is easily treatable with standard downhill methods, because only one function $\Gamma(i\omega_n)$ has to be fitted. However, the minimization problem is highly non-trivial in the case of cluster methods. For a cluster with N_c sites, N_c^2 complex functions have to be fitted simultaneously using $(N_c + 1)\, N_b$ parameters. The complexity of the problem is demonstrated in Fig. 6.1; here the functional form of $\chi^2(V_1\,, \epsilon_1^{\text{bath}})$ for the simple case of two cluster sites and one bath site is shown.

Already in the easy two dimensional case, it is clear that simple downhill methods will fail, due to the divergences in χ^2. Therefore, a multi-step minimization algorithm for the cluster problem was developed. To avoid trapping in local minima of the minimization function, a sophisticated stochastic hybrid algorithm, based on simulated annealing and parallel tempering (SA&PT minimization), is used [LPA+09]. The details of the implementation are described in Appendix A. After identifying the approximate minimum region via SA&PT minimization, the final parameters are determined by a semi-analytic local post-convergence, using standard downhill methods, e.g., simplex minimization [PTVF07]. The quality of the final fit depends on the number of used bath sites. A more detailed study on the impact of the bath discretization will be presented in Chap. 7.

6.2. Single-Site DMFT

In this section, the details of the integration of the multigrid BSS-QMC approach into the DMFT self-consistency cycle are explained. Another focal point will be the benefit of the unbiased solver compared to a finite-$\Delta\tau$ solver, originally proposed in [KLB+10]. In Fig. 6.2, the integration of different types of impurity solvers is sketched. The DMFT self-consistency cycle [upper part of Fig. 6.2 (a)] is identical

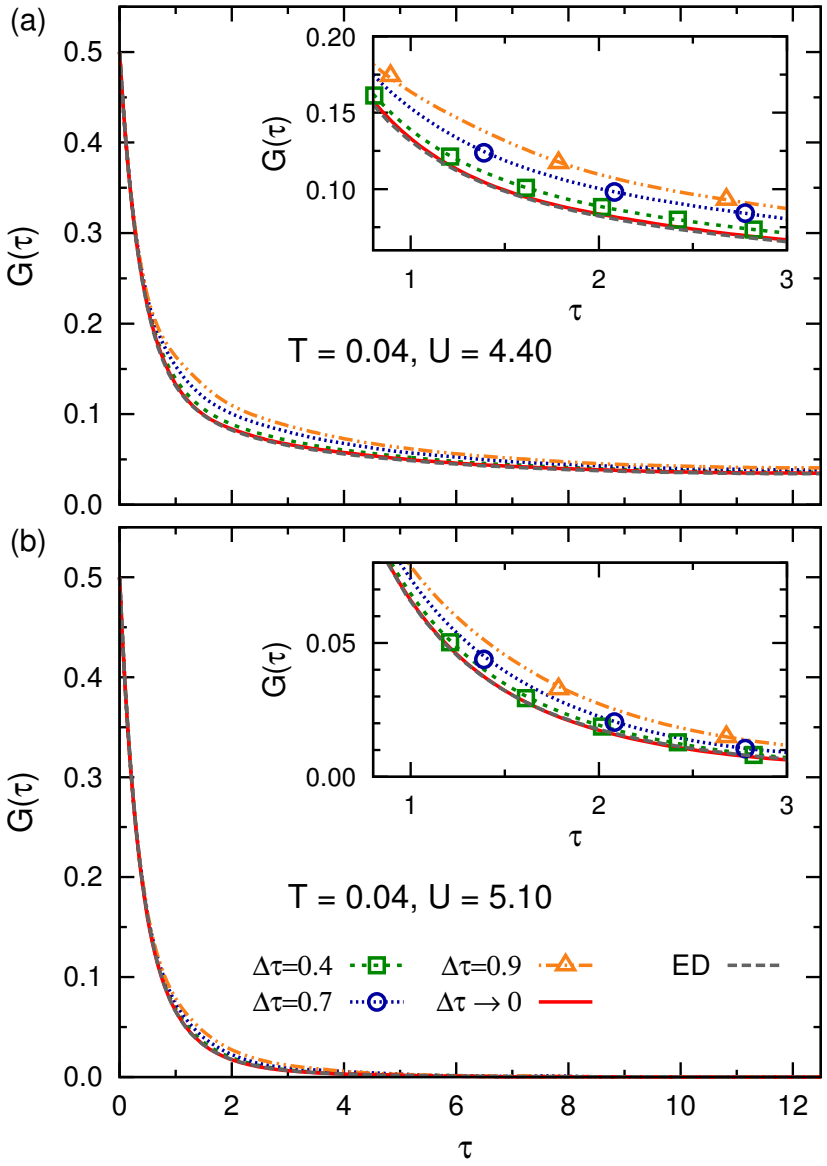

Figure 6.3. – BSS-QMC impurity Green functions at $T = 0.04$ (symbols) using a bath representation with $N_b = 4$ sites (with parameters of converged DMFT-ED solution, long-dashed lines) and results of multigrid extrapolation to $\Delta\tau = 0$ (solid lines). (a) metallic phase ($U = 4.4$) and (b) insulating phase ($U = 5.1$) [RAB13].

for all approaches, while the impurity problem (dashed box) is replaced by a specific solver. Direct solvers, like Hirsch-Fye QMC Fig. 6.2 (b), can work directly with the action representation of the problem. For Hamiltonian based approaches, like ED [Fig. 6.2 (c)] and BSS-QMC [Fig. 6.2 (d)], the bath has to be discretized (denoted by yellow boxes).

The multigrid BSS-QMC solver is implemented as follows: for a given hybridization within one DMFT iteration, the Hamiltonian Eq. (3.37) is solved for different values of $\Delta\tau$, resulting in Trotter biased Green functions. These Green functions are extrapolated to $\Delta\tau \to 0$, resulting in one unbiased, quasi continuous-time Green function, as described in Sec. 4.1. This Green function can easily be Fourier transformed to the Matsubara axis and fed back into the DMFT self-consistency cycle. To check the validity of the extrapolation, we solve the impurity problem with exact diagonalization, for a small number of bath sites and fixed bath parameters, and compare these results with Green functions from the unbiased BSS-QMC. This comparison is shown in Fig. 6.3. Here single-site DMFT results for the Bethe lattice are shown. Fig. 6.3 (a) shows Green functions for an interaction strength in the metallic phase and Fig. 6.3 (b) in the insulating phase. Broken lines show Trotter biased solutions. Only the extrapolated Green function (red solid line) can reproduce the correct results obtained with ED (gray dashed line) within the error of the method. This comparison shows that the unbiased BSS-QMC can be used in the same manner as ED, but with the possibility to simulate more sites, due to the superior scaling [N^3 vs. $\exp(N)$]. The scaling issue will become particularly important in the context of cluster extensions, where additionally more interacting cluster sites can be simulated. We investigate the impact of the bath discretization on final results by the application of the solver to the Mott transition in single-site DMFT. This study will be presented in Chap. 7.

6.3. Cluster Extensions

The algorithmic structure of the cluster solver is very similar to the case of single-site DMFT. However, new challenges arise, due to the treatment of an interacting cluster instead of a single site. Consequently, not only a single Green function, but a full $N_c \times N_c$ Green function matrix has to be extrapolated to the limit $\Delta\tau \to 0$. This is performed with the methods, presented in section Sec. 4.1, in a stable manner.

In Sec. 3.2.2 the two versions of cluster extensions were contrasted. Both, the cellular DMFT and the DCA were implemented and used in this thesis. In the case of cellular DMFT, the problem is formulated in real space and can be directly solved with BSS-QMC. Details are provided in Sec. 6.3.1. For the implementation of the DCA scheme, a representation of the (momentum space) DCA problem in real space had to be found. This representation has to fulfill the assumptions of DCA, namely periodic boundary conditions and translationally invariant bath parameters. Then, the resulting real-space problem is solved by BSS-QMC. The full DCA scheme is discussed in Sec. 6.3.2.

6.3.1. Cellular DMFT

In the case of cellular DMFT, the representation of the cluster and the discrete bath is straightforward. The truncation to the cluster in Eq. (3.48) leaves the intra cluster hopping untouched, so the cluster hopping matrix is the same as in the original lattice. The bath represents the interaction with the surrounding of the cluster and is, thus, coupled to the cluster surface only, sketched in Fig. 6.4 (a) for a one dimensional example. At this point, the translation symmetry of the original lattice is broken, i.e., the cluster sites become, in general, non-equivalent. For the final evaluation of physical quantities, one can average the core region of the cluster, where the weakest surface effects are expected. In order to benchmark the implementation, the method is applied to the one-dimensional Hubbard model, for which bare dynamical mean-field calculations are least reliable. The results are summarized in Fig. 6.4 (b); here results for the double occupancy Eq. (4.1) as function of the temperature are compared for different methods. For one spatial dimension, the Hubbard model is exactly solvable by Bethe ansatz in the thermodynamic limit, which serves as reference solution (black solid line). The result can be recaptured by direct lattice BSS-QMC for the relatively large chain length $N_c = 16$ (blue triangles). In contrast, paramagnetic single-site DMFT deviates strongly at low temperatures (red diamonds). Remarkably, antiferromagnetic (AF) DMFT (green circles) is closer to the correct results, even if it assumes AF long-range order, which is physically incorrect[1]. The better agreement can be explained with the fact that at low temperatures, short-range AF fluctuations become relevant, not captured by paramagnetic DMFT. The cellular DMFT includes AF fluctuations on the cluster and converges very fast with the cluster size. While for two interacting sites (violet open squares) a slight deviation for the intermediate temperature regimes is found, the solution obtained with three-site cluster DMFT (blue filled squares) reproduces the reference result within the error bars of the method.

6.3.2. DCA

In contrast to cellular DMFT, the DCA is formulated in momentum space and restores the translation symmetry. This symmetry has to be respected by the real-space formulation needed for BSS-QMC. The DCA self-consistency equations yield the coarse-grained hybridization function $\mathbf{\Gamma}(\mathbf{K}, i\omega_n)$, which has to be fitted with the finite-bath representation Eq. (3.60) to determine the bath parameters. One can either fit the bath parameters in momentum space and perform the Fourier transformation Eq. (3.42) for the hybridization matrix to define the real-space problem, or, as realized in the final version of the developed DCA code, first Fourier transform $\mathbf{\Gamma}(\mathbf{K}, i\omega_n)$ to $\mathbf{\Gamma}_{ij}(i\omega_n)$ and perform the fit in real-space. Both procedures were tested during the project. The quality of the results turned out to be independent of the sequence of Fourier transformation and fitting procedure.

A further difference to the cellular DMFT is the restriction of the parameter space for the fit parameter, due to required translation invariance. In practice, the

[1] No magnetic long-range order appears in the one-dimensional system and for two-dimensional systems at $T = 0$ only, as predicted by the Mermin Wagner theorem [Geb00].

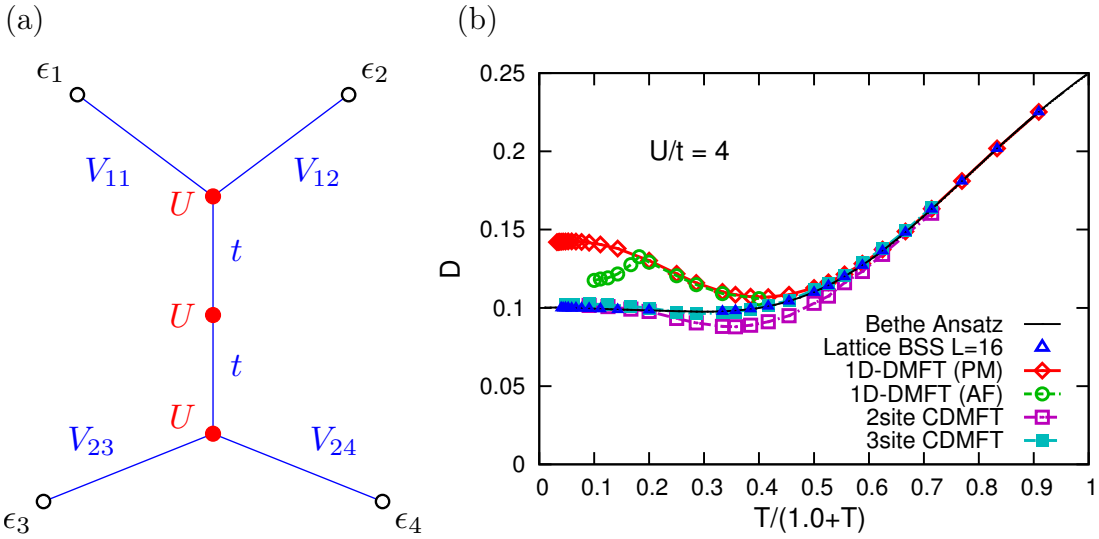

Figure 6.4. – (a) Illustration of the coupling to a discrete mean-field bath in cellular DMFT. (b) Benchmark of cellular DMFT implementation, for the one-dimensional Hubbard model at half-filling. Exact results from BSS-QMC for a 16-site cluster (blue triangles) and Bethe ansatz in the thermodynamic limit shown as reference.

fitting procedure becomes more stable, due to the smaller number of degrees of freedom. To fulfill the symmetry, the interacting real-space cluster is implemented with periodic boundary conditions and the bath sites have the same geometry as the interacting cluster. The bath sites are realized as an extra *layer* (second orbital) on top of the interacting cluster. More bath sites are added by stacking several layers on top of each other, i.e., the number of bath sites has to be a multiple of the number of cluster sites ($N_b = N \cdot N_c, N \in \mathbb{N}^+$). Further, for the bath sites within one layer ν the symmetry condition

$$\epsilon_\alpha^\nu \equiv \epsilon^\nu \quad , \qquad V_{\alpha j}^\nu \equiv V_{\|\alpha - j\|}^\nu \tag{6.4}$$

is forced. Here, α denotes bath sites and j denotes cluster sites. Similar to single-site DMFT the fit quality is better with a larger number of bath layers. This is illustrated in Fig. 6.5 for the example of a 2×2 cluster. Here the target bath Green function from DCA (red solid lines), obtained with the BSS-QMC solver, is compared to a discrete representation with one bath layer (blue short-dashed lines) and two bath layers (green dashed lines). We show the three irreducible cluster momenta $\mathbf{K} = (0, 0)$ (top row), $\mathbf{K} = (0, \pi)$ (middle row) and $\mathbf{K} = (\pi, \pi)$ (bottom row). Plots in the left column show the imaginary part of the Green function, plots in the right column the real part. By adding a second layer of bath sites, more precision is gained, in particular for the real part of the Green function. The real part is mainly determined by the dispersion of the bath sites, which is only one degree of freedom for a single layer, as directly seen from Eq. (6.4).

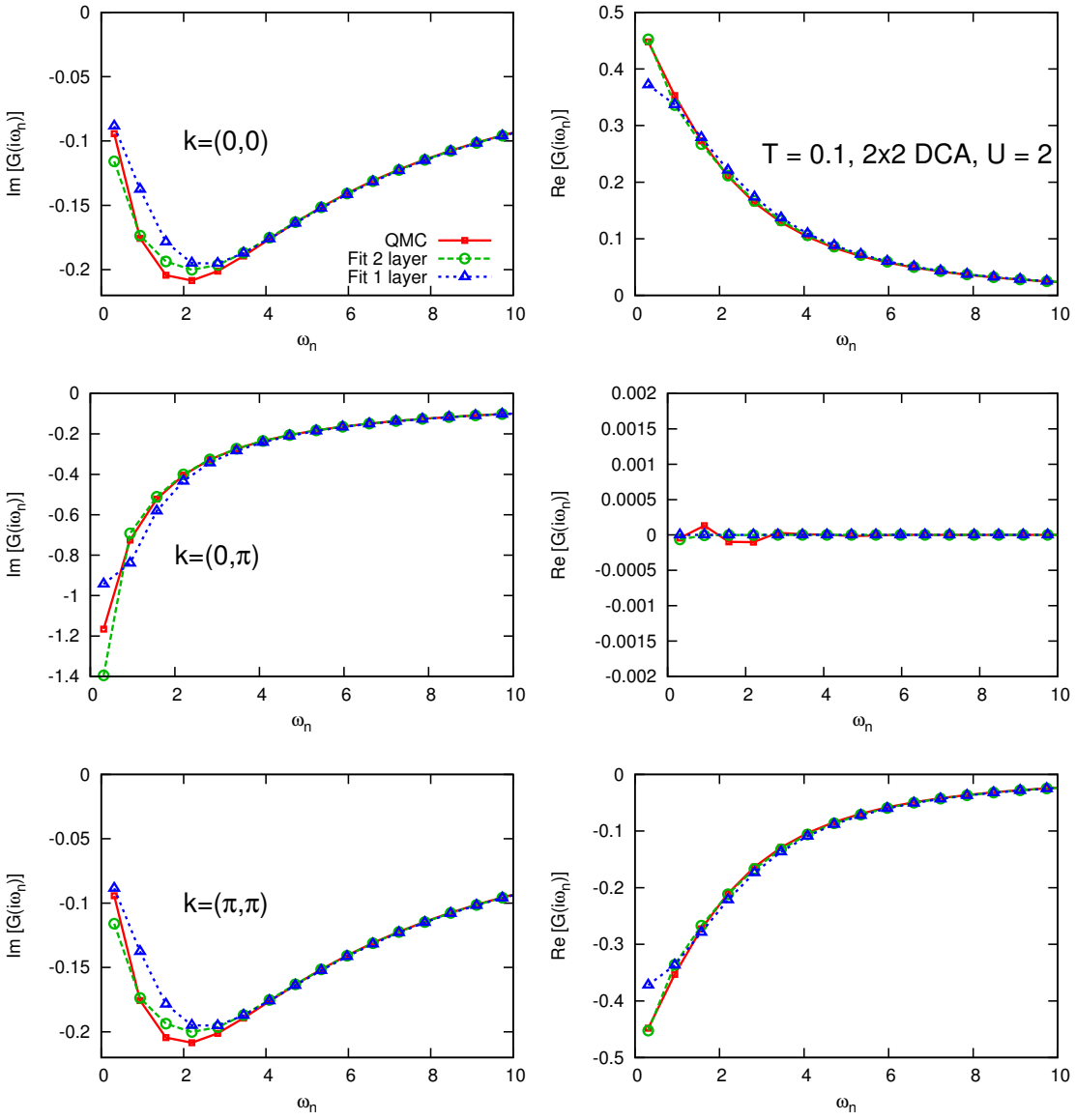

Figure 6.5. – Momentum-dependent imaginary part (left column) and real part (right column) of DCA bath Green functions on a 2×2 cluster. Not shown: $G_{(\pi,0)} = G_{(0,\pi)}$. Agreement of the bath Green function obtained via QMC solution and DCA self-consistency (red solid line) and their representation fitted with a discrete bath for one bath layer (circles, green dashed line) and two bath layers (triangles, blue dashed line).

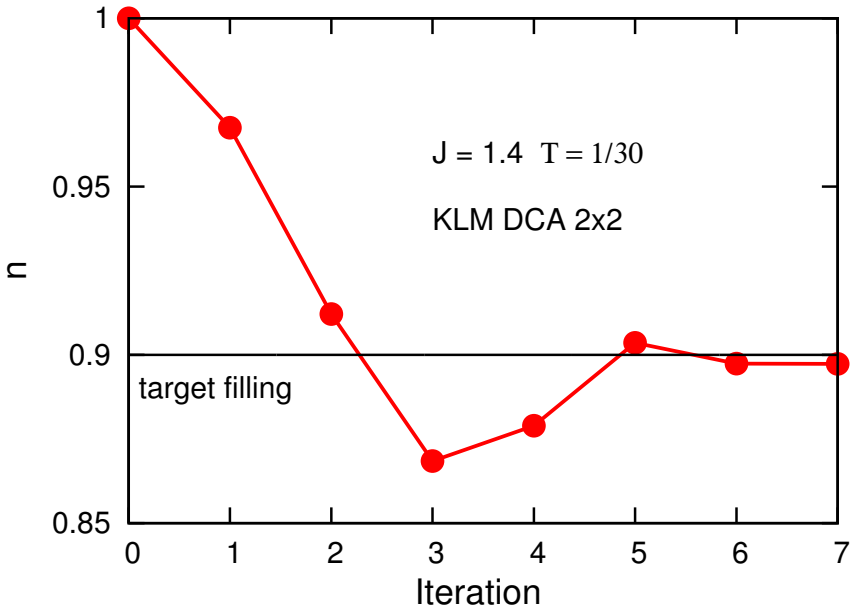

Figure 6.6. – The filling within the DCA convergence process approaches its target value, realized with controlled adjustment of the chemical potential μ and the bath dispersion ϵ_α. Here for a 2×2 DCA calculation of the Kondo lattice model.

A further difference between DCA and cellular DMFT is that the hopping matrix elements on the real-space cluster are not the same as for the original lattice. The substitution of the original dispersion $\epsilon_{\mathbf{k}}$ with the coarse grained $\bar{\epsilon}_{\mathbf{K}}$, which depends on the chosen pattern for the patching of the Brillouin zone, introduces additional phase factors. The coarse graining leads to a renormalized hopping, which is determined by the cluster Fourier transform Eq. (3.42) of $\bar{\epsilon}_{\mathbf{K}}$. Finally the determined real-space problem is solved using BSS-QMC, which gives the impurity cluster Green function matrix $\mathbf{G}$ in real space. This Green function matrix has to be Fourier transformed to cluster momenta using the cluster Fourier transformation Eq. (3.43) and the DCA self-consistency cycle can be closed.

Filling

The BSS-QMC algorithm is formulated in the grand canonical ensemble. I.e., the filling of the system is determined by the chemical potential μ on the cluster sites and the dispersion ϵ of the bath sites. E.g., for half filling and one bath layer, one may restrict the parameter space to

$$\langle n \rangle = 1 \quad \rightarrow \quad \mu = 0, \quad \epsilon = 0 \; . \tag{6.5}$$

Half filling is guaranteed, but the opportunity to use ϵ as degree of freedom for

the fit of the bath Green function is lost. Instead, for two bath layers one can set

$$\langle n \rangle = 1 \quad \rightarrow \quad \mu = 0 \quad \epsilon_1 = \epsilon, \quad \epsilon_2 = -\epsilon \; . \tag{6.6}$$

For an arbitrary target filling $\langle n \rangle$, the DCA is initialized with a guess for the chemical potential $\mu = \mu_{\text{start}}$ and μ is adjusted in every iteration step until the target filling is reached. In the DCA implementation developed in this thesis, the value of μ for the next iteration step is estimated by a linear fit of the dependence of the filling on the chemical potential and bath parameters $\langle n(\mu, \epsilon_\alpha) \rangle$, observed in previous iterations. The convergence of this procedure is demonstrated in Fig. 6.6. As example we picked a DCA calculation with a 2×2 cluster of the KLM at $T = 0.033$ and target filling $\langle n \rangle = 0.90$. The filling converges quickly to the target value.

Benchmark: Half-Filled Hubbard Model on a Square Lattice

A generic test case for the DCA implementation is the half-filled Hubbard model on a square lattice. In this case, we can compare to the unbiased numerical results that were presented in Chap. 5. The bias in the DCA results can be quantified by comparison to the impact of finite-size effects in BSS-QMC and the approximations of DΓA . Results are shown for the low temperature $T = 0.04$ [lower green cross in Fig. 5.1] at weak coupling $U = 2$. DCA calculations were performed for 2×2 and 4×4 clusters. We focus on the self-energy at $\mathbf{k} = (\pi, 0)$, since $\mathbf{k} = (\pi/2, \pi/2)$ is not available in 2×2 DCA. In Fig. 6.7 the imaginary part of the self-energy is shown, similar to Fig. 5.2. Due to particle-hole symmetry, real parts vanish on the Fermi edge. Unbiased BSS-QMC (black circles) and DΓA (orange triangles) represent the reference results. Since the DCA adds nonlocal corrections to DMFT, single-site DMFT results (gray dots) define a lower boundary for the range of consistent DCA results in the insulating phase. The DCA results lie in the expected area between the unbiased results and DMFT data. At low frequencies the results for the small 2×2 cluster show finite-size effects, which are reduced for the larger 4×4 cluster. In the frequency range of $0.63 < i\omega_n < 2.93$ the 4×4 results deviate even more from the reference than the 2×2 results[2]. For a proper judgment of the deviation of the DCA results from the reference, we compare to bare finite-size lattice BSS-QMC calculations. These data are presented as open circles in Fig. 6.8. The 4×4 lattice calculation (green circles) deviate about a factor ten more from the reference results (black filled circles) than the 4×4 DCA calculation. Even the 16×16 results (pink circles), which need a factor of ~ 150 more computer time than the 4×4 DCA for

[2]The assigned error bars may underestimate the real bias. For the BSS-QMC results, error bars are estimated by the difference between quadratic and linear FS extrapolation, as discussed in Sec. 4.2. For DCA the difference between the last self-consistency iterations are used as measure for the inaccuracy. Influence of the finite bath, biases introduced by the $\Delta\tau \rightarrow 0$ extrapolation, smoothing procedures, and subsequent Fourier transformation are not taken into account.

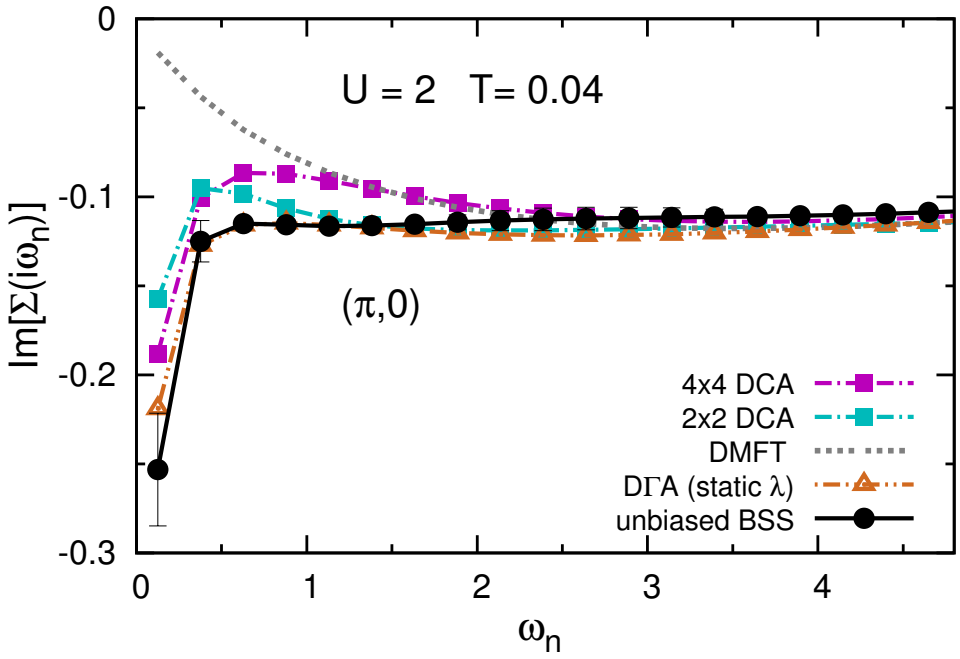

Figure 6.7. – Imaginary part of the self-energy: unbiased BSS-QMC and $D\Gamma A$, already shown in Fig. 5.2, compared to DCA data for 2×2 and 4×4 clusters.

one iteration[3], are further away than the DCA results. The deviations shown in Fig. 6.7 are much smaller than the influence of systematic bias in the direct lattice calculations. Thus, we conclude that the great agreement of DCA calculations with the unbiased results, even for small numbers of cluster sites, proves the stability and quality of the developed numerical schemes.

[3]For the estimation of the computational time, consumed by the impurity solver, one has to take the scaling of cluster and bath sites, i.e., the total number of sites, into account. In the case presented here, two bath layers in real space were used. I.e., $N = N_c + N_b = 16 + 2 \cdot 16$ and cubic scaling with the total number of sites was assumed.

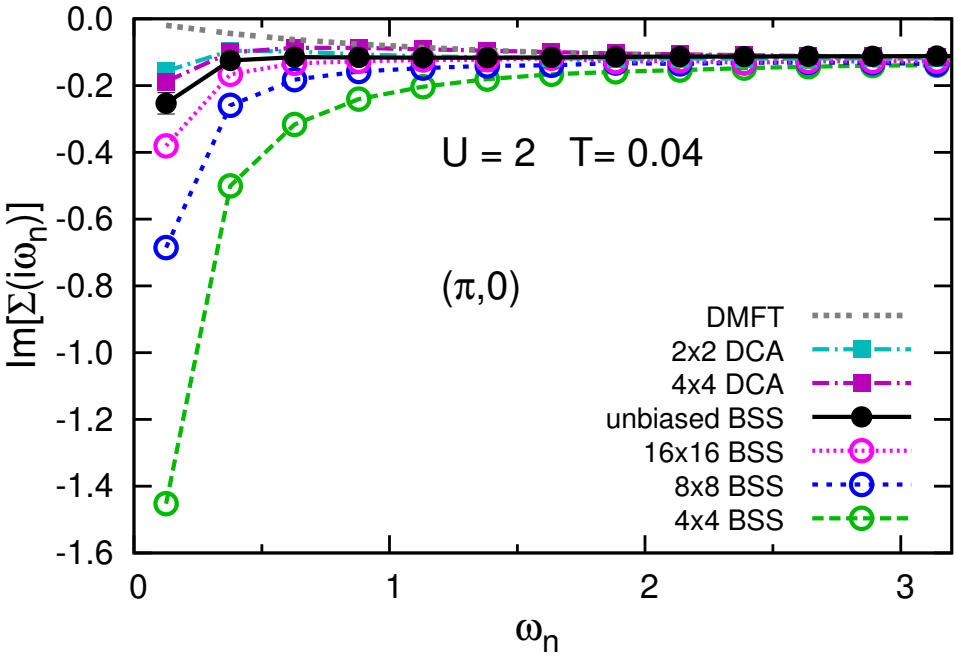

Figure 6.8. – Same unbiased QMC, DMFT and DCA data as in Fig. 6.7. Additional data for finite-size lattice BSS-QMC (open circles) underpin the good agreement of DCA with the reference data already for small cluster sizes.

7. Unbiased Study of the Mott Transition in Infinite Dimensions

In this chapter, a detailed study on the impact of systematic errors associated with the impurity solver on DMFT results is presented. We analyze the influence of the finite number of bath sites and the Trotter bias on physical quantities. As a classic example, we investigate the well known Mott metal-insulator transition (MIT) in DMFT, where reference results are available from established DMFT studies with Hirsch-Fye QMC as impurity solver [Blü02]. In Sec. 7.1, the impact of Trotter bias in the DMFT framework is studied, by comparing the developed unbiased multigrid DMFT impurity solver and a BSS-QMC solver with a fixed Trotter discretization error as well as results obtained via exact diagonalization (ED). In Sec. 7.2, the impact of the finite bath representation for the impurity problem is analyzed. The latter part of the study is not only relevant for the BSS-QMC solver, but also for all Hamiltonian based solvers, e.g., exact diagonalization. Large parts of this study were published in [RAB13].

7.1. Impact of the Trotter Bias

For investigating the impact of the Trotter error and its propagation through the DMFT self-consistency procedure, we observe the MIT in infinite dimensions for the half-filled Hubbard model on the Bethe lattice for temperatures below the critical temperature of the first order transition $T \leq T^* \approx 0.055$ [Blü02,BG13]. We observe the transition from the metallic to the insulating phase as a function of the Hubbard interaction U. The transition can be observed by investigating the interaction dependence of static observables such as the double occupancy D, related to the potential energy E_{pot}

$$D = \langle \hat{\mathbf{n}}_\downarrow \hat{\mathbf{n}}_\uparrow \rangle = \frac{E_{\text{pot}}}{U} \ , \tag{7.1}$$

and the quasiparticle weight

$$Z = \left[1 - \frac{\partial \operatorname{Re} \Sigma(\omega)}{\partial \omega} \Big|_{\omega=0} \right]^{-1} \approx \left[1 + \frac{\operatorname{Im} \Sigma(i\omega_0)}{\pi T} \right]^{-1} . \tag{7.2}$$

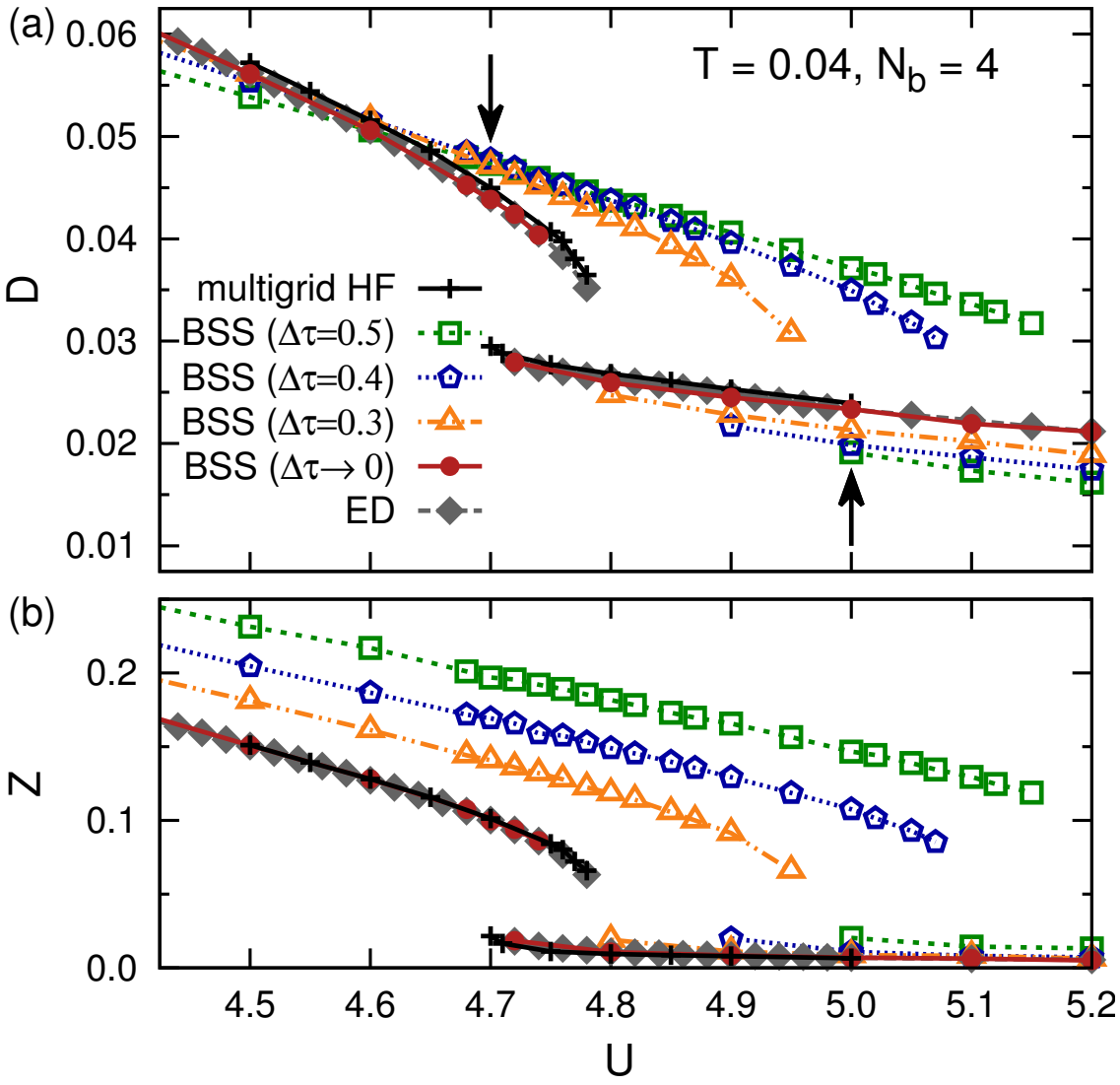

Figure 7.1. – Double occupancy and quasiparticle weight as functions of the Hubbard interaction U, obtained via self-consistent DMFT calculations using various impurity solvers: unbiased multigrid HF-QMC (crosses), BSS-QMC with fixed Trotter discretization (open symbols), unbiased multigrid BSS-QMC (circles), and ED (diamonds). Upper lines mark metallic, lower lines insulating solutions; their overlap in parameter space is the coexistence region. Due to the propagating Trotter bias, the coexistence region, in the results obtained with the finite-$\Delta\tau$ solver, is shifted with respect to the correct solution.

The latter one is proportional to the inverse of the effective mass m^*

$$Z^{-1} \propto m^* \tag{7.3}$$

and tracks the breakdown of the Fermi liquid behavior. Both quantities show a discontinuity in the interaction at the critical value $U = U^*$ when the insulating phase is entered.

The MIT is observed using DMFT with different types of solvers. We compare the Trotter biased BSS-QMC solver to ED and to the unbiased multigrid BSS-QMC solver. The results are shown in Fig. 7.1. Here the double occupancy Fig. 7.1 (a) [Eq. (7.1)] and quasiparticle weight Fig. 7.1 (b) [Eq. (7.2)] as function of the interaction U at fixed temperature $T = 0.04$ are shown. Upper curves belong to solutions in the metallic phase, lower curves to the insulating phase. In vicinity of the phase transition, a coexistence region can be identified. Within this coexistence region, the DMFT self-consistency has two meta-stable solutions, i.e., the DMFT converges to a metallic or an insulating solution, depending on the initial values. In order to determine the extend of the coexistence region, one starts with a small (large) U and initializes the next run for the larger (smaller) U with the converged metallic (insulating) solution. The interaction is increased (decreased) until the meta-stable solution is lost and the self-consistency converges to the insulating (metallic) solution, respectively.

Black lines denote reference results, obtained from an unbiased multigrid HF-QMC impurity solver. ED and BSS-QMC results are obtained using a fixed number of bath sites $N_b = 4$. Open symbols show the results from the Trotter biased BSS-QMC solver for different discretization values $\Delta\tau$. The final results are not only shifted quantitatively with respect to the reference results, but also qualitatively: a growing and a shift of the coexistence region towards larger values of U is observed. In contrast, the newly developed unbiased multigrid BSS-QMC solver (red circles) and exact diagonalization can reproduce the HF-QMC results. Remaining marginal deviations are related to the finite-bath discretization. This bias will be discussed in Sec. 7.2 in more detail.

For a more quantitative analysis of the impact of the Trotter discretization, we show the dependency of D on the squared imaginary-time discretization in Fig. 7.2. Filled symbols show values obtained via the extrapolation procedure within the multigrid solver, i.e., for a fixed Hamiltonian. Open symbols show results obtained after independent convergence of the DMFT self-consistency for different values of $\Delta\tau$. While the dependence within the multigrid procedure is regular, linear, and stable, results for the finite-$\Delta\tau$ solver show a non-monotonous dependence in the metallic regime at $U = 4.7$ (upper green curves) and even instabilities at $U = 5.0$ (lower blue curves). For the latter data set, results for larger values of the discretization ($\Delta\tau > 0.5$) are not shown, due to the fact that the Trotter biased results then converge to a metallic solution, instead to the correct insulating one.

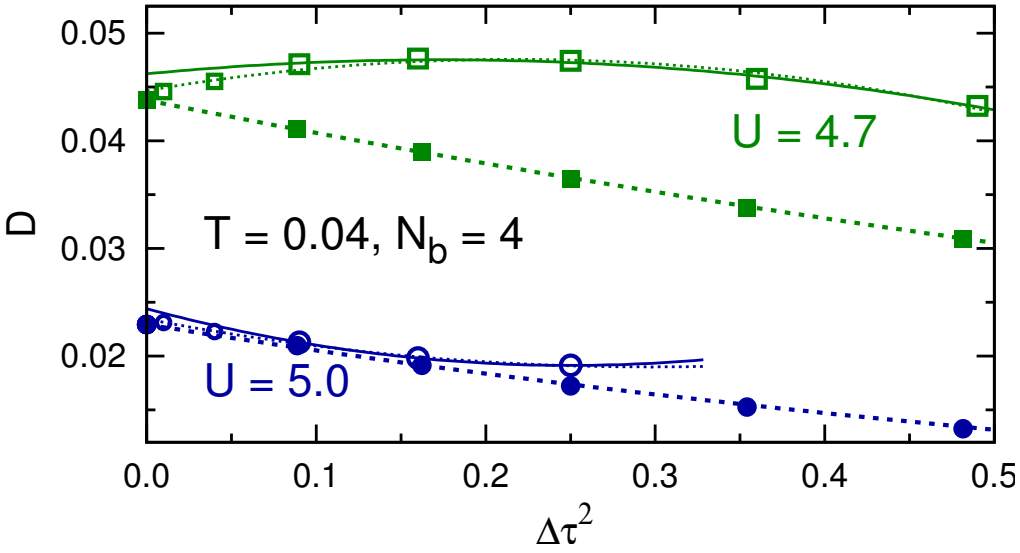

Figure 7.2. – Double occupancy as a function of the squared Trotter discretization $\Delta\tau^2$. Solid bold lines and open symbols denote results obtained via Trotter biased single-$\Delta\tau$ BSS-QMC. Filled symbols show the corresponding values within the unbiased multigrid BSS-QMC scheme. Examples for two interactions $U = 4.7$ (upper green curves) and $U = 5.0$ (lower blue curves). Curves are obtained via polynomial fits.

Small symbols and dots mark results for smaller values of $\Delta\tau = \{0.1, 0.2\}$, used for checking the validity of the $\Delta\tau \to 0$ extrapolation. Within the multigrid procedure, the extrapolation is stable and produces the correct result, even for large $\Delta\tau_{\text{min}}$. Instead, the extrapolation after the DMFT self-consistency (solid lines), can only be successful, if one includes smaller values of $\Delta\tau$ (small symbols, dotted thin lines). Even if for the multigrid procedure a whole set of BSS-QMC simulations has to be performed in every DMFT iteration, the single-$\Delta\tau$ solver needs at least the same amount of computer time to reach a comparable precision. This is attributed to the requirement of a much smaller $\Delta\tau$ value, which is computationally much more expensive. A further advantage of the multigrid procedure is that it can be highly parallelized in a trivial manner: every run for a value of $\Delta\tau$ is independent and so the set of runs can be distributed on a high-performance computing cluster.

A further important check for the stability of the multigrid procedure is the sensitivity to the $\Delta\tau$ grid chosen for the extrapolation. In Fig. 7.3, extrapolated Green functions for different $\Delta\tau$ grids are shown. The example shows imaginary-time Green functions from single-site DMFT calculations in the insulating phase ($U = 4.7$, $T = 0.04$) and for four bath sites. Within the denoted $\Delta\tau$ range, five to seven values of $\Delta\tau$ were used for the extrapolation. The convincing agreement within the statistical errors of the method demonstrates that the multigrid procedure is stable with respect to the choice of $\Delta\tau$ grids.

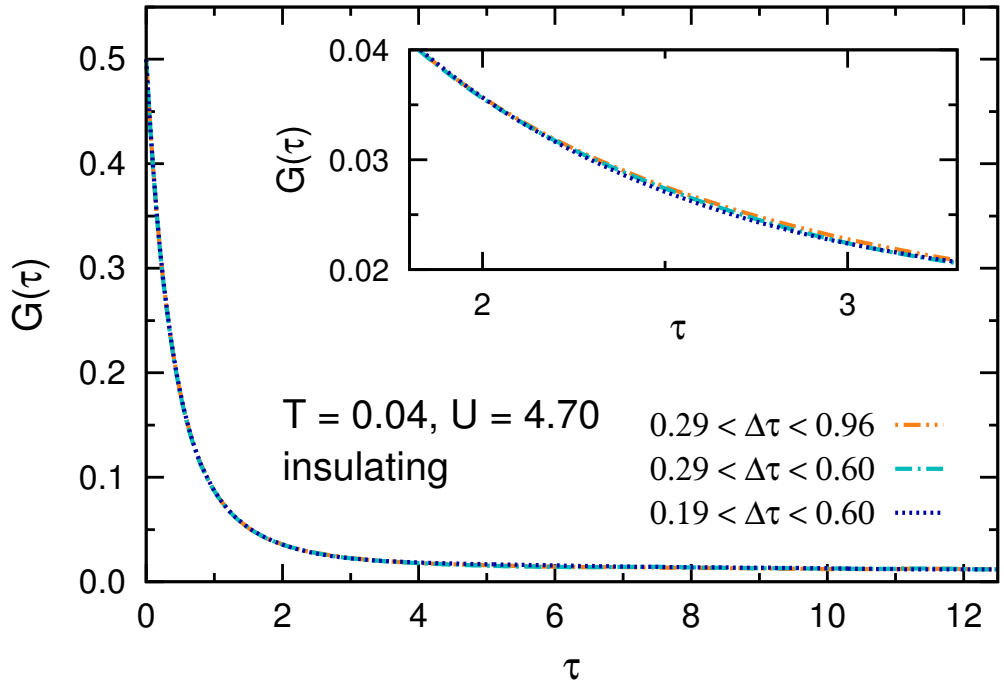

Figure 7.3. – Checking the stability of the multigrid procedure: Comparison of Green functions obtained from the BSS-QMC multigrid solver within one DMFT iteration, i.e., for the same Hamiltonian. Small deviations are of the order of the statistical errors.

Optimal Grid Determination

In the last paragraph, we showed that the results of the multigrid procedure do not depend significantly on the chosen imaginary-time grids. This freedom can be used for optimizing the $\Delta\tau$ values with respect to efficiency and stability. In Sec. 3.1 the linear scaling with the inverse temperature $\mathcal{O}(\beta = \Lambda\Delta\tau)$ was discussed. However, after a certain number of time steps a more expensive update (*wrapping*) has to be performed in order to avoid instabilities arising from round-off errors in the matrix operations. As rule of thumb, the full Green function update should be performed after

$$N_{\text{wrap}} \lesssim \Delta\tau^{-1} \tag{7.4}$$

steps. The BSS-QMC implementation, used in this project, demands the additional condition that the number of total time slices Λ has to be an integer multiple of N_{wrap}. This conditions leads to the specific situation that simulations with larger $\Delta\tau$ values can need more computational time than simulations with smaller values of $\Delta\tau$, due to the step-like form of $N_{\text{wrap}}(\Delta\tau)$. The developed cluster DMFT code optimizes the $\Delta\tau$ grid in order to minimize computer time for a given accuracy and

stability condition automatically. The expected runtime, which is minimized, can be calculated via a linear estimator

$$t[\Delta\tau] = \underbrace{\frac{\beta}{\Delta\tau}}_{=\Lambda} \left[A \left(1 - \frac{1}{N_{\mathrm{wrap}}(\Delta\tau)} \right) + B \left(\frac{1}{N_{\mathrm{wrap}}(\Delta\tau)} \right) \right] . \tag{7.5}$$

Where $N_{\mathrm{wrap}}(\Delta\tau)$ is given by Eq. (7.4) and respects the condition

$$\mathrm{mod}_{N_{\mathrm{wrap}}} \Lambda = 0 \ .$$

The time constants are determined by the time needed for a fast update (A) and a full update (B). In practice, they depend on the technical details of the supercomputer environment and can be determined empirically by simple test runs.

7.2. Impact of the Bath Discretization

In this section, the impact of the bath discretization on DMFT results is discussed. Due to limitations in the number of bath sites, one has to accept less than perfect representations of the bath and estimate the resulting inaccuracies. This is even more severe for methods like exact diagonalization, in which adding further bath sites enhances the computational costs exponentially $\mathcal{O}(e^{N_b})$. We compare the quality of the representation of the DMFT bath Green function for different sizes of the bath. In a further analysis, the propagation of the finite-size error through the self-consistency is analyzed. Analogous to Sec. 7.1, the MIT in infinite dimensions is considered.

We first analyze the agreement between the continuous and discretized bath on the level of the bath Green function $\mathcal{G}(i\omega_n)$, specifically on a metallic solution ($U = 5.1$) of the Hubbard model at half-filling. In order to resolve deviations at higher Matsubara frequencies, we show in Fig. 7.4 $\mathcal{G}(i\omega_n) \cdot \omega_n$ and thus compensate the dominant $i\omega_n^{-1}$ behavior. The picked data set was generated at the ultra-low temperature $T = 0.01$, where the impact of restrictions to a small number of bath orbitals is expected to be more severe than for higher temperatures. The more difficult fit problem at low temperatures can be explained with the increasing importance of low-energy features in the spectrum of the system; i.e., more energy levels are needed for a correct description.

Fig. 7.4 shows the agreement of the target bath Green function from DMFT (black solid line) and finite-size bath representations (colored lines), obtained by fitting of the bath parameters [Eq. (6.3)]. The representation with one bath site only is far off, even at the most important small Matsubara frequencies. With taking more bath sites into account, the fit converges monotonously to the target function. For $N_b = 4$ the low-frequency range is represented satisfyingly, but the fitted function shows remaining deviation at higher Matsubara frequencies. The bath is completely converged for $N_b = 6$, i.e., no gain in precision can be found for $N_b = 7$ on this scale. The required precision has to be decided for each application

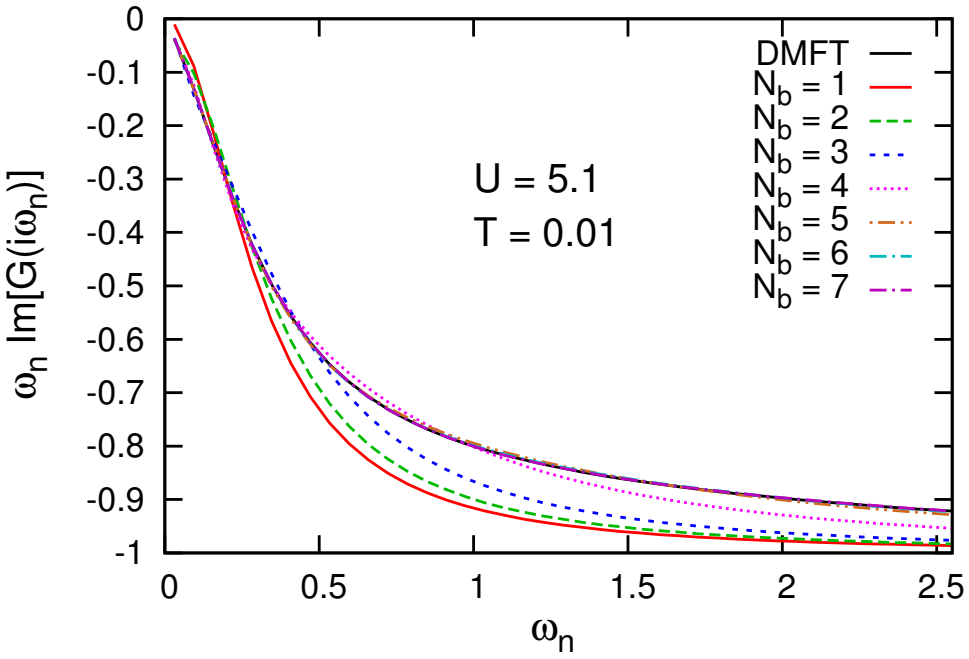

Figure 7.4. – Imaginary part of the bath Green function on Matsubara axis times frequency. Continuous bath Green function (black solid line) given from DMFT self-consistency and its representation for different number of bath sites (colored lines). Not shown $\mathrm{Re}[\mathcal{G}(i\omega_n)] = 0$, due to particle hole symmetry.

and parameter regime; the number of bath sites is usually kept constant throughout the self-consistency cycle. One could also think of a scheme, where results are pre-converged with a smaller number of bath sites, and using the resulting bath Green function as input for later high-precision simulations with a larger number of bath sites.

In order to investigate the propagation of the bath discretization error through the DMFT self-consistency cycle, we return to the MIT in the half-filled one-band Hubbard model within single-site DMFT. In Sec. 7.1, all data shown for Z and D were calculated with a fixed number of bath sites $N_b = 4$. We now proceed with the analysis, using an exact diagonalization solver [GKKR96] for small numbers of bath sites $N_b \leq 5$ and our unbiased BSS-QMC solver for a larger number of bath sites, which is feasible due to the superior scaling. Again, we use HF-QMC results as reference. At the lowest temperature $T = 0.01$, additional data were produced using the continuous-time hybridization expansion solver [WCdM$^+$06, WM06] (CT-HYB) as available from the Algorithms and Libraries for Physics Simulations (ALPS) project [BCE$^+$11].

In Fig. 7.5 results for $T = 0.04$ are shown, HF-QMC (black points) and ED/BSS-QMC for $N_b = 4$ (open circles) data are the same as in already shown in Fig. 7.1. If one uses less bath sites ($N_b = 3$), the results deviate strongly from the reference

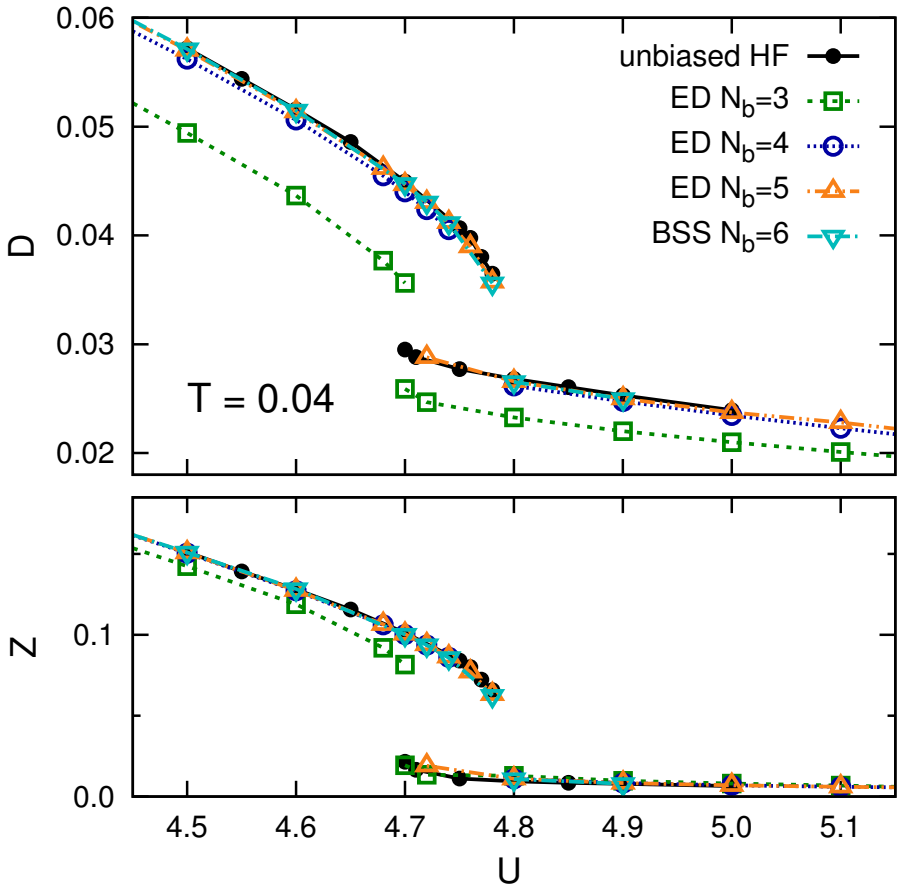

Figure 7.5. – DMFT estimates for the double occupancy D and quasiparticle weight Z as function of the interaction U at $T = 0.04$, for different numbers of bath sites: multigrid BSS-QMC (open circles), ED (open triangles and squares). Reference results are given by multigrid HF-QMC results (points).

solution. The curves converge to the correct results with $N_b = 5$ (orange triangles) and no gain in precision is found for $N_b = 6$ (blue triangles). Fig. 7.6 shows the same study at the lowered temperature $T = 0.02$, here $N_b = 6$ bath sites are necessary for reproduction of the reference results. In this regime, the multigrid BSS-QMC solver is already more efficient than corresponding ED implementations. At the lowest considered temperature $T = 0.01$, seven bath sites were used for the final result[1]. Here small deviations from the HF-QMC results remain near the transition line. For double checking the results, also CT-HYB data are shown (gray diamonds), which agree perfectly with the unbiased BSS-QMC results.

This study shows that the number of bath sites has to be increased, when the temperature is lowered. However, in the presented test cases one additional bath site had to be added when the temperature was halved, so the total linear-in-β scaling is not spoiled by the slow required increase of the number of bath sites.

[1]Here the BSS-QMC is already a factor ten faster than the used ED implementation.

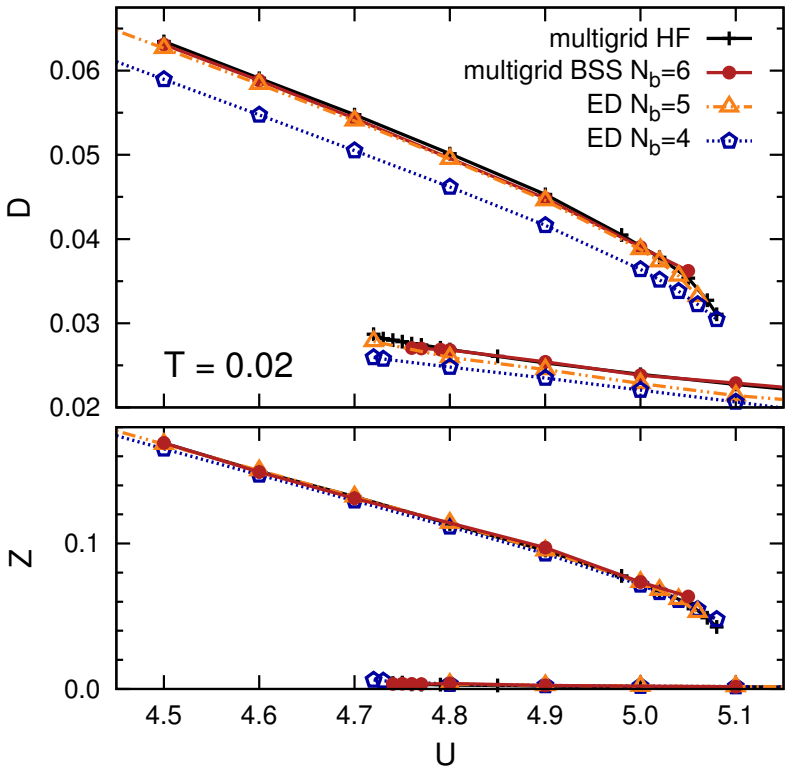

Figure 7.6. – Same as Fig. 7.5, at the lower temperature $T = 0.02$.

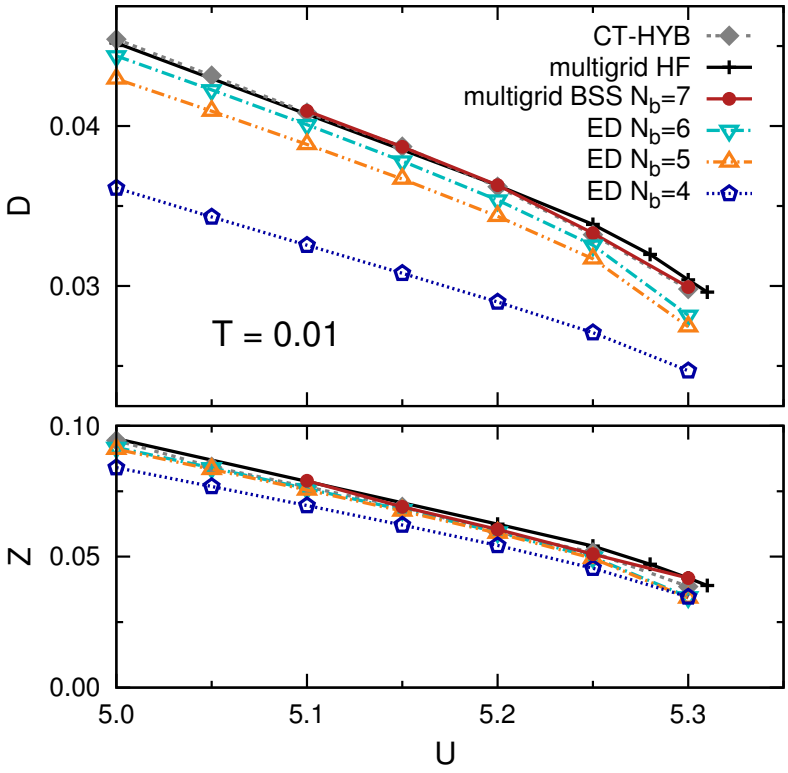

Figure 7.7. – Same as Fig. 7.5, at the lower temperature $T = 0.01$.

8. Momentum Dependence of the Self-Energy

The key approximations in DMFT is neglecting, or for its cluster extensions coarse-graining (cf. Sec. 3.2), the momentum dependence of the self-energy. These approximations are correct in the limit of infinite spatial dimensionality only. However, in this thesis we focus on systems that are mainly two dimensional. An interesting question, not studied extensively in the literature, is the precise impact of the neglect of the momentum dependence in the self-energy in lower dimensional systems. The understanding, in which cases and parameter regimes nonlocal features are more or less important, does not only tell about the reliability of (cluster) DMFT studies[1], but can also help in formulating more efficient simulation schemes. One ansatz is the DCA^+, suggested by Staar et al. [SMS13], which uses an interpolation of the self-energy between the central points of the DCA patches, instead of the constant value. However, this requires an appropriate assumption of the functional form of the self-energy for each considered model. Recently, it was found in the three-dimensional case that the static and dynamic part of the self-energy show a different order of nonlocal dependence [STT15], and, thus, can be processed on different levels.

We investigate the momentum dependence of the self-energy in two-dimensional systems by comparing direct lattice BSS-QMC data to DCA calculations. Results are shown for the anisotropic Hubbard model on rectangular lattices (Sec. 8.1) as well as for the KLM (Sec. 8.2) and for the doped Hubbard model (Sec. 8.3) on the square lattice.

The results shown in this section are part of a project with Petra Pudleiner, who performed the BSS-QMC calculation for the anisotropic Hubbard model, and which is led by Prof. Blümer. In this project, the main focus is set on the evolution of nonlocal correlations for the anisotropic Hubbard model and direct lattice calculations. Further goal is finding a suitable parametrization for the self-energy throughout the full Brillouin zone. With such a parametrization a full calculation of the self-energy is possible, i.e., continuous in momentum space. This is related to our previous study on pseudogap physics in the half-filled two-dimensional Hubbard model [RGAB12], where a continuous representation of the Green function along high-symmetry lines was found. In the case of the anisotropic Hubbard model, I restrict myself to the comparison of the BSS-QMC data with DCA (Sec. 8.1). A full study will be published elsewhere. Further, I will focus on the evolution of the momentum dependence with doping (Sec. 8.3) and compare to nonlocal correlation in the KLM (Sec. 8.2).

[1] The analysis of the momentum dependence of the self-energy can show in detail, where the neglect of nonlocal correlations misses important features.

8.1. Anisotropic Hubbard Model

We investigate the anisotropic Hubbard model Eq. (2.3) on a rectangular lattice, i.e., with hopping amplitudes in x- and y-direction $t_x \leq t_y$. We introduce the dimensionless scaling parameter

$$\alpha = \frac{t_x}{t_y} \tag{8.1}$$

that interpolates between the isotropic two-dimensional case ($\alpha = 1$) and the quasi one-dimensional case ($\alpha = 0$). The parameter α also affects the effective coordination number Z_{eff}[2], which changes the non-interacting bandwidth Eq. (3.62). A meaningful comparison of results for different values of α is only possible by using adapted energy scales. The relevant energy scale is set by the variance of the dispersion [GB11, GRP+12, CSGB13]. Thus, for all presented results the hopping amplitudes are rescaled in order to fix the variance to its the value in the isotropic case:

$$\begin{aligned}
\langle \epsilon^2 \rangle &= \frac{1}{\pi} \int_{-\pi}^{\pi} \int_{-\pi}^{\pi} dk_x dk_y \left[-2\ t_x\ \cos(k_x) - 2\ t_y\ \cos(k_y) \right]^2 \qquad (8.2) \\
&= \frac{1}{\pi} \int_{-\pi}^{\pi} \int_{-\pi}^{\pi} dk_x dk_y \left[4\ t_x^2 \cos(k_x) - 4\ t_y\ t_x \cos(k_y)\cos(k_x) + 4\ t_y^2\ \cos(k_y) \right] \\
&= \frac{4}{\pi} \left[t_x^2 \left(\frac{1}{2} k_x + \frac{1}{2} \cos(k_x)\sin(k_x) \right) + t_y^2 \left(\frac{1}{2} k_y + \frac{1}{2} \cos(k_y)\sin(k_y) \right) \right]_{-\pi}^{\pi} \\
&= 2t_x^2 + 2t_y^2 \stackrel{!}{=} \text{const.} \equiv 4 \ .
\end{aligned}$$

Combining Eq. (8.2) with the definition of α Eq. (8.1), the rescaled hopping amplitudes are given by

$$t_x = \alpha \sqrt{\frac{2}{\alpha^2 + 1}} \qquad \text{and} \qquad t_y = \sqrt{\frac{2}{\alpha^2 + 1}} \ . \tag{8.3}$$

For a deeper understanding of the impact of the DCA coarse graining on the self-energy, we compare 2×2 DCA results to data from direct lattice BSS-QMC simulations. Due to its finer momentum resolution, BSS-QMC serves as a measure

[2] The parameter α modulates the effective coordination number between the isotropic two-dimensional case $Z_{2\text{d}} = 4$ and the quasi one dimensional case $Z_{1\text{d}} = 2$.

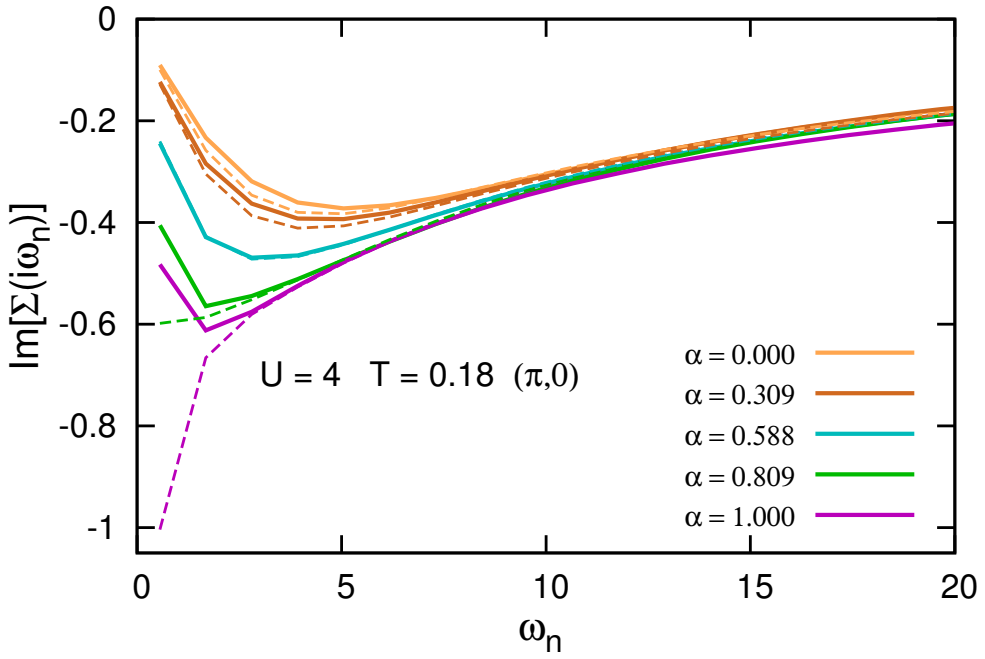

Figure 8.1. – Imaginary part of the self-energy on the Matsubara axis at $\mathbf{k} = (\pi, 0)$: direct lattice BSS-QMC (dashed lines) compared to 2×2 DCA calculations (solid lines) for different values of anisotropy $\alpha = t_x/t_y$.

for the reasonability of the DCA approximation. We compare the results for the imaginary part of the antinodal [$\mathbf{k} = (\pi, 0)$] self-energy on the Matsubara axis for different values of $\alpha \in \{0.000, 0.309, 0.588, 0.809, 1.000\}$. The data are shown in Fig. 8.1. While the DCA results (solid lines) deviate strongly from the BSS-QMC data (dashed lines) in the isotropic case (violet lines), even qualitatively, the curves seem to collapse quickly with the reduction of α. However, the collapse is not traced back to a better agreement of DCA and direct lattice calculations with stronger anisotropy. The full picture can only be understood by analyzing the full momentum dependence throughout the Brillouin zone. One idea for a better understanding was to use a suitable parametrization of the self-energy. As ansatz, we use a representation via the non-interacting dispersion [cf., Fig. 8.2 and Eq. (3.62)], i.e., instead of analyzing the self-energy as two-dimensional function of the momentum $\Sigma(k_x, k_y)$, we consider $\Sigma[\epsilon(k_x, k_y)]$. Results for the imaginary part of the self-energy at the first Matsubara frequency are shown in Fig. 8.3. It turns out that the self-energy depends smoothly on the dispersion. Strong deviations are only found at the Fermi edge (e.g., $\epsilon = 0$ for $\alpha = 1$, upper plot). At these points, the dispersion is identically, but the self-energy is significantly momentum dependent. This is a characteristic feature of the pseudogap physics[3], which we have already observed in the Green functions along the Fermi edge [RGAB12].

[3]The term *pseudogap physics* is related to properties of some cuprates that are d-wave superconductors. In these materials a momentum-dependent opening of a pseudogap in the spectral function between $\mathbf{k} = (\pi, 0)$ and $\mathbf{k} = (\pi/2, \pi/2)$ is observed.

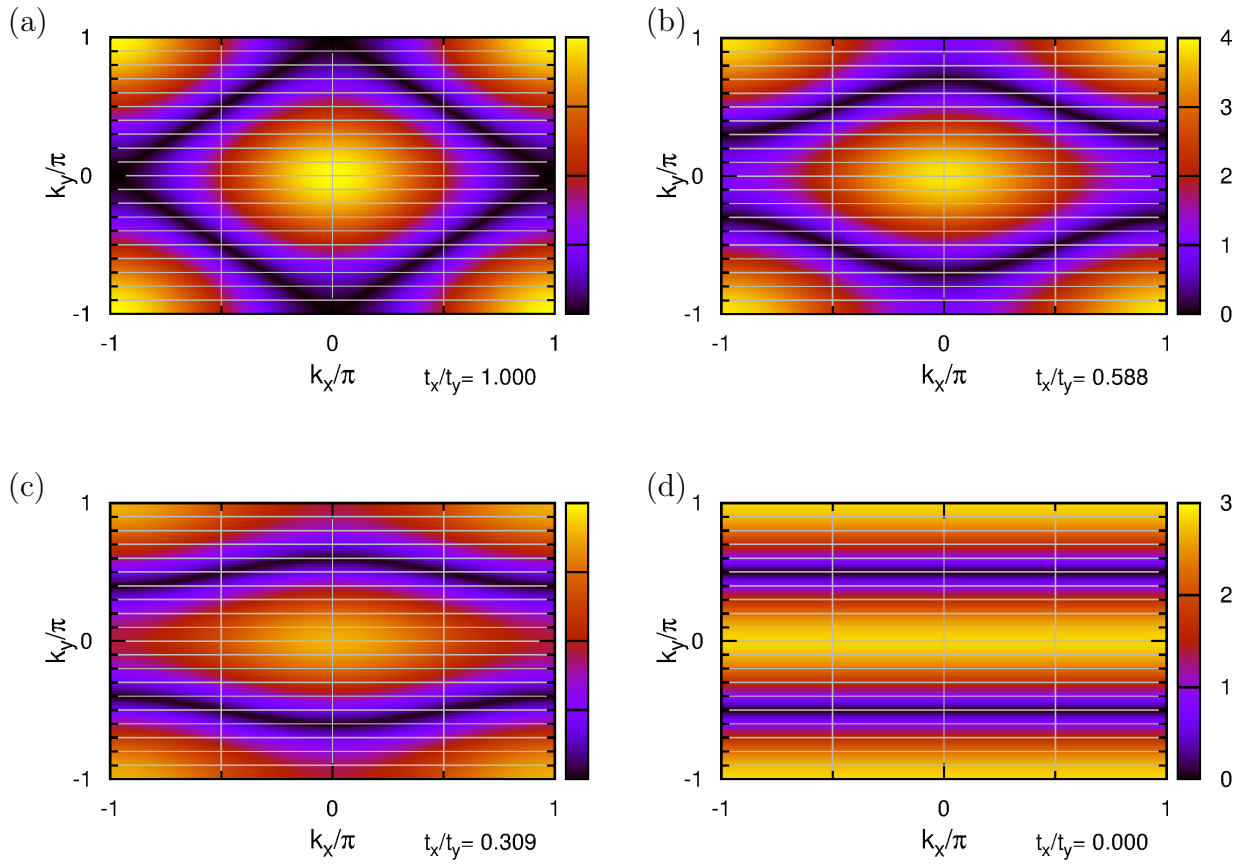

Figure 8.2. – Non-interacting dispersion of the anisotropic rectangular lattice for different values of $\alpha = t_x/t_y$. Isotropic case (a), intermediate anisotropies (b) and (c), and quasi one-dimensional model (d). Illustration created by P. Pudleiner.

We return to the mapping between momenta and dispersion, given by Eq. (3.62) and visualized in Fig. 8.2. The isotropic case Fig. 8.2 (a) shows perfect nesting at half-filling and protects the particle-hole symmetry on the Fermi edge (black areas). This leads, e.g., to a symmetric imaginary time Green function at $\mathbf{k} = (\pi, 0)$. By adding anisotropy, shown in Fig. 8.2 (b) and (c), the non-interacting Fermi surface is shifted. For finite-size calculations a smaller number of lattice points are located on the Fermi surface, which can be a disadvantage in interpreting physical quantities, e.g., spectral functions. This situation can be improved by adapting the value of anisotropy α and the ratio of the number of lattice sites on the rectangular lattice in the way that a maximum number of momentum points are located on the non-interacting Fermi surface. In the quasi one-dimensional case Fig. 8.2 (d), the Fermi surface depends on the momentum in x-direction only.

With this picture in mind, one can relate to the results shown in Fig. 8.3. For all anisotropies, the DCA approximation to the self-energy results in the correct behavior far away from the Fermi surface ($|\epsilon| \to 4$) and shows the maximum deviation at the Fermi edge ($\epsilon = 0$). In the isotropic case Fig. 8.3, this agrees with the

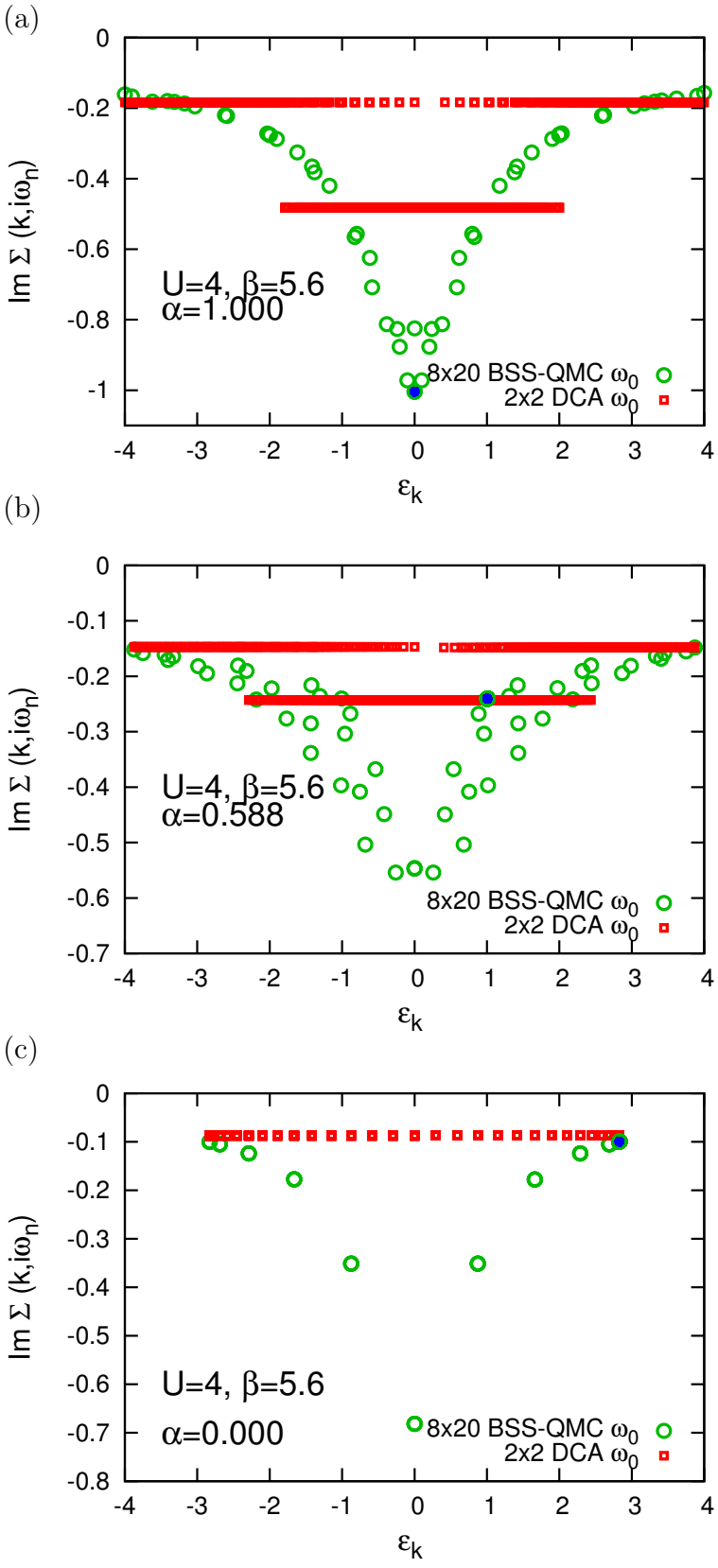

Figure 8.3. – Imaginary part of the self-energy at the first Matsubara frequency for lattice BSS-QMC (green open circles) and 2×2 DCA (red open squares) as function of the non-interacting dispersion. Isotropic lattice (a), intermediate anisotropic lattice (b) and quasi one-dimensional Hubbard model (c). Blue points mark the result at $\mathbf{k} = (\pi, 0)$.

strong deviation in the violet curves in Fig. 8.1, where $\epsilon_{\alpha=1}(\pi, 0) = 0$. The better agreement of DCA and direct lattice calculations for larger α on the first sight is traced back to the fact that the considered point $\mathbf{k} = (\pi, 0)$ is shifted away from the Fermi surface. This shift is marked with blue points in Fig. 8.3 (a) - (c). Thus, the agreement is not globally enhanced.

The used DCA scheme is not able to resolve any momentum dependence in the quasi one-dimensional case Fig. 8.3 (c). However, this result might be an artifact of the specific implementation, which is optimized for two-dimensional lattice structures. For all calculations the same patching of the Brillouin zone was used: patch centers $\mathbf{K} = \{(0, 0), (0, \pi), (\pi, 0), (\pi, \pi)\}$ with quadratically shaped areas. A rather one-dimensional patching scheme, e.g., a stripe pattern, is expected to capture the momentum resolution more successfully when smaller values of α are approached.

8.2. Kondo Lattice Model

In this section, we will focus on the quality of the DCA approximation for the Kondo lattice model (KLM). Again, the momentum dependence of the self-energy is analyzed. This topic was recently studied by Gang Li [Li13] by comparing single-site DMFT to the dual fermion (DF) extension to DMFT [RKL08], which introduces the momentum dependence diagrammatically by considering higher order diagrams of the Green function. Li found that the momentum-dependent dispersion of the DF self-energy varies around the constant value the DMFT. This result suggests that the DCA coarse graining, i.e., averaging the self-energy on the patches in momentum space, will result in values close to the single-site DMFT solution. We address the question by comparing direct lattice BSS-QMC results with DCA calculations, analogous to the Hubbard model study (Fig. 8.3). For the KLM we are restricted to smaller lattices, due to the much larger computational effort associated with the additional f-band in the model.

Results for the isotropic square lattice at $J = 1.4$ and moderate temperature $T = 1/5.6$ are presented in Fig. 8.4. Open circles show data from 6×6 direct lattice calculations using BSS-QMC. Open squares denote data obtained with DCA and the unbiased cluster solver developed in this project. In the self-energy, the momentum dependence is already weak at the first Matsubara frequency (green open circles). At the second Matsubara frequency (blue open circles) the self-energy is nearly momentum independent and collapses for higher frequencies. These results support the findings from Li, who predicted a weak dependence of the self-energy.

Comparison to the Hubbard Model

The parameters of the Hubbard model [Fig. 8.3 (a)] and KLM (Fig. 8.4) are not directly connected in the intermediate regime, but we can still compare the results under the consideration that they describe a similar phase; both parameter sets $\{U = 4, T = 1/5.6, \mu = 0\}$ and $\{J = 1.4, T = 1/5.6, \mu = 0\}$ describe a paramagnetic phase above an insulating AF ground state. The quantitative difference in the

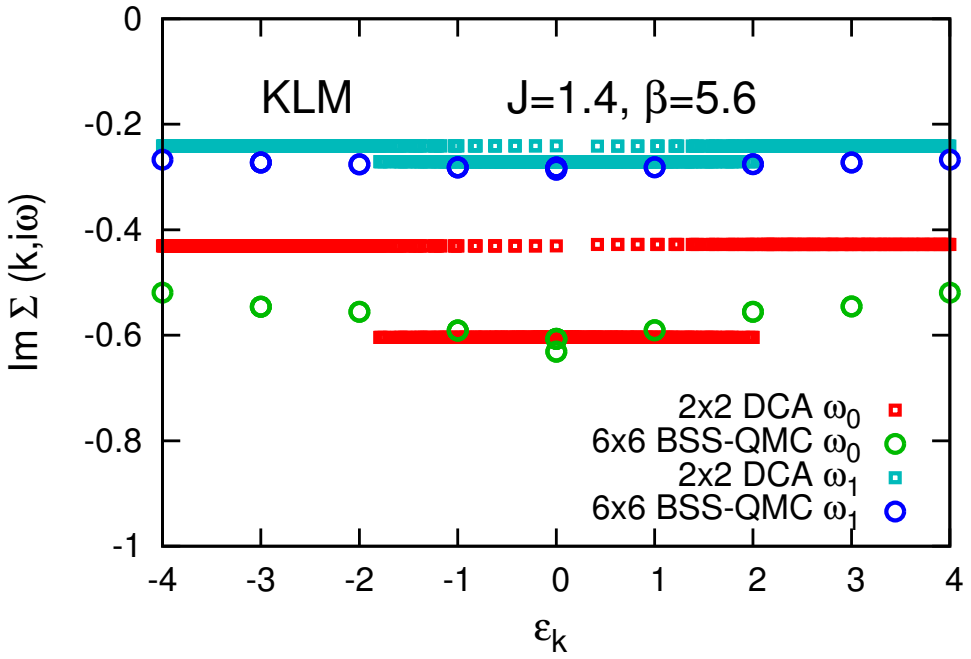

Figure 8.4. – Investigation of nonlocal effects in the two-dimensional KLM. Imaginary part of the self-energy at the first and second Matsubara frequency for lattice BSS-QMC (open circles) and 2×2 DCA (open squares).

momentum dependence of the self-energy is significant. As we have seen in the Hubbard model, DMFT or DCA with a small number of sites, are not able to describe the momentum dependence sufficiently, especially not in vicinity of the Fermi edge. Away from the Fermi edge, the DCA results fairly match the BSS-QMC data[4].

But even if the structure in momentum space is flatter and more regular for the KLM than for the Hubbard model, the DCA still provides not an optimal solution.

One has to note that these findings are valid in the considered paramagnetic phase only. Exploring further parameter regimes, e.g., the superconducting phase, could unveil different scenarios. The question, how far the properties of the self-energy are significantly changed by phase transitions represents an interesting topic for further projects.

8.3. Hole Doped Hubbard Model

Up to this point, all investigations on the anisotropic Hubbard model in Sec. 8.1 and on the KLM on a square lattice in Sec. 8.2 were performed at half-filling. In this section the impact of doping on the momentum dependent self-energy is

[4]The shown finite-size BSS-QMC data have a better momentum resolution than DCA and can point out where nonlocal features are important. However, they still contain systematic errors, which can also lead to quantitative differences between the solutions.

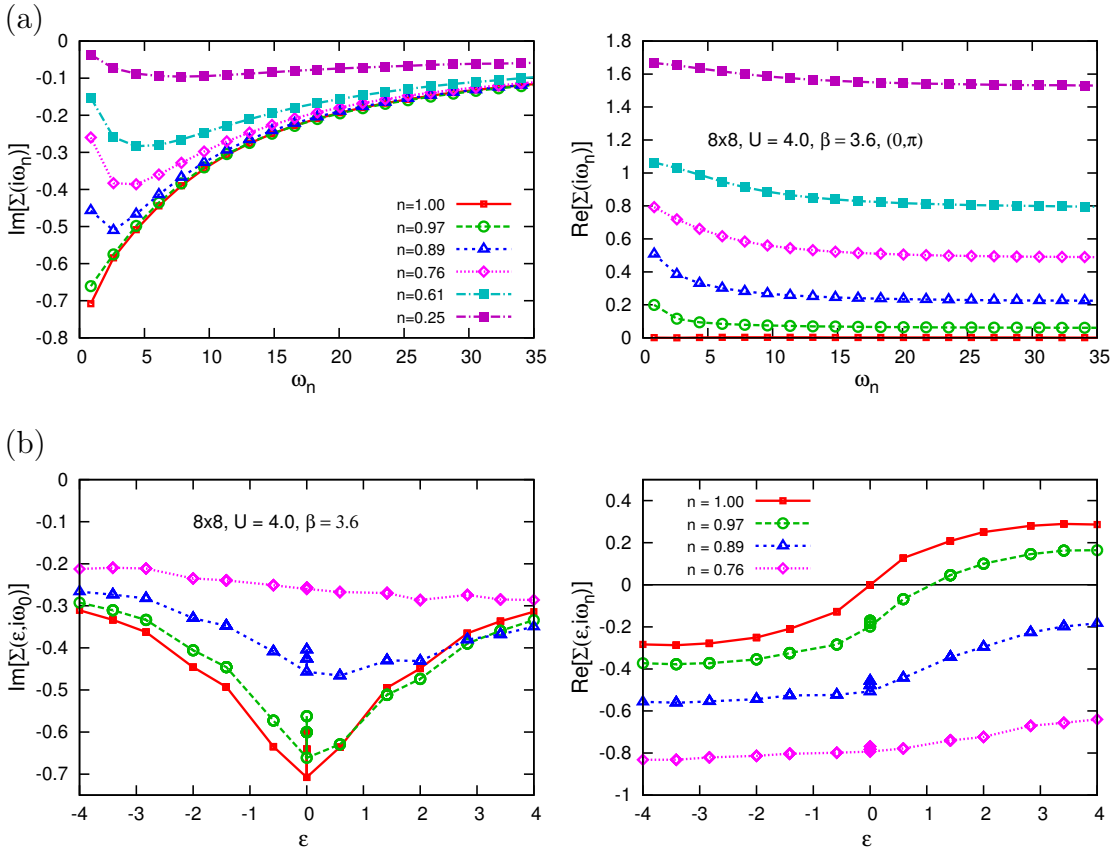

Figure 8.5. – Momentum dependence of the self-energy for various fillings; (a) as function of the Matsubara frequency at fixed momentum $\mathbf{k} = (0, \pi)$; (b) as function of the dispersion at the first Matsubara frequency $i\omega_0$.

studied. Due to the fermionic sign problem in QMC methods, the calculations were performed at the slightly elevated temperature $T = 1/3.6$ and for the comparatively small lattice size 8×8. The density n in the system is controlled by the chemical potential μ [cf. Sec. 6.3.2].

Results were obtained for the values

μ	0.00	0.25	0.50	0.75	1.40
n	1.00	0.97	0.93	0.89	0.76

The considered temperature is higher than the crossover temperature ($T^* \approx 0.18$ for $U = 4$) at half-filling and T^* is further reduced by lowered density [JMHT01], i.e., we will not cross any phase boundary by doping the system for the used parameter range.

Fig. 8.5 (a) shows the imaginary (left) and real part (right) of the self-energy on the Matsubara axis at fixed momentum $\mathbf{k} = (0, \pi)$. Again, particle-hole symmetry assures $\mathrm{Re}[\Sigma(i\omega_n)] = 0$ at half-filling (red squares). While for weak doping and half-filling the shape of $\mathrm{Im}[\Sigma(i\omega_n \to 0)]$ suggests a slightly insulating behavior, the system becomes metallic with decreased density. This behavior is expected, as well

as the overall reduction of the imaginary part of $\Sigma(i\omega_n)$, and can be explained by the decreasing correlations, due to the dilution of the system.

In Fig. 8.5 (b) the self-energy at the lowest Matsubara frequency $\Sigma(i\omega_0)$ is shown as function of the non-interacting dispersion. With increased doping of the system, the self-energy becomes flatter in ϵ and so in momentum space. Also, the momentum dependence on the Fermi edge is reduced with increased doping: the spread of the values at $\epsilon = 0$ is reduced from $\sim 16\%$ at $n = 1$ and $n = 0.97$ to 10% at $n = 0.89$ and collapses to $\sim 1\%$ at $n = 0.76$. Summarizing the results, one can conclude that the DMFT approximation (assumption of a momentum independent self-energy) is worst at half-filling and becomes better for doped systems in the paramagnetic phase.

8.4. Real-Frequency Results

In the previous sections, we analyzed the momentum dependence of the self-energy on the Matsubara axis. This is the generic approach for QMC based methods, because their direct results are Green functions in imaginary time or frequency. To gain results on the real-time or real-frequency axis, one has to perform analytical continuation, described in Sec. 3.1.2. The continuation scheme can introduce additional errors, which might make an identification of the momentum dependence more difficult. However, the physically interesting quantities are functions on the real-frequency axis, e.g., spectral functions. In this section we check the consistency of the results on the real axis with the findings of the study on the Matsubara axis. As example, we review the data for the isotropic Hubbard model, discussed in Sec. 8.1. Real-frequency data are obtained by analytic continuation of the self-energy, described in Sec. 3.1.2 and Appendix B.

In Fig. 8.6 (a) we present results for the self-energy on the real-frequency axis, obtained by analytical continuation of the data shown as violet lines in Fig. 8.1 $[U = 4, T = 1/5.6, \alpha = 1.000, \mathbf{k} = (\pi, 0)]$. BSS-QMC (green dashed lines) and DCA (red solid lines) agree very well in the high-frequency features. As already suggested by the contrary tendencies on the Matsubara axis for $\mathrm{Im}[\Sigma(i\omega_0)]$ (Fig. 8.1), the finite-size BSS-QMC data show insulating behavior [resulting in a peak at $\Sigma(\omega = 0)$], while the DCA results show Fermi liquid behavior[5].

Analogous to the procedure in the previous sections, we analyze the momentum-dependence of the self-energy via the parametrization with the non-interacting dispersion. The real-frequency self-energy at $\omega = 0$ is shown in Fig. 8.6 (b). Again, DCA and BSS-QMC deviate strongly at the Fermi surface ($|\epsilon| = 0$) and agree for momentum points far away from the Fermi surface ($|\epsilon| \to 4$). It is worth to underline the agreement of the real parts, which is much better than one could reasonably

[5] In the Fermi-liquid theory, the value of the imaginary part of the self-energy close to the Fermi surface is connected with the inverse lifetime of the quasi-particles: $\mathrm{Im}[\Sigma(\omega \approx 0)] \propto 1/\tau$. I.e., $\mathrm{Im}[\Sigma(\omega \approx 0)] = 0$ for a perfect Fermi liquid. By perturbation theory, one can show that the self-energy evolves quadratically: $\mathrm{Im}[\Sigma(\omega)] \propto \omega^2$ for $|\omega| \ll 1$ [Lut60, Lut61].

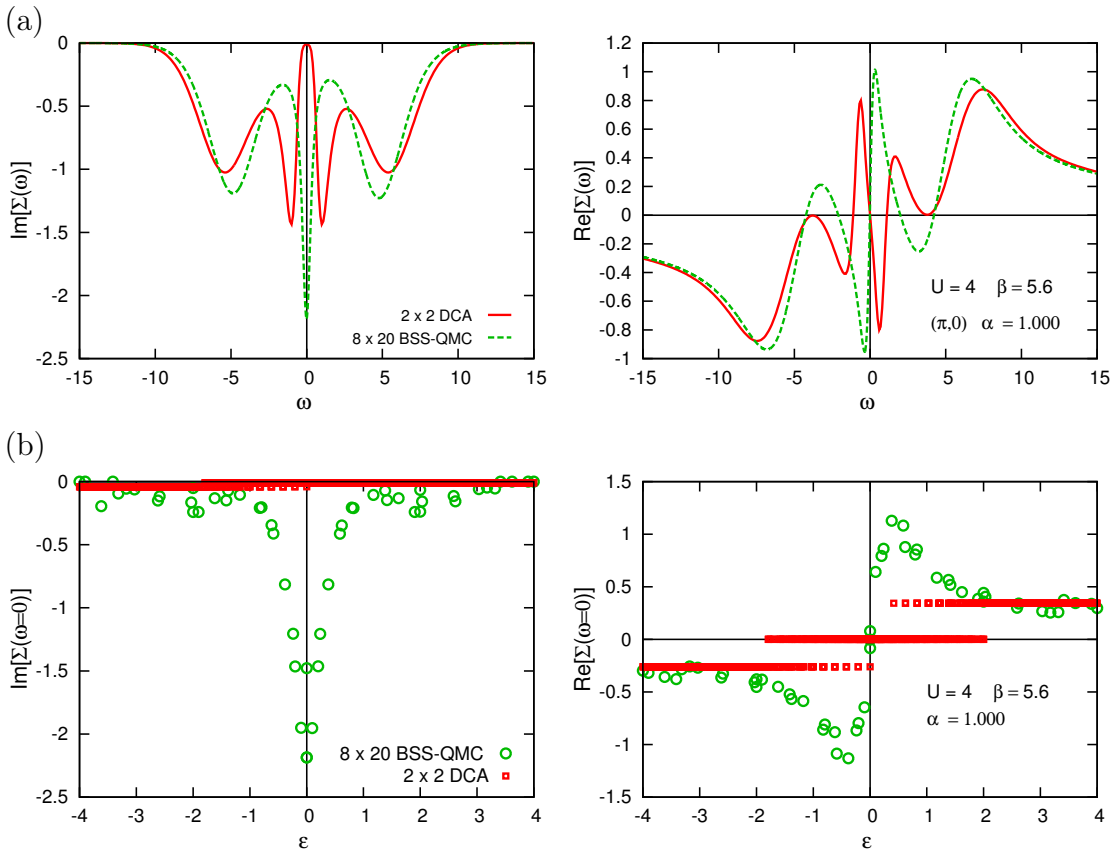

Figure 8.6. – Momentum dependence of the self-energy on the real-frequency axis in the isotropic Hubbard model in two dimensions; (a) Self-energy at $\mathbf{k} = (\pi, 0)$, observed with DCA (red solid line) and BSS-QMC (green dashed line); (b) Self-energy at $\omega = 0$ as function of the non-interacting dispersion.

expect after the application of the various numerical schemes for obtaining the final result[6].

The real-frequency results confirm the findings from the analysis on imaginary-frequency data Sec. 8.1, which proofs the reliability of the developed scheme and gives access to physically more meaningful quantities, e.g., spectral functions.

[6]Especially, the analytical continuation can introduce uncontrolled features into the imaginary part of the self-energy, which would be amplified by the application of the Kramers Kronig relation for the calculation of the real part.

9. Summary and Outlook

The intention of this thesis was the development of highly efficient and numerically exact methods for solving quantum Hamiltonians for strongly correlated systems at low temperatures. The developed algorithms are based on the Blankenbecler-Scalapino-Sugar quantum Monte Carlo (BSS-QMC) algorithm, used for direct lattice calculations and also for the application within the dynamical mean-field theory (DMFT), including its cluster extensions. BSS-QMC is very efficient at low temperatures, but suffers from systematic errors, namely Trotter bias and finite-size errors. We eliminated this Trotter error first in the context of direct lattice calculations and presented a scheme that yields unbiased Green functions from BSS-QMC (Chap. 4). This scheme was complemented by finite-size extrapolations on the level of the self-energy, to finally gain unbiased results, valid in the thermodynamic limit. In Chap. 5, these algorithms were applied to the two-dimensional Hubbard model Eq. (2.3). The study was performed in collaboration with the Group of Prof. Held from Vienna University of Technology, who approached the problem using dynamical vertex approximation ($D\Gamma A$). Although the unbiased BSS-QMC and the DΓA are two completely independent methods, both support the same physical picture: no Mott-transition occurs at any finite temperature and interaction strength in the model, which is contrary to former studies.

In Chap. 6, we integrated the unbiased BSS-QMC as impurity solver into the DMFT framework and presented the extension to cluster methods. Beside solutions for QMC specific issues, we developed algorithms for the efficient treatment of a finite bath in (cluster) DMFT. These findings are also important for related methods, e.g, exact diagonalization. The efficient impurity solver was successfully tested on the one- and two-dimensional Hubbard model and benchmarked with various complementary methods[1].

The quantitative impact of Trotter errors in the DMFT context was studied by application to the Mott transition in infinite dimensions. While the Trotter biased impurity solver yields a different critical value for the transition and a shifted coexistence region (Chap. 7), the multigrid BSS-QMC solver reproduces the reference results, obtained by exact diagonalization, exactly. For obtaining the entire picture, we also analyzed the impact of the bath discretization by comparison to well-established Hirsch-Fye QMC results, which could be reproduced down to the ultra-low temperature $T = 0.01$, with a manageable number of bath sites.

Finally, we put a prominent topic, the neglect of nonlocal correlations within DMFT, on solid grounds (Chap. 8): We compared direct lattice BSS-QMC results, which have a dense momentum grid, to coarse-grained results obtained using the dynamical cluster approximation for the half-filled anisotropic Hubbard model,

[1] Exact diagonalization, Bethe ansatz, direct lattice QMC, Hirsch-Fye QMC, continuous-time QMC, and DΓA .

the doped Hubbard model, and for the Kondo lattice model (KLM). The outcome may provide guidance for further cluster DMFT studies: The importance of nonlocal correlations strongly depends on the model and parameters. For the half-filled (anisotropic) Hubbard model in two-dimensions a momentum-independent self-energy is a poor approximation and will miss important effects in vicinity of the Fermi edge (Fig. 8.1). In contrast, a weaker momentum dependence and a better agreement with DCA is found for the KLM (Fig. 8.4) and the strongly doped Hubbard model (Fig. 8.5), at least in the paramagnetic phase[2]. We further showed that the self-energy can, at least away from the Fermi edge, be smoothly parameterized by the noninteracting dispersion. This representation paves the way for numerically more efficient schemes, due to a deeper understanding of the consequences of DMFT type approximations.

Outlook

The developed numerical schemes establish a basis for many applications. For models with a manageable fermionic sign problem, the presented unbiased impurity solver for DMFT is more efficient at ultra-low temperatures than state-of-the art algorithms such as continuous-time QMC. With this toolbox, interesting phases of the Hubbard and Kondo lattice model can be explored. A generic example is the superconducting phase of the KLM. In a follow-up project, the calculation of the pairing susceptibility described in Sec. 3.2.5 can be implemented and the full phase diagram of the doped two-dimensional KLM can be measured. The self-consistency is already implemented in the DCA code and we showed that the fermionic sign problem is manageable for the interesting parameter regime.

Our studies on the momentum-dependent self-energy were performed for paramagnetic phases only. To complete the full story, also magnetically ordered phases, superconducting phases, and the vicinity of phase transitions have to be studied. With a deep understanding of the exact momentum-dependence of the self-energy, more efficient cluster DMFT schemes could be developed, e.g., by an improved representation and parametrization in momentum space.

[2]This picture might change dramatically when a magnetic ordered or superconducting phase is entered.

Appendix A.

Stochastic Fit Algorithm

When Hamiltonian based impurity solvers are used, the fitting procedure for the bath parameters becomes a crucial point in the framework of (cluster) DMFT. Due to underdeterminedness, the problem is ill-posed. In consequence, the *energy landscape* of the function χ^2, in which the minimum has to be found, is complicated and can contain divergent regions (cf. Fig. 6.1). Thus, the application of standard downhill methods to the minimization problem fail. We present an implementation a stochastic fitting procedure, based on parallel tempering and simulated annealing (PT&SA), is used [LPA+09]. The algorithm is based on stochastic sampling of the target parameters (here: hybridization and bath dispersion), looking for the minimal value of the χ^2 [Eq. (6.3)]. Simulated annealing is a concept that is comparable to Monte Carlo methods used for classical systems. One starts with a high artificial temperature, e.g., configurations where steps in all directions are accepted with a high probability. The temperature is reduced successively until the method is converged.

Simulated annealing

1. choose starting temperature T^{start} and target temperature T^{target}
2. guess starting configuration (fitting parameters $\{V_{\alpha\beta}\}$)
3. change configuration (vary $v \in \{V_{\alpha\beta}\}$)
4. **Metropolis transition**
   acceptance probability $min\left[1, \exp\left\{-\Delta\chi^2/T\right\}\right]$
5. **Annealing** (if an appropriate condition fulfilled)
   $T^{\text{new}} = T^{\text{target}} + (T^{\text{old}} - T^{\text{target}})C \quad \text{with} \quad C < 1$
6. return to step 3. until convergence

Here, $\Delta\chi^2$ denotes the change in the quality of the fit, caused by the variation of v.

In the scheme of parallel tempering, a temperature grid is chosen. The replicas of the parameter set, simulated with high temperature, move fast through different regions in the parameter space, while low-temperature replicas may converge in a (local) minimum. After a certain number of iteration steps, replicas are interchanged with a temperature dependent probability. In terms of physical systems, the method can sample high and low energy configurations simultaneously.

Parallel tempering

1. choose artificial temperature grid $\{T_i\}$
2. guess starting configuration (fitting parameters $\{V^i_{\alpha\beta}\}$)
3. change configuration for each temperature $T \in \{T_i\}$ (vary $v \in \{V^i_{\alpha\beta}\}$)
4. **Metropolis transition** acceptance probability $min\left[1, \exp\left\{-\Delta\chi^2/T_i\right\}\right]$
5. **Replica transition** (swap configurations $\{V^i_{\alpha\beta}\} \leftrightarrows \{V^{i+1}_{\alpha\beta}\}$)
   acceptance probability $min\left[1, \exp\left\{\Delta\chi^2\left(1/T_i - 1/T_j\right)\right\}\right]$
6. return to step 3. until convergence

In the implemented PT&SA hybrid approach, these two methods are combined. The chosen temperature grid is annealed after convergence of the parallel tempering procedure. This combined method has many free parameters, e.g., the choice of the temperature grid and annealing factors. The full algorithm is sketched in Fig. A.1. Within the (cluster) DMFT self-consistency cycle, the algorithm works automatically: The free parameters are adjusted in the way that the transition and acceptance rates reach the recommended values in [LPA+09]. The improvement of the fit, compared to downhill minimization, is demonstrated in Fig. A.2 for a cellular DMFT calculation for an $N_c = 4$ site Hubbard chain and $N_b = 4$ bath sites. The order of the plots corresponds to the entries of the Green function matrix: beginning from the left plot, the upper panel shows G_{00}, G_{10}, G_{20}, G_{30} etc. Specifically, the imaginary parts are shown in the upper right triangle, including the diagonal, while the real parts are shown in the lower left triangle. The missing information follows from symmetries $G_{ij} = G_{ji}$ and $\mathrm{Re}[G_{ii}] = 0$. The bath Green function (red solid line) is fitted with semi-analytic downhill methods (blue short-dashed line) and the stochastic PT& SA approach (green dashed line). The quantitative improvement is seen in all elements of the Green function.

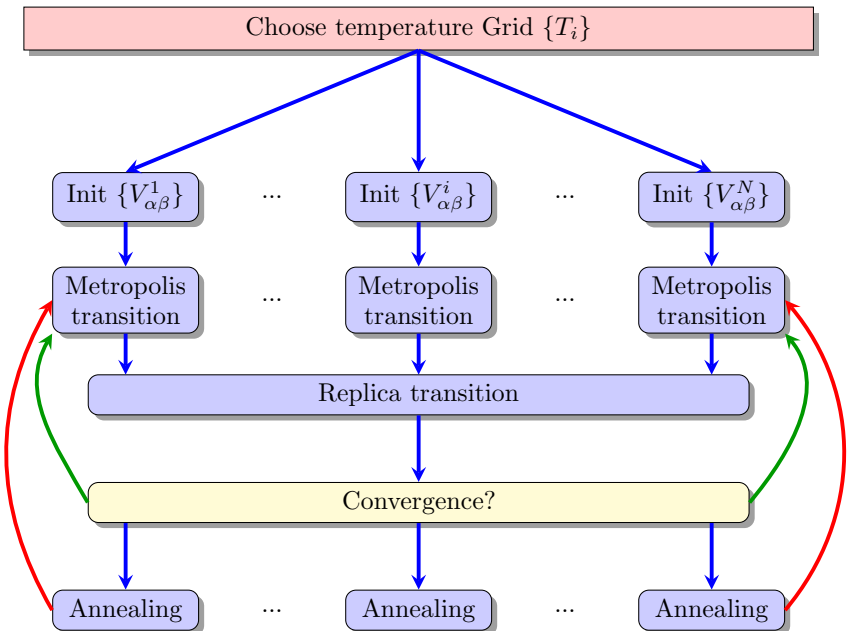

Figure A.1. – Illustration of the hybrid parallel tempering and simulated annealing scheme.

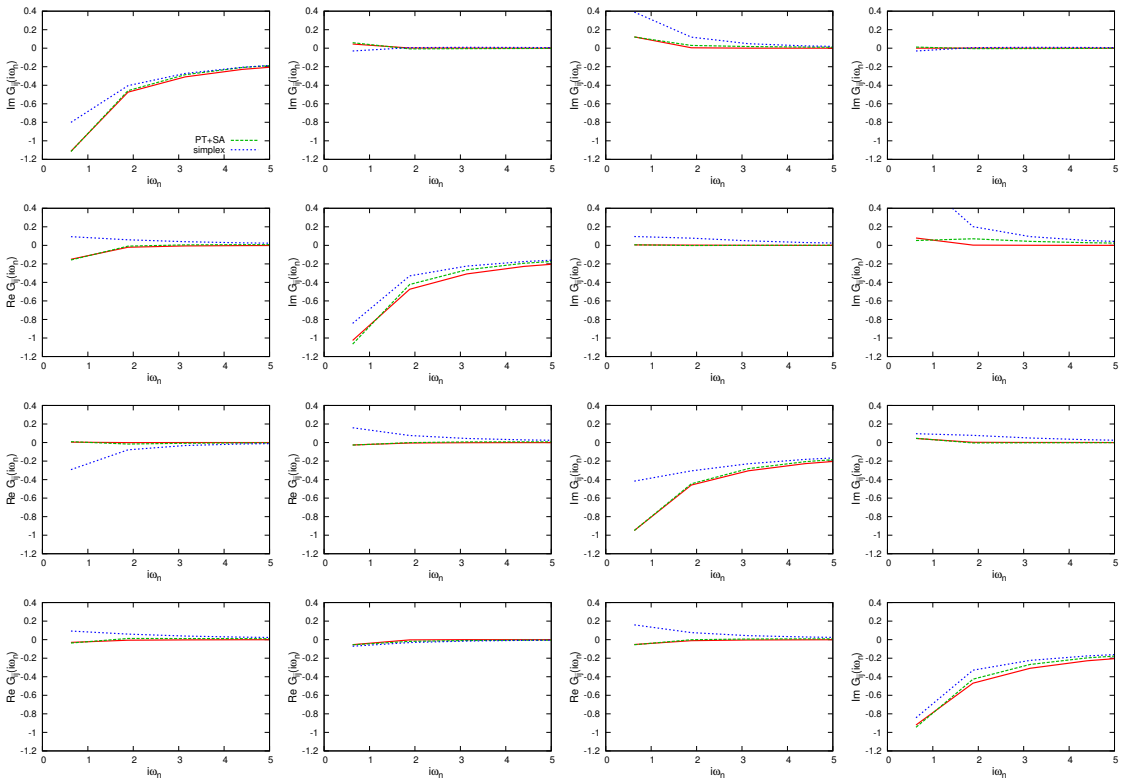

Figure A.2. – Improving of the global fit of the Green functions matrix from CDMFT (red solid line), by using the PT&SA (green dashed line), compared to semi-analytic downhill methods (blue short-dashed line).

Appendix B.

Self-Energy on the Real Axis

In this appendix, we explain the algorithmic details of the calculation of self-energies on the real axis.

In Sec. 4.2, a method for obtaining unbiased self-energies from BSS-QMC calculations was presented. However, the final unbiased self-energy is a function of Matsubara frequencies. To gain results for real frequencies, one has to perform analytical continuation. By inserting the spectral representation of the Green function Eq. (3.21) into the Dyson equation Eq. (3.33), one finds the representation of the self-energy [VZN04]:

$$\Sigma(\mathbf{k}, i\omega_n) = \Sigma^{(0)}(\mathbf{k}) + \int_{-\infty}^{\infty} d\omega' \frac{A_\Sigma(\mathbf{k}, \omega')}{i\omega_n - \omega'} \ , \tag{B.1}$$

where $\Sigma^{(0)}$ is the (real) frequency-independent part and $A_\Sigma = -\mathrm{Im}[\Sigma]/\pi$ denotes the spectral function of the self-energy. For technical reasons, the specific implementation of the *Maximum Entropy Method* (MEM) [cf. Sec. 3.1.2] used for analytical continuation works for imaginary time Green functions only. To use the same program for the self-energy as for the Green function, we have to transform the self-energy in the way that it has the same analytical properties as the Green function. Here, two major issues arise: First, the self-energy on the Matsubara axis Eq. (B.1) cannot be Fourier transformed directly to the imaginary-time axis, due to the constant contribution $\Sigma(\mathbf{k})$, which has to be subtracted. Second, the spectral function of the self-energy A_Σ is not normalized, which violates the assumption that the input function for the MEM yields normalized spectra. This can be corrected on the level of of the Matsubara axis by analysis of the behavior of the self-energy at high frequencies. We expand the Eq. (B.1):

$$\begin{aligned}
\left[\Sigma(\mathbf{k}, i\omega_n)\right]_{n\to\infty} &= \Sigma^{(0)}(\mathbf{k}) + \left[\int_{-\infty}^{\infty} d\omega' \ \frac{1}{i\omega_n} \ \frac{A_\Sigma(\mathbf{k}, \omega')}{1 - \omega'/i\omega_n}\right]_{n\to\infty} \\
&= \Sigma^{(0)}(\mathbf{k}) + \frac{1}{i\omega_n} \ \int_{-\infty}^{\infty} d\omega' \sum_{k=0}^{\infty} A_\Sigma(\mathbf{k}, \omega') \left(\frac{\omega'}{i\omega_n}\right)^k \\
&= \Sigma^{(0)}(\mathbf{k}) + \sum_{k=0}^{\infty} \left(\frac{1}{i\omega_n}\right)^{k+1} \underbrace{\int_{-\infty}^{\infty} d\omega' A_\Sigma(\mathbf{k}, \omega') \, (\omega')^k}_{\text{k-th moment of } A_\Sigma(\mathbf{k},\omega')}
\end{aligned} \tag{B.2}$$

In contrast to the Green function, the real part of the self-energy is constant $c = \Sigma^{(0)}$ in the high frequency range, which leads to a divergence in the Fourier transformation $i\omega_n \to \tau$. This constant has to be subtracted from the self-energy for the proper definition of the transformation. The shift in $\mathrm{Re}[\Sigma(i\omega_n)]$ corresponds to a different choice of the zero-energy level. The absence of normalization corresponds to a factor b in the high-frequency behavior in $\mathrm{Im}[\Sigma(i\omega_n)]$ [contribution of the $k = 0$ term in Eq. (B.2)]. For the application of the MEM tool, the input function must have the same analytical properties. To assure these properties, the following algorithm is used (**k** index suppressed):

1. determine constants c and b by fitting the tail of the self-energy $\Sigma(i\omega_n)$ to

$$\Sigma(i\omega_n) \stackrel{n\to\infty}{\longrightarrow} c + \frac{b}{i\omega_n}$$

2. calculate rescaled self-energy

$$\bar{\Sigma}(i\omega_n) = \frac{1}{b}(\Sigma(i\omega_n) - c)$$

3. transform to imaginary time

$$\bar{\Sigma}(i\omega_n) \stackrel{\mathrm{FT}}{\longrightarrow} \bar{\Sigma}(\tau)$$

4. apply MEM for analytical continuation

$$\bar{\Sigma}(\tau) \stackrel{\mathrm{MEM}}{\longrightarrow} A_{\bar{\Sigma}}(\omega) = -\frac{1}{\pi}\mathrm{Im}\left[\bar{\Sigma}(\omega)\right]$$

5. rescale imaginary part of the self-energy

$$\mathrm{Im}\left[\Sigma(\omega)\right] = b\ \mathrm{Im}\left[\bar{\Sigma}(\omega)\right]$$

6. obtain real part by Kramers Kronig relation

$$\mathrm{Im}\left[\Sigma(\omega)\right] \stackrel{\mathrm{KK}}{\longrightarrow} \mathrm{Re}\left[\Sigma(\omega)\right].$$

In the last step one uses the Kramers Kronig relation to obtain the real part of the self-energy [Kro26, Kra27]

$$\mathrm{Re}\left[\Sigma(\omega)\right] = -\frac{1}{\pi}P\int_{-\infty}^{\infty} d\omega'\ \frac{\mathrm{Im}\left[\Sigma(\omega')\right]}{\omega - \omega'}\ , \tag{B.3}$$

where P denotes the calculation of the principal value. The fitting procedure for the determination of b and c is shown in Fig. B.1, for the isotropic two-dimensional Hubbard model on a 8×20 lattice at $U = 4$ and $T = 1/5.6$. The corresponding self-energy on the real-frequency axis is plotted in Fig. B.2.

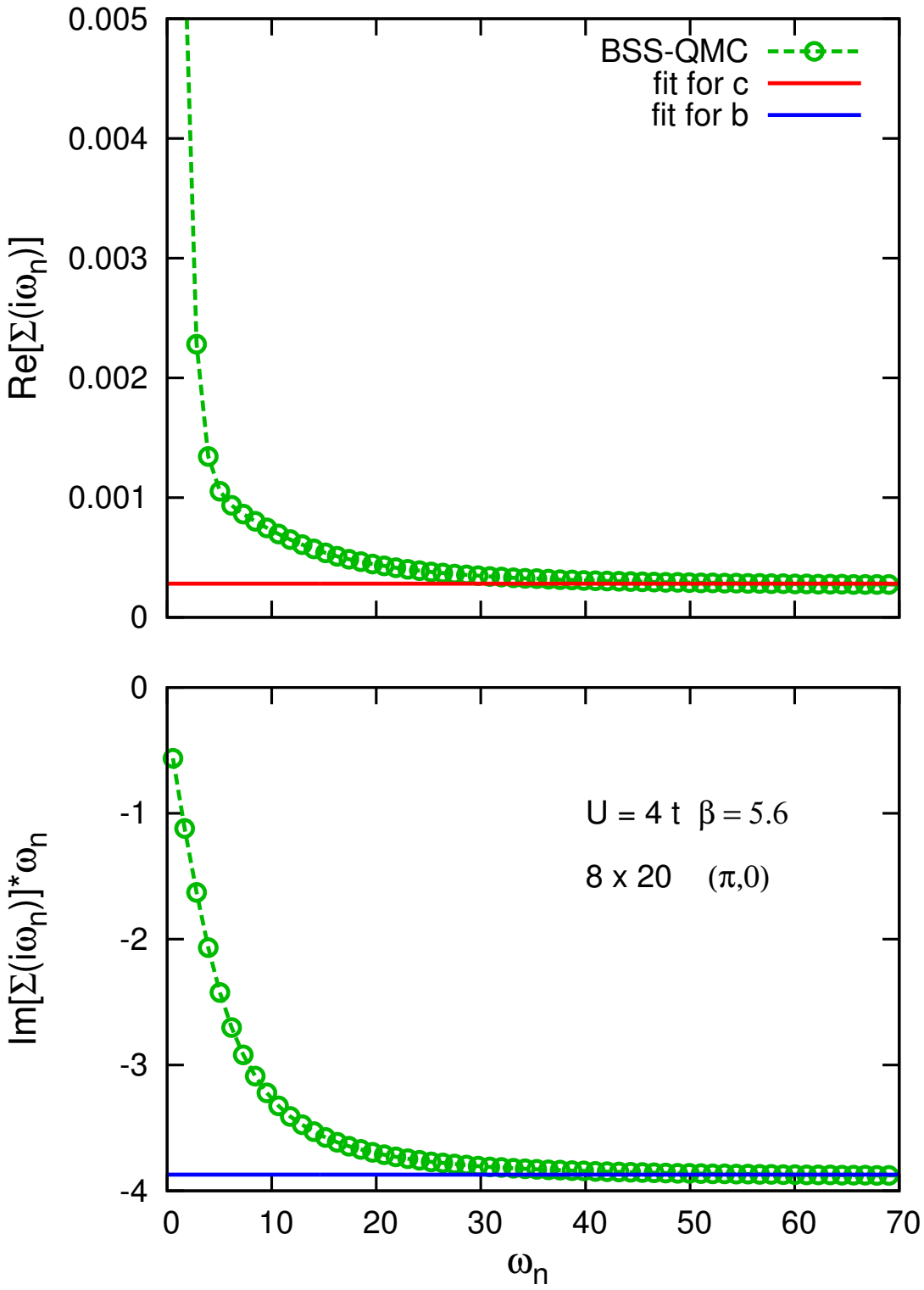

Figure B.1. – Determination of the tail correction b and constant shift c in the self-energy, needed for analytical continuation. Here for the isotropic two-dimensional Hubbard model on a 8×20 lattice at $U = 4$ and $T = 1/5.6$.

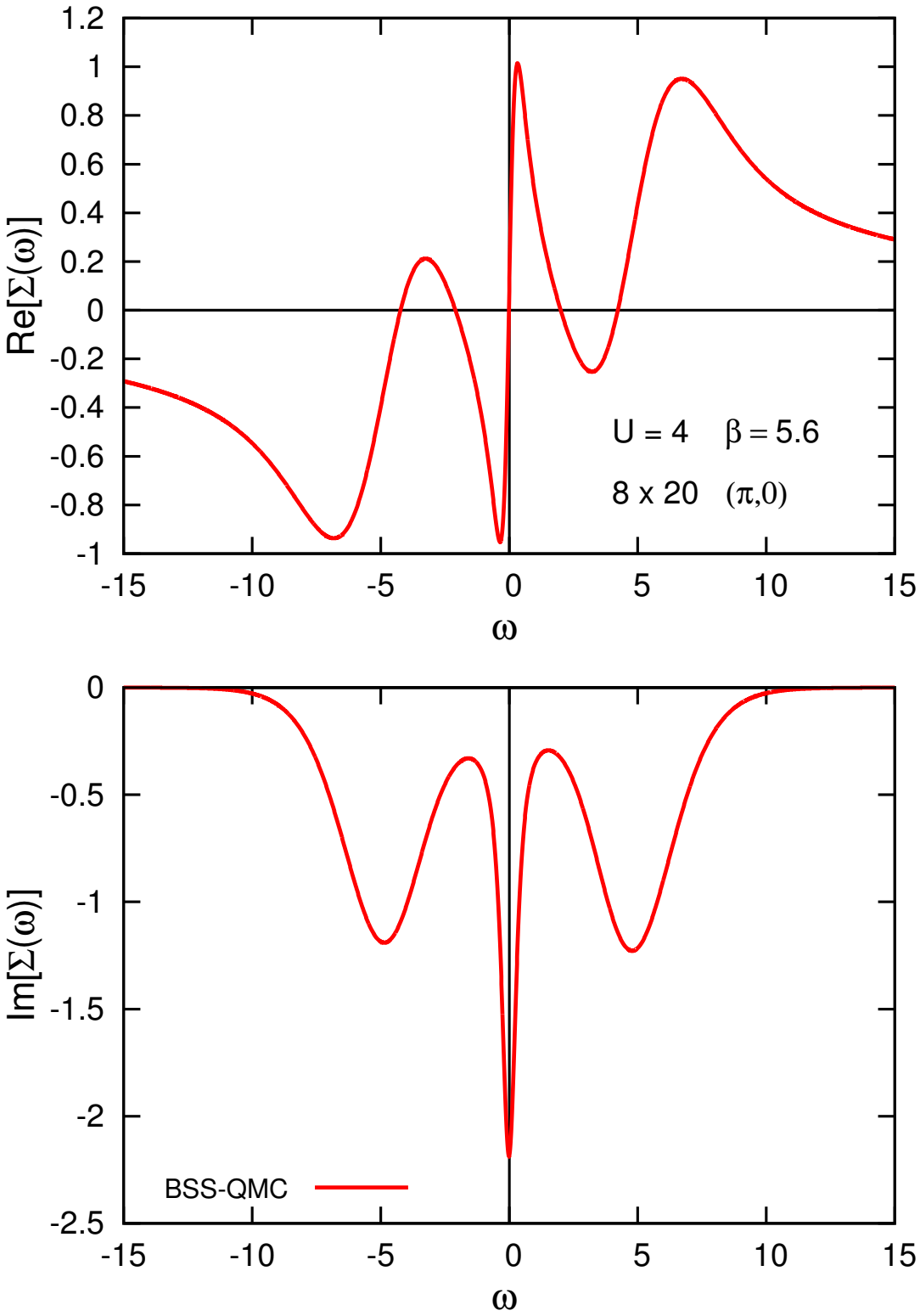

Figure B.2. – Analytical continued self-energy on the real-frequency axis, corresponding to the data shown in Fig. B.1.

Bibliography

[ADGS75] A A Abrikosov, I Dzyaloshinskii, L P Gorkov, and Richard A Silverman. *Methods of quantum field theory in statistical physics*. Dover, New York, NY, 1975.

[AFB14] Mohammad Zhian Asadzadeh, Michele Fabrizio, and Federico Becca. Superconductivity from spoiling magnetism in the Kondo lattice model. *Phys. Rev. B*, 90(20), Nov 2014.

[AFG10] N. P. Armitage, P. Fournier, and R. L. Greene. Progress and perspectives on electron-doped cuprates. *Rev. Mod. Phys.*, 82(3):2421–2487, Sep 2010.

[AIS97] F. Assaad, M. Imada, and D. Scalapino. Charge and spin structures of a dx2-y2 superconductor in the proximity of an antiferromagnetic Mott insulator. *Phys. Rev. B*, 56(23):15001–15014, Dec 1997.

[And61] P. W. Anderson. Localized Magnetic States in Metals. *Phys. Rev.*, 124:41–53, Oct 1961.

[ARH+03] F. F Assaad, V Rousseau, F Hebert, M Feldbacher, and G. G Batrouni. Spin and charge dynamics of stripes in doped Mott insulators. *Europhysics Letters (EPL)*, 63(4):569–575, Aug 2003.

[AS06] A. Altland and B. Simons. *Condensed Matter Field Theory*. Cambridge University Press, 2006.

[Ass99] F. Assaad. Quantum Monte Carlo Simulations of the Half-Filled Two-Dimensional Kondo Lattice Model. *Physical Review Letters*, 83(4):796–799, Jul 1999.

[Ass04] F. Assaad. Coherence scale of the two-dimensional Kondo lattice model. *Phys. Rev. B*, 70(2), Jul 2004.

[ATB12] R. T. Scalettar A. Tomas, C.-C. Chang and Z. Bai. Advancing Large Scale Many-Body QMC Simulations on GPU accelerated Multicore Systems. *IEEE International Symposium on Parallel & Distributed Processing (IPDPS)*, 2012.

[BCE+11] B Bauer, L D Carr, H G Evertz, A Feiguin, J Freire, S Fuchs, L Gamper, J Gukelberger, E Gull, S Guertler, and et al. The ALPS project release 2.0: open source software for strongly correlated systems. *Journal of Statistical Mechanics: Theory and Experiment*, 2011(05):P05001, May 2011.

[BCP08] Ralf Bulla, Theo Costi, and Thomas Pruschke. Numerical renormalization group method for quantum impurity systems. *Rev. Mod. Phys.*, 80(2):395–450, Apr 2008.

[Bel78] John B. Bell. *Mathematics of Computation*, 32(144):pp. 1320–1322, 1978.

[BG13] N. Blümer and E. V. Gorelik. Mott transitions in the half-filled SU($2M$) symmetric Hubbard model. *Phys. Rev. B*, 87:085115, Feb 2013.

[BGG00] S. Burdin, A. Georges, and D. Grempel. Coherence Scale of the Kondo Lattice. *Physical Review Letters*, 85(5):1048–1051, Jul 2000.

[Blo05] Immanuel Bloch. Ultracold quantum gases in optical lattices. *Nat Phys*, 1(1):23–30, Oct 2005.

[Blü02] N. Blümer. *Mott-Hubbard Metal-Insulator Transition and Optical Conductivity in High Dimensions.* PhD thesis, University of Augsburg, 2002.

[Blü08] N. Blümer. Multigrid Hirsch-Fye quantum Monte Carlo method for dynamical mean-field theory. *arXiv:0801.1222*, 2008.

[Bry90] R. Bryan. Maximum entropy analysis of oversampled data problems. *European Biophysics Journal*, 18:165–174, 1990.

[BSM08] Ilja N. Bronstein, Konstantin A. Semendjajew, and Gerhard Musiol. *Taschenbuch der Mathematik, m. CD-ROM.* Deutsch (Harri), 2008.

[BSS81] R. Blankenbecler, D. J. Scalapino, and R. L. Sugar. Monte Carlo calculations of coupled boson-fermion systems. I. *Phys. Rev. D*, 24:2278–2286, Oct 1981.

[BZV+13] Oliver Bodensiek, Rok Zitko, Matthias Vojta, Mark Jarrell, and Thomas Pruschke. Unconventional Superconductivity from Local Spin Fluctuations in the Kondo Lattice. *Physical Review Letters*, 110(14), Apr 2013.

[Cep80] D. M. Ceperley. Ground State of the Electron Gas by a Stochastic Method. *Physical Review Letters*, 45(7):566–569, Aug 1980.

[Che13] Kuang-Shing Chen. *Qunatum Simulations on square and triangular Hubbard models.* PhD thesis, Louisiana State University, 2013.

[CK94] Michel Caffarel and Werner Krauth. Exact diagonalization approach to correlated fermions in infinite dimensions: Mott transition and superconductivity. *Physical Review Letters*, 72(10):1545–1548, Mar 1994.

[CMY+13] Kuang Shing Chen, Zi Yang Meng, Unjong Yu, Shuxiang Yang, Mark Jarrell, and Juana Moreno. Unconventional superconductivity on the triangular lattice Hubbard model. *Phys. Rev. B*, 88(4), Jul 2013.

[CSGB13] Chia-Chen Chang, Richard T. Scalettar, Elena V. Gorelik, and Nils Blümer. Discriminating antiferromagnetic signatures in systems of ultracold fermions by tunable geometric frustration. *Phys. Rev. B*, 88(19), Nov 2013.

[Czy08] Gerd Czycholl. *Theoretische Festkörperphysik*. Springer Berlin / Heidelberg, 3 edition, 2008.

[DHJP13] Andreas Dirks, Jong E. Han, Mark Jarrell, and Thomas Pruschke. Imaginary-time quantum many-body theory out of equilibrium. II. Analytic continuation of dynamic observables and transport properties. *Phys. Rev. B*, 87(23), Jun 2013.

[Dir29] P. A. M. Dirac. Quantum Mechanics of Many-Electron Systems. *Proceedings of the Royal Society A: Mathematical, Physical and Engineering Sciences*, 123(792):714–733, Apr 1929.

[Don77] S. Doniach. The Kondo lattice and weak antiferromagnetism. *Physica B+C*, 91:231–234, Jul 1977.

[EBF+85] A.S. Edelstein, G.E. Brodale, R.A. Fisher, Carey M. Lisse, and Norman E. Philips. Crystal fields and the Kondo properties of CeAl3. *Solid State Communications*, 56(3):271–275, Oct 1985.

[FMNR01] W. Foulkes, L. Mitas, R. Needs, and G. Rajagopal. Quantum Monte Carlo simulations of solids. *Rev. Mod. Phys.*, 73(1):33–83, Jan 2001.

[FS91] R. Fye and D. Scalapino. Quantum Monte Carlo study of the one-dimensional symmetric Kondo lattice. *Phys. Rev. B*, 44(14):7486–7498, Oct 1991.

[FW71] A L Fetter and J D Walecka. *Quantum Theory of Many-Particle Systems*, volume 16. McGraw-Hill, 1971.

[FYC+11] H. Fotso, S. Yang, K. Chen, S. Pathak, J. Moreno, M. Jarrell, K. Mikelsons, E. Khatami, and D. Galanakis. Dynamical Cluster Approximation. *Springer Series in Solid-State Sciences*, page 271–302, Aug 2011.

[GB11] Elena V. Gorelik and Nils Blümer. Antiferromagnetism of Lattice Fermions in an Optical Trap: the Dynamical Mean-Field Perspective. *J Low Temp Phys*, 165(5-6):195–212, Sep 2011.

[Geb00] F. Gebhard. The Mott-Insulator Transition. *Springer Tracts in Modern Physics*, 137, 2000.

[GKKR96] Antoine Georges, Gabriel Kotliar, Werner Krauth, and Marcelo J. Rozenberg. Dynamical mean-field theory of strongly correlated fermion systems and the limit of infinite dimensions. *Rev. Mod. Phys.*, 68:13–125, Jan 1996.

[GME+02] Markus Greiner, Olaf Mandel, Tilman Esslinger, Theodor W. Hänsch, and Immanuel Bloch. Quantum phase transition from a superfluid to a Mott insulator in a gas of ultracold atoms. *Nature*, 415(6867):39–44, Jan 2002.

[GML+11] Emanuel Gull, Andrew J. Millis, Alexander I. Lichtenstein, Alexey N. Rubtsov, Matthias Troyer, and Philipp Werner. Continuous-time Monte Carlo methods for quantum impurity model. *Rev. Mod. Phys.*, 83(2):349–404, May 2011.

[GRP+12] E. V. Gorelik, D. Rost, T. Paiva, R. Scalettar, A. Klümper, and N. Blümer. Universal probes for antiferromagnetic correlations and entropy in cold fermions on optical lattices. *Phys. Rev. A*, 85,:061602(2012), January 2012.

[HF86] J. Hirsch and R. Fye. Monte Carlo Method for Magnetic Impurities in Metals. *Physical Review Letters*, 56(23):2521–2524, Jun 1986.

[HH04] Carsten Honerkamp and Walter Hofstetter. Ultracold Fermions and the SU(N) Hubbard Model. *Physical Review Letters*, 92(17), Apr 2004.

[Hir85] J. E. Hirsch. Two-dimensional Hubbard model: Numerical simulation study. *Phys. Rev. B*, 31:4403–4419, Apr 1985.

[Hir88] J. E. Hirsch. Stable monte carlo algorithm for fermion lattice systems at low temperatures. *Phys. Rev. B*, 38:12023–12026, Dec 1988.

[Hoh67] P. Hohenberg. Existence of Long-Range Order in One and Two Dimensions. *Phys. Rev.*, 158(2):383–386, Jun 1967.

[Hub59] J. Hubbard. Calculation of partition functions. *Phys. Rev. Lett.*, 3:77–78, Jul 1959.

[IFT98] Masatoshi Imada, Atsushi Fujimori, and Yoshinori Tokura. Metal-insulator transitions. *Rev. Mod. Phys.*, 70:1039–1263, Oct 1998.

[IYM+03] K Izawa, H Yamaguchi, Y Matsuda, H Shishido, R Settai, and Y Onuki. Gap structure and anomalous superconducting state of quasi-2D heavy-fermion CeCoIn5. *Physica C: Superconductivity*, 388-389:537–538, May 2003.

[JMHT01] M Jarrell, Th Maier, M. H Hettler, and A. N Tahvildarzadeh. Phase diagram of the Hubbard model: Beyond the dynamical mean field. *Europhysics Letters (EPL)*, 56(4):563–569, Nov 2001.

[Kad09] Leo P. Kadanoff. More is the Same; Phase Transitions and Mean Field Theories. *J Stat Phys*, 137(5-6):777–797, Sep 2009.

[KJMP05] P. Kent, M. Jarrell, T. Maier, and Th. Pruschke. Efficient calculation of the antiferromagnetic phase diagram of the three-dimensional Hubbard model. *Phys. Rev. B*, 72(6), Aug 2005.

[KKB+07] C. Krellner, N. Kini, E. Brüning, K. Koch, H. Rosner, M. Nicklas, M. Baenitz, and C. Geibel. CeRuPO: A rare example of a ferromagnetic Kondo lattice. *Phys. Rev. B*, 76(10), Sep 2007.

[KLB+10] E. Khatami, C. R. Lee, Z. J. Bai, R. T. Scalettar, and M. Jarrell. Cluster solver for dynamical mean-field theory with linear scaling in inverse temperature. *Phys. Rev. E*, 81:056703, May 2010.

[KMJ09] E. Khatami, A. Macridin, and M. Jarrell. Validity of the spin-susceptibility "glue" approximation for pairing in the two-dimensional Hubbard model. *Phys. Rev. B*, 80(17), Nov 2009.

[KmWW80] H. Krishna-murthy, J. Wilkins, and K. Wilson. Renormalization-group approach to the Anderson model of dilute magnetic alloys. II. Static properties for the asymmetric case. *Phys. Rev. B*, 21(3):1044–1083, Feb 1980.

[Koc11] E. Koch. *The LDA+DMFT approach to strongly correlated materials, ch. 8*. Schriften des FZ Jülich, 2011.

[Kon64] J. Kondo. Resistance Minimum in Dilute Magnetic Alloys. *Progress of Theoretical Physics*, 32(1):37–49, Jul 1964.

[Kra27] H. A. Kramers. La diffusion de la lumiere par les atomes. *Atti Congr. Intern. Fisica*, pages 545–557, 1927.

[Kro26] R. De L. Kronig. On the Theory of Dispersion of X-Rays. *Journal of the Optical Society of America*, 12(6):547, 1926.

[KS54] G. Koster and J. Slater. Wave Functions for Impurity Levels. *Phys. Rev.*, 95(5):1167–1176, Sep 1954.

[KSG08] Erik Koch, Giorgio Sangiovanni, and Olle Gunnarsson. Sum rules and bath parametrization for quantum cluster theories. *Phys. Rev. B*, 78(11), Sep 2008.

[KV04] Gabriel Kotliar and Dieter Vollhardt. Strongly correlated materials: Insights from dynamical mean-field theory. *Phys. Today*, 57(3):53–59, Mar 2004.

[LAN+12] D. J. Luitz, F. F. Assaad, T. Novotný, C. Karrasch, and V. Meden. Understanding the Josephson Current through a Kondo-Correlated Quantum Dot. *Physical Review Letters*, 108(22), May 2012.

[LGS+90] E. Loh, J. Gubernatis, R. Scalettar, S. White, D. Scalapino, and R. Sugar. Sign problem in the numerical simulation of many-electron systems. *Phys. Rev. B*, 41(13):9301–9307, May 1990.

[Li13] Gang Li. Kondo lattice model: from local to non-local descriptions. *arXiv:1309.0156*, 2013.

[LP00] R. B. Laughlin and D. Pines. The Theory of Everything. *Proceedings of the National Academy of Sciences*, 97(1):28–31, Jan 2000.

[LPA+09] Yaohang Li, Vladimir A. Protopopescu, Nikita Arnold, Xinyu Zhang, and Andrey Gorin. Hybrid parallel tempering and simulated annealing method. *Applied Mathematics and Computation*, 212(1):216–228, Jun 2009.

[Lut60] J. M. Luttinger. Fermi Surface and Some Simple Equilibrium Properties of a System of Interacting Fermions. *Phys. Rev.*, 119(4):1153–1163, Aug 1960.

[Lut61] J. M. Luttinger. Analytic Properties of Single-Particle Propagators for Many-Fermion Systems. *Phys. Rev.*, 121(4):942–949, Feb 1961.

[LW06] Patrick A. Lee and Xiao-Gang Wen. Doping a Mott insulator: Physics of high-temperature superconductivity. *Rev. Mod. Phys.*, 78(1):17–85, Jan 2006.

[LW07] Hilbert v. Löhneysen and Peter Wölfle. Fermi-liquid instabilities at magnetic quantum phase transitions. *Rev. Mod. Phys.*, 79(3):1015–1075, Jul 2007.

[MA08] L. C. Martin and F. F. Assaad. Evolution of the Fermi Surface across a Magnetic Order-Disorder Transition in the Two-Dimensional Kondo Lattice Model: A Dynamical Cluster Approach. *Physical Review Letters*, 101(6), Aug 2008.

[MGW+03] Olaf Mandel, Markus Greiner, Artur Widera, Tim Rom, Theodor W. Hänsch, and Immanuel Bloch. Controlled collisions for multi-particle entanglement of optically trapped atoms. *Nature*, 425(6961):937–940, Oct 2003.

[MH89a] E. Müller-Hartmann. Correlated fermions on a lattice in high dimensions. *Z. Physik B - Condensed Matter*, 74(4):507–512, Dec 1989.

[MH89b] E. Müller-Hartmann. The Hubbard model at high dimensions: some exact results and weak coupling theory. *Z. Physik B - Condensed Matter*, 76(2):211–217, Jun 1989.

[MJPH05] Thomas Maier, Mark Jarrell, Thomas Pruschke, and Matthias Hettler. Quantum cluster theories. *Rev. Mod. Phys.*, 77(3):1027–1080, Oct 2005.

[Mot68] N. F. Mott. Metal-Insulator Transition. *Rev. Mod. Phys.*, 40(4):677–683, Oct 1968.

[MRR+53] Nicholas Metropolis, Arianna W. Rosenbluth, Marshall N. Rosenbluth, Augusta H. Teller, and Edward Teller. Equation of State Calculations by Fast Computing Machines. *The Journal of Chemical Physics*, 21(6):1087, 1953.

[MV89] Walter Metzner and Dieter Vollhardt. Correlated Lattice Fermions in $d = \infty$ Dimensions. *Phys. Rev. Lett.*, 62:324–327, Jan 1989.

[MW66] N. D. Mermin and H. Wagner. Absence of Ferromagnetism or Antiferromagnetism in One- or Two-Dimensional Isotropic Heisenberg Models. *Physical Review Letters*, 17(22):1133–1136, Nov 1966.

[NRLC97] M.Dolore Núñez-Regueiro, C. Lacroix, and B. Canals. Magnetic ordering in the frustrated Kondo lattice compound CePdAl. *Physica C: Superconductivity*, 282-287:1885–1886, Aug 1997.

[PAD03] M. Potthoff, M. Aichhorn, and C. Dahnken. Variational Cluster Approach to Correlated Electron Systems in Low Dimensions. *Physical Review Letters*, 91(20), Nov 2003.

[Pfl09] Christian Pfleiderer. Superconducting phases of f-electron compounds. *Rev. Mod. Phys.*, 81(4):1551–1624, Oct 2009.

[PHK08] H. Park, K. Haule, and G. Kotliar. Cluster Dynamical Mean Field Theory of the Mott Transition. *Physical Review Letters*, 101(18), Oct 2008.

[PTVF07] William H. Press, Saul A. Teukolsky, William T. Vetterling, and Brian P. Flannery. *Numerical Recipes 3rd Edition: The Art of Scientific Computing*. Cambridge University Press, New York, NY, USA, 3 edition, 2007.

[PWN97] M. Potthoff, T. Wegner, and W. Nolting. Interpolating self-energy of the infinite-dimensional Hubbard model: Modifying the iterative perturbation theory. *Phys. Rev. B*, 55(24):16132–16142, Jun 1997.

[RAB13] D. Rost, F. Assaad, and N. Blümer. Quasi-continuous-time impurity solver for the dynamical mean-field theory with linear scaling in the inverse temperature. *Phys. Rev. E*, 87(5), May 2013.

[RB15] D. Rost and N. Blümer. Deciding the fate of the false Mott transition in two dimensions by exact quantum Monte Carlo methods. *arXiv:1504.05090*, 2015.

[RGAB12] D. Rost, E. V. Gorelik, F. Assaad, and N. Blümer. Momentum-dependent pseudogaps in the half-filled two-dimensional Hubbard model. *Phys. Rev. B*, 86(15), Oct 2012.

[RK54] M. A. Ruderman and C. Kittel. Indirect Exchange Coupling of Nuclear Magnetic Moments by Conduction Electrons. *Phys. Rev.*, 96(1):99–102, Oct 1954.

[RKL08] A. Rubtsov, M. Katsnelson, and A. Lichtenstein. Dual fermion approach to nonlocal correlations in the Hubbard model. *Phys. Rev. B*, 77(3), Jan 2008.

[Ros12] Daniel Rost. Effiziente Quanten-Monte-Carlo-Berechnungen von Green-Funktionen und Spektren korrelierter Elektronensysteme. diploma thesis, Johannes-Gutenberg Universität, Mainz, 2012.

[SAB+79] F. Steglich, J. Aarts, C. Bredl, W. Lieke, D. Meschede, W. Franz, and H. Schäfer. Superconductivity in the Presence of Strong Pauli Paramagnetism: $CeCu_2Si_2$. *Physical Review Letters*, 43(25):1892–1896, Dec 1979.

[Sca06] D. J. Scalapino. The 2D Hubbard Model and the High Tc Cuprate Problem. *J Supercond*, 19(3-5):195–200, Dec 2006.

[Sch26] E. Schrödinger. Quantisierung als Eigenwertproblem. *Annalen der Physik*, 384(4):361–376, 1926.

[Sch05] U. Schollwöck. The density-matrix renormalization group. *Rev. Mod. Phys.*, 77(1):259–315, Jan 2005.

[Sch08] Franz Schwabl. *Quantenmechanik für Fortgeschrittene (QM II) (Springer-Lehrbuch) (German Edition)*. Springer, 5., erw. u. aktualisierte aufl. edition, September 2008.

[SGR+15] T. Schäfer, F. Geles, D. Rost, G. Rohringer, E. Arrigoni, K. Held, N. Blümer, M. Aichhorn, and A. Toschi. Fate of the false Mott-Hubbard transition in two dimensions. *Phys. Rev. B*, 91(12), Mar 2015.

[Sha48] C. E. Shannon. A Mathematical Theory of Communication. *Bell System Technical Journal*, 27(3):379–423, Jul 1948.

[SMS13] Peter Staar, Thomas Maier, and Thomas C. Schulthess. Dynamical cluster approximation with continuous lattice self-energy. *Phys. Rev. B*, 88(11), Sep 2013.

[SSST87] R. T. Scalettar, D. J. Scalapino, R. L. Sugar, and D. Toussaint. Hybrid molecular-dynamics algorithm for the numerical simulation of many-electron systems. *Phys. Rev. B*, 36:8632–8641, Dec 1987.

[STT15] T. Schäfer, A. Toschi, and Jan M. Tomczak. Separability of dynamical and nonlocal correlations in three dimensions. *Phys. Rev. B*, 91(12), Mar 2015.

[SU91] Manfred Sigrist and Kazuo Ueda. Phenomenological theory of unconventional superconductivity. *Rev. Mod. Phys.*, 63(2):239–311, Apr 1991.

[Suz76] Masuo Suzuki. Relationship between d-Dimensional Quantal Spin Systems and $(d+1)$-Dimensional Ising Systems. *Progress of Theoretical Physics*, 56(5):1454–1469, 1976.

[SWGK11] Michael Sentef, Philipp Werner, Emanuel Gull, and Arno P. Kampf. Superconducting Phase and Pairing Fluctuations in the Half-Filled Two-Dimensional Hubbard Model. *Physical Review Letters*, 107(12), Sep 2011.

[TKH07] A. Toschi, A. Katanin, and K. Held. Dynamical vertex approximation: A step beyond dynamical mean-field theory. *Phys. Rev. B*, 75(4), Jan 2007.

[VZN04] M. Vogt, R. Zimmermann, and R. J. Needs. Spectral moments in the homogeneous electron gas. *Phys. Rev. B*, 69(4), Jan 2004.

[Wan37] Gregory Wannier. The Structure of Electronic Excitation Levels in Insulating Crystals. *Phys. Rev.*, 52(3):191–197, Aug 1937.

[WCdM+06] Philipp Werner, Armin Comanac, Luca de' Medici, Matthias Troyer, and Andrew Millis. Continuous-Time Solver for Quantum Impurity Models. *Physical Review Letters*, 97(7), Aug 2006.

[Wei07] P. Weiss. L'hypothèse du champ moléculaire et la propriété ferromagnétique. *J. de Phys. Rad. 6, 661-690*, 1907.

[WES+11] Christof Weitenberg, Manuel Endres, Jacob F. Sherson, Marc Cheneau, Peter Schauß, Takeshi Fukuhara, Immanuel Bloch, and Stefan Kuhr. Single-spin addressing in an atomic Mott insulator. *Nature*, 471(7338):319–324, Mar 2011.

[WH93] Steven White and David Huse. Numerical renormalization-group study of low-lying eigenstates of the antiferromagnetic S=1 Heisenberg chain. *Phys. Rev. B*, 48(6):3844–3852, Aug 1993.

[Whi92] Steven R. White. Density matrix formulation for quantum renormalization groups. *Physical Review Letters*, 69(19):2863–2866, Nov 1992.

[Wic50] G. C. Wick. The Evaluation of the Collision Matrix. *Phys. Rev.*, 80(2):268–272, Oct 1950.

[Wil75] Kenneth Wilson. The renormalization group: Critical phenomena and the Kondo problem. *Rev. Mod. Phys.*, 47(4):773–840, Oct 1975.

[WJdHvdB34] J. H. de Boer W. J. de Haas and G. J. van de Berg. The electrical resistance of gold, copper and lead at low temperatures. *Physica (Utrecht)*, 1934.

[WM06] Philipp Werner and Andrew Millis. Hybridization expansion impurity solver: General formulation and application to Kondo lattice and two-orbital models. *Phys. Rev. B*, 74(15), Oct 2006.

List of Publications

Selected parts of this thesis have been published in:

D. Rost, E.V. Gorelik, F.F. Assaad, and N. Blümer, *"Momentum-dependent pseudogaps in the half-filled two-dimensional Hubbard model"*, Phys. Rev. B **86**, 155109 (2012).

D. Rost, F.F. Assaad, and N. Blümer, *"Quasi-continuous-time impurity solver for the dynamical mean-field theory with linear scaling in the inverse temperature"*, Phys. Rev. E **87**, 053305 (2013).

T. Schäfer, F. Geles, D. Rost, G. Rohringer, E. Arrigoni, K. Held, N. Blümer, M. Aichhorn, and A. Toschi, *"Fate of the false Mott-Hubbard transition in two dimensions"*, Phys. Rev. B **91**, 155109 (2015).

D. Rost and N. Blümer, *"Deciding the fate of the false Mott transition in two dimensions by exact quantum Monte Carlo methods"*, arXiv:1504.05090 (2015) (to be published in Journal of Physics: Conference Series).

Curriculum Vitae

Personal Information

Name	Daniel Christopher Rost
Date of birth	04.10.1985, Wiesbaden-Dotzheim
Nationality	German

Education

Since 05/2012	PhD student at the group of Prof. Dr. Nils Blümer
05/2012	Diploma in physics (Grade: 1.0)
05/2011 - 05/2012	Diploma student at the group of Prof. Dr. Nils Blümer
07/2009 - 03/2010	Studies of physics, Linköpings Universitet, Sweden
10/2006 - 05/2012	Studies of physics, Universität Mainz
06/2005	Abitur
1996 - 2005	Gutenberg-Gymnasium Wiesbaden

Employments

10/2006 – now	Self-employed Webdesigner
04/2009 – 05/2012	Student Research Assistant
11/2005 – 07/2006	Civilian national service at Lebenshilfe Wiesbaden e.V.

Scholarships

07/2011 - 12/2011	Scholarship of the Stipendienstiftung Rheinland-Pfalz
Since 01/2013	Member of excellence graduate school Materials-Science-in-Mainz
Since 04/2014	Juniormembership of the Gutenbergakademie

Languages

German - native speaker
English - fluent
Swedish - basic

Momentum-dependent pseudogaps in the half-filled two-dimensional Hubbard model

D. Rost,[1] E. V. Gorelik,[1] F. Assaad,[2] and N. Blümer[1]
[1]*Institute of Physics, Johannes Gutenberg University, Mainz, Germany*
[2]*Institute of Theoretical Physics and Astrophysics, University of Würzburg, Würzburg, Germany*
(Received 13 June 2012; revised manuscript received 1 August 2012; published 4 October 2012)

We compute unbiased spectral functions of the two-dimensional Hubbard model by extrapolating Green functions, obtained from determinantal quantum Monte Carlo simulations, to the thermodynamic and continuous time limits. Our results clearly resolve the pseudogap at weak to intermediate coupling, originating from a momentum selective opening of the charge gap. A characteristic pseudogap temperature T^*, determined consistently from the spectra and from the momentum dependence of the imaginary-time Green functions, is found to match the dynamical mean-field critical temperature, below which antiferromagnetic fluctuations become dominant. Our results identify a regime where pseudogap physics is within reach of experiments with cold fermions on optical lattices.

DOI: 10.1103/PhysRevB.86.155109 PACS number(s): 71.10.Fd, 71.27.+a, 71.30.+h, 74.72.−h

I. INTRODUCTION

A peculiar feature of (underdoped) high-T_c superconductors is the coupling of antiferromagnetic fluctuations to charge degrees of freedom, which leads to a strong momentum dependence of the spectral functions. In particular, it induces pseudogaps in the normal state, i.e., a suppression of the density of states at the Fermi energy, which can be probed using (angular resolved) photoemission, inverse photoemission, and related techniques. The pseudogap shares the d-wave symmetry with the order parameter of the superconducting phases occurring at low temperatures and near optimal doping.[1–3]

Pseudogap physics can also be expected in the undoped Hubbard model. In the absence of electronic correlations, the tight binding model is characterized by a coherence temperature T_{coh}, set by the bandwidth W. For weak Hubbard interaction $U \lesssim W$, antiferromagnetic spin fluctuations, with energy scale T_{spin}, will develop below the coherence temperature. Hence, the temperature window $T_N < T < T_{\mathrm{spin}} < T_{\mathrm{coh}}$ is characterized by a metallic state coupled to antiferromagnetic fluctuations, which sets the stage for pseudogap physics. Here T_N is the Néel temperature, at or below which long range order generates a full gap in the presence of perfect nesting (in dimensions $d \geqslant 2$, with $T_N = 0$ in $d = 2$).

Theorists have tried to verify this scenario on the basis of numerical simulations and to compute reliable spectra for decades. Direct simulations can only be performed for clusters of finite extent, usually employing periodic boundary conditions. Early determinantal quantum Monte Carlo[4] (DQMC) studies at moderately weak coupling ($U/t = 4$) led to spectra with significant low-temperature pseudogap features only for small cluster sizes; thus, pseudogaps in the undoped $2d$ Hubbard model were regarded as pure finite-size (FS) artifacts.[5,6] Later studies at similar coupling strengths[7–10] found pseudogaps also at large cluster sizes, but did not allow for quantitative predictions in the thermodynamic limit. A recent study using the dynamical vertex approximation (DΓA) observed reentrant behavior incompatible with the earlier results.[11]

A central limitation of all previous numerical pseudogap studies is that results for different cluster sizes (e.g., in DQMC simulations) were compared only at fixed temperatures and at the level of spectral functions. With increasing cluster size, these show diverse effects: shifts of spectral peaks, transfer of spectral weight, and the opening or closing of gaps. A direct *pointwise* extrapolation of these positive semidefinite and normalized functions is clearly impossible. In fact, we are not aware of any published attempts of deriving spectral properties in the thermodynamic limit from DQMC data in any context.

In this paper, we present (i) the local spectral function, (ii) momentum-resolved spectral functions at high-symmetry points, and (iii) momentum-resolved spectral functions along high-symmetry lines of the Brillouin zone in the thermodynamic limit. All results are based on FS extrapolations of imaginary-time Green functions, obtained from DQMC, with subsequent analytic continuation to the real axis using the maximum entropy method (MEM)[12] and, in case (iii), a Fourier fit of the momentum dependence. The final results are free of significant systematic errors and represent the thermodynamic and continuous time limits in an unbiased way.

Thereby, we can not only unambiguously confirm the pseudogap scenario and study the nodal-antinodal dichotomy in unprecedented detail, but also explore the temperature dependence of the pseudogap opening and identify a characteristic temperature T^*. At weak to intermediate couplings, T^* tracks the onset of short-ranged magnetic fluctuations, and is equally shown to compare remarkably well with the dynamical mean-field critical temperature for antiferromagnetic long-range order.

In Sec. II, we introduce the model, set up our notation, characterize the established methods (DQMC, MEM) underlying our approach, and specify our implementations. The new methods for eliminating systematic biases from Green function and spectra are, then, presented in Sec. III, first for the DQMC Trotter error, then for finite-size effects. Our main results are discussed in Sec. IV, starting with pseudogap features in the spectral functions for the "nodal" and "antinodal"[13] high-symmetry $\mathbf{k}$ points on the Fermi surface and their evolution as a function of temperature. We then show, with continuous momentum resolution, how the pseudogap evolves throughout the Brillouin zone (BZ) and discuss non-Fermi liquid physics that is not accessible by conventional methods. Finally, we

determine the characteristic pseudogap temperature T^* for $U \leqslant W$ and relate it to spin correlation functions and other characteristic temperature scales of the model.

II. MODEL AND CONVENTIONAL METHODS

A. Hubbard model

Our starting point is the single-band Hubbard Hamiltonian with nearest-neighbor hopping t on a square lattice (with unit lattice spacing $a \equiv 1$):

$$\hat{H} = \hat{H}_0 + U \sum_i \hat{n}_{i\uparrow} \hat{n}_{i\downarrow} \tag{1}$$

$$\hat{H}_0 = -t \sum_{\langle ij \rangle, \sigma} \hat{c}^\dagger_{i\sigma} \hat{c}_{j\sigma} = \sum_{\mathbf{k},\sigma} \varepsilon_{\mathbf{k}} \hat{n}_{\mathbf{k}\sigma} \tag{2}$$

$$\varepsilon_{\mathbf{k}} = -2t[cos(k_x) + cos(k_y)]. \tag{3}$$

Here, $\hat{c}_{i\sigma}$ ($\hat{c}^\dagger_{i\sigma}$) are annihilation (creation) operators for a fermion with spin $\sigma \in \{\uparrow, \downarrow\}$ at site i; $\hat{n}_{i\sigma} = \hat{c}^\dagger_{i\sigma} \hat{c}_{i\sigma}$. In the following, the energy scale will be set by $t \equiv 1$.

At half filling $n \equiv \langle \hat{n}_{i\uparrow} + \hat{n}_{i\downarrow} \rangle = 1$ and in the noninteracting limit $U = 0$, the occupied momentum states form a square (dark shaded) within the square Brillouin zone illustrated in Fig. 1(a) (in the thermodynamic limit), which implies a perfect nesting instability: The Fermi surface (gray line) transforms into itself when shifted by the antiferromagnetic wave vector (π,π). As a consequence, any finite interaction $U > 0$ drives this model to long-range antiferromagnetic order (only) in the ground state.

While a conventional notation is well established for the center $\mathbf{\Gamma}$ and the corner $\mathbf{M}$ of the BZ of the square lattice as well as for the antinodal $\mathbf{X}$ point, this seems not to be the case for the nodal point; in Fig. 1 and in the following, we denote this midpoint of $\overline{\mathbf{\Gamma M}}$ as $\mathbf{M}'$.

B. Determinantal quantum Monte Carlo algorithm

The Hubbard model, Eq. (1), is solved in this work for clusters with a finite number N of sites [implying a discrete momentum grid, see Fig. 1(b)] at finite temperatures T using the DQMC algorithm developed by Blankenbecler, Scalapino, and Sugar,[4] with modifications by Hirsch.[14] It is based on (i) a uniform discretization of the imaginary-time interval $0 \leqslant \tau \leqslant \beta$ [with $\beta = 1/(k_B T)$], occurring in the path integral, into Λ time slices of width $\Delta\tau = \beta/\Lambda$, (ii) a Trotter decoupling of kinetic and interaction terms, and (iii) a Hubbard-Stratonovich transformation which replaces the electron-electron interaction at each time slice and site by the coupling of the electrons to a binary auxiliary field. Expectation values are obtained by Monte Carlo importance sampling of field configurations, with weights given by a product of two determinants for the two spin components. In the particle-hole symmetric case considered in this study, this product is always positive, i.e., the sign problem is absent. The numerical effort scales as βN^3. A detailed review of the algorithm used can be found in Ref. 15.

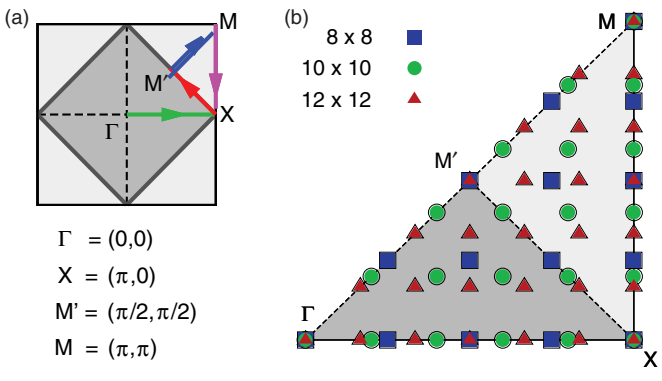

FIG. 1. (Color online) Brillouin zone (BZ) of the square lattice: (a) full BZ with Fermi surface (gray line) and occupied momenta in thermodynamic limit (dark shaded) at $U = 0$; letters denote high-symmetry points; color lines and arrows indicate the path used in Fig. 9. (b) Irreducible wedge of BZ with momenta occurring in finite-size clusters of linear dimension $L = 8, 10, 12$ with periodic boundary conditions.

In this work, we obtained imaginary-time Green functions and spin correlation functions between each pair of sites by applying the DQMC method to square lattice clusters $L \times L$ of the linear size $L = 8, 10, 12, 14, 16$ with periodic boundary conditions, using a set of Trotter discretizations with $0.1 \leqslant \Delta\tau \leqslant 0.42$ and typically 50 bins with 5000 sweeps over the auxiliary field each. For the largest systems, individual runs took about a month of computer time; up to five such runs were averaged over in order to reduce error bars. This resulted in typical statistical errors in the (finite-size) Green functions of $\mathcal{O}(10^{-4})$. Note that the DQMC scaling with L^6 makes it difficult to access much larger system sizes directly: $L = 20$ ($L = 32$) would increase the effort by a factor of about 4 (64) compared to $L = 16$. Local properties were averaged over all sites, momentum ($\mathbf{k}$) dependent properties were obtained by Fourier transforms of the real-space measurements.

C. Maximum entropy method

Since DQMC calculations provide Green functions G (and correlation functions) only at imaginary times, their interpretation as dynamical information requires an analytic continuation to the real axis. Specifically, one has to invert relations of the form

$$G(\tau) = -\int_{-\infty}^{\infty} d\omega\, A(\omega) \frac{e^{-\tau\omega}}{1 + e^{-\beta\omega}},$$

where $A(\omega) = -\mathrm{Im}\, G(\omega)/\pi$ is the corresponding spectral function. This is an ill-posed problem, as the exponential kernel suppresses the impact of features in $A(\omega)$ at large $|\omega|$ on $G(\tau)$; in the DQMC context, further complications arise from the fact that G is only measured on the discrete imaginary-time grid $\{\tau_l = l\Delta\tau\}_{l=0}^{\Lambda-1}$. The MEM finds the most probable spectrum, given the data $\bar{G}_l \pm \Delta G_l$, by balancing the misfit of a given candidate spectrum (measured by the corresponding χ^2) with an entropy constraint which favors smooth spectra.[12,16] In our implementation, the resulting minimization problem is solved deterministically using a Newton scheme in the singular space of the kernel. Its application both to DQMC raw data for local and $\mathbf{k}$ dependent Green functions and to Green functions obtained from Trotter and/or FS extrapolations always resulted in reliable and consistent maximum entropy spectra.

III. EXTRACTION OF UNBIASED SPECTRA IN THE THERMODYNAMIC LIMIT

What sets our main results, to be presented in Sec. IV, apart from earlier work, is their direct relevance in the thermodynamic limit, i.e., the absence of significant bias. We now specify our methodology for eliminating Trotter and finite-size errors from Green functions and establish its accuracy and reliability on the level of Green functions and spectra.

A. Trotter errors and extrapolation $\Delta\tau \to 0$

As discussed in subsection II B, the DQMC method decouples electronic interactions (and evaluates, e.g., Green functions) at the cost of introducing an artificial imaginary-time discretization $\Delta\tau$, which implies an unphysical bias in all DQMC estimates of observables. In the absence of phase transitions, DQMC raw results are expected (and observed) to depend smoothly on $\Delta\tau$, in the form of a power series; for some static observables, such as the total energy, it is easy to prove[17] polynomial dependence on $\Delta\tau^2$.

The effects of the Trotter discretization on the imaginary-time Green function $G(\tau)$ are illustrated in Fig. 2(a): (i) each of the raw data sets (symbols) lives on a different τ grid; (ii) at fixed values of τ, the data (or a linear interpolation—dashed/dotted lines) is shifted to smaller absolute values at larger $\Delta\tau$. Obviously, unbiased results (for a fixed cluster size L in real space) can only be expected after an extrapolation of $\Delta\tau \to 0$. On the other hand, such an extrapolation is not possible locally, i.e., at fixed τ, but requires a global approach that can use input from DQMC raw data at all discretizations $\Delta\tau$ for each imaginary time τ of interest.

The black solid lines in Fig. 2(a) represent the result of a multigrid procedure, originally developed in the context of the Hirsch-Fye quantum Monte Carlo method for the Anderson impurity model.[18] The multigrid method is based on the fact that "reference" Green functions $G_{\rm ref}(\tau)$ with sufficiently accurate asymptotics at $\tau \to 0$ (and $\tau \to \beta$), in particular for the curvature, can easily be derived from weak-coupling expansions (or, alternatively, from the "best" QMC data via MEM); consequently, the difference between the measured Green functions $G_{\Delta\tau}(\tau_i)$ and the reference $G_{\rm ref}(\tau_i)$ can be adequately represented by a natural cubic spline for each value of $\Delta\tau$; all of these splines can, then, be evaluated on a common (fine) grid. For this transformed data, we find a nearly linear dependence on $\Delta\tau^2$ (plus a small curvature), so that pointwise extrapolations $\Delta\tau \to 0$ are reliable and accurate. At the level of G, the shift of the unbiased result [black solid line in Fig. 2(a)] of about 10^{-3} compared to the best raw data [at $\Delta\tau = 0.1$, squares and dash-dotted line in Fig. 2(a)] is still significant.

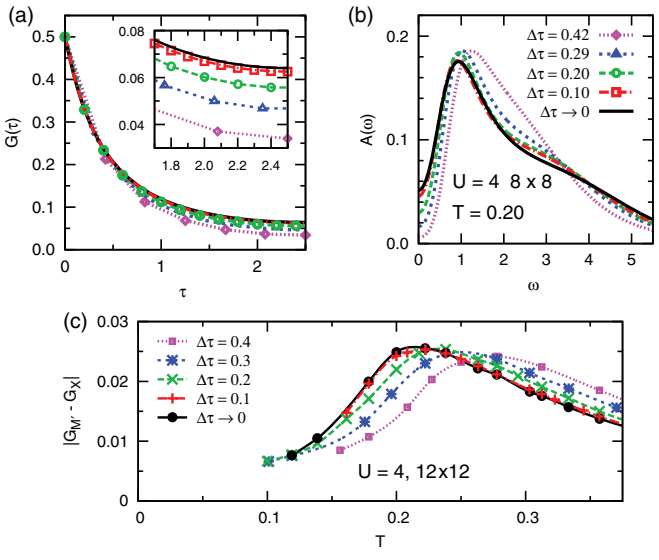

FIG. 2. (Color online) Impact of Trotter discretization and extrapolation of $\Delta\tau \to 0$: (a) for local imaginary-time Green functions $G(\tau)$ at $U = 4$, $T = 0.20$, $L = 8$ in the range $0 \leqslant \tau \leqslant \beta/2 = 2.5$ (inset: magnified view for $\tau \geqslant 1.7$); (b) corresponding local spectral functions $A(\omega)$. (c) for the difference between nodal and antinodal Green functions (cf. subsection IV C) versus temperature.

This is no longer true on the level of spectra, shown in Fig. 2(b), due to the intrinsic complications of MEM: The results for $\Delta\tau = 0.1$ agree within accuracy with the unbiased spectrum. Thus, we may conclude that $\Delta\tau = 0.1$ is "good enough" for spectral data (at $U = 4$) and that an elimination of the Trotter error is not necessary for reducing unphysical bias below significance. At the same time, the smooth consistent evolution of the spectra with $\Delta\tau$ confirms our MEM procedure both for the DQMC raw data and for extrapolated Green functions.

Even smaller Trotter errors than observed in Fig. 2(a) can be expected for differences of Green functions, due to error cancellation. Indeed, the scalar pseudogap measure $|G_{\mathbf{M}'} - G_{\mathbf{X}}|$, to be introduced in subsection IV C, is impacted significantly by Trotter errors only for large discretizations; the bias become negligible for $\Delta\tau \lesssim 0.1$, as shown in Fig. 2(c). Therefore an explicit elimination of this error is, again, not necessary.

B. Finite-size extrapolations of local spectra and on high-symmetry k points in the BZ

A FS extrapolation of local properties or **k** resolved properties at high-symmetry points is relatively straightforward: One accumulates raw data at various values of the linear extent L and then extrapolates using polynomial least-square fits in $1/L^2$. In the case of imaginary-time Green functions, independent extrapolations have to be performed for each value of τ (on the grid with spacing $\Delta\tau$ in the case of DQMC raw data or the grid chosen in the extrapolation $\Delta\tau \to 0$ discussed in the previous section). As shown in Fig. 3 for $U = 4$, $T = 0.2$, the Green function depends on system size quite significantly at generic imaginary times [except for the limits $\tau \to 0$ or, equivalently, $\tau \to \beta$ (not shown)] both at the antinodal (a) and nodal (b) momentum points. At the same time, the dependence is quite regular so that least-square extrapolations (lines) can be restricted to low orders.

Obviously, this "local" procedure can only include lattice sizes for which the **k** point under consideration exists [cf. Fig. 1(b)]; for the antinodal point, this requirement is fulfilled for all even values of L, while the nodal $\mathbf{M}'$ point is only present if L is a multiple of 4 (which restricts the set to $L = 8, 12, 16$ in our study). Still, as seen in Fig. 3(b), the extrapolation

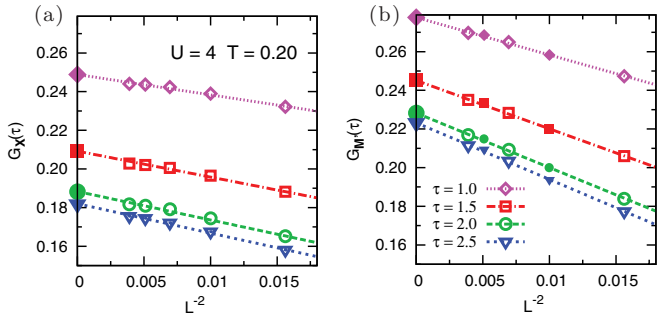

FIG. 3. (Color online) Imaginary-time Green functions (for selected values of τ) versus squared inverse linear dimension (empty symbols) and least-squares extrapolation $L \to \infty$ (lines and large full symbols) at high-symmetry momentum points: (a) at antinodal $\mathbf{X}$ point, (b) at nodal $\mathbf{M}'$ point (small symbols for $L = 10,14$: from Fourier fit as shown in Fig. 5).

is reliable even with only three data points (per fit), as the dependence is almost perfectly linear.[19] At the same time, the FS extrapolation is particularly important at the nodal $\mathbf{M}'$ point, as FS effects are much stronger than in the antinodal case [shown in Fig. 3(a)].

Note that 4×4 clusters (with periodic boundary conditions) have a special symmetry: They have the same topology as a $2 \times 2 \times 2 \times 2$ hypercube with open boundary conditions; as a consequence, the next-nearest neighbors along one of the axes and the ones along the diagonal become equivalent, which implies that the $\mathbf{X}$ and $\mathbf{M}'$ points are identical in momentum space at $L = 4$. In order to avoid the associated extra bias we exclude this system size and consider only lattices with $L \geqslant 8$ in this study.

The full resulting Green functions in the thermodynamic limit are shown as solid lines in Fig. 4 for the antinodal (a) and

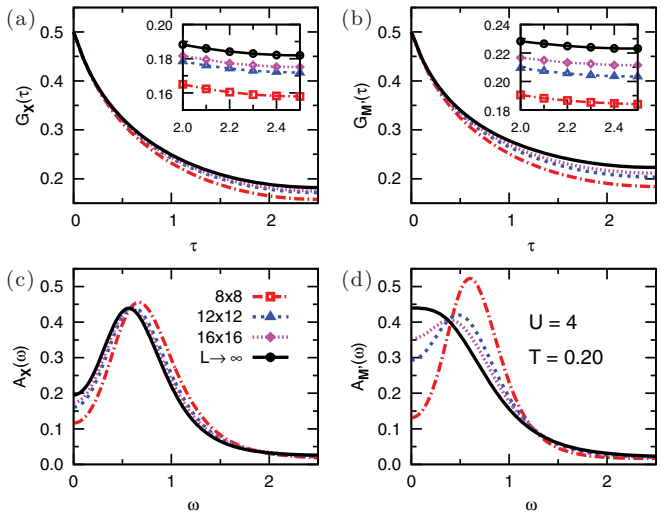

FIG. 4. (Color online) Upper row: imaginary-time DQMC Green functions ($U = 4$, $T = 0.2$, $\Delta\tau = 0.1$) at antinodal (a) and nodal (b) points, respectively, for finite-size clusters (open symbols and broken lines) plus extrapolated (cf. Fig. 3) results in thermodynamic limit (filled circles and solid lines). Lower row: corresponding spectral functions.

nodal (b) $\mathbf{k}$ points, respectively, together with their finite-size equivalents (dashed and dotted lines).

We see, again, that FS effects are much more prominent at $\mathbf{M}'$ [note the different scales in the insets of Fig. 4(a) and 4(b)]. The effect is even much stronger on the level of the corresponding spectra, shown in Fig. 4(c) and 4(d), respectively: In an 8×8 system (dashed-dotted line), nodal and antinodal spectra are qualitatively very similar, with a clear pseudogap feature, and differ mainly in peak height (at $|\omega| \approx 0.7$); at $\mathbf{k} = \mathbf{X}$, the spectrum remains nearly unchanged at larger system sizes and in the thermodynamic limit. At $\mathbf{k} = \mathbf{M}'$, in contrast, the pseudogap dip shrinks significantly for larger systems and is completely lost in the thermodynamic limit, where a quasiparticle shape appears. This shows that essential pseudogap physics, with a nodal-antinodal dichotomy, is really a property of the thermodynamic limit and that the bias inherent in finite-size systems dangerously distorts the physical picture.

C. FS extrapolations of spectra along high-symmetry momenta in the BZ

The elimination of FS errors at generic momenta requires "global" extrapolations that involve some kind of functional fitting procedures in momentum space. For momenta along high-symmetry lines, these fits have the form of Fourier series which may be adapted in order to take all symmetries into account. In the following, we will illustrate the algorithm for the most important path, the irreducible portion $\overline{\mathbf{XM}'}$ of the noninteracting Fermi surface. This path can be parametrized as

$$k_x = (2-\kappa)\,\pi/2; \quad k_y = \kappa\,\pi/2; \quad \kappa \in [0,1];$$

then $\kappa = 0$ corresponds to $\mathbf{X} \equiv (\pi,0)$ while $\kappa = 1$ corresponds to $\mathbf{M}' \equiv (\pi/2,\pi/2)$. At particle-hole symmetry, all functions f have to be symmetric with respect to both end points, which implies that they can be represented in the form

$$f(\kappa) = a_0 + \sum_{n=1}^{\infty} a_n \sin^2(n\,\kappa\,\pi/2)$$

with coefficients a_n. We have chosen to fit the difference of the Green function for each $\mathbf{k}$ (along the line) with respect to the antinodal Green function (corresponding to $\kappa = 0$); this implies that the zeroth-order coefficient vanishes exactly. The symbols in Fig. 5(a) represent DQMC data for the difference Green functions at $\tau = \beta/2 = 2.5$; evidently their interpolation using the above Fourier series up to third order (dashed/dotted lines) works quite well. Furthermore, the associated Fourier coefficients depend very regularly (i.e., almost perfectly linearly) on $1/L^2$, as seen in Fig. 5(b), and decay exponentially as a function of order. Consequently, an extrapolation to the thermodynamic limit is possible on the level of the coefficients (using a least-squares fit) with high precision; the extrapolated coefficients yield a reliable estimate $G_{\mathbf{k}}(\tau = 2.5)$ for all $\mathbf{k}$ along the path [solid line in Fig. 5(a)]. This procedure has to be performed independently for each value of τ; spectra can then be obtained using MEM on an arbitrarily dense $\mathbf{k}$ grid. Similar procedures were employed separately for each high-symmetry line indicated in Fig. 1(a).

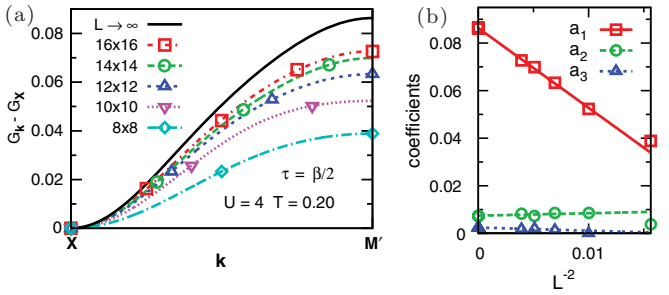

FIG. 5. (Color online) Example of finite-size extrapolation of imaginary-time Green functions along high-symmetry lines in the BZ, here for the path $\mathbf{X} \to \mathbf{M}'$ [cf. Fig. 1(a)] and $\tau = \beta/2$: (a) difference Green functions with respect to $G_{\mathbf{X}}$ (symbols), fitted with a Fourier series (broken lines) and final result of the extrapolation to the thermodynamic limit (black solid line), (b) extrapolation of the corresponding Fourier coefficients.

IV. RESULTS

A. Pseudogap signatures at nodal and antinodal k points

Let us, first, turn to the antinodal and nodal spectra shown in Fig. 6(a) and 6(b), respectively. At the elevated temperature $T = 0.50$ (dotted lines) the spectra have quasiparticle (QP) shape at all system sizes and for both momentum points. FS effects are negligible: Even the spectra of the smallest systems considered (8×8, left column) do not deviate visibly from those in the thermodynamic limit (right column); also the momentum dependence along the Fermi surface is minimal at $T = 0.50$, with about 20% larger peak height at the nodal $\mathbf{M}'$ point.

In the 8×8 case (left column), the largest system size fully considered in previous studies, a pseudogap dip appears almost simultaneously at $T = 0.28$ and $T = 0.24$ (dashed lines) at the $\mathbf{X}$ and $\mathbf{M}'$ points, respectively, and quickly deepens to an almost complete gap at $T = 0.18$ (dashed-dotted line). Given only this data, one would conclude that any momentum dependences

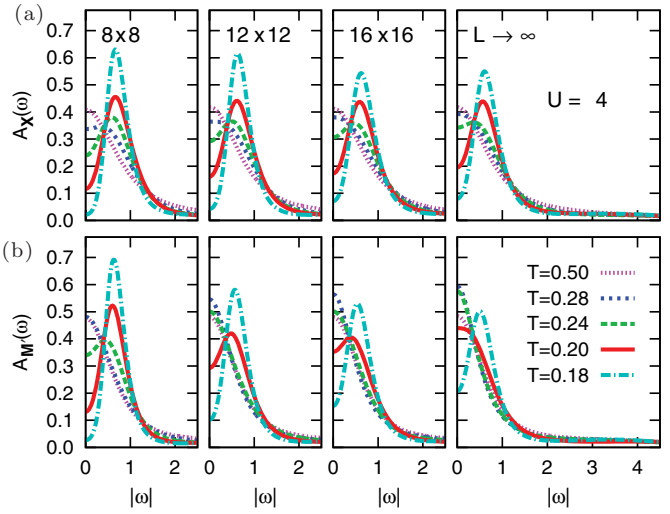

FIG. 6. (Color online) Evolution of the DQMC spectral functions with temperature at $U = 4$ for finite clusters with $8 \leqslant L \leqslant 16$ and in the thermodynamic limit: (a) at the antinodal point [$\mathbf{k} = \mathbf{X} \equiv (\pi,0)$], (b) at the nodal point [$\mathbf{k} = \mathbf{M}' \equiv (\pi/2,\pi/2)$].

beyond the free dispersion are inessential, i.e., that the physics might be in reach of theories with a momentum-independent self-energy [in particular, the dynamical mean-field theory (DMFT)]. However, this picture is distorted by finite-size effects and far from the truth: In the thermodynamic limit (right column in Fig. 6), the antinodal spectra have QP shape only for $T \geqslant 0.28$; at $T = 0.24$, a slight dip emerges at $\omega = 0$ which develops to a significant PG at $T = 0.20$ and an almost complete gap at $T = 0.18$. [20] In contrast, the nodal spectrum retains QP form down to $T = 0.20$ (while even the 16×16 system shows a PG dip at this temperature), before a PG emerges at $T = 0.18$. Thus, the FS extrapolation detailed above is really essential for fully resolving the nodal-antinodal dichotomy, which is at the heart of PG physics at finite temperatures. Only in the limit $T \to 0$, i.e., in the presence of long-range order, one expects a DMFT-like picture to become valid (again, as for high T) with fully gapped spectra all along the Fermi surface.

This implies that finite-size effects should mainly have two consequences on the level of spectra: (i) shift characteristic PG temperatures upwards, (ii) dilute the nodal-antinodal dichotomy in the vicinity of these characteristic temperatures.

Characteristic PG temperature T^*: As the opening of the PG is not a thermodynamic phase transition, it lacks a unique critical temperature. It is still useful (and common)[1–3,21] to define a *characteristic PG temperature* T^*, for comparison with other temperature or energy scales of the system. An obvious choice of the required scalar PG measure is a dip in the spectral function. We specify this "pseudogap strength" by the reduction of spectral weight at $\omega = 0$, compared to the maximum:

$$r_{\mathbf{k}} \equiv 1 - A_{\mathbf{k}}(\omega = 0)/\max_{\omega} A_{\mathbf{k}}(\omega)\,,$$

as shown for the (anti)nodal points in Fig. 7. This representation reveals that the onset of the PG is slow only at $\mathbf{k} = \mathbf{X}$: As soon as $r_{\mathbf{X}} \approx 0.5$, $r_{\mathbf{M}'}$ jumps to the full value within a narrow temperature range $\Delta T \approx 0.03$. The results in the thermodynamic limit (filled circles) can be fitted with a Fermi function form (solid lines); using their inflection points yields $T^*_{\mathbf{X}} \approx 0.20$, $T^*_{\mathbf{M}'} \approx 0.18$. Note that, again, the FS effects are much stronger at $\mathbf{k} = \mathbf{M}'$ than at $\mathbf{k} = \mathbf{X}$.

Comparison with the literature: In a pioneering study, Huscroft *et al.*[10] had obtained first bounds on the FS errors in DQMC spectra by complementing DQMC results for $N \leqslant 64$ sites with those of the dynamical cluster approximation (DCA)

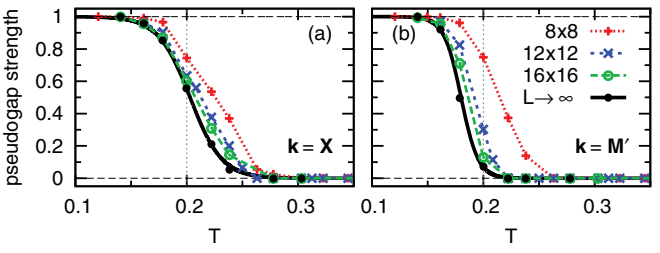

FIG. 7. (Color online) Scalar measure of pseudogap strength (see text) versus temperature: (a) at antinodal, (b) at nodal point. The nodal-antinodal dichotomy is fully apparent only in the thermodynamic limit (solid lines).

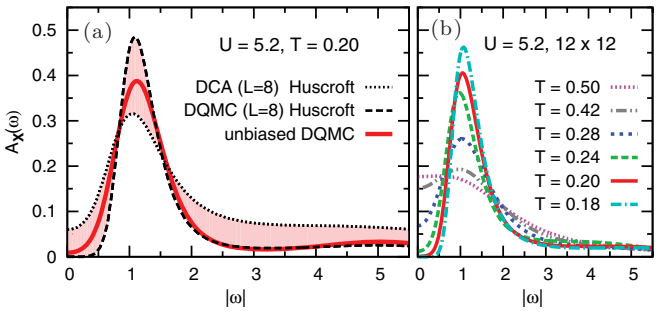

FIG. 8. (Color online) Spectral functions of the half-filled Hubbard model at the antinodal point [$\mathbf{k} = \mathbf{X} \equiv (\pi,0)$] and for weak coupling $U = 5.2$: (a) Unbiased spectrum at $T = 0.20$ (solid line), in comparison with earlier DCA and finite-size DQMC results.[10] (b) DQMC spectra for 12×12 lattice.

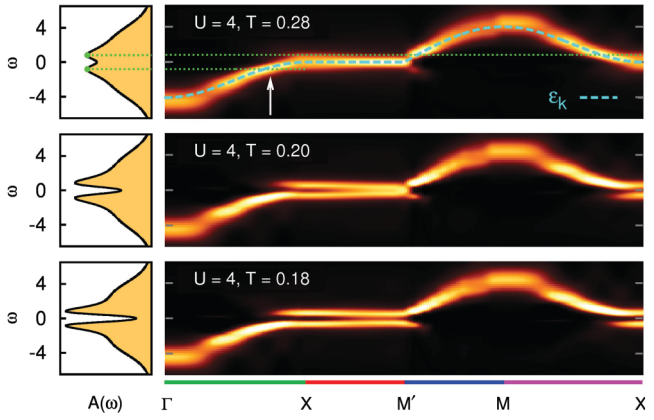

FIG. 9. (Color online) Unbiased local spectra $A(\omega)$ (first column) and momentum-resolved spectra $A_{\mathbf{k}}(\omega)$ for $U = 4$ and $\mathbf{k}$ along the path through the Brillouin zone illustrated in Fig. 1(a); the pseudogap opens with strong $\mathbf{k}$ dependence at $T \leqslant T^* \approx 0.20$. A local maximum in the spectral density at $\omega \neq 0$ (arrow) is indicative of spin-polaron physics.

employing N $\mathbf{k}$ patches in the self-energy. The resulting antinodal spectral functions for $U = 5.2$ are shown as dashed and dotted lines in Fig. 8(a), respectively. The shaded region denotes the bounds in which one would expect the true spectrum, according to the opposite FS tendencies (with DQMC over- and DCA underestimating gaps at small cluster sizes) of both methods. Note that the remaining uncertainty is still significant and that the bounds are not rigorous, due to numerical noise and the difficulties of the MEM.

Our unbiased estimate of $A_{\mathbf{X}}(\omega)$, shown as solid line in Fig. 8(a), reduces these uncertainties drastically: We find that the spectral weight at low frequencies ($|\omega| \lesssim 0.3$) is much smaller than predicted by DCA, but still significant (i.e., larger than the raw DQMC prediction). The true peak height at $|\omega| \approx 1.1$ is close to the average of the DCA and DQMC predictions. At large frequencies $|\omega| \gtrsim 1.5$, we find excellent agreement with the earlier DQMC estimates[10] which shows that the DQMC FS errors are small in this region (cf. Fig. 6) and also verifies the procedures for analytic continuation; in contrast, DCA is still far off (at $N = 64$).

Compared with the results for $U = 4$ presented in Fig. 6, our unbiased result [solid line in Fig. 8(a)] shows much stronger PG characteristics, as is certainly expected at the stronger interaction $U = 5.2$. Spectra for a full range of temperatures at this interaction are shown in Fig. 8(b) for a 12×12 system; these results can directly be compared with the second column in Fig. 6. Already at the highest temperature $T = 0.50$ [dotted line in Fig. 8(b)], the spectral peak is much broader, i.e., more spectral weight has been shifted away from the origin than at $U = 4$. This tendency towards more insulating behavior remains at lower T: The peak-to-peak width is about twice as large as for $U = 4$. At $T = 0.18$ (dash-dotted line), no spectral weight can be resolved at $|\omega| \lesssim 0.5$, so that the PG looks numerically like a full gap. In addition, the characteristic PG temperature is clearly shifted upwards, with a well-developed PG already at $T = 0.28$; the dependence of T^* on U will be studied more broadly in subsection IV C.

B. Evolution of pseudogap in full momentum-resolved spectral function

So far, we have presented results which, for given parameters U and T, are of a similar nature as those previously discussed in the literature. The main advances of our study of nodal and antinodal spectra are (i) our elimination of the (enormous) finite-size bias inherent in raw results and (ii) our explicit analysis of temperature effects. We will now turn to fundamentally new results, namely spectra with full momentum resolution.

Figure 9 shows unbiased momentum-resolved spectra $A_{\mathbf{k}}(\omega)$ throughout the whole Brillouin zone, along the path indicated in Fig. 1(a), at weak coupling $U = 4$ and in a temperature range $0.18 \leqslant T \leqslant 0.28$; in addition, the left column contains the local spectra $A(\omega)$, corresponding to an average over all $\mathbf{k}$. We have chosen a path $\overline{\mathbf{\Gamma X M' M X}}$ that contains the irreducible portion $\overline{\mathbf{XM'}}$ of the noninteracting Fermi surface (at half filling). The inclusion of this subpath allows us to study the nodal-antinodal dichotomy continuously and in detail; more generally, all variations along this path (where $\varepsilon_{\mathbf{k}} = 0$) arise from a $\mathbf{k}$ dependent self-energy, i.e., effects beyond DMFT.

At $T = 0.28$ (first row in Fig. 9), the local intensity maxima are unique at each $\mathbf{k}$ point and agree rather well with the noninteracting dispersion $\varepsilon_{\mathbf{k}}$ (dashed line), except for the edges $\omega \gtrsim 4$. A well-defined quasiparticle peak at $\omega \approx 0$ (especially sharp near $\mathbf{k} = \mathbf{M'}$ and more diffuse at $\mathbf{k} = \mathbf{X}$) is consistent with a Fermi liquid description. This picture changes at $T = 0.20$ (second row), when the spectrum splits at $\mathbf{k} \approx \mathbf{X}$, i.e., a pseudogap opens at the antinodal point, while the rest of the spectrum (at momenta with $\varepsilon_{\mathbf{k}} \neq 0$) is essentially unchanged. The gap size decreases smoothly on the line $\mathbf{X} \to \mathbf{M'}$. Only at $T \leqslant 0.18$ (third row) the QP is destroyed also at $\mathbf{k} = \mathbf{M'}$; a PG then extends over all momenta.

Compared to the strong temperature dependence along the path $\overline{\mathbf{XM'}}$, the spectra appear nearly unchanged in the rest of the BZ. In particular, a sharp dispersive quasiparticle-like band, indicated by an arrow in the top panel, evolves from the $\mathbf{X}$ point about halfway towards the $\mathbf{\Gamma}$ point (and, equivalently by particle-hole symmetry, from the $\mathbf{X}$ point towards the $\mathbf{M}$ point). We interpret this feature, which is not accessible in conventional DQMC studies at FS, as the formation of a spin polaron band (arrow in Fig. 9), with an energy offset at lower

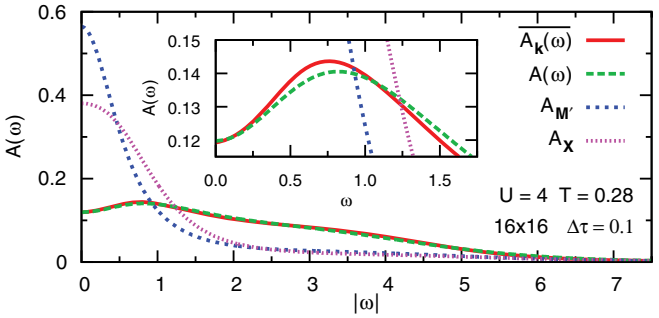

FIG. 10. (Color online) Test of MEM accuracy at $U = 4$, $T = 0.28$: The local spectral function $A(\omega)$ (dashed line), calculated from the local Green function $G(\tau)$, agrees well with the average $\overline{A_{\mathbf{k}}(\omega)} \equiv \frac{1}{N}\sum_{\mathbf{k}} A_{\mathbf{k}}(\omega)$ (solid line). Both curves reveal a dip at $\omega \lesssim 0.8$ which is absent at this temperature in $A_{\mathbf{M}'}(\omega)$ (short-dashed line) and $A_{\mathbf{X}}(\omega)$ (dotted line).

T indicating the magnetic exchange scale. It ends (at higher $|\epsilon_{\mathbf{k}}|$) in a "waterfall" which breaks up the band structure into low and high energy features.[22]

Taken together, our results indicate that, apart from incoherent features at $|\omega| \approx 4$ which are present at all temperatures and should continuously evolve into Hubbard bands with increasing U, interaction effects come into play with lowering T first very locally (in momentum space) around the antinodal $\mathbf{X}$ point; apparently, the strong enhancement of scattering by the van Hove singularity at $\mathbf{X}$ completely determines the physics in this region. This explains why the spectra can become sharper, implying a reduction in the imaginary part of the self energy, on the path from $\mathbf{X}$ towards $\mathbf{\Gamma}$ (up to the position of the arrow in Fig. 9, corresponding to the energy ω indicated by dotted lines), i.e., with increasing $\varepsilon_{\mathbf{k}}$ and ω; a behavior which is exactly opposite to usual Landau Fermi liquid and also to DMFT physics.

This suppression of spectral weight around $\mathbf{X}$ already at elevated temperatures also explains the slight dip seen in the local spectrum at $T = 0.28$ (dots and dotted lines in top panel of Fig. 9; cf. also Fig. 10): While the momenta around $\mathbf{M}'$ and in the spin-polaron band region (arrow) contribute "normally" to the local spectrum, the contributions from momenta near $\mathbf{X}$ are spread out to about a much larger width (with a significant fraction at $|\omega| \gtrsim 1$); the missing weight at $\omega \ll 1$ results in the dip.

One might worry that this analysis puts too much confidence in the accuracy of our data and that the dip in the local spectrum at $T = 0.28$, a local suppression in $A(\omega)$ by abound 10% in a narrow frequency range, corresponding to a "missing weight" of about 1%, could also result from uncertainties in the MEM procedure. Therefore, we have checked its consistency and accuracy in the largest finite-size system (16×16) by comparing the local spectrum $A(\omega)$ (dashed line in Fig. 10), obtained by direct analytic continuation using MEM from the local Green function $G(\tau)$ with the average of all (here 256) momentum-resolved spectra $A_{\mathbf{k}}(\omega)$ in Fig. 10. As $G(\tau) \equiv \frac{1}{N}\sum_{\mathbf{k}} G_{\mathbf{k}}(\tau) \equiv \overline{G_{\mathbf{k}}(\tau)}$, both spectra should agree, if evaluated exactly: $A(\omega) \stackrel{!}{=} \overline{A_{\mathbf{k}}(\omega)} \equiv \frac{1}{N}\sum_{\mathbf{k}} A_{\mathbf{k}}(\omega)$. As the MEM is inherently nonlinear, due to the entropy constraint, deviations must be expected in practice. However, our procedure, with very accurate DQMC data, seems to be quite stable:

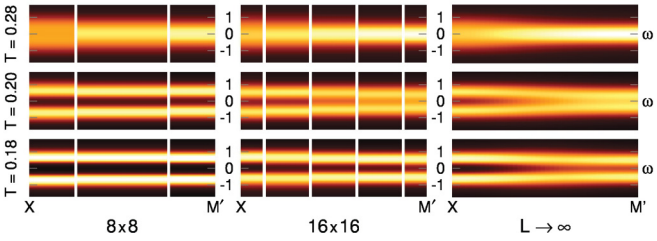

FIG. 11. (Color online) Spectral functions $A_{\mathbf{k}}(\omega)$ for $\mathbf{k}$ along the Fermi edge (line from $\mathbf{X} \to \mathbf{M}'$; cf. Fig. 1). FS results ($L = 8,16$) converge (slowly) to the thermodynamic limit both pointwise and by refinements of the $\mathbf{k}$ resolution.

Although the $\mathbf{k}$ dependent spectral functions $A_{\mathbf{k}}(\omega)$ differ substantially at different $\mathbf{k}$ points (shown in Fig. 10 only for the nodal and antinodal points using short-dashed and dotted lines, respectively) and have much more pronounced features than the local spectral function $A(\omega)$ (long-dashed line), their average $\overline{A_{\mathbf{k}}(\omega)}$ (solid line) agrees with it nearly within linewidth; only the magnified inset reveals tiny differences at small frequencies. So we conclude that our techniques are more than adequate and that the small dip discussed above is, indeed, physical.

Let us, finally, stress that our eliminations of finite-size errors have been absolutely essential for obtaining unbiased momentum-resolved spectra, as illustrated in Fig. 11 for the path $\mathbf{X} \to \mathbf{M}'$: Not only is the convergence at the end points $\mathbf{k} = \mathbf{X}$ and $\mathbf{k} = \mathbf{M}'$ slow, the $\mathbf{k}$ resolution is also quite coarse, with only one intermediate point for $L = 8$ and only three intermediate points for $L = 16$. It is clear that a very significant extension of the cluster size (e.g., to 64×64, implying a factor of $4^6 = 4096$ in computer time) would be needed in order to match the momentum resolution of our extrapolation procedure.

C. Evolution of characteristic pseudogap temperature T^* with interaction U

Apart from yielding a momentum dependent T^*, the criterion used in subsection IV A has the disadvantage of depending on the ill-conditioned analytic continuation of the imaginary-time DQMC Green functions to the real axis. On the other hand, it is difficult to define specific PG criteria on the level of the imaginary-time Green functions [cf. Fig. 4(a) and 4(b)].[23] However, the nodal-antinodal dichotomy, i.e., the *momentum dependence* of the Green functions along the line $\mathbf{X} \to \mathbf{M}'$ (arising from a momentum dependence of the irreducible self-energy) turns out to be illuminating: Fig. 12(a) shows that the norm of the difference between the imaginary-time Green functions,

$$|G_{\mathbf{M}'} - G_{\mathbf{X}}| \equiv \left\{ \int_0^\beta d\tau |G_{\mathbf{M}'}(\tau) - G_{\mathbf{X}}(\tau)|^2/\beta \right\}^{1/2},$$

is strongly enhanced (at $U = 4$) in the temperature range where the PG opens. Not surprisingly, this peak becomes sharper and shifts towards lower T in the thermodynamic limit; the position of the maximum yields a natural unique definition of the characteristic PG temperature $T^* \approx 0.20$, indicated by a vertical dotted line in Fig. 12.

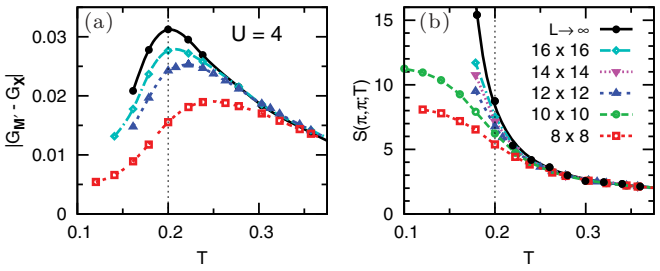

FIG. 12. (Color online) Properties of finite clusters and in the thermodynamic limit at $U = 4$: (a) Difference between nodal and antinodal Green functions versus temperature; its maximum defines the characteristic PG temperature $T^* \approx 0.20$. (b) Unnormalized spin structure factor at antiferromagnetic wave vector $\mathbf{k} = (\pi,\pi)$. Dotted vertical lines mark T^*.

As discussed in the introduction, the PG is associated (at $n \approx 1$) with AF correlations and may be regarded as a precursor of a fully gapped long-range ordered AF phase which, in $d = 2$, is realized only in the ground state.[24] Thus, we should expect to see a strong enhancement in suitable spin correlation functions. While the nearest-neighbor spin correlations are only very moderately enhanced at $T \lesssim T^*$ (not shown), the spin structure function is seen in Fig. 12(b) to increase by a full factor of 4 in the range $0.9\,T^* \leqslant T \leqslant 1.1\,T^*$. At the same time, FS effects explode at $T \lesssim T^*$. All this shows that the PG is driven by the development of AF order at a scale which is large compared to the lattice spacing.

The PG physics and, in particular, the momentum dependence observed at $U = 4$ should disappear at strong coupling, when already the high-temperature phase is gapped at $n = 1$.[25] The dichotomy should also vanish in the limit $U \to 0$, where the energy scale T_{spin} vanishes, and so does the magnitude of the pseudogap. Indeed, the momentum dependence is seen in Fig. 13 to peak at $U \approx 4$ and to decay quickly for larger couplings, where also FS effects (which can be estimated from the thin lines, corresponding to 8×8, in comparison to the main 12×12 results) become irrelevant. At fixed cluster size, also the results at weaker coupling ($U = 3$, $U = 2$) fall off; unfortunately, they suffer from significant FS effects which are too costly to eliminate. Still, the peak positions allow us to estimate $T^*(U)$ in the full range of weak to intermediate coupling as denoted by symbols in the inset of Fig. 13.[26] Also shown is the mean-field estimate of the critical temperature for AF long-range order (solid line). At first sight, this DMFT estimate of the Néel temperature $T_{\text{N}}^{\text{DMFT}}$ would appear irrelevant, as the true $T_{\text{N}} = 0$ by the Mermin-Wagner theorem. However, we find that $T^* \approx 0.9\,T_{\text{N}}^{\text{DMFT}}$ for $4 \leqslant U \leqslant 8$; a correction of FS effects for $U = 2$ and $U = 3$ should push the corresponding values of T^* also below $T_{\text{N}}^{\text{DMFT}}$. So the DMFT identifies the relevant temperature scale for spin coherence

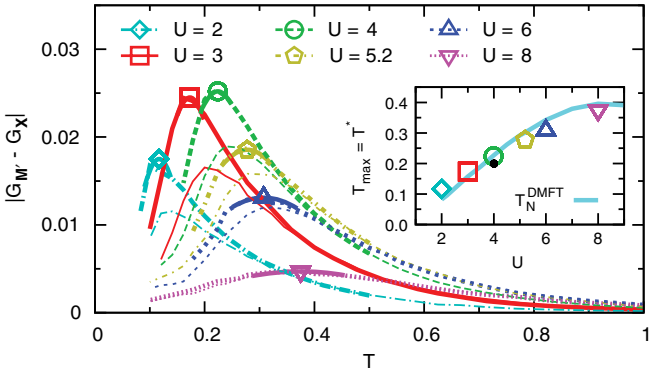

FIG. 13. (Color online) Difference between nodal and antinodal Green functions versus temperature: DQMC results at weak to intermediate coupling ($2 \leqslant U \leqslant 8$) for 12×12 clusters (thick lines) and 8×8 clusters (thin lines). Inset: associated T^* in comparison with DMFT Néel temperature.

(as was previously observed in the strong-coupling regime[27]); however, it lacks the momentum resolution which is essential to capture the pseudogap physics explored in this paper.

V. CONCLUSION

After decades of research, our understanding of the two-dimensional Hubbard model, especially regarding the extent to which it captures the pseudogap and high-T_c physics of cuprates, is still far from complete. Numerical simulations[21,28–33] give valuable hints, but continue to be dominated by finite-size effects.[34] We have overcome the finite-size barrier and presented momentum-resolved spectral functions in the thermodynamic limit, obtained by systematic extrapolation of DQMC Green functions ($L \to \infty$ and $\Delta\tau \to 0$). Based on this achievement, we were able to disentangle the delicate interplay of dynamical and spatial magnetic correlations. At weak to intermediate couplings, this interplay leads, indeed, to the formation of a pseudogap in the half-filled band. The pseudogap originates from a strong $\mathbf{k}$ dependence of the self-energy, which results in a d-wave-like anisotropy in the opening of the charge gap and a "waterfall" substructure of the spectrum. The associated temperature scale T^* is determined by the onset of antiferromagnetic fluctuations (and nearly agrees with $T_{\text{N}}^{\text{DMFT}}$), i.e., is rather high compared to other coherence scales and should be in reach of experiments with ultracold fermions on optical lattices.[35,36]

ACKNOWLEDGMENTS

We thank G. Sangiovanni for valuable discussions. Financial support by the Deutsche Forschungsgemeinschaft through FOR 1346 and, in part, through SFB/TR 49 is gratefully acknowledged.

[1]D. S. Marshall, D. S. Dessau, A. G. Loeser, C. H. Park, A. Y. Matsuura, J. N. Eckstein, I. Bozovic, P. Fournier, A. Kapitulnik, W. E. Spicer, and Z. X. Shen, Phys. Rev. Lett. **76**, 4841 (1996).

[2]P. A. Lee and X.-G. Wen, Rev. Mod. Phys. **78**, 17 (2006).

[3]N. Armitage, P. Fournier, and R. Greene, Rev. Mod. Phys. **82**, 2421 (2010).

[4]R. Blankenbecler, D. J. Scalapino, and R. L. Sugar, Phys. Rev. D **24**, 2278 (1981).

[5]S. R. White, D. J. Scalapino, R. L. Sugar, and N. E. Bickers, Phys. Rev. Lett. **63**, 1523 (1989).
[6]S. R. White, Phys. Rev. B **46**, 5678 (1992).
[7]M. Vekić and S. R. White, Phys. Rev. B **47**, 1160 (1993).
[8]C. E. Creffield, E. G. Klepfish, E. R. Pike, and S. Sarkar, Phys. Rev. Lett. **75**, 517 (1995).
[9]S. Moukouri, S. Allen, F. Lemay, B. Kyung, D. Poulin, Y. M. Vilk, and A. M. S. Tremblay, Phys. Rev. B **61**, 7887 (2000).
[10]C. Huscroft, M. Jarrell, T. Maier, S. Moukouri, and A. N. Tahvildarzadeh, Phys. Rev. Lett. **86**, 139 (2001).
[11]A. A. Katanin, A. Toschi, and K. Held, Phys. Rev. B **80**, 075104 (2009).
[12]M. Jarrell and J. Gubernatis, Phys. Rev. **269**, 133 (1996).
[13]The terms "nodal" and "antinodal" refer originally to the d-wave order parameter in high-T_c superconductors, which has a node (vanishing gap) near the point $\mathbf{M}'$ and is maximal near the antinode $\mathbf{X}$ [cf. Fig. 1(a) and Fig. 9]. The same is true for the pseudogap, which is maximal at $\mathbf{X}$.
[14]J. Hirsch, Phys. Rev. B **38**, 12023 (1988).
[15]F. Assaad and H. Evertz, in *Computational Many-Particle Physics, Lecture Notes in Physics, Vol. 739*, edited by H. Fehske, R. Schneider, and A. Weiße (Springer Verlag, Berlin, 2008), p. 277.
[16]J. Gubernatis, M. Jarrell, R. Silver, and D. Sivia, Phys. Rev. B **44**, 6011 (1991).
[17]R. Fye, Phys. Rev. B **33**, 6271 (1986).
[18]N. Blümer, arXiv:0801.1222; E. Gorelik and N. Blümer, Phys. Rev. A **80**, 051602 (2009).
[19]Additional data points for $L = 10,14$ [small symbols in Fig. 3(b)] were not included in the FS extrapolations (lines), but are clearly consistent with them; this confirms the accuracy of the Fourier fits of momentum dependencies (see subsection III C) from which they originate.
[20]The evolution of the peak position toward low T is consistent with a ground state charge gap (Ref. 24) $\Delta_c \approx 0.67$.
[21]N. S. Vidhyadhiraja, A. Macridin, C. Şen, M. Jarrell, and M. Ma, Phys. Rev. Lett. **102**, 206407 (2009).
[22]R. Preuss, W. Hanke, C. Gröber, and H. G. Evertz, Phys. Rev. Lett. **79**, 1122 (1997).
[23]The observable $\beta G(\beta/2)$ gives also hints about PG physics (Refs. 28,29 and 31), but is not a sharp PG criterion: Its value changes only by some 20% between the curves, e.g., for 12×12 and $L \to \infty$ in the inset of Fig. 6, although the former corresponds to PG and the latter to QP behavior.
[24]F. F. Assaad and M. Imada, J. Phys. Soc. Jpn. **65**, 189 (1996).
[25]The onset of strong AF correlations should still be visible in the higher-frequency portions of the spectral function as it leaves signatures in the kinetic energy (Ref. 27) and optical conductivity (Ref. 37).
[26]Our estimate of $T^* \approx 0.30$ at $U = 6t$ agrees well with a recent DCA result (Ref. 21).
[27]E. V. Gorelik, D. Rost, T. Paiva, R. Scalettar, A. Klümper, and N. Blümer, Phys. Rev. A **85**, 061602(R) (2012).
[28]P. Werner, E. Gull, O. Parcollet, and A. J. Millis, Phys. Rev. B **80**, 045120 (2009).
[29]E. Gull, O. Parcollet, P. Werner, and A. J. Millis, Phys. Rev. B **80**, 245102 (2009).
[30]N. Lin, E. Gull, and A. J. Millis, Phys. Rev. B **82**, 045104 (2010).
[31]E. Gull, M. Ferrero, O. Parcollet, A. Georges, and A. J. Millis, Phys. Rev. B **82**, 155101 (2010).
[32]G. Sordi, K. Haule, and A. M. S. Tremblay, Phys. Rev. B **84**, 075161 (2011).
[33]E. Gull, O. Parcollet, and A. J. Millis, arXiv:1207.2490v1.
[34]In particular, the recent prediction of a Fermi liquid—superconductor crossover at weak coupling (Ref. 33), based on paramagnetic DCA (Ref. 38) with only 8 (or 16) $\mathbf{k}$ patches, appears inconsistent with our unbiased results.
[35]W. Hofstetter, J. I. Cirac, P. Zoller, E. Demler, and M. D. Lukin, Phys. Rev. Lett. **89**, 220407 (2002).
[36]For pseudogaps in ultracold Fermi gases (without optical lattices) near unitarity, see, e.g., Refs. 39–42.
[37]C. Taranto, G. Sangiovanni, K. Held, M. Capone, A. Georges, and A. Toschi, Phys. Rev. B **85**, 085124 (2012).
[38]T. A. Maier, M. Jarrell, T. C. Schulthess, P. R. C. Kent, and J. B. White, Phys. Rev. Lett. **95**, 237001 (2005).
[39]J. P. Gaebler, J. T. Stewart, T. E. Drake, D. S. Jin, A. Perali, P. Pieri, and G. C. Strinati, Nat. Phys. **6**, 569 (2010).
[40]P. Magierski, G. Wlazlowski, and A. Bulgac, Phys. Rev. Lett. **107**, 145304 (2011).
[41]S. Tsuchiya, R. Watanabe, and Y. Ohashi, Phys. Rev. A **84**, 043647 (2011).
[42]A. Perali, F. Palestini, P. Pieri, G. C. Strinati, J. T. Stewart, J. P. Gaebler, T. E. Drake, and D. S. Jin, Phys. Rev. Lett. **106**, 060402 (2011).

Quasi-continuous-time impurity solver for the dynamical mean-field theory with linear scaling in the inverse temperature

D. Rost,[1,2] F. Assaad,[3] and N. Blümer[1]
[1]*Institute of Physics, Johannes Gutenberg University, Mainz, Germany*
[2]*Graduate School Materials Science in Mainz, Johannes Gutenberg University, Mainz, Germany*
[3]*Institute of Theoretical Physics and Astrophysics, University of Würzburg, Würzburg, Germany*
(Received 20 March 2013; revised manuscript received 7 May 2013; published 29 May 2013)

We present an algorithm for solving the self-consistency equations of the dynamical mean-field theory (DMFT) with high precision and efficiency at low temperatures. In each DMFT iteration, the impurity problem is mapped to an auxiliary Hamiltonian, for which the Green function is computed by combining determinantal quantum Monte Carlo (BSS-QMC) calculations with a multigrid extrapolation procedure. The method is numerically exact, i.e., yields results which are free of significant Trotter errors, but retains the BSS advantage, compared to direct QMC impurity solvers, of linear (instead of cubic) scaling with the inverse temperature. The new algorithm is applied to the half-filled Hubbard model close to the Mott transition; detailed comparisons with exact diagonalization, Hirsch-Fye QMC, and continuous-time QMC are provided.

DOI: 10.1103/PhysRevE.87.053305 PACS number(s): 02.70.Ss, 71.10.Fd, 71.27.+a

I. INTRODUCTION

The dynamical mean-field theory (DMFT) [1–4] and its cluster extensions [5,6] are powerful approaches for the numerical treatment of correlated electron systems, both in the model context and for materials science, e.g., embedded in the LDA + DMFT [7] or GW + DMFT [8–11] frameworks which extend density functional theory to strongly correlated materials [3,12]. Recently, many DMFT studies have also appeared in the context of ultracold fermions on optical lattices [13–15]. The DMFT reduces electronic lattice models to impurity problems, which have to be solved self-consistently [16–18]. A challenging part of this iterative procedure is the computation of the interacting Green function for a given impurity configuration (defined by the fixed local interactions and the self-consistent Weiss field). Thus, the availability of efficient and reliable *impurity solvers* determines the complexity of models and the parameter space that can be accessed using the DMFT.

Quantum Monte Carlo (QMC) impurity solvers allow for numerically exact solutions of the DMFT self-consistency equations at finite temperatures. In the case of the Hirsch-Fye auxiliary field (HF-QMC) method [16,19,20], all raw estimates contain systematic errors due to the inherent Trotter decomposition and associated imaginary-time discretization [19,21]; unbiased results can only be obtained after an extrapolation of the discretization interval $\Delta\tau \to 0$ [22,23]. Diagrammatic QMC impurity solvers [24–27] sample partition function and Green functions in continuous (imaginary) time (CT), i.e., avoid systematic biases. However, in all of these direct QMC approaches, the computational effort scales cubically [28] with the inverse temperature $\beta = 1/k_{\mathrm{B}}T$, which limits their access to low-temperature phases.

Exact diagonalization (ED)-based impurity solvers [29] require a discrete representation of the impurity action in terms of an auxiliary Hamiltonian, which is then solved either by full diagonalization (for evaluations at arbitrary temperature) or using a Lanczos procedure [30] (e.g., at $T = 0$). As the numerical effort scales exponentially with the number N_b of auxiliary "bath" sites, N_b has to be kept quite small, which introduces, again, a bias and is a particularly severe limitation for multiorbital or cluster DMFT studies at finite temperatures.

Recently, Khatami *et al*. proposed another Hamiltonian-based scheme [31], in which the Green function and other relevant properties of the auxiliary problem are computed using the determinantal BSS-QMC method developed by Blankenbecler, Scalapino, and Sugar [32]. The advantage of this scheme, compared to ED, is the possibility of using more bath sites (due to cubic instead of exponential scaling with N_b); the advantage over the direct QMC impurity solvers is the linear, instead of cubic, scaling in β [33]. The authors established the feasibility of the method and proved that the associated sign problem (arising at general band filling in cluster extensions of DMFT, in frustrated lattices, and for generic multiband models) converges to that of HF-QMC for sufficiently fine bath discretization [31]. However, as all BSS-QMC applications to date, the Green functions and all observable estimates resulting from their implementation suffer from systematic Trotter errors.

In this work, we construct a similar algorithm where the Trotter bias inherent in the BSS Green functions is eliminated using a multigrid procedure before feeding them back in the self-consistency cycle. As a DMFT building block, the resulting method is an exact quasi-CT QMC impurity solver with linear scaling in the inverse temperature. Its scaling advantage over direct QMC impurity solvers should allow access to lower temperatures, in particular in multiorbital and cluster DMFT studies.

The paper is organized as follows: In Sec. II we briefly review the DMFT equations and the BSS-QMC algorithm and fully specify our multigrid DMFT-BSS approach. As a test case, the new method is applied (in single-site DMFT) to the half-filled Hubbard model in the vicinity of the Mott transition in Sec. III. Here, we first focus on the Green function at moderately low temperature $T = t/25$ and then discuss important observables, namely the double occupancy and quasiparticle weight, also at lower temperatures. The accuracy of our approach is established by comparisons with the results of the (multigrid) HF-QMC, ED and CT-QMC solvers, as well

as with the previous (finite $\Delta\tau$) DMFT-BSS implementation. We show that our elimination of the Trotter error improves the results dramatically. We also discuss the impact of the bath discretization and establish convergence to the thermodynamic limit. A summary and outlook conclude the paper in Sec. IV.

II. THEORY AND ALGORITHMS

In this section, we lay out the proposed algorithm for solving the DMFT self-consistency equations without significant Trotter errors and with a computational effort that grows only linearly with the inverse temperature. We start out by reviewing the general DMFT framework and established methods (ED, HF-QMC, CT-QMC) for its solution in Sec. II A in sufficient detail to expose the similarities and differences with respect to the new method. Here we also discuss some algorithmic choices, in particular regarding the Hamiltonian representation in our ED implementation, that are essential ingredients also for the BSS-QMC-based approaches. We then turn to the BSS-QMC method and its applicability in the DMFT context in Sec. II B, and specify, finally, our new numerically exact implementation in Sec. II C. For simplicity, and in line with the numerical results to be presented in Sec. III, we write down the formalism for the single-band Hubbard model and the original, single-site variant of DMFT. Extensions to cluster DMFT (and to multiband models) should be straightforward, but require some generalizations (e.g., for the treatment of offdiagonal Green functions) and will be pursued in a subsequent publication.

A. DMFT and established impurity solvers

1. The Hubbard model on a lattice or graph

We consider the single-band Hubbard model

$$H = H_0 + H_{\rm int} = \sum_{ij,\sigma} t_{ij}\, c^\dagger_{i\sigma} c_{j\sigma} + U \sum_i n_{i\uparrow} n_{i\downarrow}\,, \qquad (1)$$

where $c^\dagger_{i\sigma}$ ($c_{i\sigma}$) creates (annihilates) an electron with spin $\sigma \in \{\uparrow, \downarrow\}$ on lattice site i; $n_{i\sigma} = c^\dagger_{i\sigma} c_{i\sigma}$ is the corresponding density, $t_{ij} = t_{ji}$ the hopping amplitude between sites i and j (or the local potential for $i = j$); U quantifies the on-site interaction. Usually, the hopping is defined to be translationally invariant, e.g., $t_{ij} = -t$ for nearest-neighbor bonds on an infinite mathematical lattice [as illustrated in Fig. 1(a) for a square lattice] or on a finite cluster with periodic boundary conditions. However, neither the DMFT nor direct QMC approaches to the Hubbard model depend crucially on such assumptions, as will be discussed in Sec. II B.

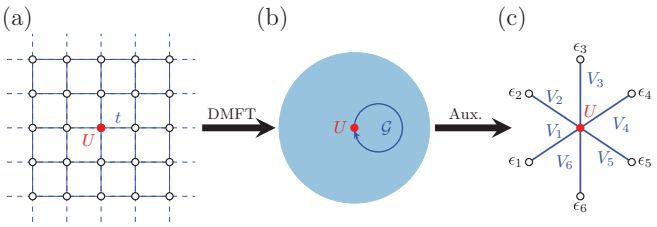

FIG. 1. (Color online) Mapping of the original lattice problem (a), with local interaction U and hopping t, on a single impurity (b), embedded in an effective bath $\mathcal{G}$. (c) Discretization of the bath in terms of an auxiliary Hamiltonian (treatable with ED or BSS-QMC), here with star topology.

2. General DMFT self-consistency procedure

If all lattice sites are equivalent and for spatially homogeneous phases, the DMFT maps the original lattice problem (1), illustrated in Fig. 1(a), onto a single-impurity Anderson model [Fig. 1(b)], which has to be solved self-consistently. The impurity problem is defined by its action

$$\mathcal{A}[\psi,\psi^*,\mathcal{G}] = \int_0^\beta \int_0^\beta d\tau\, d\tau' \sum_\sigma \psi^*_\sigma(\tau)\, \mathcal{G}^{-1}_\sigma\, \psi_\sigma(\tau') - U \int_0^\beta d\tau\, \psi^*_\uparrow(\tau)\, \psi_\uparrow(\tau)\, \psi^*_\downarrow(\tau)\, \psi_\downarrow(\tau), \qquad (2)$$

here in imaginary time $\tau \in [0,\beta]$ and in terms of Grassmann fields ψ, ψ^*. $\mathcal{G}$ is the "bath" Green function, i.e., the noninteracting Green function of the impurity, which is related to the full impurity Green function G,

$$G_\sigma(\tau) = -\langle \mathcal{T}_\tau\, \psi_\sigma(\tau)\, \psi^*_\sigma(0)\rangle_{\mathcal{A}} \qquad (3)$$

(with the time ordering operator $\mathcal{T}_\tau$), and the self-energy Σ by the (impurity) Dyson equation

$$G^{-1}_\sigma(i\omega_n) = \mathcal{G}^{-1}_\sigma(i\omega_n) - \Sigma_\sigma(i\omega_n), \qquad (4)$$

here written in terms of fermionic Matsubara frequencies $\omega_n = (2n+1)\pi T$ at finite temperature T; here and in the following, we set $\hbar = k_{\rm B} = 1$.

The central DMFT assumption is that of a local self-energy on the lattice [1]: $\Sigma_{ij\sigma}(i\omega_n) = \delta_{ij}\Sigma_{ii\sigma}(i\omega_n)$, which is identified with the impurity self-energy. Similarly, the impurity Green function is identified with the local component of the lattice Green function:

$$G_\sigma(i\omega_n) = G_{ii\sigma}(i\omega_n) = \{\mathbb{t} + [i\omega_n + \mu - \Sigma_\sigma(i\omega_n)]\mathbb{1}\}^{-1}_{ii} = \int_{-\infty}^{\infty} d\varepsilon\, \frac{\rho(\varepsilon)}{i\omega_n + \mu - \Sigma_\sigma(i\omega_n) - \varepsilon}, \qquad (5)$$

where the last expression is valid in the homogeneous case, $\rho(\varepsilon)$ denotes the noninteracting density of states, and $\mathbb{t}$ is the matrix with elements t_{ij}.

The general DMFT iteration scheme is illustrated in Fig. 2(a): starting, e.g., with an initial guess $\Sigma = \Sigma_0$ of the self-energy, the Green function G is computed using the lattice Dyson equation (5). In a second step, Σ and G yield the bath Green function $\mathcal{G}$ via the impurity Dyson equation (4), which defines, in combination with the local interactions, the impurity problem [illustrated in Fig. 1(b)], the solution of which is the nontrivial part of the algorithm. A second application of the impurity Dyson equation (4), to the resulting G and to $\mathcal{G}$, yields a new estimate of the self-energy Σ, which closes the self-consistency cycle. In the following, we discuss the primary options for addressing the impurity problem.

3. Direct impurity solvers

One class of methods directly evaluates the path integral representation of the Green function [Eqs. (3) and (2)] for a continuous bath $\mathcal{G}$, which corresponds to a DMFT solution

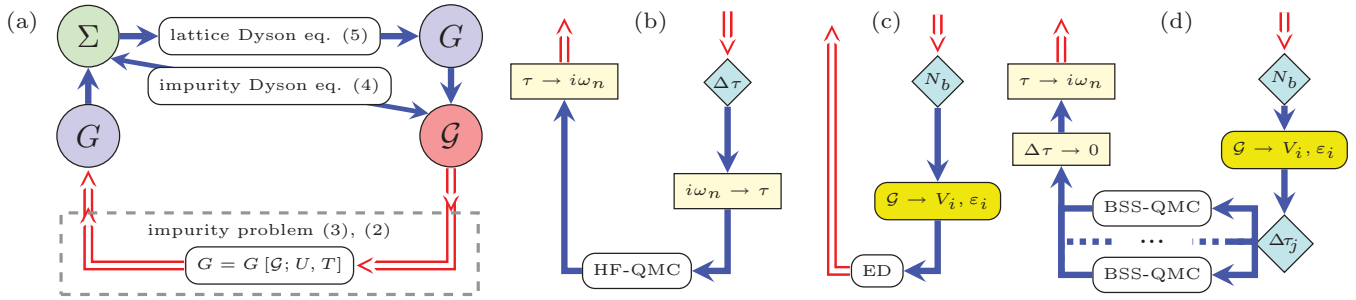

FIG. 2. (Color online) (a) Scheme of the general DMFT self-consistency cycle, including the "impurity problem" (dashed box). Established impurity solvers include (b) the Hirsch-Fye (HF-QMC) algorithm and (c) exact diagonalization (ED): cf. the main text. (d) The proposed algorithm approximates the bath Green function $\mathcal{G}$ in terms of the parameters V_i, ϵ_i of an auxiliary Hamiltonian (6) with N_b "bath" sites [like ED (c)]. Corresponding Green functions are computed using BSS-QMC for a grid $\Delta\tau_{\min} \leqslant \Delta\tau_j \leqslant \Delta\tau_{\max}$ of Trotter discretizations. The subsequent extrapolation of $\Delta\tau \to 0$ yields the Green function, free of significant Trotter errors and continuous in τ, which is easily Fourier transformed and fed back into the self-consistency cycle.

of the original lattice problem in the thermodynamic limit after self-consistency. We will refer to such methods as "direct impurity solvers."

For a long time, the Hirsch-Fye QMC (HF-QMC) algorithm has been the method of choice for nonperturbative DMFT calculations [16]. HF-QMC is based on a discretization of the imaginary time $\tau \in [0,\beta]$ into Λ "time slices" of width $\Delta\tau = \beta/\Lambda$, a Trotter decomposition of the interaction and kinetic terms in Eq. (2), and a Hubbard-Stratonovich transformation, which replaces the electron-electron interaction by an auxiliary binary field on each time slice; the resulting problem is then solved employing Wick's theorem and Monte Carlo importance sampling over the field configurations. As configurations can be updated in the case of a single spin flip (i.e., an auxiliary-field change on a single time slice) with a matrix-vector operation of cost $\mathcal{O}(\Lambda^2)$ and Λ local updates are needed for a global configuration update, the numerical cost of the HF-QMC algorithm scales as Λ^3. All HF-QMC results have statistical errors (which decay as $N^{-1/2}$ for N "sweeps," each consisting of Λ attempted single-spin updates) and systematic errors resulting from the Trotter decomposition. As $\Delta\tau$ has to be kept constant for roughly constant systematic error upon variation of T, the numerical effort of HF-QMC scales as the cube of the inverse temperature, β^3. This is also true for the numerically exact (unbiased) "multigrid" HF-QMC method [34].

The integration of the (conventional) HF-QMC method into the DMFT self-consistency cycle is illustrated in Fig. 2(b) [as a specification of the lower dashed box in Fig. 2(a)]: a fixed choice of $\Delta\tau$ (diamond-shaped selection box) defines the grid $\tau_l = l\Delta\tau$ with $0 \leqslant l \leqslant \Lambda$ for a Fourier transform (square box) of the Matsubara bath Green function $\mathcal{G}(i\omega_n)$ (with $|\omega_n| \leqslant \omega_{\max}$ for some cutoff frequency $\omega_{\max}$) to the imaginary-time equivalent $\{\mathcal{G}(\tau_l)\}_{l=0}^{\Lambda}$. After application of the HF-QMC algorithm (rounded box), the result $\{G(\tau_l)\}_{l=0}^{\Lambda}$ is transformed back to Matsubara frequencies (square box); this step requires special care in order to get around the Nyquist theorem, e.g., using analytic weak-coupling results [23,35,36].

More recently, conceptionally different QMC approaches have been formulated, which are based on diagrammatic expansions of the action (2) in continuous imaginary time, either in the interaction U (CT-INT [37]) or in the bath hybridization (CT-HYB [25,26]), and on a stochastic sampling of Feynman diagrams; CT-AUX [38] is related to the HF-QMC method [27]. All of these continuous time (CT-QMC) algorithms require Fourier transforms, before and (with the exception of CT-INT) after the QMC part; the numerical cost is associated primarily with matrix updates, similar to those arising in HF-QMC, with a total scaling of the computational effort, again, as β^3.

Thus, all direct QMC-based impurity solvers are very costly at low T, which limits their access to low-temperature phases of particular physical interest.

4. *Auxiliary Hamiltonian and exact diagonalization*

Another class of numerical approaches, such as the "exact diagonalization" methods, cannot directly be applied to the action-based formulation of the impurity problem, but requires a Hamiltonian representation [39]. One possibility is the "star topology" illustrated in Fig. 1(c), where a central "impurity" site (with the same interactions as the impurity problem, here U) is connected by hopping matrix elements $V_{i\sigma}$ to a number N_b of noninteracting "bath sites," each characterized by a local potential $\epsilon_{i\sigma}$. In general, this representation has to be spin-dependent, leading to the Anderson Hamiltonian

$$H_{\text{And}} = \epsilon_0 \sum_\sigma n_\sigma + U n_\uparrow n_\downarrow + \sum_\sigma \sum_{i=1}^{N_b} [\epsilon_{i\sigma} n_{i\sigma} + V_{i\sigma}(a_{i\sigma}^\dagger c_\sigma + \text{H.c.})], \quad (6)$$

where $c_\sigma^\dagger$ (c_σ) creates (annihilates) an electron with spin $\sigma \in \{\uparrow,\downarrow\}$ on the impurity site and $a_{i\sigma}^\dagger$ ($a_{i\sigma}$) creates (annihilates) an electron with spin σ on bath site i; $n_\sigma = c_\sigma^\dagger c_\sigma, n_{i\sigma} = a_{i\sigma}^\dagger a_{i\sigma}$ are the corresponding number operators. In this work, we consider only nonmagnetic phases, which implies spin symmetric bath parameters $V_{i\downarrow} = V_{i\uparrow}, \epsilon_{i\downarrow} = \epsilon_{i\uparrow}$.

For a fixed choice of N_b, the bath parameters $\epsilon_{i\sigma}, V_{i\sigma}$ are determined such that the noninteracting impurity Green

function $\mathcal{G}_{\mathrm{And},\sigma}$ associated with H_{And}, with

$$\mathcal{G}^{-1}_{\mathrm{And},\sigma}(\omega) = \omega + \mu_\sigma - \sum_{i=1}^{N_b} \frac{V_{i\sigma}^2}{\omega - \epsilon_{i\sigma}}, \tag{7}$$

is "close" to the target bath Green function $\mathcal{G}$ according to some metric (see below). Note that the resulting spectrum $-\frac{1}{\pi}\mathrm{Im}\,\mathcal{G}_{\mathrm{And},\sigma}(\omega + i0^+)$ is necessarily discrete (for finite N_b), in contrast to piecewise smooth spectrum of the true bath Green function; in this sense, the mapping to a Hamiltonian implies a "bath discretization" in frequency space; this step clearly introduces a bias which has to be controlled particularly carefully within iterative procedures such as the DMFT.

The integration of this type of approach in the DMFT cycle is illustrated for the case of ED in Fig. 2(c): for a fixed choice of N_b (diamond shaped box), the parameters V_i, ϵ_i (here and in the following we suppress spin indices) are adjusted (rounded box) as to minimize the bath misfit

$$\chi^2\left[\{V_i,\varepsilon_i\}\right] = \sum_{n=0}^{n_c} \mathrm{w}_n \left|\mathcal{G}_{\mathrm{And}}(i\omega_n;\{V_i,\varepsilon_i\}) - \mathcal{G}(i\omega_n)\right|^2, \tag{8}$$

with a cutoff Matsubara frequency $i\omega_{n_c}$ and the weighting factor w_n, which can be used to optimize the bath parametrization [40] and which we set to $\mathrm{w}_n = 1$ [41]. As this fit is performed directly on the Matsubara axis, no Fourier transform is needed for $\mathcal{G}$. Using ED (rounded box), the Green function G can be evaluated on the Matsubara axis [29]; therefore, the DMFT cycle is closed without any Fourier transform.

The minimization of χ^2 [as defined in Eq. (8)] is performed in our ED and BSS-DMFT calculations using the Newton method, based on analytic expressions for the derivative $\nabla\chi^2$ with respect to the bath parameters. Due to the multidimensional character of the problem, this deterministic method is often trapped in local minima; thus, a naive implementation of Newton-based methods will, in general, not find globally optimal parameters, which can induce unphysical fixed points in the DMFT iteration procedure. Therefore, we use not only the solution $\{V_i,\epsilon_i\}$ of the previous iteration as initialization, but perform a large number (up to 1000) of independent Newton searches, starting also from random initial parameters. Of the resulting locally optimal solutions, we choose the one with minimum χ^2 as the final result of the minimization procedure; typically, about 1% of the individual searches come close to this (estimated) global optimum.

An advantage of ED, compared to QMC algorithms, is that Green functions and spectra can be computed directly on the real axis, without analytic continuation; however, numerical broadening of the resulting discrete peaks is required. This discretization problem is particularly severe as the numerical effort of the matrix diagonalization scales exponentially with the total number of sites (here $N_b + 1$), which limits the applicability of ED for cluster extensions of DMFT or multiband models.

B. Principles of the BSS-QMC algorithm and application as a DMFT impurity solver

In Eq. (6), we have used the conventional notation for the auxiliary Hamiltonian that emphasizes its interpretation as an impurity model, e.g., with different creation operators for electrons on the central "impurity" site ($c^\dagger_\sigma$) and on the bath sites ($a^\dagger_{i\sigma}$), respectively. However, with the changes $c_\sigma \to c_{0\sigma}$, $n_\sigma \to n_{0\sigma}$, and $a^\dagger_{i\sigma} \to c^\dagger_{i\sigma}$, $V_{i\sigma} \to t^\sigma_{0i}$ it essentially reproduces the Hubbard model (1) on a graph, just with nonuniform interaction (U acting only on site 0) and, possibly, spin-dependent hopping amplitudes and local energies.

As a consequence, the model (6) is not only treatable with the universal ED approach, but also with more specific methods developed for Hubbard-type models. As pointed out recently by Khatami *et al.* [31], this includes the determinantal quantum Monte Carlo approach by Blankenbecler, Scalapino, and Sugar [32,42] (BSS-QMC), which, thereby, becomes applicable as a DMFT impurity solver. In the following, we will first sketch the established BSS-QMC approach (for an extended discussion, including issues of parallelization, see Ref. [43]) and then discuss its application in the DMFT context.

Similarly to the HF-QMC method (cf. Sec. II A3), the BSS-QMC approach is based on a Trotter-Suzuki decomposition, here of the partition function

$$Z = \mathrm{Tr}(e^{-\beta(H_K+H_V)}) \tag{9}$$

$$\approx Z_{\Delta\tau} = \mathrm{Tr}\left(\prod_{l=0}^{\Lambda} e^{-\Delta\tau H_K} e^{-\Delta\tau H_V}\right), \tag{10}$$

where H_V (H_K) corresponds to the interaction (kinetic and local potential) contribution to the Hubbard-type models (1) or (6) and $\Delta\tau = \beta/\Lambda$. Again, a discrete Hubbard-Stratonovich transformation replaces the interaction term by a binary auxiliary field $\{h\}$ with $h_i(l) = \pm 1$ at each site i and time slice l. The trace in Eq. (10) then simplifies to

$$Z_{\Delta\tau} = \sum_{\{h\}} \det[M^{\{h\}}_\uparrow]\det[M^{\{h\}}_\downarrow] \quad \text{with}$$

$$M^{\{h\}}_\sigma = \mathbb{1} + B_{\Lambda,\sigma}\left[\{h_i(\Lambda)\}_{i=1}^N\right]\cdots B_{1,\sigma}\left[\{h_i(1)\}_{i=1}^N\right], \tag{11}$$

where B is defined in terms of the hopping matrix K:

$$B_{l,\sigma}\left[\{h_i(l)\}_{i=1}^N\right] = e^{\sigma\lambda\,\mathrm{diag}[h_1(l),\ldots,h_N(l)]}\, e^{-\Delta\tau K}. \tag{12}$$

The interaction strength is encoded in the parameter $\lambda = \cosh^{-1}(e^{U\Delta\tau/2})$. The computation of thermal averages of physical observables O takes the form:

$$\langle O\rangle = \sum_{\{h\}}\left[O^{\{h\}}\,\mathcal{P}^{\{h\}}_{\Delta\tau}\right],$$
$$\mathcal{P}^{\{h\}}_{\Delta\tau} = \frac{1}{Z_{\Delta\tau}}\det[M^{\{h\}}_\uparrow]\det[M^{\{h\}}_\downarrow]. \tag{13}$$

At particle-hole symmetry, the weights $\mathcal{P}^{\{h\}}_{\Delta\tau}$ are always positive; i.e., the sums can be evaluated at arbitrary precision, without any sign problem. As in HF-QMC, the problem is solved by Monte Carlo importance sampling of the auxiliary field $\{h\}$ and evaluation of the Green function at time slice l, with

$$G^{\{h\}}_{l,\sigma} = [\mathbb{1} + B_{l-1,\sigma}\cdots B_{1,\sigma}B_{\Lambda,\sigma}\cdots B_{l,\sigma}]^{-1}. \tag{14}$$

As a spin flip in the auxiliary field $h_i(l)$ at time slice l and site i only affects $B_{l,\sigma}$ at this site, the ratio of the weights, needed for the decision whether a proposed spin flip is accepted, involves only local quantities; a full recomputation of the determinants

of $N \times N$ matrices appearing in Eq. (11) is not needed. The computational effort is further reduced by calculating the Green function at time slice $l+1$ from the quantities at time slice l, using so-called "wrapping":

$$G_{l+1,\sigma} = B_{l,\sigma}^{-1} G_{l,\sigma} B_{l,\sigma}. \tag{15}$$

In order to avoid the accumulation of numerical errors in the matrix multiplications, it is necessary to recalculate the full Green function at regular intervals. This is particularly important at low temperatures.

All this considered, the numerical cost scales cubically with the number of sites and linearly with the number of time slices; at constant $\Delta\tau$, this translates to a total effort $\mathcal{O}(N^3\beta)$, where $N = N_b + 1$. Note that a need for finer bath discretizations at lower temperatures could potentially spoil the scaling advantage of the method over direct impurity solvers; we will show in Sec. III C that this is not the case for our test applications.

The application in the DMFT context [31] starts with the computation of the Hamiltonian parameters (for some choice of N_b), exactly like in the ED approach. As in the HF-QMC approach, one then chooses some discretization $\Delta\tau$, computes $\{G(l\Delta\tau)\}_{l=0}^{\Lambda}$ for the impurity site, and applies a (nontrivial) Fourier transform back to Matsubara frequencies. The result is an impurity solver with superior scaling (linear in β) compared to the direct impurity solvers (cubic in β), however, with a bias due to the Trotter discretization $\Delta\tau$ (in addition to a possible bias due to the bath discretization with N_b sites), which, as we will show in Sec. III, can be quite significant.

C. Specification of multigrid BSS-QMC algorithm

The central feature of our new algorithm is the elimination of this systematic Trotter error, while retaining the advantage of linear-in-β scaling inherent in the BSS-QMC method. In the following, we will specify the method and illustrate it using an example (Fig. 3), that will be discussed in detail in Sec. III.

In contrast to the previous DMFT-BSS implementation with a unique discretization $\Delta\tau$ in all BSS computations throughout the DMFT self-consistency cycle, the (impurity) Green function of the Hamiltonian H_{And} at hand is computed in $M \gtrsim 20$ parallel BSS runs (indexed by $1 \leqslant i \leqslant M$), each employing a homogeneous imaginary-time grid with a specific discretization $(\Delta\tau)_i$, chosen from a set $\{(\Delta\tau)_i | (\Delta\tau)_{\min} \leqslant (\Delta\tau)_i \leqslant (\Delta\tau)_{\max}\}$ with typically 6–9 different elements. Green functions resulting from BSS-QMC runs with the same discretization $(\Delta\tau)_i = (\Delta\tau)_j$ are averaged over, thereby reducing the dependencies on initialization conditions and further enhancing the parallelism.

This leads to a set of Green functions defined, in general, on incommensurate imaginary-time grids (symbols in Fig. 3). In order to apply a local $\Delta\tau \to 0$ extrapolation, all $G_{(\Delta\tau)_i}$ have to be transformed to a common grid. This is possible since the true $G(\tau)$ is a smooth function; however, a direct spline interpolation of the raw QMC results, neglecting higher derivatives, would not be accurate [44]. Instead, we consider differences between the raw data $\{G_{(\Delta\tau)_i}(l\Delta\tau)\}_{l=0}^{\Lambda_i}$ and a reference Green function, obtained via Eq. (5) from a model self-energy $\Sigma_\sigma^{\mathrm{ref}}(i\omega_n)$ [35,36], written here for the single-band

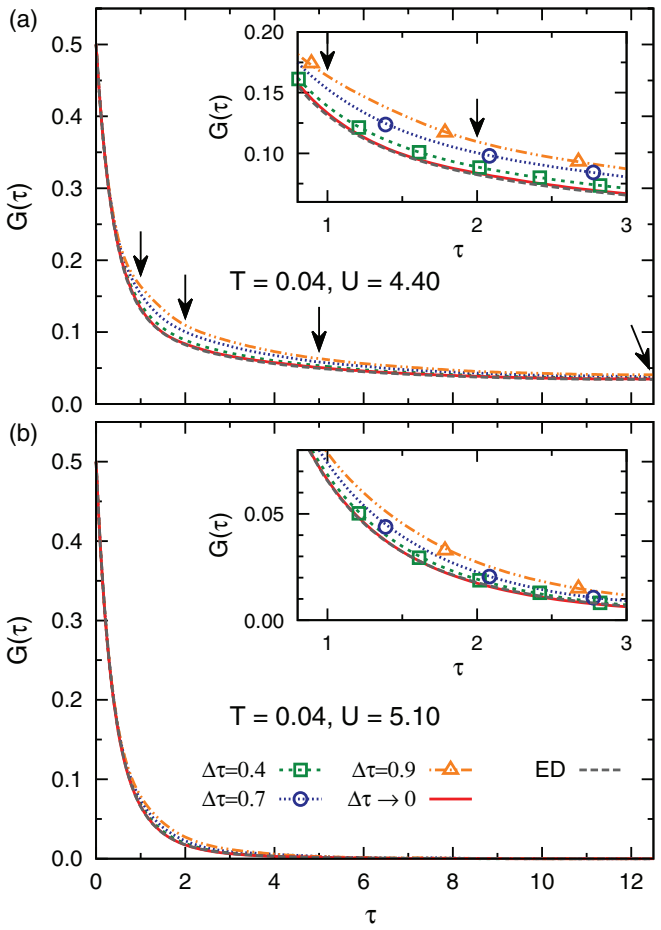

FIG. 3. (Color online) BSS-QMC impurity Green functions at $T = 0.04$ (symbols) using a bath representation with $N_b = 4$ sites (with parameters of converged DMFT-ED solution, long-dashed lines) and results of multigrid extrapolation to $\Delta\tau = 0$ (solid lines). Upper panel: metallic phase ($U = 4.4$). Lower panel: insulating phase ($U = 5.1$). Arrows denote τ values for which the extrapolation is shown in Fig. 4.

case (for multiband generalizations, see Ref. [45]):

$$\Sigma_\sigma^{\mathrm{ref}}(i\omega_n) = U\left(\langle n_{-\sigma}\rangle - \frac{1}{2}\right) + \frac{1}{2}U^2\langle n_{-\sigma}\rangle(1-\langle n_{-\sigma}\rangle) \times \left(\frac{1}{i\omega_n + \omega_0} + \frac{1}{i\omega_n - \omega_0}\right), \tag{16}$$

which recovers the exact high-frequency asymptotics of $\Sigma(i\omega_n)$ and $G(i\omega_n)$ for any choice of the free parameter ω_0 and, therefore, approximates the second and higher-order derivatives of $G(\tau)$ at $\tau \to 0$ (and $\tau \to \beta$) well. This match can be further improved by adjusting ω_0. Consequently, the differences $\{G_{(\Delta\tau)_i}(l\Delta\tau) - G^{\mathrm{ref}}(l\Delta\tau)\}_{l=0}^{\Lambda_i}$ have smaller absolute values and much smaller higher derivatives than the original data; in particular, their curvature vanishes asymptotically at the boundaries [46]. Thus, they are well represented by natural cubic splines.

Usually, the parameters of the piecewise polynomials constituting such a spline $f_{\mathrm{spline}}(x)$ are determined from discrete data $\{f_{\mathrm{meas}}(x_i)\}_{i=0}^{N}$ such that the discrete data are

reproduced exactly: $f_{\text{spline}}(x_i) = f_{\text{meas}}(x_i)$ for all $0 \leqslant i \leqslant N$. However, in the QMC context, all measurements have statistical errors; i.e., the discrete data are better represented as $\{f_{\text{meas}}(x_i) \pm \Delta f_{\text{meas}}(x_i)\}_{i=0}^{N}$ with standard deviations Δf_{meas}, which are also estimated within the QMC procedure. It is clear that the usual interpolating splines, which do not take the uncertainties of the discrete data into account, contain more features than warranted by the data (in particular at the Nyquist frequency); in the context of Green functions this includes the possibility of acausal behavior. We use, instead, smoothing spline fits [47,48] which reproduce the discrete data only within error bars, which are typically $\mathcal{O}(10^{-3})$, (and minimize the curvatures under this constraint); these fits can be computed in a very similar procedure and at the same cost as interpolating splines.

After combining these approximating "difference" splines with exact expressions for $G^{\text{ref}}(\tau)$ resulting from Eqs. (16) and (5), we obtain smooth approximations of the Green functions, as seen in Fig. 3(a); the inset also demonstrates slight deviations of the continuous spline fits from the discrete data (within error bars), e.g., for the discretization $\Delta\tau = 0.7$ (dotted line) at $\tau \approx 1.4$ (circle), while most other data points are reproduced within the line widths.

These smooth approximations can be evaluated on an arbitrarily fine common grid (e.g., with $\Delta\tau_{\text{fine}} = 0.005$) and extrapolated to $\Delta\tau \to 0$. This is illustrated in Fig. 4 for the representative values of τ denoted by arrows in Fig. 3(a). Even though most of the raw BSS-QMC data do not include estimates of the Green functions at these precise values of τ, the transformed data (symbols in Fig. 4) depend very regularly on $\Delta\tau$, falling on nearly straight lines as a function of $(\Delta\tau)^2$. Therefore, they can accurately and reliably be extrapolated to $\Delta\tau \to 0$ (lines in Fig. 4 and symbols at $\Delta\tau = 0$); an application of this procedure at all τ (on the fine grid) leads to quasi-continuous Green functions without significant Trotter errors, shown as solid lines in Fig. 3. These results can be Fourier transformed to Matsubara frequencies in a straightforward manner [cf. Fig. 1(d)]. A similar approach has also been useful for computing unbiased spectra from BSS-QMC [49].

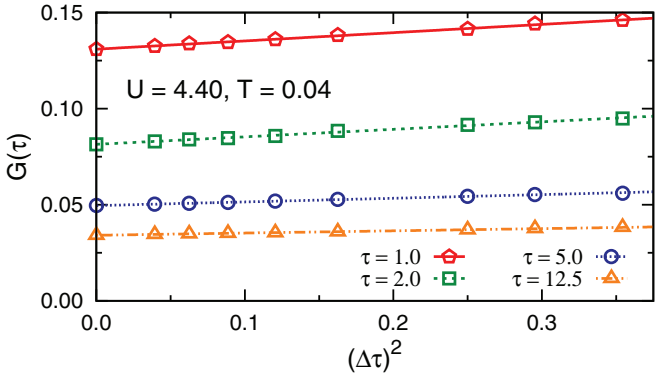

FIG. 4. (Color online) BSS-QMC estimates of imaginary-time Green functions $G_{\Delta\tau}(\tau)$ at $T = 0.04$, $U = 4.4$ after interpolation (corresponding to the colored broken lines in Fig. 3) for selected values of τ (symbols) and extrapolation to $\Delta\tau = 0$ using least-squares fits (lines).

At first sight, the computational advantage of the multigrid procedure is less obvious in the BSS-QMC context than for HF-QMC [34,50], since the numerical effort for direct computations at small $\Delta\tau$ grows only linearly, not cubically, with $(\Delta\tau)^{-1}$ in the BSS case (while the systematic errors decay generically as $(\Delta\tau)^2$ for a given impurity problem). However, even for a fixed Hamiltonian, so much accuracy can be gained by extrapolation that it more than offsets the cost of the additional grid points. This is true, in particular, since stable results are best obtained by averaging over independent BSS-QMC runs; performing these on variable grids then allows for extrapolation without additional cost. Furthermore, the individual runs thermalize faster in the multigrid variant, due to the smaller number of time slices (and proportionally shorter run time per sweep), which enhances the parallelism. Most importantly, as we will see below, the DMFT self-consistency can magnify any bias of the employed impurity solvers in complicated ways (in the vicinity of phase transitions), so that controlled results are really dependent on unbiased methods, such as our multigrid approach.

III. RESULTS

In this section, we compare results of the new numerically exact "multigrid" BSS-QMC method with raw BSS-QMC results (at finite Trotter discretization), with reference ED results (which are exact at the level of the auxiliary Hamiltonian), and with the predictions of established impurity solvers (multigrid HF-QMC [34] and CT-HYB [25,26,51]). These comparisons are performed in three stages: In Sec. III A we keep the bath $\mathcal{G}$ and its approximation by an auxiliary Hamiltonian fixed and discuss the impact of the Trotter error and its elimination without the complications of the DMFT self-consistency. In Sec. III B, we compare full DMFT solutions obtained using the various algorithms at moderate temperature ($T = 0.04$), focusing on the impact of Trotter errors on the resulting estimates of double occupancy and quasiparticle weight. Finally, we present results also at lower temperatures $T \geqslant 0.01$ (with DMFT self-consistency), where the impact of the bath discretization becomes particularly relevant, in Sec. III C.

Following the established practice for the evaluation of DMFT impurity solvers [23,28], all of these comparisons are performed for the half-filled Hubbard model with semi-elliptic "Bethe" density of states [52] (full band width $W = 4$) within the paramagnetic phase. Specifically, we choose temperatures $T \leqslant 0.04$, which are below the critical temperature $T^* \approx 0.055$ [36,50] of the first-order metal-insulator transition, and interactions close to or within the coexistence region of metallic and insulating solutions, which arises from the mean-field character of the DMFT.

A. Green function extrapolation at fixed bath Hamiltonian parameters

In general, a bias present in an impurity solver has a two-fold impact: On the one hand, it affects estimates of Green functions and all other properties for a given impurity problem, defined by its bath Green function $\mathcal{G}$. On the other hand, it shifts the fixed point of the DMFT self-consistency

cycle; i.e., it also modifies the converged bath Green function, which, in turn, also affects the measured Green functions and all other properties. In this subsection, we study the first effect in isolation by fixing the bath Green function to the converged solution of the ED procedure for $N_b = 4$ bath sites (with Hamilton parameters $\{\epsilon_i, V_i\}_{i=1}^4$). As the same auxiliary Hamiltonian is used also in the BSS-QMC algorithm, the ED estimates of the Green function are exact for the purpose of the current comparison; the impact of the bath discretization (which corresponds to a bias on the DMFT level) will be discussed in Sec. III C.

Local imaginary-time Green functions $G(\tau)$ are shown in Fig. 3(a) for the metallic phase, at $U = 4.4$, and in Fig. 3(b) for the insulating phase, at $U = 5.1$. Here and in the following, we restrict the imaginary-time range to $0 \leqslant \tau \leqslant \beta/2$; data for $\tau > \beta/2$ follow from the particle-hole symmetry $G(\beta - \tau) = G(\tau)$. Symbols (in the magnified insets) represent raw BSS-QMC results (with discretizations $\Delta\tau = 0.4$, $\Delta\tau = 0.7$, and $\Delta\tau = 0.9$); colored long-dashed, dotted, and dash-dotted lines denote interpolations obtained using the methods described in Sec. II C. Due to the large discretization, these data deviate significantly from the ED reference results (gray long-dashed lines), in particular at moderately low imaginary times $\tau \approx 2$. In contrast, multigrid BSS-QMC Green functions (solid lines) are indistinguishable from the ED data at $U = 5.1$ and very close to them at $U = 4.4$, with deviations of the order of statistical errors. Thus, our method yields, indeed, quasi-continuous Green functions without significant Trotter errors in both test cases, although the discretizations of the underlying raw BSS-QMC computations (with $0.3 \leqslant \Delta\tau \leqslant 1.0$) would be considered much too coarse in conventional applications.

A very similar picture emerges in an analogous comparison for the two coexisting solutions at $U = 4.74$, shown in Fig. 5. Again, the raw BSS-QMC results (symbols and colored broken lines) show a strong systematic bias, towards more metallic Green functions and of different magnitude in the different phases, while the extrapolated Green functions agree nearly perfectly with the ED references. In fact, some of the BSS Green functions calculated for an insulating bath (lower set of symbols and broken lines) show such large discretization errors at small $\tau \lesssim 2$, that they approach the exact Green function of the metallic DMFT solution (upper solid and long-dashed lines). One may suspect from this observation that these biased "insulating" solutions will not be associated with stable DMFT fixed points if they are fed back in the self-consistency cycle; such shifts of stability regions induced by the Trotter bias at $\Delta\tau > 0$ will, indeed, be seen in Sec. III B.

It is clear that the proposed multigrid extrapolation technique can only be useful as a practical method if it is insensitive to the particular set $\{(\Delta\tau)_i\}$ of discretizations in the underlying BSS-QMC runs; i.e., if no sensible choice leads to a significant bias. This is demonstrated in Fig. 6 for the insulating phase at $U = 4.7$: the Green functions for the same auxiliary problem obtained from multigrid extrapolations with three different $\Delta\tau$ grids [53] agree perfectly within the precision of the method. The latter is primarily determined by the statistical errors, i.e., by the number of sweeps and, possibly, by the numerical precision in the matrix operations. Only if raw BSS-QMC data

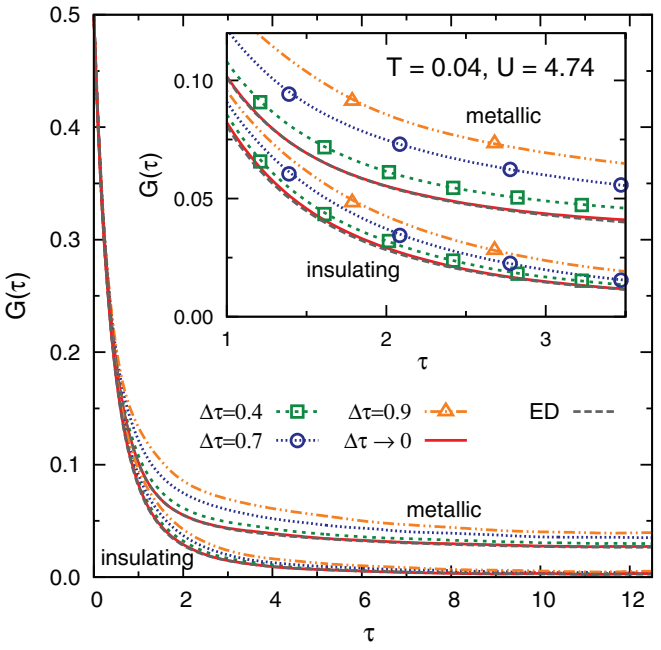

FIG. 5. (Color online) BSS-QMC impurity Green functions at $T = 0.04$ and $U = 4.74$ (symbols and colored broken lines) using a bath representation with $N_b = 4$ sites (with parameters fixed by converged DMFT-ED solution, long-dashed lines) and extrapolation to $\Delta\tau = 0$ (solid lines). Upper (lower) set of curves: metallic (insulating) bath.

of much higher precision was available (with many millions of sweeps per run), additional accuracy could be gained by choosing smaller discretizations (e.g., $0.1 \leqslant \Delta\tau \leqslant 0.3$). As a rule of thumb, the multigrid procedure can be based on discretizations $\Delta\tau$ that are 3 to 10 times as large as the discretization that one would choose in a conventional BSS-QMC procedure.

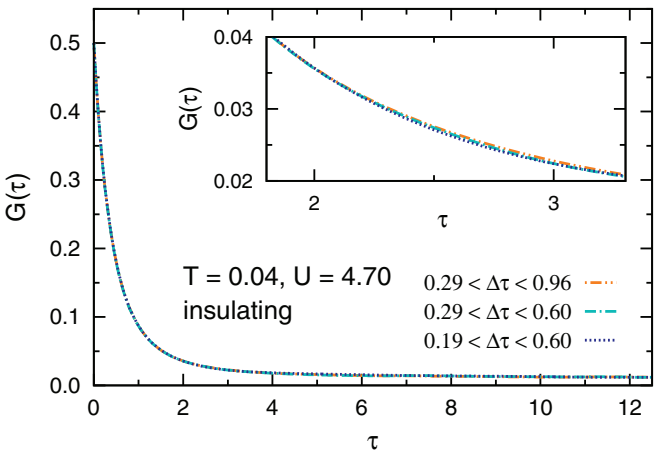

FIG. 6. (Color online) Green functions in the insulating phase at $T = 0.04$, $U = 4.7$, extrapolated from BSS-QMC results using different imaginary-time grids [53] (at fixed bath representation). The excellent agreement shows that the multigrid procedure is stable with respect to its technical parameters.

B. Comparisons of impurity solvers at full DMFT self-consistency: Impact of Trotter errors

So far, we have compared different algorithms just at the impurity level, i.e., for a fixed bath Green function (determined from a self-consistent DMFT-ED calculation). In contrast, we will now discuss results of completely independent DMFT solutions, each of which corresponds to full self-consistency for a given impurity solver (cf. Fig. 2). For all Hamiltonian-based methods (ED, BSS-QMC, and multigrid BSS-QMC), the number of bath sites is restricted to $N_b = 4$ (as above); the impact of this parameter will be studied in Sec. III C.

Specifically, we discuss static observables that are particularly useful for discriminating between metallic and (possibly coexisting) insulating DMFT solutions, namely, the double occupancy

$$D = \langle n_\uparrow n_\downarrow \rangle, \tag{17}$$

which is proportional to the interaction energy $E_{\rm int} = U D$, and the quasiparticle weight

$$Z = \left[1 - \frac{\partial\, \mathrm{Re}\, \Sigma(\omega)}{\partial \omega}\Big|_{\omega=0}\right]^{-1} \approx \left[1 + \frac{\mathrm{Im}\, \Sigma(i\omega_1)}{\pi T}\right]^{-1}. \tag{18}$$

Open symbols in Fig. 7 denote estimates resulting from self-consistent DMFT solutions using the conventional BSS-QMC impurity solver at finite discretization $0.3 \leqslant \Delta\tau \leqslant 0.5$, i.e., using the scheme established in Ref. [31]. The estimated values of Z, shown in Fig. 7(b), have a nearly uniform offset in the metallic phase at $U \lesssim 4.8$ relative to each other and relative to the reference ED solution (gray diamonds). The Trotter bias inherent in the conventional BSS-QMC procedure also leads to a significant overestimation of the range of stability of the metallic solution: The metallic BSS-QMC solutions extend to much larger interactions (e.g., to $U \approx 5.1$ at $\Delta\tau = 0.4$) than the ED reference solution.

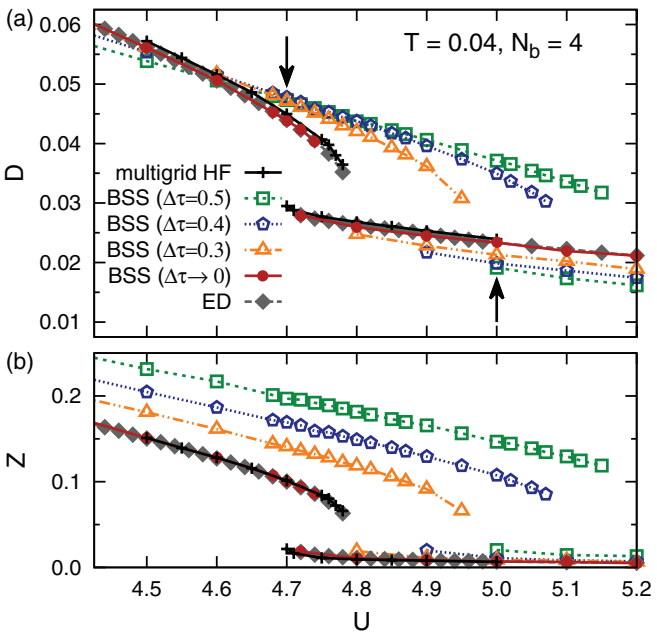

FIG. 7. (Color online) Estimates of double occupancy $D(U)$ and quasiparticle weight $Z(U)$ obtained in independent self-consistent DMFT calculations using various impurity solvers: multigrid HF-QMC (crosses), conventional BSS-QMC (open symbols), multigrid BSS-QMC (circles), and ED (diamonds). In each panel, the upper (lower) sets of curves correspond to metallic (insulating) solutions. Lines are guides to the eye only. Arrows in (a) indicate parameters for which the discretization dependence is studied in Fig. 8.

This is also seen in corresponding estimates of the double occupancy [Fig. 7(a)]; however, for these observables the Trotter bias is highly nonuniform (in the metallic solution): at $U = 4.7$ (arrow), the conventional BSS-QMC estimates are nearly on top of each other; relative deviations are only clearly seen at stronger interactions $U \gtrsim 4.9$ and (to a lesser degree) at weaker interactions $U \lesssim 4.5$. At the same time, nearly all of these data deviate significantly (and without obvious systematics) from the reference ED result (diamonds), so that an *a posteriori* elimination of the Trotter bias seems impossible.

In contrast, the new multigrid BSS-QMC procedure, as discussed in Sec. II C and illustrated in Fig. 2(d), leads to estimates of both D and Z (filled circles) which perfectly recover the ED solutions, even though they are based on BSS-QMC runs with $\Delta\tau \geqslant 0.3$.

This is also true for the insulating solutions (lower sets of curves in Fig. 7), the stability range of which is also shifted towards stronger interactions in the case of conventional BSS-QMC calculations (open symbols); here the Trotter bias appears roughly uniform for D and very nonuniform for Z. Again, the multigrid BSS-QMC results agree perfectly with the ED reference data.

For comparison, crosses and black solid lines in Fig. 7 denote estimates of an unbiased direct impurity solver, namely the multigrid HF-QMC method [34]; these show good overall agreement with both the ED and the multigrid BSS-QMC data. A slight negative deviation in the estimates of D of the latter, Hamiltonian-based, methods can be traced back to the relatively poor bath discretization with $N_b = 4$ auxiliary sites (cf. Sec. III C).

Since the double occupancy D is best computed directly on the impurity level (in QMC-based approaches), its physical value has to be extrapolated from raw estimates $D_{\Delta\tau}$, with discretizations corresponding to the different grid points used within the multigrid procedure (in contrast to the quasiparticle weight Z, which follows from the self-energy Σ, which, in turn, is determined from unbiased Green functions).

As seen in Fig. 8, the Trotter bias inherent in these raw estimates (filled symbols) is perfectly regular [54] even at large $\Delta\tau$, so that reliable extrapolations $\Delta\tau \to 0$ (thick dashed lines) are possible both in the metallic phase, at $U = 4.7$ (upper set of curves), and in the insulating phase, at $U = 5.0$ (lower set of curves).

In contrast, estimates of D resulting from conventional BSS-QMC calculations in the same range of discretizations $\Delta\tau \geqslant 0.3$ (large open symbols in Fig. 8) show such irregular dependencies on $\Delta\tau$ that quadratic least-square fits (solid lines) lead to extrapolations $\Delta\tau \to 0$ with significant offsets. Roughly accurate results (dotted lines) can only be obtained

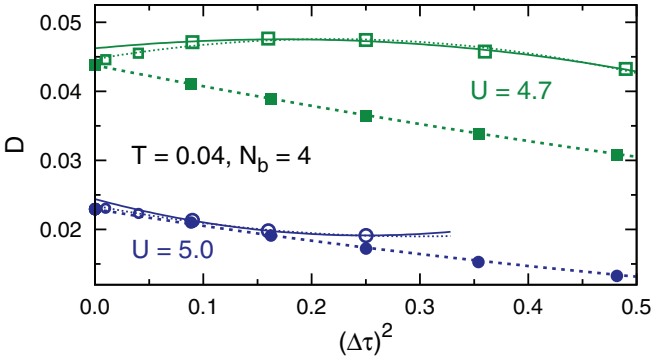

FIG. 8. (Color online) Discretization dependence of the double occupancy D as estimated from BSS-QMC, using either the multigrid scheme (filled symbols) or self-consistent BSS-QMC solutions at finite $\Delta\tau$ (open symbols), within the metallic phase at $U = 4.7$ (upper data set) or the insulating phase at $U = 5.0$ (lower data set). Dashed (solid) lines denote least squares fits to the multigrid (conventional) BSS-QMC data at $\Delta\tau \geqslant 0.3$; dotted lines denote fits that include also data at $\Delta\tau = 0.1$ and $\Delta\tau = 0.2$ (small open symbols).

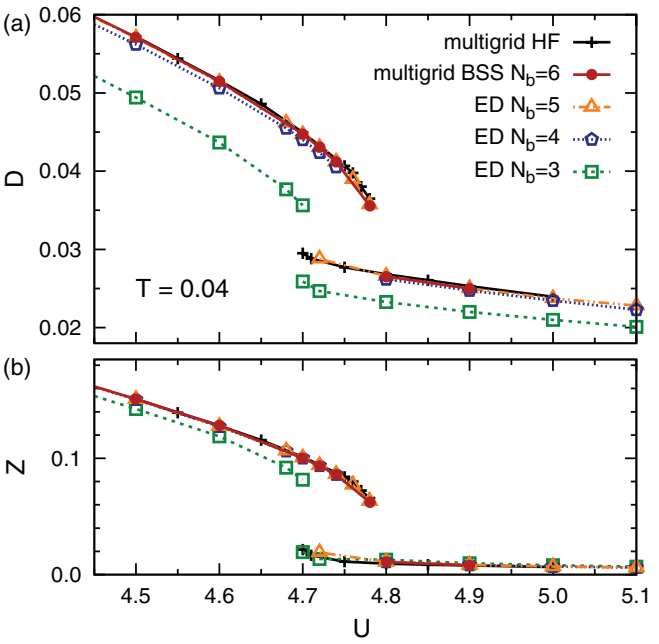

FIG. 9. (Color online) Estimates of double occupancy $D(U)$ and quasiparticle weight $Z(U)$ at $T = 0.04$, obtained in self-consistent DMFT calculations using Hamiltonian-based impurity solvers with $3 \leqslant N_b \leqslant 6$ bath sites: multigrid BSS-QMC (circles), ED (open symbols). Multigrid HF-QMC results (crosses) represent the limit $N_b \to \infty$. In each panel, the upper (lower) sets of curves correspond to metallic (insulating) solutions. Lines are guides to the eye only.

when including raw data at much smaller discretizations (small open symbols). This shows, again, that only an elimination of all Trotter errors *within* the self-consistency cycle, as introduced by our multigrid approach, can efficiently generate high-precision results.

C. Comparisons of impurity solvers at full DMFT self-consistency: Impact of bath discretization

So far, we have restricted the bath representation in all Hamiltonian-based impurity solvers (ED and both variants of BSS-QMC) to only $N_b = 4$ bath sites and focused on the impact of the Trotter errors and their elimination. From the mutual agreement with multigrid HF-QMC, an impurity solver which treats the bath directly on the action level, we can conclude that this coarse bath discretization allows for reasonably accurate estimates of D and, in particular, Z at the moderately low temperature $T = 0.04$. However, the ED and multigrid BSS-QMC estimates of D were found in Fig. 7 to lie a bit below the multigrid HF-QMC data; this deviation must be an artifact of the bath discretization if the multigrid HF-QMC reference data are correct. Moreover, we must suspect that the bath discretization bias gets worse (at constant N_b) at lower temperatures.

Figure 9 shows estimates of $D(U)$ and $Z(U)$ at $T = 0.04$, similarly to Fig. 7 and with the same multigrid HF-QMC reference data (crosses), but now using Hamiltonian-based impurity solvers with $3 \leqslant N_b \leqslant 6$ bath sites. Here and in the following, "BSS" refers to multigrid BSS-QMC data, i.e., without significant Trotter errors; for simplicity, we have used this method only for the largest auxiliary Hamiltonian ($N_b = 6$). Smaller bath sizes ($N_b = 3$, $N_b = 4$, and $N_b = 5$) are represented only by the ED solution, which is cheaper and free of statistical noise. At the resolution of Fig. 9, the estimates associated with the finer bath discretizations $N_b = 5$ (triangles) and $N_b = 6$ (circles) agree with each other. Therefore and since they are also consistent with the unbiased multigrid HF-QMC data (crosses), we conclude that convergence with respect to the bath discretization is reached already at $N_b = 5$ at $T = 0.04$. In contrast, the ED estimates of D are apparently slightly too small at $N_b = 4$ (pentagons); corresponding results at $N_b = 3$ (squares) are far off both for D and Z.

Note that consistent convergence of observable estimates with N_b, as demonstrated in Fig. 9 (as well as Fig. 10 and Fig. 11) can only be observed when optimal Hamiltonian parameters are determined with great care, as described in Sec. II A, within each self-consistency cycle; otherwise some bath sites may remain ineffective or the estimates can even get worse upon increasing N_b. In addition (as always in the DMFT context), it is essential that enough DMFT iterations are performed at each phase point in order to ensure convergency with respect to the self-consistency cycle (cf. Fig. 2).

Halving the temperature amplifies the bath discretization effects, as seen in Fig. 10: At $T = 0.02$, only the best Hamiltonian representation ($N_b = 6$, evaluated with multigrid BSS-QMC, circles) recovers all reference multigrid HF-QMC results (crosses) within their accuracy. At $N_b = 5$, the estimates of D in the insulating phase are already slightly too small; at $N_b = 4$, strong negative deviations in $D(U)$ are apparent also for the metallic solution. The impact of the bath discretization becomes even much stronger at $T = 0.01$, as shown in Fig. 11 for the metallic phase, which is interesting as a strongly renormalized Fermi liquid (while the properties of the insulating phase are asymptotically independent of temperature). We find that even the results for $N_b = 5$ and $N_b = 6$ deviate significantly in Fig. 11(a) from each other and from the

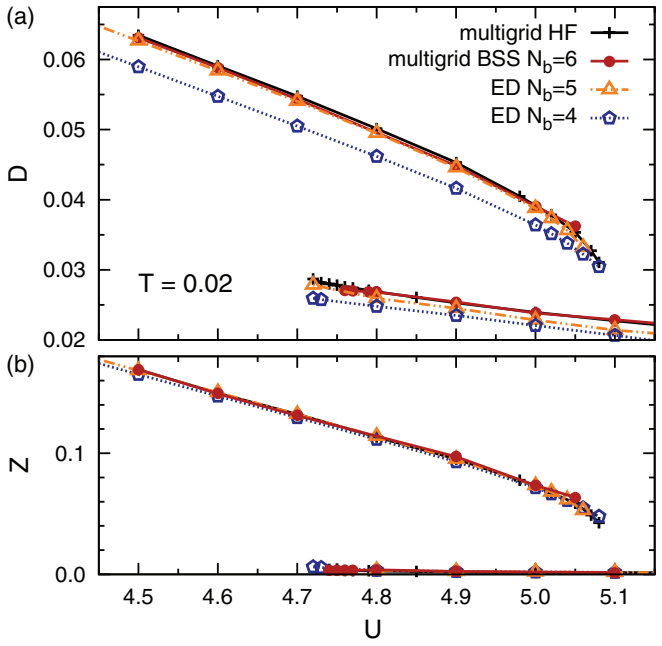

FIG. 10. (Color online) Estimates of double occupancy $D(U)$ and quasiparticle weight $Z(U)$ at $T = 0.02$, using bath discretizations with $4 \leqslant N_b \leqslant 6$ sites, analogous to Fig. 9.

multigrid HF-QMC reference result, especially at $U = 5.3$, near the edge of the stability region of the metallic phase. Only the multigrid BSS-QMC results using $N_b = 7$ bath sites (circles) agree with the reference data within their precision; even better agreement is observed with data obtained using the CT-HYB impurity solver (diamonds). Note that BSS-QMC

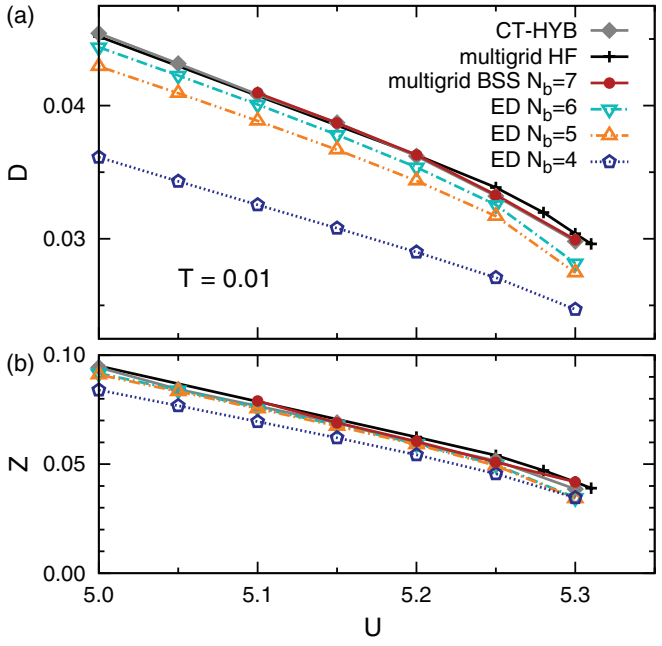

FIG. 11. (Color online) Estimates of double occupancy $D(U)$ and quasiparticle weight $Z(U)$ at $T = 0.01$, using bath discretizations with $4 \leqslant N_b \leqslant 7$ sites, analogous to Fig. 9. The CT-HYB data (diamonds) also represent the limit $N_b \to \infty$.

is much more efficient than ED at $N_b = 7$; in particular, the latter would need orders of magnitude more main memory than the former.

As noted in Sec. II B, a strong increase with inverse temperature of the number N_b of bath sites needed for a given accuracy could, in principle, eliminate the scaling advantage of the DMFT-BSS approach, as its computational cost does not only include the direct factor β, but also a factor $N_b^3 \equiv N_b^3(\beta)$. However, our results indicate that this effect is minor: In our test case, we needed to add one bath site upon halving the temperature for roughly constant accuracy; this is consistent with a scaling $N_b \propto \ln(\beta)$, i.e., an overall computational cost proportional to $\beta[\ln(\beta)]^3$ which is still linear up to logarithmic corrections.

IV. CONCLUSIONS

The DMFT and its extensions are invaluable tools for the study of phenomena associated with strong electronic correlations and for quantitative predictions of properties of correlated materials. However, the numerical solution of the DMFT self-consistency equations remains a great challenge: the established, direct, QMC impurity solvers yield unbiased results, but provide only limited access to the low-T phase regions of interest, due to the cubic scaling of their computational cost with the inverse temperature β. Exact diagonalization (ED) approaches, on the other hand, are limited by their exponential scaling with the number of sites N of the auxiliary Hamiltonian.

The multigrid BSS-QMC algorithm presented in this work allows for solving the DMFT self-consistency equations with an effort that grows only linearly with β; in contrast to an earlier BSS-QMC-based method [31], it is free of significant Trotter errors, i.e., numerically exact at the level of the auxiliary Hamiltonian. Since the computational cost grows only cubically with N, much better representations of the bath are possible than for ED. As demonstrated by applications to the half-filled Hubbard model in and near the coexistence region of metallic and insulating solutions and by comparisons with direct QMC impurity solvers, the new method yields unbiased results (for sufficiently fine bath discretization), in spite of using quite coarse Trotter discretizations in the underlying BSS-QMC evaluations.

The new unbiased quasi-CT impurity solver should show its full potential in multi-band cases and in cluster extensions of DMFT, where the prefactor N^3 of the BSS-QMC scheme (compared to a factor of 1 in HF-QMC calculations in single-site DMFT) is leveled off by the increased complexity of the original DMFT problem. Our approach can also be extended beyond Hubbard models; it could be particularly valuable for the cellular DMFT treatment of the Kondo lattice model, where interesting temperature regimes are out of reach of the existing impurity solvers [26,55].

ACKNOWLEDGMENTS

We thank E. Gorelik, E. Khatami, R. Scalettar, and P. Werner for valuable discussions. Financial support by the Deutsche Forschungsgemeinschaft through FOR 1346 is gratefully acknowledged.

[1] W. Metzner and D. Vollhardt, Phys. Rev. Lett. **62**, 324 (1989).

[2] A. Georges, G. Kotliar, W. Krauth, and M. J. Rozenberg, Rev. Mod. Phys. **68**, 13 (1996).

[3] G. Kotliar, S. Y. Savrasov, K. Haule, V. S. Oudovenko, O. Parcollet, and C. A. Marianetti, Rev. Mod. Phys. **78**, 865 (2006).

[4] D. Vollhardt, Ann. Phys. **524**, 1 (2012).

[5] G. Kotliar, S. Y. Savrasov, G. Pálsson, and G. Biroli, Phys. Rev. Lett. **87**, 186401 (2001).

[6] T. Maier, M. Jarrell, T. Pruschke, and M. H. Hettler, Rev. Mod. Phys. **77**, 1027 (2005).

[7] K. Held, I. A. Nekrasov, G. Keller, V. Eyert, N. Blümer, A. K. McMahan, R. T. Scalettar, T. Pruschke, V. I. Anisimov, and D. Vollhardt, Phys. Stat. Sol. B **243**, 2599 (2006).

[8] S. Biermann, F. Aryasetiawan, and A. Georges, Phys. Rev. Lett. **90**, 086402 (2003).

[9] K. Held, C. Taranto, G. Rohringer, and A. Toschi, in *The LDA + DMFT Approach to Strongly Correlated Materials*, edited by E. Pavarini, E. Koch, D. Vollhardt, and A. Lichtenstein (Forschungszentrum Jülich, Institute for Advanced Simulations, Jülich, 2011), p. 13.1.

[10] C. Taranto, M. Kaltak, N. Parragh, G. Sangiovanni, G. Kresse, A. Toschi, and K. Held, arXiv:1211.1324.

[11] J. M. Tomczak, M. Casula, T. Miyake, F. Aryasetiawan, and S. Biermann, Europhys. Lett. **100**, 67001 (2012).

[12] G. Kotliar and D. Vollhardt, Phys. Today **3**, 53 (2004).

[13] R. Jördens, L. Tarruell, D. Greif, T. Uehlinger, N. Strohmaier, H. Moritz, T. Esslinger, L. De Leo, C. Kollath, A. Georges, V. Scarola, L. Pollet, E. Burovski, E. Kozik, and M. Troyer, Phys. Rev. Lett. **104**, 180401 (2010).

[14] E. V. Gorelik, I. Titvinidze, W. Hofstetter, M. Snoek, and N. Blümer, Phys. Rev. Lett. **105**, 065301 (2010).

[15] E. V. Gorelik, D. Rost, T. Paiva, R. Scalettar, A. Klümper, and N. Blümer, Phys. Rev. A **85**, 061602(R) (2012).

[16] M. Jarrell, Phys. Rev. Lett. **69**, 168 (1992).

[17] A. Georges and G. Kotliar, Phys. Rev. B **45**, 6479 (1992).

[18] V. Janiš and D. Vollhardt, Int. J. Mod. Phys. B **06**, 731 (1992).

[19] J. E. Hirsch and R. M. Fye, Phys. Rev. Lett. **56**, 2521 (1986).

[20] N. Blümer, in *The LDA + DMFT Approach to Strongly Correlated Materials*, edited by E. Pavarini, E. Koch, D. Vollhardt, and A. Lichtenstein (Forschungszentrum Jülich, Institute for Advanced Simulations, Jülich, 2011), p. 9.1.

[21] R. M. Fye and R. T. Scalettar, Phys. Rev. B **36**, 3833 (1987).

[22] N. Blümer and E. Kalinowski, Phys. Rev. B **71**, 195102 (2005); Physica B **359–361**, 648 (2005).

[23] N. Blümer, Phys. Rev. B **76**, 205120 (2007).

[24] A. N. Rubtsov, V. V. Savkin, and A. I. Lichtenstein, Phys. Rev. B **72**, 035122 (2005).

[25] P. Werner, A. Comanac, L. de' Medici, M. Troyer, and A. J. Millis, Phys. Rev. Lett. **97**, 076405 (2006).

[26] P. Werner and A. J. Millis, Phys. Rev. B **74**, 155107 (2006).

[27] E. Gull, A. J. Millis, A. I. Lichtenstein, A. N. Rubtsov, M. Troyer, and P. Werner, Rev. Mod. Phys. **83**, 349 (2011).

[28] E. Gull, P. Werner, A. Millis, and M. Troyer, Phys. Rev. B **76**, 235123 (2007).

[29] M. Caffarel and W. Krauth, Phys. Rev. Lett. **72**, 1545 (1994).

[30] E. Koch, in *The LDA + DMFT Approach to Strongly Correlated Materials*, edited by E. Pavarini, E. Koch, D. Vollhardt, and A. Lichtenstein (Forschungszentrum Jülich, Institute for Advanced Simulations, Jülich, 2011), p. 8.1.

[31] E. Khatami, C. R. Lee, Z. J. Bai, R. T. Scalettar, and M. Jarrell, Phys. Rev. E **81**, 056703 (2010).

[32] R. Blankenbecler, D. J. Scalapino, and R. L. Sugar, Phys. Rev. D **24**, 2278 (1981).

[33] E. Khatami, K. Mikelsons, D. Galanakis, A. Macridin, J. Moreno, R. T. Scalettar, and M. Jarrell, Phys. Rev. B **81**, 201101 (2010).

[34] N. Blümer, arXiv:0801.1222; E. V. Gorelik and N. Blümer, Phys. Rev. A **80**, 051602 (2009).

[35] C. Knecht, Master's thesis, Johannes Gutenberg-Universität Mainz, 2003.

[36] N. Blümer, Ph.D. thesis, University of Augsburg, 2002.

[37] A. Rubtsov and A. Lichtenstein, Sov. Phys. JETP **80**, 61 (2004).

[38] E. Gull, P. Werner, O. Parcollet, and M. Troyer, Europhys. Lett. **82**, 57003 (2008).

[39] E. Koch, G. Sangiovanni, and O. Gunnarsson, Phys. Rev. B **78**, 115102 (2008).

[40] D. Sénéchal, Phys. Rev. B **81**, 235125 (2010).

[41] In our experience, this choice for w_n is not crucial: other choices lead to very similar results.

[42] F. F. Assaad and H. G. Evertz, in *Computational Many Particle Physics*, Lecture Notes in Physics, Vol. 739, edited by H. Fehske, R. Schneider, and A. Weiße (Springer Verlag, Berlin, 2008), p. 277.

[43] C.-R. Lee, I.-H. Chung, and Z. Bai, in *IEEE International Parallel and Distributed Processing Symposium (IPDPS)* (IEEE Computer Society Press, Washington, DC, 2010), pp. 1–9.

[44] J. Joo and V. Oudovenko, Phys. Rev. B **64**, 193102 (2001).

[45] C. Knecht, N. Blümer, and P. G. J. van Dongen, Phys. Rev. B **72**, 081103 (2005).

[46] A reasonably good approximation of the curvature of $G(\tau)$ at the boundaries by the reference Green function is the only crucial requirement for this procedure; it can also be achieved using other model self-energies or, alternatively, via maximum entropy analytic continuation of the "best" measured $G_{(\Delta\tau)_i}$.

[47] P. Craven and G. Wahba, Numer. Math. **31**, 377 (1978).

[48] I. G. Enting, C. M. Trudinger, and D. M. Etheridge, Tellus B **58**, 305 (2006).

[49] D. Rost, E. V. Gorelik, F. Assaad, and N. Blümer, Phys. Rev. B **86**, 155109 (2012).

[50] N. Blümer and E. V. Gorelik, Phys. Rev. B **87**, 085115 (2013).

[51] B. Bauer, L. D. Carr, H. G. Evertz, A. Feiguin, J. Freire, S. Fuchs, L. Gamper, J. Gukelberger, E. Gull, S. Guertler, A. Hehn, R. Igarashi, S. V. Isakov, D. Koop, P. N. Ma, P. Mates, H. Matsuo, O. Parcollet, G. Pawłowski, J. D. Picon, L. Pollet, E. Santos, V. W. Scarola, U. Schollwöck, C. Silva, B. Surer, S. Todo, S. Trebst, M. Troyer, M. L. Wall, P. Werner, and S. Wessel, J. Stat. Mech. Theor. Exp. (2011) P05001.

[52] M. Kollar, M. Eckstein, K. Byczuk, N. Blümer, P. van Dongen, M. Radke De Cuba, W. Metzner, D. Tanasković, V. Dobrosavljević, G. Kotliar, and D. Vollhardt, Ann. Phys. **14**, 642 (2005).

[53] The results shown in Fig. 6 correspond to the following grids of the discretization $\Delta\tau$: [0.29, 0.40, 0.50, 0.60, 0.69, 0.78, 0.89, 0.96] (yellow line), [0.29 0.34 0.40 0.44 0.50 0.54 0.60] (light blue line), and [0.19 0.25 0.29 0.34 0.40 0.44 0.50 0.54 0.60] (dark blue line).

[54] Specifically, we have used fit laws of the form $\ln[D(\Delta\tau)] = D(\Delta\tau = 0) + A(\Delta\tau)^2$.

[55] L. C. Martin and F. F. Assaad, Phys. Rev. Lett. **101**, 066404 (2008); L. C. Martin, M. Bercx, and F. F. Assaad, Phys. Rev. B **82**, 245105 (2010).

Fate of the false Mott-Hubbard transition in two dimensions

T. Schäfer,[1] F. Geles,[2] D. Rost,[3,4] G. Rohringer,[1] E. Arrigoni,[2] K. Held,[1] N. Blümer,[3] M. Aichhorn,[2] and A. Toschi[1]

[1]*Institute of Solid State Physics, Vienna University of Technology, 1040 Vienna, Austria*

[2]*Institute of Theoretical and Computational Physics, Graz University of Technology, Graz, Austria*

[3]*Institute of Physics, Johannes Gutenberg University, Mainz, Germany*

[4]*Graduate School Materials Science in Mainz, Johannes Gutenberg University, Mainz, Germany*

(Received 13 June 2014; revised manuscript received 10 February 2015; published 3 March 2015)

We have studied the impact of nonlocal electronic correlations at all length scales on the Mott-Hubbard metal-insulator transition in the unfrustrated two-dimensional Hubbard model. Combining dynamical vertex approximation, lattice quantum Monte Carlo, and variational cluster approximation, we demonstrate that scattering at long-range fluctuations, i.e., Slater-like paramagnons, opens a spectral gap at weak-to-intermediate coupling, irrespective of the preformation of localized or short-range magnetic moments. This is the reason why the two-dimensional Hubbard model has a paramagnetic phase which is insulating at low enough temperatures for any (finite) interaction and no Mott-Hubbard transition is observed.

DOI: 10.1103/PhysRevB.91.125109 PACS number(s): 71.27.+a, 71.10.Fd, 71.30.+h

I. INTRODUCTION

The Mott-Hubbard metal-insulator transition (MIT) [1] is one of the most fundamental hallmarks of the physics of electronic correlations. Nonetheless, astonishingly little is known exactly, even for its simplest modeling, i.e., the single-band Hubbard Hamiltonian [2]: Exact solutions for this model are available only in the extreme, limiting cases of one and infinite dimensions.

In one dimension, the Bethe ansatz shows that there is actually no Mott-Hubbard transition [3–5]; in other words, it occurs for a vanishingly small Hubbard interaction U. At any $U > 0$ the one-dimensional (1D) Hubbard model is insulating at half filling. One dimension is, however, rather peculiar: While there is no antiferromagnetic ordering even at temperature $T = 0$, antiferromagnetic spin fluctuations are strong and long ranged, decaying slowly, i.e., algebraically. Also, the (doped) metallic phase is not a standard Fermi liquid but a Luttinger liquid.

For the opposite extreme, infinite dimensions, the dynamical mean-field theory (DMFT) [6] becomes exact [7], which allows for a clear-cut and, to a certain extent, almost "idealized" description of a pure Mott-Hubbard MIT. In fact, since in $D=\infty$ only local correlations survive [7], the Mott-Hubbard insulator of DMFT consists of a collection of localized (but not long-range ordered) magnetic moments. This way, if antiferromagnetic order is neglected or sufficiently suppressed, DMFT describes a first-order MIT [6,8], ending with a critical end point.

As an approximation, DMFT is applicable to the more realistic cases of the three- and two-dimensional Hubbard models. However, the DMFT description of the MIT is the very same here since only the noninteracting density of states (DOS) and, in particular, its second moment enter. This is a natural shortcoming of the mean-field nature of DMFT: antiferromagnetic fluctuations have *no* effect at all on the DMFT spectral function or self-energy above the antiferromagnetic ordering temperature T_N.

In three dimensions, antiferromagnetic fluctuations reduce T_N sizably compared to the DMFT (see Fig. 1), although they are significant only at $T \simeq T_N$. Hence, the reliability of the DMFT results for the spectral functions is not spoiled in three dimensions except for the proximity of the antiferromagnetic transition [9–12], whereas deviations from the DMFT entropy and susceptibilities can be significant also at higher T [12,13]. With this background, it is maybe not surprising that DMFT also yields a good description of the MIT even for realistic material cases, such as the textbook example V_2O_3 [14].

Much more intriguing, and challenging, is the two-dimensional (2D) case, which is most relevant for high-temperature superconductivity and the rapidly emerging field of oxide thin films and heterostructures. In fact, this issue has been intensely debated since the 1970s: On the one hand, several analytical and numerical results [15–20] suggested that a metallic phase is found at weak coupling, with a MIT at a finite U_c. At the same time, calculations with the two-particle self-consistent (TPSC) approach [21–23] showed a pseudogap in the perturbative regime of small U [24]. Finally, in Anderson's view [25] the 2D physics should be considered fully nonperturbative, similar [5] to that in one dimension, yielding a Mott gap and the localized physics of the 2D Heisenberg Hamiltonian for all $U > 0$.

More recently, most precise numerical studies have shown unambiguously that the short-range spin fluctuations do actually reduce the critical interaction U_c for the MIT in two dimensions compared to DMFT *and* reverse its slope (see Fig. 1). (Note that the DMFT insulating phase has the full entropy of free spins, i.e., $\ln 2$ per site, implying the positive DMFT slope $dU_c/dT > 0$ of Fig. 1.) Such a 2D picture has been established by cluster DMFT (CDMFT) [26], dynamical cluster approximation (DCA) [27,28], and second-order dual-fermion [29] studies [30], which systematically include nonlocal correlations beyond DMFT. However, given the limited cluster sizes of CDMFT and DCA calculations, only short-range correlations are included.

In this paper, we revisit the MIT in two dimensions and the effect of antiferromagnetic spin-fluctuations thereupon. To this end, we employ three methods: (i) the variational cluster approximation (VCA) [31], which includes short-range correlations, (ii) the dynamical vertex approximation (DΓA), which includes short- *and* long-range correlations beyond DMFT on the same footing [32], and (iii) lattice quantum Monte Carlo (QMC) simulations [33–35] of unprecedented accuracy

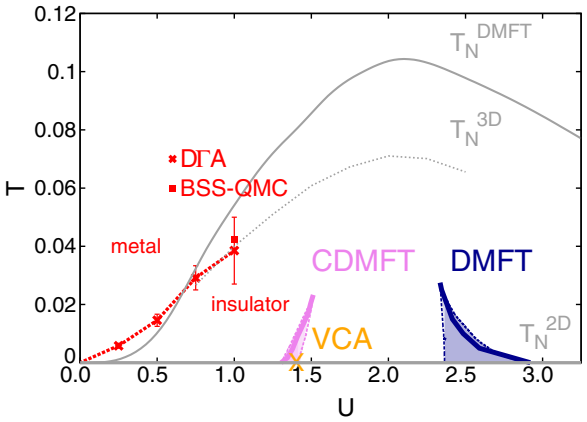

FIG. 1. (Color online) MIT of the Hubbard model on a square lattice determined by different nonperturbative techniques. The DMFT transition line (blue [39]) is shifted towards lower interaction values due to short-range spatial correlations (violet line: CDMFT [26]; orange cross at $T = 0$: VCA). This trend is accompanied by a simultaneous shrinking of the coexistence regions (hatched regions). The inclusion of long-range fluctuations leads to a vanishing U_c in the low-temperature regime (crosses and red dashed line: DΓA; solid red box: BSS-QMC). Error bars mark the temperature range, where the onset of an insulating behavior on the whole Fermi surface has been found, according to the electronic self-energy of DΓA (see Fig. 3). Also shown are the DMFT [9] and the DΓA 3D Néel temperatures (light gray dotted lines) [11] as well as the DΓA 2D one (gray line at $T = 0$) [40] which fulfills the Mermin-Wagner theorem [41]; $4t \equiv 1$ sets the energy scale.

made possible by the algorithmic progress, increased computer power, and careful extrapolations (see the Appendix) [36,37].

II. PHASE DIAGRAM IN TWO DIMENSIONS

Let us first summarize the results of our combined comparative studies for the half-filled Hubbard model on a square lattice with nearest-neighbor hopping $t \equiv 1/4$ using the phase diagram in Fig. 1; all details on the spectra and the underlying physics of the different regimes are presented afterwards.

Our VCA data for the MIT at zero temperature (orange cross in Fig. 1) appear to be consistent with the previous CDMFT, DCA, and older VCA [38] studies, as well as with second-order dual-fermion [29] calculations [30]: short-range antiferromagnetic correlations reduce the critical U_c (violet line) significantly with respect to DMFT. Moreover, the width of the coexistence region is considerably reduced (see the violet hatched area for CDMFT [26]). The VCA calculations performed on different clusters, however, also suggest something more definite in this respect: At low temperatures, the smaller U is, the more important the effect of longer-range antiferromagnetic fluctuations becomes.

To address this issue in more detail, we include such long-range correlations by means of DΓA. Results are also compared with lattice Blankenbecler-Scalapino-Sugar (BSS) QMC calculations [33]. The red dashed line in Fig. 1 marks the interaction $U_c(T)$, above which, for a given temperature T, a spectral gap is opened because of a strong enhancement of the electronic scattering rate in the very low frequency regime (see below).

These DΓA data, confirmed by our extrapolated BSS-QMC data, strongly suggest that at low enough T strong antiferromagnetic spin fluctuations *always* open a spectral gap, even at arbitrarily small values of U (red dashed line in Fig. 1). Hence, for $T \to 0$, $U_c \to 0$; that is, *no* MIT can be identified any longer for the 2D unfrustrated Hubbard model, similar to what happens in one dimension. As we will elaborate in the following, the mechanism is, however, rather different in this case. By increasing U the temperature of the onset of the insulating behavior is enhanced until the high-temperature crossover regime of DMFT at intermediate U is reached: Here, the electron mobility is already suppressed by purely local correlations.

Our results for the phase diagram indicate that the "idealized" physical picture of the Mott-Hubbard metal-insulator transition of DMFT is completely overturned in two dimensions by strong, spatially extended antiferromagnetic correlations. In the following, we will discuss explicitly the most important aspects in terms of spatial correlations over different length scales and their underlying physics by analyzing in detail the numerical data used for determining the phase diagram in two dimensions.

III. SHORT-RANGE CORRELATIONS

The physics of short-range correlations at $T = 0$ is captured very well by VCA in the paramagnetic phase. In fact, our results for a VCA cluster of $N_c = 4$ sites (plus four bath sites) show a clear-cut MIT at a finite $U_c = 1.4$ for $T = 0$, within the CDMFT coexistence region of a metallic and an insulating solution. The local spectral function $A(\omega)$ and the self-energy $\Sigma(i\omega_n)$ at the Fermi level of the two coexisting solutions at $U = U_c = 1.4$ are reported in Fig. 2. The two solutions differ qualitatively, showing a correlated metallic behavior with a quasiparticle weight of $Z_{\mathrm{VCA}} = 0.37$ at $\mathbf{k} = (\pi,0)$ (bottom panel) and an insulating behavior (top panel) characterized by a divergence of Im $\Sigma(i\omega_n)$ and a corresponding spectral gap, respectively. The VCA calculation of the grand potential indicates that for $U < U_c = 1.4$ the thermodynamically stable solution is the metallic one, while for $U > 1.4$ the insulator is stabilized, with a level crossing at $U = U_c$. Such a U_c value is in fairly good agreement with CDMFT [26]; it gets reduced by slightly increasing the lattice size in the VCA calculations from $U_c = 1.4$ for $N_c = 4 = 2 \times 2$ to $U_c = 1.325$ for $N_c = 6 = 2 \times 3$. This reflects the fact that correlations of very short range (actually two sites in the case of $N_c = 4$) are strong enough to destroy the low-temperature metallic phase at intermediate coupling but are less effective for lower values of the interaction. In fact, in the presence of a $T = 0$ (magnetic) instability, a correct description of the weak-coupling regime in two dimensions cannot be obtained without the inclusion of correlations on *all* length scales, as we show in the following.

IV. LONG-RANGE CORRELATIONS

We include correlations on all length scales by either extrapolating lattice BSS-QMC results to $N_c \to \infty$ or using DΓA [32] in its ladder version [40], a diagrammatic extension

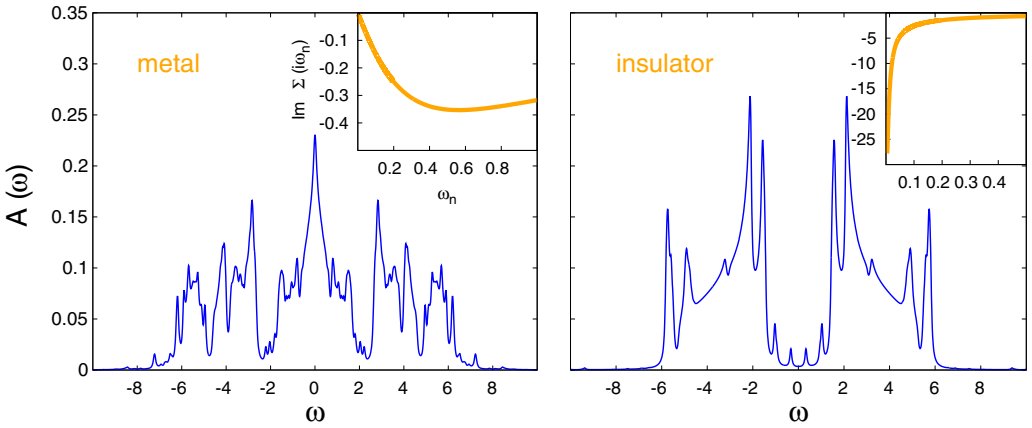

FIG. 2. (Color online) Local spectral function of the two coexisting solutions obtained in VCA at the $T = 0$, $U = U_c = 1.4$ MIT for a four-site cluster plus four bath sites. (left) Metallic solution; (right) insulating solution. The insets show the corresponding self-energies at $\mathbf{k} = (\pi,0)$.

of DMFT (see [29,42,43]) based on the two-particle vertex [44,45]. Certainly, both approaches have their limitations, either due to the extrapolation procedure of the cluster results (see the Appendix) or due to the selection of the more relevant subsets of diagrams. Hence, cross-checking the results of these complementary approaches, as we do here, is of utmost importance. In fact, the good agreement observed (top panels of Fig. 3) validates our results and at the same time supports the physical interpretation discussed below. The top panels of Fig. 3 show our DΓA and BSS-QMC data of the imaginary part of the electronic self-energy $\Sigma(\mathbf{k},i\omega_n)$ for the most significant $\mathbf{k}$ points at the Fermi surface [i.e., the "nodal" point $\mathbf{k} = (\frac{\pi}{2},\frac{\pi}{2})$ and the "antinodal" point $\mathbf{k} = (\pi,0)$] as a function of Matsubara frequencies for a rather small value of $U = 0.5$ at two different temperatures ($T = 0.025$ and $T = 0.010$). Here, one can immediately appreciate how the one-particle physics changes even qualitatively when reducing T: At $T = 0.025$ both DΓA (top left panel) and lattice QMC (left inset) self-energies display a Fermi-liquid behavior for all $\mathbf{k}$ points, not radically different from the DMFT results (blue squares in Fig. 3). Even the quasiparticle renormalization $Z = (1 - \frac{\partial \mathrm{Im}\Sigma(\mathbf{k},i\omega_n)}{\partial\omega_n}|_{\omega_n\to 0})^{-1} \simeq 0.9$ is similar. In contrast, the scattering rate γ at the Fermi surface is increased from $\gamma_{\mathrm{DMFT}} = -\mathrm{Im}\Sigma_{\mathrm{DMFT}}(\mathbf{k},i0^+) = 0.002$ to ($\mathbf{k}$ averaged) $\bar{\gamma}_{D\Gamma A} \simeq 0.014$, with a moderate $\mathbf{k}$ differentiation [46]. By reducing T, $\gamma_{D\Gamma A}$ quickly gets enhanced on the whole Fermi surface, always displaying its largest value at $\mathbf{k} = (\pi,0)$. At $T = 0.010$ the self-energy has already changed completely (see Fig. 3, right): $\mathrm{Im}\Sigma(\mathbf{k},i\omega_n)$ acquires an evident downturn for all $\mathbf{k}$ points at very low frequencies. This shows that the Fermi surface is completely destroyed at low T, even at the nodal momentum $\mathbf{k} = (\pi/2,\pi/2)$. Such a qualitative change in the low-frequency self-energy behavior has been exploited for defining the red dashed line marking the destruction of the whole Fermi surface and hence insulating behavior in our phase diagram (Fig. 1).

V. PHYSICAL INTERPRETATION

Our combined numerical analysis shows that there is no Mott-Hubbard transition at finite U in the unfrustrated 2D Hubbard model, but it also clarifies unambiguously the physical origin of this result. Evidently, the shift of the border of the MIT towards $U = 0$ (Fig. 1) already represents an indication for rather extended spatial fluctuations, which emerge from the proximity to the $T = 0$ long-range antiferromagnetic order. The important questions still to be answered are, Can this intuitive picture be confirmed in a less heuristic and more direct way? What is the exact nature of these extended antiferromagnetic spin fluctuations? These questions can be answered by extending our study of the low-T weak-coupling regime to the DΓA spin-correlation function $\chi_s(\mathbf{r},i\Omega_n = 0) = \int_0^\beta d\tau \langle S_z(\mathbf{r},\tau)S_z(0,0)\rangle$ in real space. Our results for $U = 0.5$ are reported in the middle panels of Fig. 3, where we show, as a representative case, the spatial decay of χ_s along the x direction, normalized to its $\mathbf{r} = 0$ value at $T = 0.025$ (metal) and $T = 0.010$ (insulator): In both cases, χ_s displays an alternating sign, which is the typical hallmark of predominant antiferromagnetic fluctuations. The spatial extensions of such fluctuations are quite different, however. In fact, the long-distance behavior of χ_s can be approximated by its asymptotic expression $|\chi_s(r\to\infty)| \propto \sqrt{\frac{\xi}{r}}\, e^{-r/\xi}$ [47]. But the correlation length ξ varies from ~ 4 in the metallic phase to values of $\xi \approx 1000$ in the low-T insulating phase. A more quantitative understanding is provided by the study of the T dependence of ξ in DΓA (see bottom panels of Fig. 3). By reducing T, ξ displays a well-defined crossover to an exponential behavior, which approximately matches the onset of the low-T insulating regime at weak coupling. This shows that the spin fluctuations responsible for the destruction of the Fermi surface at low T have such a large spatial extension that it is difficult to capture with (nonextrapolated) cluster calculations [48,49]. For instance, the corresponding VCA self-energy at $T = 0$ (orange curve in Fig. 3) displays a very clear metallic behavior, similar to that of DMFT.

Insight can also be gained from the potential energy. Our DΓA and BSS-QMC results show that the destruction of the metallic state upon decreasing T is accompanied by a slight reduction in potential energy $U\langle n_\uparrow n_\downarrow\rangle$ by about 1% for the data in Fig. 3. However, this effect occurs in the presence of strong and very extended ($\xi \gg 100$) spin correlations.

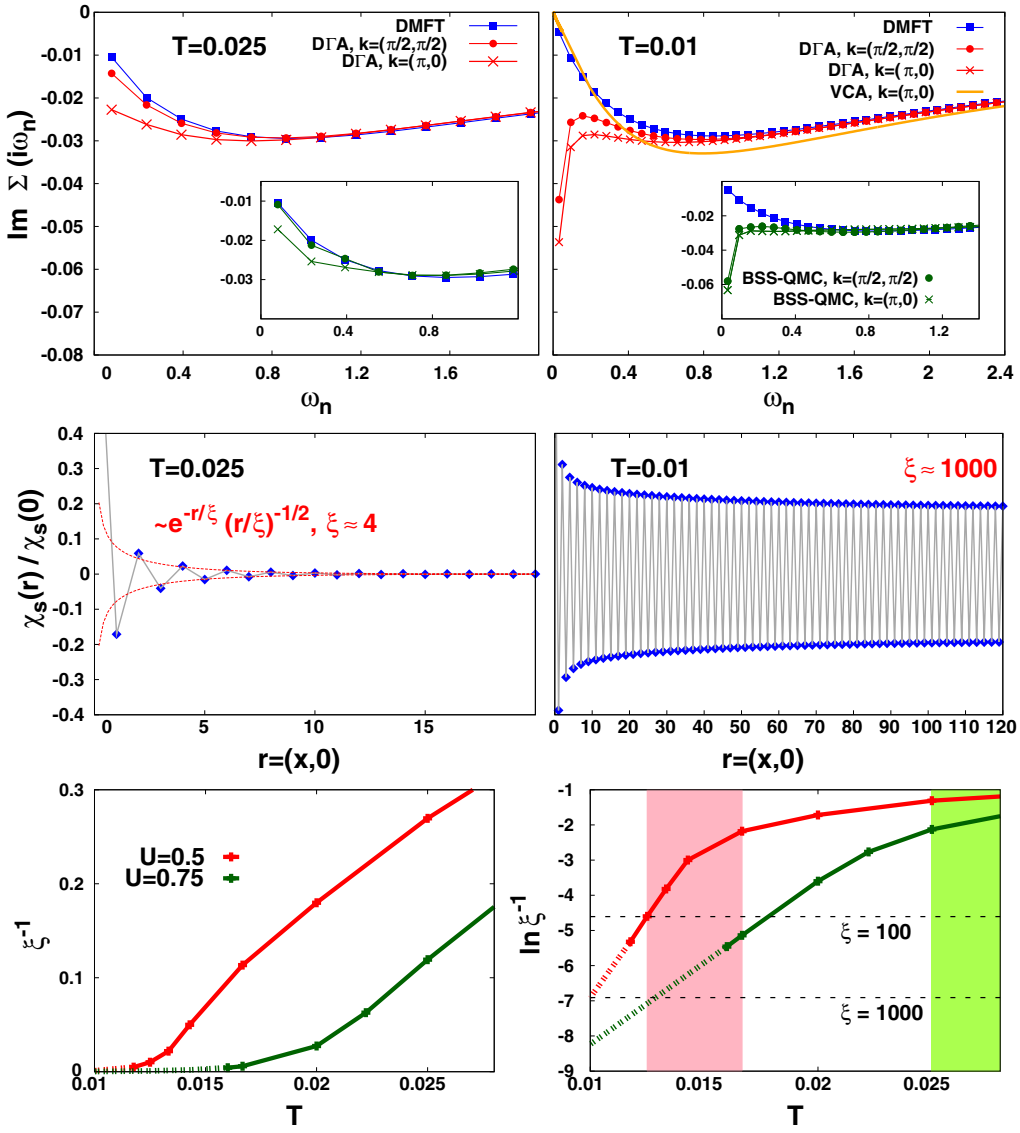

FIG. 3. (Color online) (top) Imaginary parts of the self-energies for $U = 0.5$ and $T = 0.025$ (left) and $T = 0.010$ (right), comparing DMFT (blue squares), DΓA [red circles: $\mathbf{k} = (\pi/2,\pi/2)$; red crosses: $\mathbf{k} = (\pi,0)$], VCA (orange; $T = 0$), and BSS-QMC (insets; see the Appendix). Even for the very small interaction $U = 0.5$ an insulating gap is opened at $T \approx 0.014$ in DΓA as well as in BSS-QMC. (middle) Real-space dependence of the DΓA spin-correlation function $\chi_s(\mathbf{r})/\chi_s(\vec{0})$ for the same parameters as above. Shown is the cut $\mathbf{r} = (x,0)$, where x is given in units of the lattice spacing $a = 1$. The solid gray line (guide to the eye) interpolates between the values at different lattice vectors (blue diamonds). By fitting (see also the dashed lines in the bottom panels) we obtain the correlation lengths $\xi \approx 4$ at $T = 0.025$ (left), while $\xi \approx 1000$ at $T = 0.010$ (right). (bottom) T dependence of ξ^{-1} for different interaction values. A crossover to an exponential behavior is observed at T consistent with the onset of the insulating behavior [pink (green) area for $U = 0.5$ (0.75)].

Therefore, the physics cannot be really different from the truly long-range ordered phase [50]. This rules out any particular role of prelocalization of the magnetic moments in destroying the Fermi-liquid state, as well as the possibility of mapping the whole low-T physics onto the 2D Heisenberg model, as proposed by Anderson [25]. Rather, the emerging physics appears to be more consistent with the description of the TPSC approach [22,23], at least in the weak-coupling regime, and of the low-T calculations with the nonlinear sigma model [51], as well as to the experimental estimates of ξ in electron-doped cuprates [52]. In fact, the slight decrease in the potential energy is a clear hallmark [53–55] of the Slater-like nature of the antiferromagnetic fluctuations as is the large ξ. We can hence interpret this as "Slater paramagnons." The corresponding physical picture is the following: For all $U > 0$, a gap is opened at low enough T because of the enhanced electronic scattering with extended antiferromagnetic paramagnons. The nature of such spin fluctuations, reflecting the behavior of the $T = 0$ ordered phase [51,56] from which they originate, smoothly evolves from Slater (weak to intermediate coupling) to Heisenberg (strong coupling). In this respect, it is worth recalling that DCA results [53] on small clusters ($N_c = 4$) also suggest the crossover from Slater-like to Heisenberg-like fluctuations for U larger than (at least) 1.25. Although still smaller [48], these interaction values are not too far away from the regime where the crossover to Heisenberg physics

is predicted to occur in the long-range ordered phase by DMFT [54].

VI. CONCLUSIONS

We have studied the effects of spatial correlations on different length scales on the MIT in the 2D half-filled Hubbard model: for all $U > 0$, at low enough (but finite) T, we find a paramagnetic insulator. This is the result of strong scattering at extended antiferromagnetic fluctuations (paramagnons). The nature of these fluctuations gradually evolves from Slater-like to Heisenberg-like, tracking an analogous evolution for the $T = 0$ antiferromagnet. This physical picture is quite different from both state-of-the art DMFT/CDMFT, which finds a finite U_c for the (metastable) paramagnetic phase, and the strong-coupling idea of an effective low-T 2D Heisenberg model, which assumes preformed spins even at low U. Instead, the 2D Hubbard model has $U_c = 0$, and the nature of the most relevant spin fluctuations is Slater-like in the whole weak- to intermediate-coupling regime. Let us stress that if we frustrate the 2D square lattice away from perfect nesting, e.g., by adding a nearest-neighbor hopping, antiferromagnetism and hence the MIT originating from antiferromagnetic fluctuations are expected to shift to a finite $U_c > 0$, implying a quantum critical point.

ACKNOWLEDGMENTS

We thank S. Andergassen, M. Capone, M. Fabrizio, E. Gull, O. Gunnarsson, H. Hafermann, J. Le Blanc, A. Katanin, C. Taranto, and A. Valli for discussions. We acknowledge support from the Austrian Science Fund (FWF) through the Doctoral School "Building Solids for Function" (T.S.; FWF project ID W1243), SFB ViCoM (E.A., F.G., K.H., M.A., A.T.; FWF project ID F4103), and NAWI Graz; from the research unit FOR 1346 and the graduate school GSC 266 of the German Research Foundation (DFG) (DR,NB). Calculations were performed on the Vienna Scientific Cluster (VSC).

APPENDIX

The numerical results presented in this paper have been obtained using complementary techniques with quite different characteristics. Among those, the dynamical vertex approximation (DΓA) yields results directly in the thermodynamic limit [32]; the variational cluster approximation (VCA), on the other hand, is good for short-range correlations [31], and finally, the Blankenbecler-Scalapino-Sugar (BSS) QMC calculations for the Hubbard model are applicable to clusters with a finite number N of lattice sites, with $N = L^2$ for square lattices with linear extent L. In its generic formulation, the BSS-QMC algorithm introduces a further systematic bias due to a Trotter discretization of the imaginary time [33]. In this work, we employ a multigrid approach for obtaining quasicontinuous imaginary-time Green's functions without significant Trotter bias [37], which can be reliably Fourier transformed in order to compute self-energies; similar strategies have proven successful in the context of DMFT studies using the Hirsch-Fye QMC algorithm [36,57,58]. As a result, all "raw" data shown in this appendix should be regarded as numerically exact for a given cluster size. The BSS-QMC computational effort scales as N^3/T at temperature T, i.e., proportionally to L^6 at fixed T, which limits high-precision calculations (as we need here for determining the self-energy on the percent level) to $L \lesssim 16$. The properties of such finite systems will, in general, depend on the exact system size (and shape as well as boundary conditions) and may deviate drastically from the thermodynamic limit.

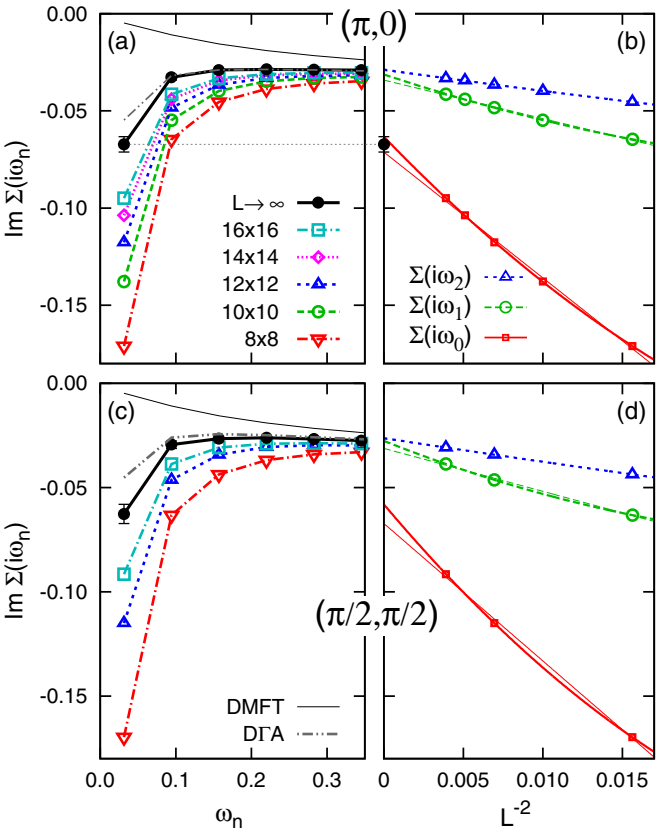

FIG. 4. (Color online) Self-energy on the imaginary axis at $U = 0.5$, $\beta = 100$. (a) Finite-size BSS-QMC data (open symbols and colored lines), extrapolated BSS-QMC results in the thermodynamic limit (circles and thick black solid line), and DΓA data (gray dash-double-dotted line) vs Matsubara frequency ω_n at momentum $\mathbf{k} = (\pi,0)$; also shown are momentum-independent single-site DMFT results (thin black line). (b) Finite-size BSS-QMC (symbols) data for the first three Matsubara frequencies vs inverse system size plus extrapolations in linear order in L^{-2} (thin lines) and quadratic order (thick lines). (c) and (d) Analogous analysis at $\mathbf{k} = (\pi/2,\pi/2)$.

We will show in the following that reliable extrapolations to the thermodynamic limit, as shown in Fig. 3, are still possible in the parameter range of interest based on BSS-QMC data obtained for quadratic clusters (with periodic boundary conditions) and linear extents $L = 8,10,12,14,16$.

In the left column of Fig. 4, estimates of the self-energy $\Sigma(\mathbf{k},i\omega_n)$ at interaction $U = 0.5$ and inverse temperature $\beta = 100$ are shown versus Matsubara frequency ω_n for the two momenta $\mathbf{k} = (\pi,0)$ [Fig. 4(a)] and $\mathbf{k} = (\pi/2,\pi/2)$ [Fig. 4(c)]; due to particle-hole symmetry the self-energy is purely imaginary at these $\mathbf{k}$ points. Finite-size (FS) BSS-QMC data

(open symbols and colored lines) depend strongly on the lattice size: with decreasing linear extent L, they show increasingly insulating tendencies, i.e., larger absolute values of Im $\Sigma(i\omega_n)$ at the lowest ω_n. However, as demonstrated in Fig. 4(b), for the lowest three Matsubara frequencies at $\mathbf{k} = (\pi,0)$, this bias is very systematic: Already linear extrapolations in the inverse size L^{-2} (thin solid lines) yield reasonable first estimates of the thermodynamic limit $L^{-2} \to 0$. Much better fits can be obtained at higher orders, e.g., using quadratic fits in L^{-2} (thick lines); however, these become increasingly unstable (in the presence of statistical noise) at higher orders. In order to define a consistent procedure that is also stable at $\mathbf{k} = (\pi/2,\pi/2)$, where fewer system sizes are available (see below), we use the average of linear and quadratic extrapolation as the final result, with error bars that coincide with the individual extrapolations, as illustrated by the black circle with error bars for $\Sigma(i\omega_0)$ in Fig. 4(b):

$$\Sigma^{\infty} = \tfrac{1}{2}\left(\Sigma^{\infty}_{\text{lin}} + \Sigma^{\infty}_{\text{quad}}\right), \quad \Delta\Sigma^{\infty} = \tfrac{1}{2}\left|\Sigma^{\infty}_{\text{lin}} - \Sigma^{\infty}_{\text{quad}}\right|.$$

The final result of this extrapolation [black circles in Fig. 4(a)] shows perfect agreement with DΓA (gray dash-double-dotted line) at almost all Matsubara frequencies. A minor quantitative deviation is only observed at the smallest Matsubara frequency, at which the absolute value of $\text{Im}\Sigma(\mathbf{k},\omega)$ is somewhat smaller in DΓA.

Since only lattices with linear dimensions $L = 4,8,12,\ldots$ contain the momentum $\mathbf{k} = (\pi/2,\pi/2)$ in the Brillouin zone (for periodic boundary conditions), we have only three system sizes available for extrapolation in this case [symbols in Fig. 4(d)]. However, the curvatures of the (here, necessarily perfect but intrinsically somewhat unstable) quadratic fits agree well with those obtained at $\mathbf{k} = (\pi,0)$, which supports their reliability. Again, the DΓA prediction (here, a metallic self-energy with a visible momentum differentiation) agrees well with the final BSS-QMC results [black circles in Fig. 4(c)].

At the elevated temperature $T = 1/40$, the finite-size bias affects the raw BSS-QMC results even more drastically, as seen in Fig. 5: at both $\mathbf{k}$ points, the smallest systems (8×8, red downward triangles) have clearly insulating character, while DΓA (dash-double-dotted line) yields a metallic solution,

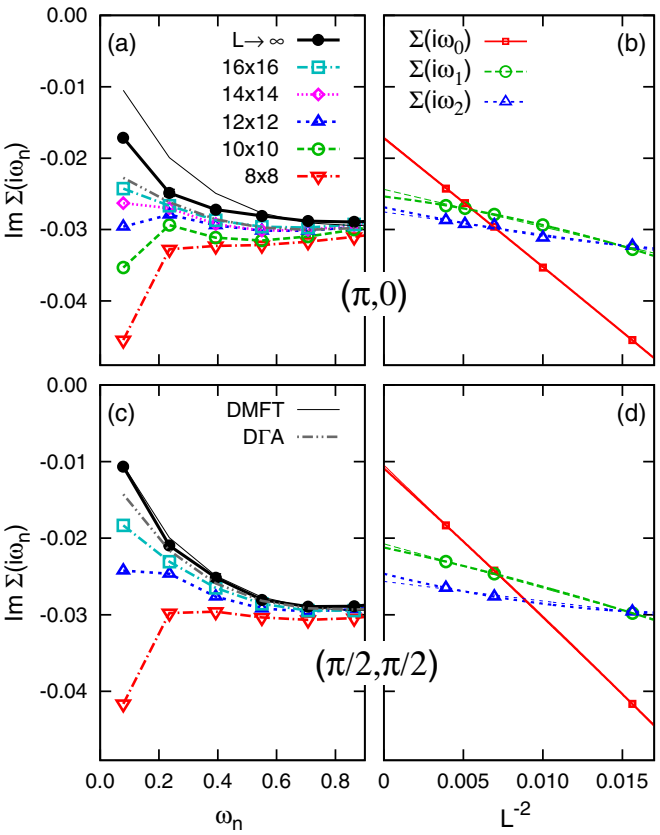

FIG. 5. (Color online) Self-energy on the imaginary axis at $U = 0.5$, $\beta = 40$, analogous to Fig. 4.

just like (paramagnetic) DMFT (thin gray line). However, the 16×16 system (squares) is already large enough to show significant metallic tendencies. Even more importantly, Figs. 5(b) and 5(d) demonstrate that the dependency of the raw BSS-QMC data on L^{-2} is very regular and almost linear again (even across the FS-induced metal-insulator crossover), so that the extrapolation $L^{-2} \to 0$ is still reliable, with even smaller resulting error bars than at $T = 1/100$. Interestingly, the final BSS-QMC results at $\mathbf{k} = (\pi/2,\pi/2)$ [black circles in Fig. 5(c)] agree with DMFT within error bars; only at $\mathbf{k} = (\pi,0)$ do nonlocal antiferromagnetic correlations induce a significantly more insulating character.

[1] N. F. Mott, Rev. Mod. Phys. **40**, 677 (1968); *Metal-Insulator Transitions* (Taylor and Francis, London, 1990); F. Gebhard, *The Mott Metal-Insulator Transition* (Springer, Berlin, 1997).

[2] J. Hubbard, Proc. R. Soc. London, Ser. A **276**, 238 (1963); M. C. Gutzwiller, Phys. Rev. Lett. **10**, 159 (1963); J. Kanamori, Prog. Theor. Phys. **30**, 275 (1963).

[3] F. Essler, H. Frahm, F. Göhmann, A. Klümper, and V. Korepin, *The One-Dimensional Hubbard Model* (Cambridge University Press, Cambridge, 2010).

[4] K. Kawakami, T. Usuki, and A. Okiji, Phys. Lett. A **137**, 287 (1989).

[5] T. D. Stanescu and P. Phillips, Phys. Rev. B **64**, 235117 (2001).

[6] A. Georges, G. Kotliar, W. Krauth, and M. Rozenberg, Rev. Mod. Phys. **68**, 13 (1996).

[7] W. Metzner and D. Vollhardt, Phys. Rev. Lett. **62**, 324 (1989).

[8] A. Georges and G. Kotliar, Phys. Rev. B **45**, 6479 (1992).

[9] P. R. C. Kent, M. Jarrell, T. A. Maier, and Th. Pruschke, Phys. Rev. B **72**, 060411(R) (2005).

[10] R. Staudt, M. Dzierzawa, and A. Muramatsu, Eur. Phys. J. B **17**, 411 (2000); E. Kozik, E. Burovski, V. W. Scarola, and M. Troyer, Phys. Rev. B **87**, 205102 (2013).

[11] G. Rohringer, A. Toschi, A. Katanin, and K. Held, Phys. Rev. Lett. **107**, 256402 (2011).

[12] S. Fuchs, E. Gull, L. Pollet, E. Burovski, E. Kozik, T. Pruschke, and M. Troyer, Phys. Rev. Lett. **106**, 030401 (2011).

[13] E. Gull, P. Staar, S. Fuchs, P. Nukala, M. S. Summers, T. Pruschke, T. C. Schulthess, and T. Maier, Phys. Rev. B **83**, 075122 (2011).

[14] P. Hansmann, A. Toschi, G. Sangiovanni, T. Saha-Dasgupta, S. Lupi, M. Marsi, and K. Held, Phys. Status Solidi B **250**, 1251 (2013).

[15] C. Castellani, C. Di Castro, D. Feinberg, and J. Ranninger, Phys. Rev. Lett. **43**, 1957 (1979).

[16] M. Vekic and S. R. White, Phys. Rev. B **47**, 1160 (1993).

[17] F. Mancini, Eur. Phys. Lett. **50**, 229 (2000).

[18] R. Eder, C. Gröber, M. C. Zacher, and W. Hanke, in *Open Problems in Strongly Correlated Electron Systems*, edited by J. Bonca *et al.*, NATO Science Series, Series II, Mathematics, Physics, and Cchemistry Vol. 15, (Kluwer Academic, Dordrecht, 2001), Part I, pp. 23–31.

[19] A. Avella, F. Mancini, and R. Münzner, Phys. Rev. B **63**, 245117 (2001).

[20] F. Mancini and A. Avella, Adv. Phys. **53**, 537 (2007).

[21] J. M. Vilk and A.-M. S. Tremblay, Eur. Phys. Lett. **33**, 159 (1996); J. Phys. I **7**, 1309 (1997).

[22] S. Moukouri, S. Allen, F. Lemay, B. Kyung, D. Poulin, Y. M. Vilk, and A.-M. S. Tremblay, Phys. Rev. B **61**, 7887 (2000).

[23] A.-M. Darè, L. Raymond, G. Albinet, and A.-M. S. Tremblay, Phys. Rev. B **76**, 064402 (2007).

[24] Due to the strong-coupling nature of correlations in two dimensions at low T the applicability of more conventional perturbative schemes is typically very limited. Specifically, the fluctuation exchange approximation (FLEX) is unable to predict a pseudogap phase in the 2D Hubbard model in the sense of momentum differentiation (see, e.g., [21]). The one-loop functional renormalization group/parquet approximations (PA) do not satisfy the Mermin-Wagner theorem (see [59]) and find long-range antiferromagnetic order at finite T.

[25] P. W. Anderson, *The Theory of Superconductivity in the High-T_C Cuprates*, Princeton Series in Physics (Princeton University Press, Princeton, NJ, 1997).

[26] H. Park, K. Haule, and G. Kotliar, Phys. Rev. Lett. **101**, 186403 (2008).

[27] T. A. Maier, M. Jarrell, T. Pruschke, and M. H. Hettler, Rev. Mod. Phys. **77**, 1027 (2005).

[28] Early pioneering DCA results [60] indicating a reduction of U_c have been questioned [61, 53] and show imprecise estimates of U_c as well as no coexistence region. These have been superseded by more recent cluster-DMFT [26] and DCA analyses [62, 63].

[29] A. N. Rubtsov, M. I. Katsnelson, and A. I. Lichtenstein, Phys. Rev. B **77**, 033101 (2008); S. Brener, H. Hafermann, A. N. Rubtsov, M. I. Katsnelson, and A. I. Lichtenstein, *ibid.* **77**, 195105 (2008).

[30] H. Hafermann, Ph.D. thesis, University of Hamburg, 2009.

[31] M. Potthoff, M. Aichhorn, and C. Dahnken, Phys. Rev. Lett. **91**, 206402 (2003).

[32] A. Toschi, A. A. Katanin, and K. Held, Phys. Rev. B **75**, 045118 (2007); K. Held, A. A. Katanin, and A. Toschi, Prog. Theor. Phys. Suppl. **176**, 117 (2008).

[33] R. Blankenbecler, D. J. Scalapino, and R. L. Sugar, Phys. Rev. D **24**, 2278 (1981).

[34] F. F. Assaad and H. G. Evertz, in *Computational Many Particle Physics*, edited by H. Fehske, R. Schneider, and A. Weiße, Lecture Notes in Physics Vol. 739 (Springer, Berlin, 2008), p. 277.

[35] M. Golor, T. Reckling, L. Classen, M. M. Scherer, and S. Wessel, Phys. Rev. B **90**, 195131 (2014).

[36] N. Blümer, Phys. Rev. B **76**, 205120 (2007).

[37] D. Rost, E. V. Gorelik, F. Assaad, and N. Blümer, Phys. Rev. B **86**, 155109 (2012).

[38] M. Balzer, B. Kyung, D. Senechal, A.-M. S. Tremblay, and M. Potthoff, Europhys. Lett. **85**, 17002 (2009).

[39] N. Blümer, Ph.D. thesis, University of Augsburg, 2002.

[40] A. A. Katanin, A. Toschi, and K. Held, Phys. Rev. B **80**, 075104 (2009).

[41] N. D. Mermin and H. Wagner, Phys. Rev. Lett. **17**, 1133 (1966).

[42] G. Rohringer, A. Toschi, H. Hafermann, K. Held, V. I. Anisimov, and A. A. Katanin, Phys. Rev. B **88**, 115112 (2013).

[43] C. Taranto, S. Andergassen, J. Bauer, K. Held, A. Katanin, W. Metzner, G. Rohringer, and A. Toschi, Phys. Rev. Lett. **112**, 196402 (2014); N. Wentzell, C. Taranto, A. Katanin, A. Toschi, and S. Andergassen, Phys. Rev. B **91**, 045120 (2015).

[44] G. Rohringer, A. Valli, and A. Toschi, Phys. Rev. B **86**, 125114 (2012).

[45] T. Schäfer, G. Rohringer, O. Gunnarsson, S. Ciuchi, G. Sangiovanni, and A. Toschi, Phys. Rev. Lett. **110**, 246405 (2013).

[46] E. Gull, M. Ferrero, O. Parcollet, A. Georges, and A. J. Millis, Phys. Rev. B **82**, 155101 (2010).

[47] A. Altland and B. Simons, *Condensed Matter Field Theory* (Cambridge University Press, Cambridge, 2006).

[48] J. P. F. Le Blanc and E. Gull, Phys. Rev. B **88**, 155108 (2013).

[49] S. R. White, D. J. Scalapino, R. L. Sugar, E. Y. Loh, J. E. Gubernatis, and R. T. Scalettar, Phys. Rev. B **40**, 506 (1989).

[50] T. Baier, E. Bick, and C. Wetterich, Phys. Rev. B **70**, 125111 (2004).

[51] K. Borejsza and N. Dupuis, Europhys. Lett. **63**, 722 (2003); Phys. Rev. B **69**, 085119 (2004).

[52] E. M. Motoyama, G. Yu, I. M. Vishik, O. P. Vajk, P. K. Mang, and M. Graven, Nature (London) **445**, 186 (2007).

[53] E. Gull, P. Werner, X. Wang, M. Troyer, and A. J. Millis, Eur. Phys. Lett. **84**, 37009 (2008).

[54] C. Taranto, G. Sangiovanni, K. Held, M. Capone, A. Georges, and A. Toschi, Phys. Rev. B **85**, 085124 (2012); A. Toschi, M. Capone, and C. Castellani, *ibid.* **72**, 235118 (2005).

[55] E. Gull and A. J. Millis, Phys. Rev. B **86**, 241106(R) (2012).

[56] P. Korbel, W. Wójcik, A. Klejnberg, J. Spałek, M. Acquarone, and M. Lavagna, Eur. Phys. J. B **32**, 315 (2003).

[57] E. V. Gorelik and N. Blümer, Phys. Rev. A **80**, 051602(R) (2009).

[58] N. Blümer and E. V. Gorelik, Phys. Rev. B **87**, 085115 (2013).

[59] A. T. Zheleznyak, V. M. Yakovenko, and I. E. Dzyaloshinskii, Phys. Rev. B **55**, 3200 (1997).

[60] S. Moukouri and M. Jarrell, Phys. Rev. Lett. **87**, 167010 (2001).

[61] B. Kyung, J. S. Landry, D. Poulin, and A.-M. S. Tremblay, Phys. Rev. Lett. **90**, 099702 (2003).

[62] J. Merino and O. Gunnarsson, Phys. Rev. B **89**, 245130 (2014).

[63] E. Gull, O. Parcollet, and A. J. Millis, Phys. Rev. Lett. **110**, 216405 (2013).

Deciding the fate of the false Mott transition in two dimensions by exact quantum Monte Carlo methods

D. Rost[1,2] **and N. Blümer**[1]

[1] Institute of Physics, Johannes Gutenberg University, Mainz, Germany
[2] Grad. School Materials Science in Mainz, Johannes Gutenberg University, Mainz, Germany

E-mail: rostda@uni-mainz.de

Abstract. We present an algorithm for the computation of unbiased Green functions and self-energies for quantum lattice models, free from systematic errors and valid in the thermodynamic limit. The method combines direct lattice simulations using the Blankenbecler-Scalapino-Sugar quantum Monte Carlo (BSS-QMC) approach with controlled multigrid extrapolation techniques. We show that the half-filled Hubbard model is insulating at low temperatures even in the weak-coupling regime; the previously claimed Mott transition at intermediate coupling does not exist.

1. Introduction

Numerous studies of the Hubbard model [1] have greatly enhanced our understanding of strongly correlated electron systems within the last four decades. Specialized methods, namely the semi-analytic Bethe ansatz and the density matrix renormalization group (DMRG) [2], yield reliable high-precision results (only) in the case of one spatial dimension. Conversely, the dynamical mean-field theory (DMFT) [3, 4] provides deep insight in the limit of high dimensionality. However, the intermediate regime of two (and three) dimensions is less well understood, e.g., with respect to pseudogap physics [5–7] and high-T_c superconductivity. In this paper, we will address another open question: the nature of the Mott metal-insulator transition (MIT) [8,9] of the half-filled Hubbard model in two dimensions ($D = 2$).

As indicated by shaded regions in Fig. 1, the Hubbard model is insulating at half filling (1 electron per site) and sufficiently strong coupling, in any dimension, while it is metallic at weak coupling – as long as the translational symmetry is not broken, e.g., by magnetic order. For $D = 3$, one finds antiferromagnetic (AF) ordering [10], which implies insulating behavior, below the Néel temperature T_N (gray dash-dotted line). Such long-range order is ruled out by the Mermin-Wagner theorem in $D = 2$ (at temperature $T > 0$). Single-site DMFT predicts a MIT with critical interactions $2.3 \lesssim U_c \lesssim 2.9$ (pink dotted line). This transition line is shifted to weaker interactions within cluster DMFT (CDMFT), which includes short-range correlations on small clusters (violet solid line) [11]. However, the low-T metallic phase implied by the CDMFT result is incompatible with several earlier studies highlighting effects of "short-range antiferromagnetism" [7, 12, 13]. To clarify the situation, we apply the Blankenbecler-Scalapino-Sugar quantum Monte Carlo (BSS-QMC) [14] approach with controlled multigrid extrapolation techniques to selected points in the phase diagram (green crosses). We will show that these points are separated by a MIT line (or narrow crossover) and conclude that the $2D$ Mott physics is quite similar to the $3D$ case [15], in spite of the Mermin-Wagner theorem.

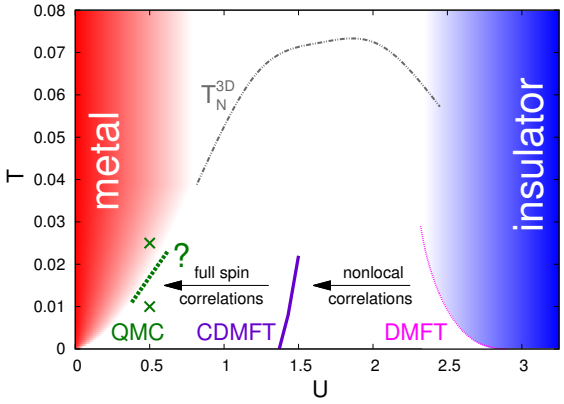

Figure 1. Schematic representation of the MIT in the Hubbard model at half filling on a square lattice. Green crosses: parameters selected for our unbiased QMC study. Gray dash-dotted line: Néel temperature for the cubic lattice (rescaled).

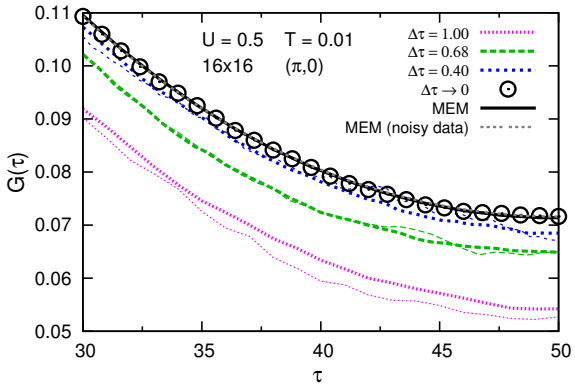

Figure 2. Extrapolation of BSS-QMC Green functions to $\Delta\tau \to 0$. Analytic continuation (MEM, black line) regularizes the results of pointwise extrapolations (symbols) and yields stable results (gray line) even in the case of noisy raw data (thin color lines).

2. Model and Methods

The single-band Hubbard Hamiltonian is given by

$$\hat{H} = -\,t \sum_{\langle ij\rangle,\sigma} \hat{c}^\dagger_{i\sigma}\hat{c}_{j\sigma} + U\sum_i \left(\hat{n}_{i\uparrow} - \frac{1}{2}\right)\left(\hat{n}_{i\downarrow} - \frac{1}{2}\right), \tag{1}$$

with number operators $\hat{n}_{i\sigma} = \hat{c}^\dagger_{i\sigma}\hat{c}_{i\sigma}$, next-neighbor hopping t, and local interactions U. In this paper, we set $t = 0.25$ and consider finite-size clusters with periodic boundary conditions.

The BSS-QMC algorithm is based on a Trotter-Suzuki decomposition of the partition function

$$Z = \mathrm{Tr}\left(e^{-\beta(H_t+H_U)}\right) \approx Z_{\Delta\tau} = \mathrm{Tr}\left(\prod_{l=0}^{\Lambda} e^{-\Delta\tau H_t} e^{-\Delta\tau H_U}\right), \tag{2}$$

where H_U (H_t) corresponds to the interaction (kinetic) term in (1), $\beta = 1/T$ is the inverse temperature ($k_b \equiv 1$) and Λ denotes the number of time slices ($\Lambda = \beta/\Delta\tau$). A discrete Hubbard-Stratonovich transformation simplifies the interaction term, which is quartic in the fermionic operators, to a quadratic form and a coupling to an auxiliary Ising field h. As usual for quadratic Hamiltonians, the fermionic degrees of freedom can be integrated out and the partition function is expressed by determinants of matrices:

$$Z_{\Delta\tau} = \sum\nolimits_{\{h\}} \det\left[M_\uparrow^{\{h\}}\right] \det\left[M_\downarrow^{\{h\}}\right]. \tag{3}$$

The sum in (3), and finally the computation of all observables, is performed by Monte Carlo methods. The main results of the BSS-QMC algorithm are Green functions $G_{ij}(\tau_l)$ on a discrete imaginary-time grid $\{\tau_l \in [0,\beta]\}$ for each pair of real-space coordinates $\{i,j\}$ on the given lattice. The involved matrix operations for the calculation of the determinants in (3) lead to a scaling of $\mathcal{O}(\Lambda\, N_c^3)$, which restricts the algorithm to relatively small clusters ($N_c \lesssim 400$).

To arrive at reliable conclusions regarding the Mott transition using BSS-QMC, one has first to eliminate all systematic errors (finite-size as well as Trotter errors) and, secondly, calculate the self-energy on the Matsubara axis, $\Sigma(i\omega_n)$, from the imaginary-time Green function in a stable manner. These steps are described in the following.

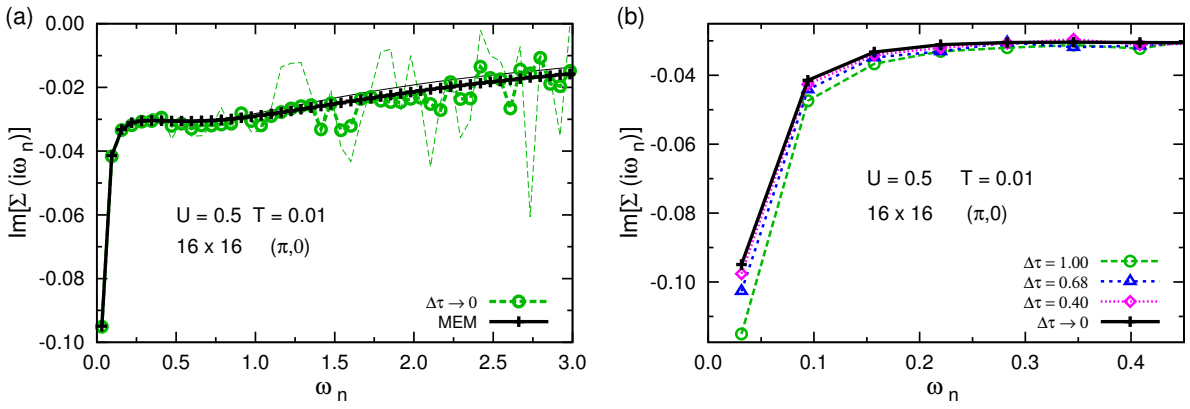

Figure 3. (a) Influence of statistical noise in the raw data $G(\tau)$ on the self-energy $\Sigma(i\omega_n)$ and stabilization by MEM regularization. Thin lines: noisy data, thick lines and symbols: high precision results. (b) Impact of Trotter discretization $\Delta\tau$ on the Matsubara self-energy.

3. Elimination of systematic errors

As the elimination of Trotter errors is well established [16–19], we will sketch the scheme only briefly and focus on the problem specific and physically more relevant finite-size analysis and present a stable method to calculate unbiased Green functions, even if the raw data are noisy.

Trotter bias – The raw BSS-QMC Green functions (thick colored lines in Fig. 2) do not only live on different imaginary-time grids $\{\tau_i\}$, depending on the chosen discretization $\Delta\tau$, but are also shifted with respect to each other (and to the exact solution). After aligning them on a common fine grid [20] the Trotter errors can be eliminated with high precision by piecewise extrapolations of $\Delta\tau \to 0$ (circles) [19]. However, some fluctuations remain inevitably, especially when using noisy raw data (using a factor of 10 less QMC sweeps; thin colored lines). These can be greatly reduced by regularization via a maximum entropy method (MEM), which computes corresponding spectral functions via the inversion of

$$G(\tau) = -\int_{-\infty}^{\infty} d\omega\, A(\omega)\, \frac{e^{-\omega\tau}}{1+e^{-\omega\beta}} \quad . \tag{4}$$

Note that the intermediate spectra $A(\omega)$ are used only for producing continuous and smooth Green functions $G(\tau)$ via (4); in this combination, the procedure is stable. After this step, the results based on high- or low-precision data (thick black line vs. gray line) are hardly distinguishable and can both be used for stable computations of self-energies.

Self-energy – These quasi-continuous $G(\tau)$ can be reliably Fourier transformed to the Matsubara axis:

$$G(i\omega_n) = \int_0^{\beta} d\tau\, G(\tau)\, e^{-i\omega_n\tau} \quad . \tag{5}$$

A quantity of great interest for the analysis of the Mott transition is the imaginary part of the momentum-resolved self-energy, which is connected to the BSS-QMC Green function G and the non-interacting Green function $\mathcal{G}$ via a Dyson equation [21]

$$\Sigma_{\mathbf{k}}(i\omega_n) = \mathcal{G}^{-1}_{\mathbf{k}}(i\omega_n) - G^{-1}_{\mathbf{k}}(i\omega_n) = i\omega_n + \mu - \epsilon_{\mathbf{k}} - G^{-1}_{\mathbf{k}} \quad , \tag{6}$$

where μ is the chemical potential and $\epsilon_{\mathbf{k}}$ the dispersion of the noninteracting problem. As shown in Fig. 3 (b), the MEM regularizing procedure leads to estimates (crosses and black line) of the imaginary part of the self-energy (the real part vanishes at $\mathbf{k} = (\pi, 0)$ due to particle-hole

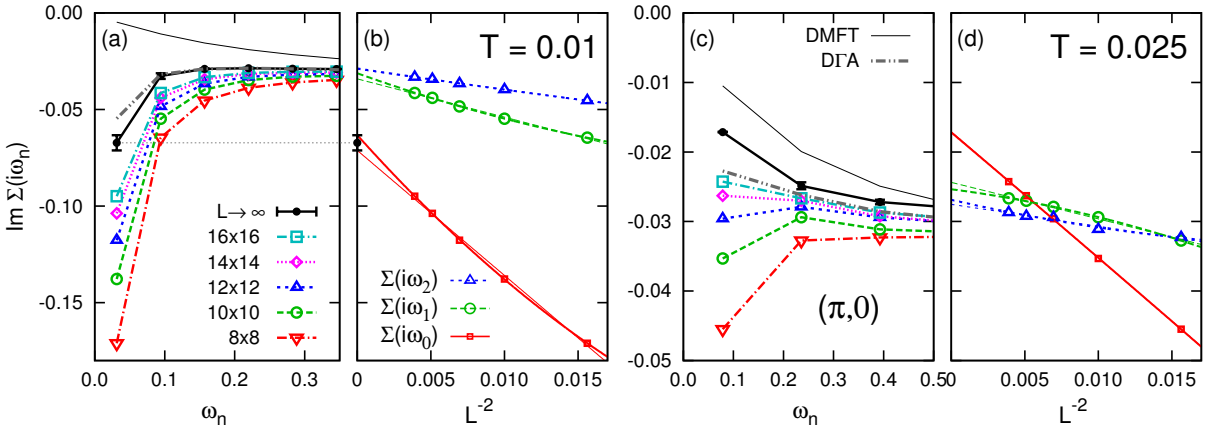

Figure 4. Finite-size scaling of Matsubara self-energy at $U = 0.5$, $\mathbf{k} = (\pi, 0)$. Finite-size BSS-QMC data (open symbols and broken colored lines), extrapolated BSS-QMC results in the thermodynamic limit (circles and black bold solid line), and DΓA data (gray line) versus Matsubara frequency ω_n at $T = 0.01$ (a) and $T = 0.025$ (c); also shown are momentum-independent single-site DMFT results (thin black lines). (b)+(d) Finite-size BSS-QMC (symbols) data for the first three Matsubara frequencies versus inverse system size plus extrapolations in linear order in L^{-2} (thin lines) and quadratic order (thick lines).

symmetry) which are smooth even at higher frequencies. In contrast, the direct results (green circles) fluctuate significantly even when based on high-precision raw data (and even more so for noisy raw data; thin dashed green lines). Note that both methods agree very well at the lowest Matsubara frequencies, where the QMC predictions are most reliable.

In Fig. 3 (b) the influence of the Trotter discretization is shown. The Trotter biased self-energies (broken colored lines) deviate from the exact result (black solid line) for large values of $\Delta\tau$, in particular at the lowest frequencies. However, in the parameter regime explored in this study, we can afford small enough values of $\Delta\tau$ so that the elimination of Trotter errors is less essential than the finite-size extrapolation to be discussed below.

Finite-size extrapolation of the self-energy – Using the methods described above, unbiased and stable estimates of the Matsubara self-energy have been obtained for square $L \times L$ clusters with sizes ranging from 8×8 to 16×16 (with a computational effort that varies as $N_c^3 = L^6$, i.e., by a factor of $2^6 = 64$ in this range). Results at the "anti-nodal" [22] momentum point $\mathbf{k} = (\pi, 0)$ [throughout the paper, unit lattice spacing $a = 1$ is assumed] are shown (colored symbols and broken lines) in Fig. 4(a) for the low temperature $T = 0.01$ and in Fig. 4(c) for the elevated temperature $T = 0.025$, respectively. Evidently, the finite-size effects are enormous: while the smallest systems (8×8, triangles) show insulating behavior, i.e., a strong enhancement of $\Sigma(i\omega_n)$ towards small frequencies, at both temperatures, this tendency is reduced with increasing L at $T = 0.01$ [Fig. 4(a)] and completely eliminated at $T = 0.025$ [Fig. 4(c)]. Obviously, careful extrapolations are needed for reliable predictions in the thermodynamic limit.

These are, indeed, possible, as shown in Fig. 4(b) for $T = 0.01$ and in Fig. 4(d) for $T = 0.025$, respectively, for the three lowest Matsubara frequencies (where the finite-size effects are largest): as a function of L^{-2}, the finite-size results (symbols) can be fitted with second-order polynomials (thick lines) with high precision; as these fit functions have small curvatures, linear extrapolations (thin lines) to the thermodynamic limit (i.e., $L^{-2} \to 0$) deviate only slightly from the quadratic ones. We use these deviations as error bars and the arithmetic average of both extrapolation procedures as final result, as indicated for $\Sigma(i\omega_0)$ by a black symbol in Fig. 4(b).

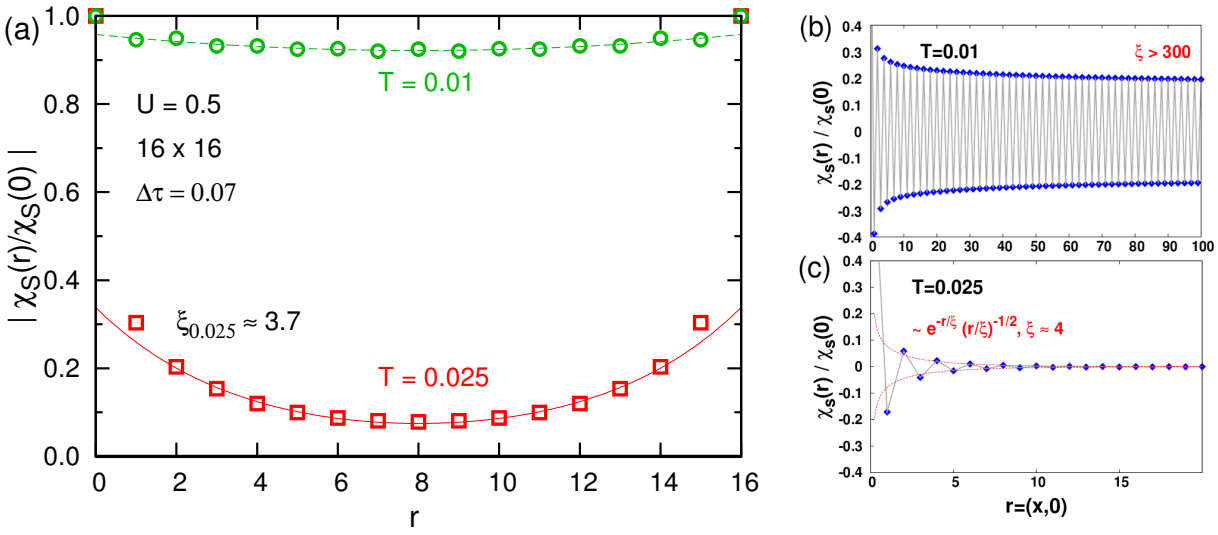

Figure 5. Real-space spin correlation function. (a) The correlation length for $T = 0.025$ (red squares) from BSS-QMC calculations for a 16×16 lattice is estimated by an exponential fit (red solid line). For $T = 0.01$ (green circles) ξ is much larger than the extend of the lattice. *Right panel:* The corresponding estimations from DΓA data [25] for $T = 0.01$ (b) and $T = 0.025$ (c) confirm the BSS-QMC results.

4. Mott physics and correlation lengths

These final QMC results [black symbols and lines in Fig. 4(a) and Fig. 4(c)] show that the character of the system changes drastically between the selected phase points (crosses in Fig. 1): while the QMC self-energy indicates a metallic phase at $T = 0.025$, very similar to the DMFT solution [thin black line in Fig. 4(c)], the low-temperature phase is clearly insulating - and completely unlike the paramagnetic DMFT solution [thin black line in Fig. 4(a)]. In contrast, the QMC results are strikingly similar to the DΓA predictions (gray dash-dotted lines), especially at low T. The dynamical vertex approximation ($D\Gamma A$) [23, 24] is a diagrammatic extension of DMFT which works directly in the thermodynamic limit (without any need for finite-size extrapolations); for the full set of $D\Gamma A$ results see [25]. QMC and DΓA together show convincingly that the suspected phase transition (dotted line in Fig. 1) is, indeed, present.

The question remains how exactly this metal-insulator transition (or crossover) is related to magnetic properties. After all, long-range AF order is excluded, in $D = 2$, by the Mermin-Wagner theorem. However, as shown in Fig. 5(a), the spin correlations decay much more slowly at $T = 0.01$ (circles) than at $T = 0.025$ (squares). More precisely, the correlation length at the elevated temperature can be estimated (using 16×16 QMC data) to $\xi \approx 3.7$ while it is clearly too large ($\xi \gg 30$) at $T = 0.01$ to allow precise determination using QMC. For this observable, DΓA predictions, shown in Fig. 5(b) and Fig. 5(c) are more reliable, yielding correlation lengths of $\xi \approx 4$ at the higher temperature, in excellent agreement with QMC, and $\xi > 300$ at $T = 0.01$, also consistent with QMC. Using DΓA we could also show that the temperature dependence of ξ changes its character at the Mott transition (see [25]).

Conclusion and acknowledgements

In spite of its simplifications, the Hubbard model remains a challenging target for theorists, especially in the interesting case of two spatial dimensions. All available methods have certain limitations, many of which are of particular concern in the nonperturbative intermediate-

coupling regime at low temperatures and in the presence of longer-range correlations. Therefore, a single method can hardly yield authoritative results; some predictions may even be completely off (such as the CDMFT transition line in Fig. 1).

In the study presented in this work (with focus on the QMC methodology; for the full story, see [25]), we have applied two methods (an unbiased variant of BSS-QMC as well as the dynamical vertex approximation) with completely different characteristics. Only the near-perfect agreement between both sets of results makes the predictions truly authoritative (and validates technical choices on either side). We have settled one important question at half filling, namely the character of the Mott metal-insulator transition on the square lattice: it is driven by exponentially long-ranged [25] antiferromagnetic correlations, which act similarly to the AF long-range order in the cubic case, and is **not** connected to a quantum-critical point at $U > 0$.

The same methodology may be useful in other parameter ranges, e.g., for frustrated or anisotropic Hubbard models, doped systems, or multi-band models. It might also be worthwhile to compute transport properties, within bubble approximation or beyond, in order to observe the metal-insulator transition even more directly (than via the self-energy).

We acknowledge support from the research unit FOR 1346 of the German Research Foundation (DFG) and the graduate school GSC 266.

References

[1] Hubbard J 1959 *Phys. Rev. Lett.* **3** 77–78
[2] Schollwöck U 2005 *Rev. Mod. Phys.* **77** 259
[3] Metzner W and Vollhardt D 1989 *Phys. Rev. Lett.* **62** 324–327
[4] Georges A, Kotliar G, Krauth W and Rozenberg M J 1996 *Rev. Mod. Phys.* **68** 13–125
[5] Lee P A and Wen X-G 2006 *Rev. Mod. Phys.* **78** 17
[6] Armitage N, Fournier P and Greene R 2010 *Rev. Mod. Phys.* **82** 2421
[7] Rost D, Gorelik E V, Assaad F F and Blümer N 2012 *Phys. Rev.* B **86** 155109
[8] Mott N F 1968 *Rev. Mod. Phys.* **40** 677
[9] Gebhard F 1997 *The Mott Metal-Insulator Transition* (Springer Berlin)
[10] Staudt R, Dzierzawa M and Muramatsu A 2000 *Eur. Phys. J. B* **17** 411
[11] Park H, Haule K and Kotliar G 2008 *Phys. Rev. Lett.* **101** 186403
[12] Gorelik E V, Rost D, Paiva T, Scalettar R, Klümper A and Blümer N 2012 *Phys. Rev.* A **85** 061602
[13] Chang C-C, Scalettar R T, Gorelik E V and Blümer N 2013 *Phys. Rev.* B **88** 195121
[14] Blankenbecler R, Scalapino D J, and Sugar R L 1981 *Phys. Rev.* D **24** 2278
[15] Fuchs S, Gull E, Troyer M, Jarrell M and Pruschke T 2011 *Phys. Rev.* B **83** 235113
[16] Blümer N 2007 *Phys. Rev.* B **76** 205120
[17] Blümer N 2008 Preprint *arXiv*:08011222
[18] Gorelik E V and Blümer N 2009 *Phys. Rev.* A **80** 051602(R)
[19] Rost D, Assaad F F and Blümer N 2013 *Phys. Rev.* E **87** 053305
[20] This nontrivial task is achieved using reference models and spline interpolation of differences between measured and reference Green functions [7, 16, 17, 27, 30].
[21] Fetter A L and Walecka J D 1971 *Quantum Theory of Many-Particle Systems* McGraw-Hill
[22] In the context of high-T_c and pseudogap physics, one distinguishes "nodal" from "anti-nodal" points on the noninteracting Fermi surface. The observed dichotomy in the pseudogap phase can be viewed as "momentum-selective" Mott physics [26], in analogy to orbital-selective Mott phases [27–29] observed in systems with inequivalent bands.
[23] Toschi A, Katanin A A and Held K 2007 *Phys. Rev.* B **75** 045118
[24] Held K, Katanin A A and Toschi A 2008 *Prog. Theor. Phys. Suppl.* **176** 117
[25] Schäfer T, Geles F, Rost D, Rohringer G, Arrigoni E, Held K, Blümer N, Aichhorn M and Toschi A 2014 *Phys. Rev.* B **91** 125109
[26] Ferrero M, Cornaglia P, De Leo L, Parcollet O, Kotliar G and Georges A 2009 *Phys. Rev.* B **80** 064501
[27] Knecht C, Blümer N and van Dongen P G V 2005 *Phys. Rev.* B **72** 081103(R)
[28] Jakobi E, Blümer N and van Dongen P G V 2009 *Phys. Rev.* B **80** 115109
[29] Jakobi E, Blümer N and van Dongen P G V 2013 *Phys. Rev.* B **87** 205135
[30] Blümer N and Kalinowski E 2005 *Phys. Rev.* B **71** 195102